

**Symmetry and non-Hermiticity
in anomalous Floquet topological insulators**

Inauguraldissertation

zur

Erlangung des akademischen Grades eines

Doktors der Naturwissenschaften
(Dr. rer. nat.)

der

Mathematisch-Naturwissenschaftlichen Fakultät

der

Universität Greifswald

vorgelegt von

Bastian Höckendorf

geboren am 28.02.1993

in Ribnitz-Damgarten

Greifswald, 30.03.2020

Dekan:	Prof. Dr. Gerald Kerth
1. Gutachter:	Prof. Dr. Holger Fehske
2. Gutachter:	Prof. Dr. Netanel Lindner
3. Gutachter:	Prof. Dr. Jiangbin Gong
Tag der Disputation:	07.08.2020

Contents

1	Summary	1
1.1	Introduction	1
1.2	Topological invariants	3
1.3	Implementation	9
1.4	Non-Hermitian engineering	15
1.5	Conclusions	23
2	Thesis articles	25
2.1	Article I — Topological invariants for Floquet-Bloch systems with chiral, time-reversal, or particle-hole symmetry	27
2.2	Article II — Universal driving protocol for symmetry-protected Floquet topological phases	39
2.3	Article III — Fermionic time-reversal symmetry in a photonic topological insulator	53
2.4	Article IV — Non-Hermitian Boundary State Engineering in Anomalous Floquet Topological Insulators	87
2.5	Article V — Non-Hermitian Floquet Chains as Topological Charge Pumps	99
2.6	Article VI — Cutting of the non-Hermitian boundary from an anomalous Floquet topological insulator	113
	Bibliography	119
	Scientific contributions	125
	Acknowledgement	127

1 Summary

1.1 Introduction

This thesis contains studies on a special class of topological insulators, so called anomalous Floquet topological insulators, which exclusively occur in periodically driven systems. At the boundary of an anomalous Floquet topological insulator, topologically protected transport occurs even though all of the Floquet bands are topologically trivial [1, 2]. This is in stark contrast to ordinary topological insulators of both static [3–10] and Floquet type [11–14], where the topological invariants of the bulk bands completely determine the chiral boundary states via the bulk-boundary correspondence [15–17]. In anomalous Floquet topological insulators, the boundary states are instead characterized by bulk invariants that account for the full dynamical evolution of the Floquet system [2].

In this thesis we focus on anomalous Floquet topological phases in two-dimensional Floquet systems. Our contributions to this field are grouped into three sections (see Fig. 1): topological invariants (Sec. 1.2), implementation (Sec. 1.3), and non-Hermitian engineering (Sec. 1.4).

The central quantity that classifies two-dimensional anomalous Floquet topological insulators in the absence of symmetries is the \mathbb{Z} -valued W_3 invariant [2, 18]. First, we show that the W_3 invariant can be expressed as a sum over all degeneracy points of the propagator that occur during time evolution (article I). This generalizes a similar expression introduced in Ref. [19]. To each degeneracy point, two integers are assigned that account for the topological properties of the eigenvectors and eigenvalues of the propagator. Second, we analyze symmetry-protected anomalous Floquet topological insulators with counterpropagating boundary states for which the W_3 invariant necessarily vanishes. We find that the degeneracy points of the propagator appear in symmetric pairs that cancel in the expression of the W_3 invariant. By counting only one partner of each pair, symmetry-adapted \mathbb{Z}_2 invariants are deduced which correctly predict the symmetry-protected boundary states (also article I). In this manner, the construction introduced here enables a unified topological classification of anomalous Floquet topological phases in terms of degeneracy points and the efficient computation of the relevant topological invariants with the algorithm we developed in Ref. [20].

Anomalous Floquet topological phases can potentially occur in any Floquet lattice model [21, 22], but the natural framework for their theoretical study as well as experimental realization are so called driving protocols [1, 2, 23–27]. A driving protocol consists of a finite number of consecutive steps during which the Hamiltonian is constant and pairwise coupling occurs between adjacent lattice sites. An anomalous Floquet topological phase occurs when the steps are arranged such that the pairwise coupling enforces closed trajectories in the bulk of the lattice, but chiral transport at the boundaries. Photonic lattices of evanescently coupled waveguides are well-suited to implement these protocols [28–32]. In photonic lattices, the pairwise coupling in each step is

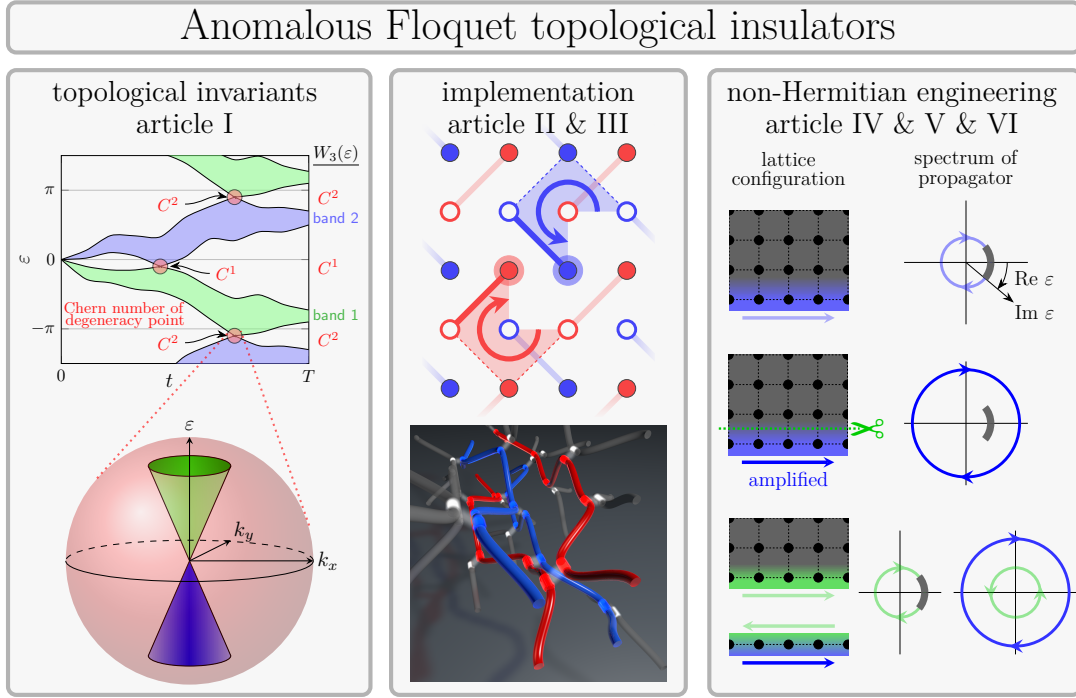


Figure 1: Illustration of the main results of this thesis. Left column: Degeneracy-point expressions of the topological invariants. Central column: The universal driving protocol (top) and its implementation in photonic waveguide lattices (bottom). Right column: Non-Hermitian engineering of boundary transport. Adapted from articles I, II, III, and VI.

realized by spatially periodic modulation of the interwaveguide distance through waveguide bending. Prior to our work, driving protocols for anomalous Floquet topological phases without symmetries had been theoretically proposed [1, 2] and experimentally realized [30, 31], but theoretical proposals for symmetry-protected anomalous Floquet topological phases were still missing. Here, we construct a universal driving protocol for symmetry-protected anomalous Floquet topological phases (article II). The construction is based on the analysis of the possible symmetry operators for a driving protocol with only pairwise couplings. A unique feature of the time-reversal symmetric variant of the universal driving protocol is the occurrence of Kramers degenerate counterpropagating boundary states without fermionic spin 1/2 degrees of freedom. The experimental implementation of the time-reversal symmetric protocol in photonic waveguide lattices (article III) thus constitutes the first realization of a bosonic topological insulator with fermionic time-reversal symmetry.

The waveguide bending introduces losses [30, 31], i.e. non-Hermiticity, into the photonic implementation of anomalous Floquet topological insulators. Therefore, the influence of non-Hermiticity on the topological properties of Floquet systems has to be investigated. For static systems, the interplay between non-Hermiticity and topology has been rapidly explored in the last few years [33–47]. New non-Hermitian topological phases which arise from imaginary and point gaps in the complex-valued spectrum [33–35, 45–47] have been discovered and the topological classification of non-Hermitian static

systems has recently been established [34, 35]. For anomalous Floquet topological insulators, the role of non-Hermiticity remained unexplored prior to our work. We find that the interplay between non-Hermiticity and anomalous Floquet topological phases provides a powerful tool to engineer the transport properties of the boundary states. When non-Hermiticity is introduced at the boundary of an anomalous Floquet topological insulator, the boundary states can spectrally detach from the bulk bands. During this process, an imaginary gap opens between the bulk bands and boundary states. We denote the spectral detachment and the ensuing possibilities to manipulate the spectrally detached boundary states as non-Hermitian boundary state engineering (article IV). The versatility of boundary state engineering is demonstrated for the time-reversal symmetric variant of the universal driving protocol, where it allows us to amplify the boundary transport relative to the bulk motion and even suppress one of the two counterpropagating boundary states. Beyond the amplification or attenuation of boundary transport, the spectral detachment has another important consequence: The imaginary gap provides topological protection for the detached boundary states. Consequently, the detached boundary states no longer depend on the bulk topology. In particular, the non-Hermitian boundary can be physically cut off from the bulk while retaining its topological transport properties (article VI). The resulting one-dimensional chain possesses a novel non-Hermitian Floquet topological phase which has no counterpart in static or Hermitian systems. The transport signature of this phase is charge pumping which is robustly quantized in the limit of large non-Hermiticity (article V). Note that quantized charge pumping can also occur in Hermitian anomalous Floquet topological insulators, but is restricted to fine-tuned parameter values [1, 2] and thus not robust. Even in anomalous Floquet-Anderson insulators [48] (anomalous Floquet topological insulators with an Anderson localized bulk), only the charge pumped over a large number of driving periods is robustly quantized. In the present non-Hermitian setting, robustly quantized charge pumping occurs in each individual driving cycle.

In total, this thesis explores the interplay between topology, symmetry, and non-Hermiticity in the joint platform of two-dimensional Floquet systems. The (symmetry-adapted) degeneracy-point expressions of the topological invariants, the universal driving protocol, and the concept of boundary state engineering constitute the central results of this exploration.

1.2 Topological invariants

The starting point for all of our calculations is the propagator $U(t)$, which is the solution of the Schrödinger equation $i\partial_t U(t) = H(t)U(t)$ for a two-dimensional lattice model. At $t = 0$, the propagator reduces to the identity $U(0) = \mathbb{1}$. We assume that the Hamiltonian $H(t)$ is Hermitian $H^\dagger(t) = H(t)$ so that the propagator is a unitary operator $U^\dagger(t) = U^{-1}(t)$ (this constraint will be dropped in Sec. 1.4). We further assume that the Hamiltonian, and thus also the propagator, are invariant under lattice translations so that we can utilize the Bloch Hamiltonian $H(\mathbf{k}, t)$ and Bloch propagator $U(\mathbf{k}, t)$ in reciprocal space with the momentum $\mathbf{k} = (k_x, k_y)$. Finally, we assume that $H(t)$ and $U(t)$ do not include nonlinearities and interactions. The role of disorder [48–50], interaction [51, 52], and non-linearity [53] in anomalous Floquet topological insulators will not be discussed here.

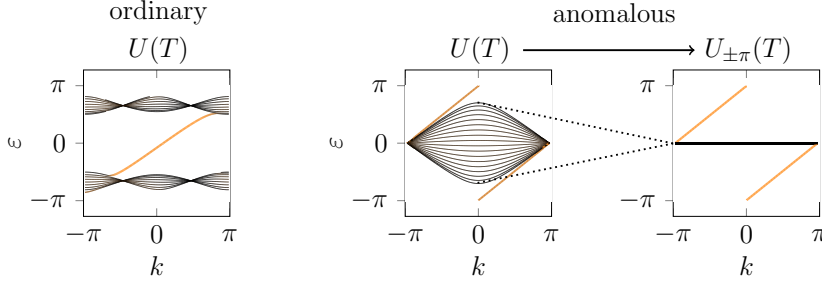


Figure 2: Dispersion of Floquet bands (black) and boundary states (orange) for an ordinary Floquet topological phase (left panel) and an anomalous Floquet topological phase, before (central panel) and after regularization (right panel). Here, and in Figs. 4, 13, we show the states on one boundary of a semi-infinite ribbon, and do not include the states on the opposite boundary. Quasienergies are restricted to the Floquet-Brillouin zone $\varepsilon \in [-\pi, \pi]$.

The spectral decomposition $U(\mathbf{k}, t) = \sum_{\nu=1}^n \xi^{\nu} |\mathbf{s}^{\nu}\rangle \langle \mathbf{s}^{\nu}|$ contains the eigenvalues $\xi^{\nu} \equiv \xi^{\nu}(\mathbf{k}, t)$ and the corresponding eigenvectors $\mathbf{s}^{\nu} \equiv \mathbf{s}^{\nu}(\mathbf{k}, t)$ of the bulk spectrum. The eigenvalues $\xi^{\nu}(\mathbf{k}, t) = e^{-i\varepsilon^{\nu}(\mathbf{k}, t)}$ form $\nu = 1, \dots, n$ quasienergy bands $\varepsilon^{\nu}(\mathbf{k}, t)$ that are defined up to multiples of 2π . In all of our examples, the number of bands n coincides with the size of the unit cell.

The Bloch propagator $U(\mathbf{k}, t)$ provides the adequate platform for analysis of the bulk topology, while information about the topologically protected boundary transport is contained within the real space propagator $U(t)$ for a finite or semi-infinite lattice with boundaries. Both are connected through the bulk-boundary correspondence [18].

For a Floquet system with a time-periodic Hamiltonian $H(t) = H(t + T)$, the eigenstates of the Floquet propagator $U(T)$, which are often called Floquet states, provide the natural basis of the Hilbert space. If the system is initialized in a Floquet state, it will remain in this state during propagation [54]. Because of this property, many of the concepts familiar from the theory of topological insulators with static Hamiltonians [3, 4] can also be applied to Floquet topological insulators: Boundary states emerge in the spectrum of $U(T)$ as dispersive chiral modes that traverse the quasienergy gaps between the Floquet bands $\varepsilon^{\nu}(\mathbf{k}, T)$ (see Fig. 2 for examples). As long as the quasienergy gaps do not close, the chiral boundary states cannot disappear. In this way, they are topologically protected.

In static systems, the topological invariants associated with the energy bands, Chern numbers C [16, 55] or Kane-Mele KM invariants [17, 56, 57], uniquely determine the number of chiral boundary states in each gap [15]. In Floquet systems, the invariants of the Floquet bands can only predict the boundary states if the system is in an ordinary topological phase. A Floquet system is in an ordinary topological phase if it possesses at least one trivial gap with no chiral boundary states [11–14] as in the left panel of Fig. 2, where the gap at $\varepsilon = \pm\pi$ is trivial. Here, the crucial difference between static and Floquet systems is that the energy spectrum $\{E\}$ of a time-independent Hamiltonian lies on the real axis while the spectrum $\{e^{-i\varepsilon(T)}\}$ of $U(T)$ lies on the unit circle. The energy spectrum generically possesses a trivial gap at $E = \pm\infty$, but not so the 2π -periodic quasienergies. Anomalous Floquet topological phases have no analogue

in static systems where only ordinary phases are possible.

Bulk-boundary correspondence in anomalous Floquet topological insulators In an anomalous Floquet topological insulator, the invariants of the Floquet bands are all zero, but the system still possesses chiral boundary states as in the middle panel of Fig. 2. The number and chirality of the boundary states is necessarily the same in each quasienergy gap.

The boundary states of an anomalous Floquet topological insulator are connected with quantized charge pumping via regularization of the Floquet-Bloch propagator $U(\mathbf{k}, T)$. The Floquet-Bloch propagator is regularized if it reduces to the identity $U(\mathbf{k}, T) = \mathbb{1}$ such that all Floquet bands are flattened to $\varepsilon^\nu(\mathbf{k}, T) = 0$ and the bulk states are localized. Charge pumping at a boundary is quantified by

$$\bar{C} = 1/n \sum_{m=1}^n \langle m | U^\dagger(T) (\hat{x} - m) U(T) | m \rangle, \quad (1)$$

which measures the propagation distance of wave packets initially localized at individual sites $|m\rangle$ of the boundary after they evolved into $U(T)|m\rangle$. Here, $\hat{x} = \sum_{m \in \mathbb{Z}} m |m\rangle\langle m|$ is the position operator parallel to the boundary. The propagation distance is averaged over a unit cell. For an anomalous Floquet topological insulator with a regularized Floquet-Bloch propagator, the transferred charge \bar{C} is quantized [18]. In other words, particles at the boundary are pumped an integer number of sites along the boundary in each driving cycle. In contrast to a Thouless charge pump [58], the driving is allowed to be non-adiabatic here.

Eq. (1) coincides with the W_3 invariant

$$W_3[U] = \frac{1}{8\pi^2} \int_0^T \iint_{\mathcal{B}} \text{tr} \left(U^{-1}(\mathbf{k}, t) \partial_t U(\mathbf{k}, t) [U^{-1}(\mathbf{k}, t) \partial_{k_x} U(\mathbf{k}, t), U^{-1}(\mathbf{k}, t) \partial_{k_y} U(\mathbf{k}, t)] \right) dk_x dk_y dt, \quad (2)$$

which exclusively depends on the bulk topology. Here, $[\cdot, \cdot]$ denotes the commutator and \mathcal{B} the Brillouin zone. The identity $\bar{C} = W_3[U]$ is derived in Refs. [2, 18]. The derivation requires some alternative expressions of \bar{C} , which can be found in the supplemental material of article V. Note that the full time evolution $0 \leq t \leq T$ enters into Eq. (2). The temporal periodicity $U(\mathbf{k}, 0) = U(\mathbf{k}, T) = \mathbb{1}$ and Brillouin zone periodicity together ensure that the W_3 invariant is an integer [18, 20].

The boundary transport is not quantized if the Floquet bands are dispersive as in the central panel of Fig. 2. Nevertheless, the chiral boundary states remain topologically protected. In this case, the W_3 invariant still allows us to predict the number of chiral boundary states in each quasienergy gap by inserting the auxiliary propagator

$$U_\varepsilon(\mathbf{k}, t) = \begin{cases} U(\mathbf{k}, 2t) & \text{if } 0 \leq t \leq T/2, \\ \exp([2T - 2t] \log_\varepsilon U(\mathbf{k}, T)) & \text{if } T/2 \leq t \leq T \end{cases} \quad (3)$$

into Eq. (2). The second half period of Eq. (3) deforms $U(\mathbf{k}, T)$ continuously to the identity $U_\varepsilon(\mathbf{k}, T) = \mathbb{1}$ without closing the quasienergy gap at ε (see the right panel

of Fig. 2). For this purpose, the branch cut of the complex logarithm \log_ε is placed along the line from 0 through $e^{-i\varepsilon}$. The integer $W_3[U_\varepsilon]$ thus gives the number of chiral boundary states in the respective gap ε of $U(\mathbf{k}, T)$ [2, 18].

In summary, the W_3 invariant serves two complementary roles in anomalous Floquet topological insulators: (i) If the Floquet propagator is regularized, a non-zero W_3 invariant indicates quantized charge pumping at the boundary. (ii) If the Floquet propagator is not regularized, the W_3 invariant predicts the number of chiral boundary states in each quasienergy gap. In the rest of this section, we focus on (ii). We return to the topic of quantized charge pumping in the next two sections. In Sec. 1.3, we discuss how the regularization of the Floquet propagator is achieved in practice. In Sec. 1.4, we show that quantized charge pumping can be achieved even when the constraint $U(\mathbf{k}, T) = \mathbb{1}$ is violated, provided that the system is non-Hermitian.

Degeneracy point expression of the W_3 invariant Our goal is to understand how the bulk topology enters into $W_3[U_\varepsilon]$. Understanding this aspect of the W_3 invariant will allow us to generalize it to symmetry-protected anomalous Floquet topological phases.

For this purpose, we insert $U_\varepsilon(\mathbf{k}, t)$ into Eq. (2) with $U(\mathbf{k}, t)$ given in its spectral decomposition. After various manipulations (see Ref. [20] for the first part and article I for the second part), we can express $W_3(\varepsilon) \equiv W_3[U_\varepsilon]$ as

$$W_3(\varepsilon) = \sum_{i=1}^{\text{dp}} \sum_{\nu=1}^n N^\nu(\varepsilon, \mathbf{d}_i) C^\nu(\mathbf{d}_i), \quad (4)$$

which is a sum over all degeneracy points $i = 1, \dots, \text{dp}$ of $U(\mathbf{k}, t)$ that occur during time evolution $0 \leq t \leq T$. We assume in this expression that the bands $\varepsilon^\nu(\mathbf{k}, t)$ are topologically trivial for $t \rightarrow 0$. The general case is given in Appendix A of article I.

In contrast to band invariants, which depend only on the eigenvectors, or winding numbers [1], which depend only on the eigenvalues, the W_3 invariant depends on both. The integers $C^\nu(\mathbf{d}_i)$ encode the topological properties of the eigenvectors $\mathbf{s}^\nu(\mathbf{k}, t)$ of $U(\mathbf{k}, t)$ in the vicinity of the degeneracy points. The integers $N^\nu(\varepsilon, \mathbf{d}_i)$ follow from the quasienergies $\varepsilon^\nu(\mathbf{k}, t)$ and ensure that only the degeneracy points which are relevant for the gap ε contribute to the sum.

A degeneracy point $\mathbf{d}_i = (\mathbf{k}_i, t_i, \varepsilon_i)$ occurs whenever the quasienergies $\varepsilon^\nu(\mathbf{k}_i, t_i)$, $\varepsilon^\mu(\mathbf{k}_i, t_i)$ of two bands $\nu \neq \mu$ differ by a multiple of 2π , such that $e^{-i\varepsilon^\nu} = e^{-i\varepsilon^\mu} = e^{-i\varepsilon_i}$ for two eigenvalues of $U(\mathbf{k}_i, t_i)$. With each degeneracy point, we can associate a Chern number $C^\nu(\mathbf{d}_i) = \oint_{\mathcal{S}(\mathbf{d}_i)} F_\alpha^\nu dS^\alpha$, given as the integral of the Berry curvature $2\pi i F_\alpha^\nu(\mathbf{k}, t) = \epsilon_{\alpha\beta\gamma} \partial^\beta (\mathbf{s}^\nu(\mathbf{k}, t)^\dagger \partial^\gamma \mathbf{s}^\nu(\mathbf{k}, t))$ over a small surface $\mathcal{S}(\mathbf{d}_i)$ enclosing the degeneracy point. Here, $\epsilon_{\alpha\beta\gamma}$ denotes the antisymmetric Levi-Civita symbol and summation over repeated indices α, β, γ is implied. It is $C^\nu(\mathbf{d}_i) = -C^\mu(\mathbf{d}_i) \neq 0$ only for the bands ν, μ that touch in the degeneracy point.

The contribution from each degeneracy point is multiplied by the integer $N^\nu(\varepsilon, \mathbf{d}_i) = \lceil (\varepsilon^\nu(\mathbf{k}_i, t_i) - \varepsilon) / (2\pi) \rceil + \lceil (\varepsilon - \varepsilon^\nu(\mathbf{k}, T)) / (2\pi) \rceil$ that counts how often band ν crosses the gap ε while it evolves from the degeneracy point at $t = t_i$ to its final position at $t = T$. Here, $\lceil \cdot \rceil$ denotes the ceiling function. Since ε lies in a gap, $N^\nu(\varepsilon, \mathbf{d}_i)$ does not depend on \mathbf{k} .

In the situation sketched in Fig. 3, we have $N^\nu(\varepsilon, \mathbf{d}_i) = 1$ (or $N^\nu(\varepsilon, \mathbf{d}_i) = 0$) for the

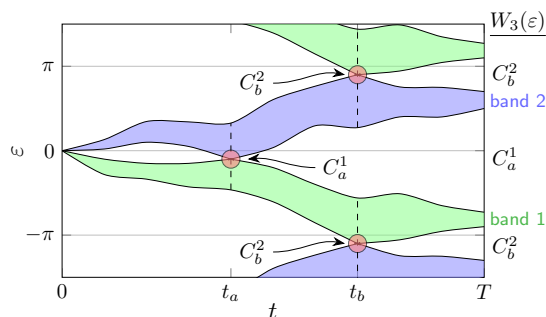


Figure 3: Schematic illustration of two bands $\nu = 1, 2$, which touch in two degeneracy points $i = a, b$ during the time evolution from $t = 0$ to $t = T$. At each degeneracy point, the W_3 invariant changes by the integer $C_i^1(\mathbf{d}_i) = -C_i^2(\mathbf{d}_i)$ according to Eq. (4). Adapted from article I.

band directly below (or above) the gap ε . Here, $W_3(\varepsilon)$ is the sum over the degeneracy points in the gap ε .

The bulk-boundary correspondence is expressed as follows in the degeneracy-point picture: If a boundary is introduced into the system, say along the x -direction, a degeneracy point \mathbf{d}_i gives rise to a chiral boundary state that appears immediately after t_i at momenta $(\mathbf{k}_i)_x$ and quasienergy ε_i . During the subsequent time-evolution, the boundary state can disappear only if the same quasienergy gap closes at a second degeneracy point \mathbf{d}_j with $C^\nu(\mathbf{d}_j) = -C^\nu(\mathbf{d}_i)$ at a later $t_j > t_i$. In this way, the system evolves to $t = T$, with the number of boundary states in the gap ε given by $W_3(\varepsilon)$.

Eq. (4) generalizes another prominent expression of the W_3 invariant which is based on degeneracy points [19] (see article I). The main advantages of our expression are the invariance of all quantities under 2π -shifts $\varepsilon^\nu(\cdot) \mapsto \varepsilon^\nu(\cdot) + 2\pi m^\nu$, and that the algorithm we developed in Ref. [20] allows for efficient computation of Eq. (4). The degeneracy-point expression in Ref. [19] requires a specific choice of the quasienergies which is not well-suited for numerical evaluation.

Invariants for symmetry-protected anomalous Floquet topological phases The relevant symmetries for the topological classification of Floquet systems are time-reversal, chiral, and particle-hole symmetry [59, 60]. In each case, the symmetry relations fulfilled by the Hamiltonian imply that the degeneracy points of the propagator appear in symmetric pairs. In some cases, the contributions from these pairs cancel such that $W_3(\varepsilon) = 0$ while symmetry-protected boundary states emerge in the gap ε . We establish the bulk-boundary correspondence for the symmetry-protected boundary states by introducing \mathbb{Z}_2 invariants which count only one partner of each pair of degeneracy points, in analogy to Ref. [19]. To avoid redundancy in our presentation, we give a detailed account of the construction for time-reversal symmetry, but only a brief overview for chiral and particle-hole symmetry.

The symmetry relation for time-reversal symmetry is

$$H_{\text{tr}}(T - t) = \Theta H_{\text{tr}}(t) \Theta^{-1}, \quad (5)$$

with an anti-unitary operator Θ for which $\Theta^2 = \pm 1$. Note that the anti-unitary operator

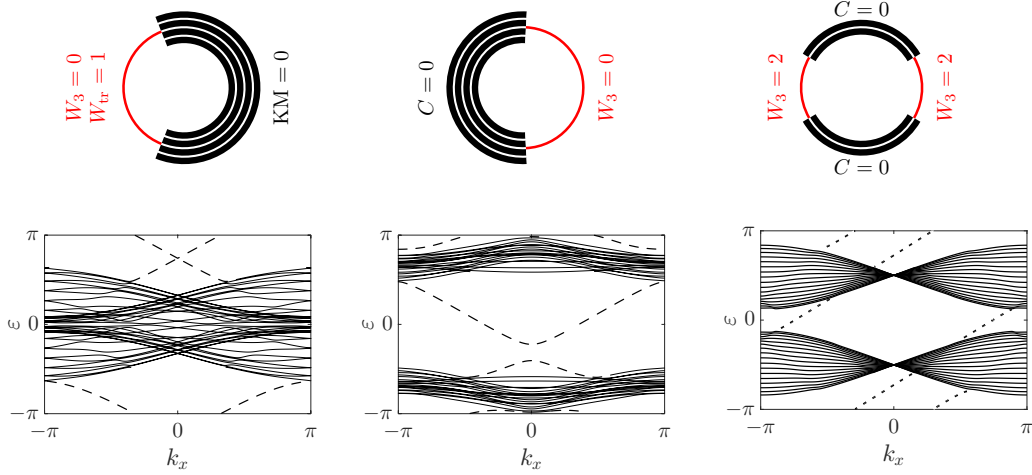


Figure 4: Spectrum of a Floquet system (model is provided in Sec. 1.3) with fermionic time-reversal symmetry (left column), bosonic time-reversal symmetry (central column), and particle-hole symmetry $\Pi^2 = -1$ (right column). Top row: Spectrum $\{e^{-i\epsilon(T)}\}$ on the unit circle. Black arcs indicate the (four- or two-fold degenerate) Floquet bands, red arcs the gaps. Included are the invariants of the bands (Kane-Mele KM or Chern number C), and the W_{tr} invariant or the W_3 invariant associated with the gaps. The invariants prove that the left and right column are in an anomalous Floquet topological phase, while the middle column is topologically trivial. Bottom row: Dispersion of Floquet bands (solid) and boundary states (dashed). Adapted from article II, which provides the parameters for this figure.

$\Theta = \theta\mathcal{K}$ can be represented with a unitary operator θ and the complex conjugation operator \mathcal{K} . In this representation, θ has to satisfy $\theta^*\theta = \pm 1$. Since the sign of Θ^2 is commonly associated with the spin of the particles [5], we denote time-reversal symmetry with $\Theta^2 = 1$ ($\Theta^2 = -1$) as bosonic (fermionic) time-reversal symmetry. The symmetry relation (5) implies that the degeneracy points appear in pairs $\mathbf{d}_i = (\mathbf{k}_i, t_i, \varepsilon_i)$, $\hat{\mathbf{d}}_i = (-\mathbf{k}_i, t_i, \varepsilon_i)$ with opposite sign of $C^\nu(\mathbf{d}_i) = -C^\nu(\hat{\mathbf{d}}_i)$. Here, we have to use the degeneracy points of a time-symmetrized propagator $U_\star(t)$ which coincides with the original propagator $U(t)$ at $t = T$ (see article I for details). The W_3 invariant consequently vanishes in each gap. Thus, we define a \mathbb{Z}_2 invariant

$$W_{\text{tr}}(\varepsilon) \equiv \sum_{\nu=1}^n \sum_{i=1}^{\text{dp}/2} N^\nu(\varepsilon, \mathbf{d}_i) C^\nu(\mathbf{d}_i) \pmod{2}, \quad (6)$$

where the upper limit $\text{dp}/2$ in the sum over i indicates that exactly one degeneracy point of each symmetric pair is included. The considerations leading to a bulk-boundary correspondence are similar to those for the W_3 invariant. A pair of degeneracy points $\mathbf{d}_i, \hat{\mathbf{d}}_i$ gives rise to two boundary states $B_{\text{I}}, B_{\text{II}}$ with opposite chirality, which appear at momenta $(\mathbf{k}_i)_x, -(\mathbf{k}_i)_x$. Their dispersion relations are connected by $\varepsilon_{\text{I}}(k_x) = \varepsilon_{\text{II}}(-k_x)$. For $\Theta^2 = -1$, the boundary states are Kramers degenerate [5, 17] at the invariant

momenta $k_x \equiv -k_x$, which prevents their mutual annihilation (see Fig. 4). They can disappear only through the appearance of a second pair of degeneracy points which is why the invariant is \mathbb{Z}_2 -valued. For $\Theta^2 = 1$ there is no Kramers degeneracy and the counterpropagating boundary states cancel, leading to the trivial boundary state in Fig. 4. A non-zero value of $W_{\text{tr}}(\varepsilon)$ implies the existence of a pair of symmetry-protected boundary states with opposite chirality in the gap ε only for fermionic time-reversal symmetry.

Eq. (5) is also invariant under shifts $\varepsilon^\nu(\cdot) \mapsto \varepsilon^\nu(\cdot) + 2\pi m^\nu$ and thus a generalization of the corresponding degeneracy point expression in Ref. [19]. Efficient computation of the \mathbb{Z}_2 invariant is again possible with the algorithm in Ref. [20].

The symmetry relation for chiral symmetry is

$$H_{\text{ch}}(T - t) = -\Gamma H_{\text{ch}}(t) \Gamma^{-1} \quad (7)$$

with a unitary operator Γ . The symmetry relation (7) also implies that the degeneracy points appear in pairs such that $W_3(\varepsilon) = -W_3(-\varepsilon)$, especially $W_3(\varepsilon) = 0$ for the gaps $\varepsilon = 0, \pm\pi$. For conventional chiral symmetry, non-trivial boundary states cannot emerge in these gaps [59–61]. To obtain symmetry-protected boundary states, chiral symmetry must be realized as a bipartite even-odd sublattice symmetry [62–64], where the operator Γ includes a minus sign on every second unit cell (see App. B in article I). In that case, a \mathbb{Z}_2 invariant W_{ch} can be constructed, in analogy to the case of fermionic time-reversal symmetry (see Eq. (3) in article I).

The symmetry relation for particle-hole symmetry is

$$H_{\text{ph}}(t) = -\Pi H_{\text{ph}}(t) \Pi^{-1}, \quad (8)$$

with an anti-unitary operator Π for which $\Pi^2 = \pm 1$. For $\Pi^2 = -1$, the symmetry relation (8) implies that the degeneracy points occur in pairs $\mathbf{d}_i = (\mathbf{k}_i, t_i, \varepsilon_i)$, $\hat{\mathbf{d}}_i = (-\mathbf{k}_i, t_i, -\varepsilon_i)$ with the same sign of $C^\nu(\mathbf{d}_i) = C^\nu(\hat{\mathbf{d}}_i)$. Thus, we have $W_3(\varepsilon) = W_3(-\varepsilon)$, and in particular $W_3(\varepsilon) \in 2\mathbb{Z}$ for the gaps $\varepsilon = 0, \pm\pi$ where boundary states appear in pairs $\varepsilon_{\text{I}}(k_x) = -\varepsilon_{\text{II}}(-k_x)$ with the same chirality (see Fig. 4). Here, a symmetry-adapted invariant is not required since the W_3 invariant suffices to predict the boundary states.

In addition to the paired degeneracy points, unpaired degeneracy points can occur for $\Pi^2 = 1$ which are pinned at the invariant momenta. They correspond to symmetry-protected unpaired boundary states in the gaps $\varepsilon = 0, \pm\pi$. Here, a \mathbb{Z}_2 invariant W_{ph} can be defined that connects the unpaired degeneracy points with the unpaired boundary states (see Eq. (9) in article I).

1.3 Implementation

We now introduce driving protocols which possess anomalous Floquet topological phases and discuss their experimental implementation in photonic waveguide lattices. We start with the driving protocol proposed in Ref. [2] which is the minimal driving protocol for an anomalous Floquet topological insulator with a non-zero W_3 invariant. It provides the basis for our construction of a universal driving protocol for symmetry-protected anomalous Floquet topological phases.

Minimal driving protocol The minimal driving protocol is implemented on a bipartite square lattice with $n = 2$ lattice sites \bullet, \circ as sketched in Fig. 5(a). The time-periodic Hamiltonian $H(t + T) = H(t)$ of the driving protocol cycles through four consecutive steps during which the Hamiltonian is constant. In each step, adjacent sites of the lattice are coupled in a pairwise manner. The parameter $J \in \mathbb{R}$ controls the coupling strength, which is identical in each step.

The explicit expressions of the lattice Hamiltonians in each step can be deduced from their graphical representation in Fig. 5(a), or found in the supplemental material of article III. For our purposes, the expressions are not important as all relevant information is contained within the 2×2 Hamiltonians

$$H_J = J \begin{pmatrix} 0 & 1 \\ 1 & 0 \end{pmatrix} = J\sigma_x, \quad (9)$$

which describe the pairwise coupling between two sites in each of the four steps. The associated propagator, for a step of duration δt , is $U_J = \exp(-iH_J\delta t) = \cos(J\delta t) - i\sin(J\delta t)\sigma_x$. Here, and in the following, we set $\delta t \equiv 1$ for the duration of each step such that the period T coincides with the number of steps in the driving protocol. The propagator U_J is a periodic function of J . Since

$$U_J = (-1)^l U_{J+l\pi} \quad (10)$$

for every $l \in \mathbb{Z}$, we may restrict ourselves to the parameter range $J \in [0, \pi)$.

Each site at the boundary of the lattice is isolated, i.e. uncoupled, in at least one step of the protocol. For example, the \bullet (\circ) sites at the bottom boundary in Fig. 5(b) are isolated in step 2 (4). Isolated sites are described by the trivial Hamiltonian $H_{\text{is}} = 0$ and propagator $U_{\text{is}} = \exp(-iH_{\text{is}}) = 1$. A wave packet which is initialized on an isolated site remains localized on it for the duration of the respective step.

For each value of J , the spectrum of the Floquet-Bloch propagator consists of a two-fold degenerate Floquet band centered around $\varepsilon = 0$ with a vanishing Chern number (the central panel of Fig. 2 shows the case $J = \pi/3$). A topological phase transition occurs at $J = \pi/4$ and $J = 3\pi/4$ where the quasienergy gap at $\varepsilon = \pm\pi$ closes. For $0 \leq J < \pi/4$ and $3\pi/4 < J < \pi$, the W_3 invariant vanishes, which indicates that the system is topologically trivial. On the other hand, we have $W_3 = 1$ for $\pi/4 < J < 3\pi/4$. This indicates that the driving protocol is in the anomalous Floquet topological phase.

The emergence of the anomalous Floquet topological phase becomes obvious for the special value $J = \pi/2$, which we call perfect coupling. At perfect coupling, we have $U_J = -i\sigma_x$. A full amplitude transfer occurs between coupled sites and the driving protocol enforces the trajectories shown in Fig. 5(b). An excitation in the bulk moves in a closed loop, but an excitation starting on, e.g., a \bullet site at the bottom boundary is transported two sites to the right. This corresponds to the quasienergy dispersions $\varepsilon^\nu(\mathbf{k}, T) = 0$ for the Floquet bands and $\varepsilon(k, T) = \pi + k$ for the chiral boundary state on the bottom boundary. The transferred charge at the boundaries is quantized, $\bar{C} = 1$, in accordance with $U(\mathbf{k}, T) = \mathbb{1}$.

This is how regularization of the propagator, and thus quantized charge pumping, is achieved in practice, by fine-tuning to perfect coupling. Alternatively, one could include disorder which is strong enough to localize all bulk states, but also weak enough that

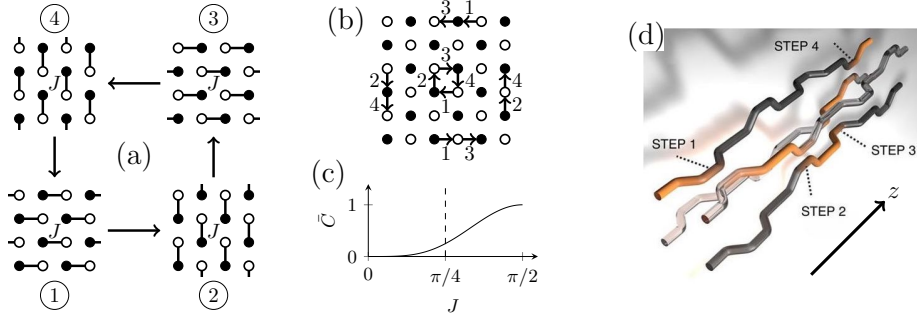


Figure 5: (a) Sketch of the minimal driving protocol. (b) Patterns of motion on a finite lattice during one cycle of the driving protocol at perfect coupling. (c) The transferred charge \bar{C} , evaluated for one of the boundaries in panel (b). (d) Experimental realization in photonic waveguide lattices. Panel (d) is adapted from Ref. [30].

the system remains topological. In that case, quantized transport also occurs for non-perfect coupling in the anomalous Floquet topological phase, but only after averaging over multiple driving periods [48]. Quantized charge pumping in each individual driving period is only possible for perfect coupling, or with non-Hermiticity (see Sec. 1.4).

Here, without disorder, the bulk bands become dispersive and the boundary transport continuously decreases when we move away from perfect coupling [see Fig. 5(c)]. Note that the topological phase transition at $J_c = \pi/4$ cannot be extracted from \bar{C} , which is non-zero even in the trivial phase. The transport that occurs for $J < J_c$ is not topologically protected. When accounting for disorder, the transferred charge drops to zero below the phase transition [48].

The minimal driving protocol can be realized in photonic waveguide lattices [30, 31] by exploiting the equivalence between the time-dependent Schrödinger equation and the paraxial Helmholtz equation

$$i\partial_z\psi_m(z) = \sum_{k \in \langle m \rangle} J_{k,m}(z)\psi_k(z), \quad (11)$$

here written in the tight-binding approximation. The propagation distance z [see Fig. 5(d)] replaces the time argument t in the Schrödinger equation. The field amplitude $\psi_m(z)$ of the guided light mode in waveguide m interacts with its nearest neighbours $k \in \langle m \rangle$ via the coupling $J_{k,m}(z)$. The coupling strength can be modulated by increasing or decreasing the distance between the waveguides. Fig. 5(d) illustrates how this modulation is used to implement the driving protocol. At $z = 0$, the waveguides are arranged such that $J_{k,m}(z) = 0$. The distance between the individual waveguides is $40 \mu\text{m}$. As z increases, the distance is locally reduced in a pairwise manner such that $J_{k,m}(z) = J$. In this way, the individual steps of the driving protocol are realized. For perfect coupling, each step encompasses a propagation length of 10 mm. The current experimental limit is around 20 consecutive steps due to waveguide losses (see Sec. 1.4). The experimental techniques involved in the fabrication, excitation, and characterization of the waveguide lattices will not be discussed here. The interested reader may

consult Ref. [29].

Universal driving protocol On a bipartite square lattice, there are four distinct patterns in which the adjacent lattice sites \bullet , \circ can be coupled in a pairwise manner. The minimal driving protocol arranges these four pairwise coupling patterns in a cyclic sequence to realize the anomalous Floquet topological phase.

Symmetry-protected anomalous Floquet topological phases require more complex coupling patterns than a two-element unit cell can offer (see Appendix D in article II). A square lattice with $n = 4$ lattice sites \bullet , \circ , \blacklozenge , \circ provides the necessary complexity. This is our starting point for the construction of the universal driving protocol.

On this lattice, pairwise coupling of neighboring lattice sites can occur along three directions: horizontal, vertical, and diagonal. This gives a total of 4 horizontal + 4 vertical + 12 diagonal = 20 possible coupling patterns, nine of which are depicted in Fig. 6. We arrive at this number by excluding all diagonal coupling patterns in which couplings “cross each other” on the lattice. Such patterns can not be easily implemented in waveguide lattices. For the same reason, we do not consider long range couplings.

The coupling patterns now have to be arranged in a non-trivial cyclical sequence such that the symmetry relations for time-reversal (5), chiral (7), or particle-hole symmetry (8) are satisfied. In the following, we outline the core arguments that lead to the proper arrangement of the coupling pattern. Detailed explanations can be found in article II.

Each symmetry relation involves a transformation $SH(t)S^{-1}$ of the Hamiltonian with a translational-invariant unitary operator S . The symmetry relations can only be satisfied if the transformed Hamiltonian has the same structure as the original Hamiltonian, and is again composed of pairwise couplings. Therefore, the operator S has to either exchange lattice sites in a pairwise manner or act as an on-site operator. Otherwise, the transformed Hamiltonian $SH(t)S^{-1}$ would contain couplings between three or more lattice sites.

An on-site operator S is not compatible with $S^*S = -1$ which is required for fermionic time-reversal symmetry and particle-hole symmetry $\Pi^2 = -1$. This leaves us with the five possible symmetry operators S_1, \dots, S_5 shown in the top row of Fig. 7, not counting rotations, reflections, or translations. These operators map every lattice site onto exactly one other lattice site.

Each symmetry operator is compatible with the pairwise couplings shown in the bottom row of Fig. 7. These couplings are mapped again to couplings between adjacent sites in the transformation $SH(t)S^{-1}$ with the respective symmetry operator. The remaining pairwise couplings are mapped onto long-range couplings that do not occur in the Hamiltonian, and must be excluded.

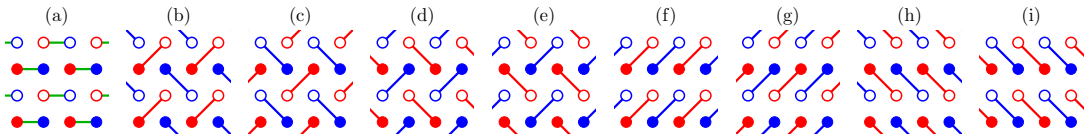


Figure 6: Nine examples of pairwise coupling patterns on a square lattice with four distinct sites. Adapted from article II.

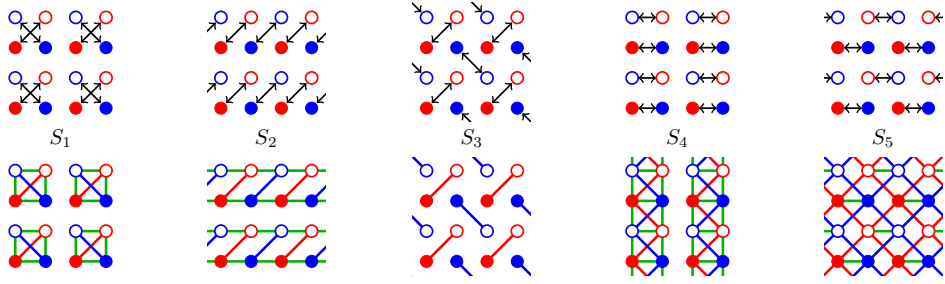


Figure 7: Graphical representation of the five symmetry operators S_1, \dots, S_5 . The arrows in the top row indicate how each symmetry operator maps a site onto one of its eight neighbors. The lines in the bottom row indicate the compatible pairwise coupling terms. Adapted from article II.

The graph spanned by the compatible pairwise couplings in Fig. 7 is disconnected for the operators S_1, \dots, S_4 , such that propagation is restricted to a lower-dimensional subset of the lattice and a two-dimensional topological phase is impossible. We are left with the operator S_5 for the construction of the universal driving protocol.

The operator S_5 is incompatible with all vertical and horizontal coupling patterns, except for the horizontal pattern (a) which is mapped onto itself by S_5 . Further analysis of the diagonal coupling patterns shows that a non-trivial driving protocol with fermionic time-reversal symmetry [particle-hole symmetry $\Pi^2 = -1$] must consist of the diagonal patterns (b), (c), (d), (e) [(f), (g), (h), (i)] and the horizontal pattern (a). This leads to the two variants of the universal driving protocol: the time-reversal symmetric protocol in Fig. 8 and the particle-hole symmetric protocol in Fig. 9. We use a minimal set of parameters $\pm J$ for the diagonal couplings in steps 1, 3, 4, 6 and $\pm J'$ for the horizontal couplings in steps 2, 5. The signs are determined by the symmetry relations (5), (8) with $\Theta = \Pi = S_5 \mathcal{K}$. Here, we set $\Theta^2 = \Pi^2 = -1$ which leads to the signs as indicated in Figs. 8, 9.

The two variants implement a \mathbb{Z}_2 anomalous Floquet topological phase with Kramers degenerate counterpropagating boundary states, and a $2\mathbb{Z}$ anomalous Floquet topological phase with copropagating boundary states. In addition, \mathbb{Z}_2 topological phases with non-zero W_{ch} or W_{ph} invariants can be enforced on the driving protocol in Fig. 8 by rearranging the signs of the couplings J, J' (see article II).

Quantized charge pumping at the boundary and localization in the bulk occurs if we set $J = \pi/2$ and $J' = 0$, which we also denote as perfect coupling. At perfect coupling, the red and blue sublattices are decoupled and the time-reversal symmetric protocol (particle-hole symmetric protocol) reduces to two inverse copies (two identical copies) of the minimal driving protocol. The corresponding patterns of motion are shown in Figs. 8, 9. In the time-reversal symmetric case, the boundary state on the red (blue) sublattice moves in counter-clockwise (clockwise) direction along the lattice perimeter. In the particle-hole symmetric case, both boundary states move in the same direction.

For non-perfect coupling, the Floquet band and boundary state dispersions of the two protocols are shown in the left and right column of Fig. 4 together with the relevant bulk invariants. The computation of these invariants becomes possible through the degeneracy point expressions developed in the last section. Now with non-zero sublattice coupling J' , only the presence of fermionic time-reversal symmetry prevents the coun-

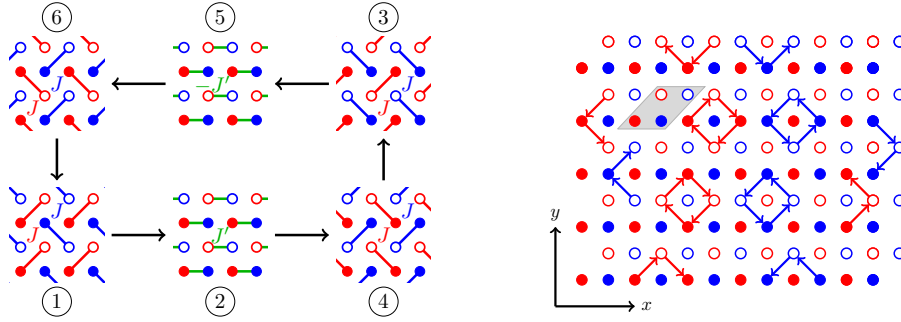


Figure 8: Left panel: Time-reversal symmetric variant of the universal driving protocol with $\Theta^2 = -1$. Right panel: Patterns of motion during one cycle at perfect coupling. The lattice comprises only entire unit cells (one unit cell is shown as a gray rhomboid), such that the boundaries are compatible with the symmetry operator S_5 . Adapted from article II.

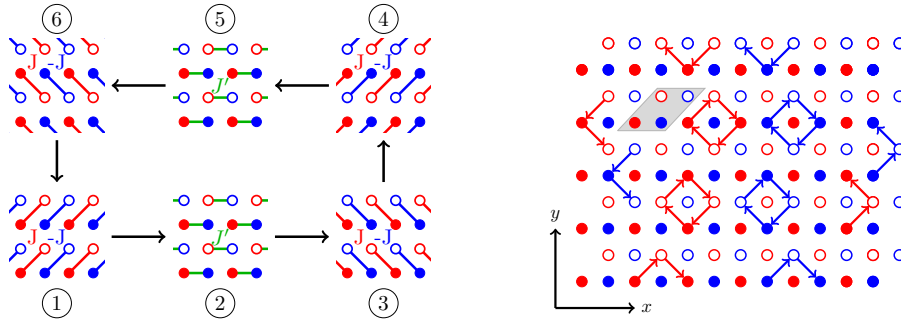


Figure 9: Left panel: Particle-hole symmetric variant of the universal driving protocol with $\Pi^2 = -1$. Right panel: Patterns of motion during one cycle at perfect coupling. Adapted from article II.

terpropagating boundary state from disappearing. Note that fermionic time-reversal symmetry turns into bosonic time-reversal symmetry if we replace $-J'$ in step 5 of the time-reversal symmetric protocol with J' . The counterpropagating boundary states then cancel and we get a trivial phase, see the middle column of Fig. 4.

Significance of the time-reversal symmetric protocol Time-reversal symmetry inverts the direction of the spin. This property usually restricts the square of the time-reversal symmetry operator to $\Theta^2 = 1$ for bosons and $\Theta^2 = -1$ for fermions [5]. In agreement with this statement, \mathbb{Z}_2 topological insulators with fermionic time-reversal symmetry had only been observed in fermionic systems [8–10] prior to our work. The present spinless driving protocol circumvents this restriction by encoding the lattice with a pseudo-spin 1/2. Specifically, we can associate the red and blue sublattice with the up and down components of a spin 1/2 (see article III).

This idea is not new and has appeared in several works [65–70] which combine two bosonic topological insulators with opposite chirality to implement counterpropagating boundary states. The major distinction between these works, which are all based on static systems, and our driving protocol is that we couple the two pseudo-spin states

while retaining fermionic time-reversal symmetry. This requires a driving protocol because the opposite signs of the sublattice coupling $\pm J'$ in steps 2, 5 would cancel in a static system.

Implementation in photonic lattices Negative couplings do not naturally occur in waveguide lattices [71], but the periodicity (10) of the propagator allows us to shift any negative coupling to a positive value. With only positive couplings, the time-reversal symmetric protocol can be experimentally implemented in the exact same way as the minimal driving protocol. The left panel of Fig. 10 shows the coupling patterns of the six steps in a waveguide lattice. The experimental details are provided in article IV.

To demonstrate the symmetry protection of the counterpropagating boundary states for non-zero J' , light is injected at single sites on the blue (middle panel of Fig. 10) and red (right panel of Fig. 10) sublattice at the boundaries. This predominantly excites the clockwise and counter-clockwise moving boundary state, respectively. The light propagates over three driving periods and traverses a corner of the lattice in the process. Were it not for fermionic time-reversal symmetry, the boundary states would be reflected at the corner, as in the case of bosonic time-reversal symmetry.

Eq. (5) relates forward propagation, i.e., propagation from the front to the back of the waveguide structure [see Fig. 11(a)], to backward propagation [see Fig. 11(c)]. This allows us to “measure” the time-reversal symmetry operator Θ and thus directly verify the fermionic time-reversal symmetry of the photonic platform. For this purpose, an input state is generated that spans two adjacent waveguides with the same amplitude but a relative phase ϕ . The two sites are mapped onto each other by S_5 . The input state is then injected at the front (back) and the output intensity distribution on the blue sublattice $I^b(\phi)$ at the back (on the red sublattice $\tilde{I}^r(\phi)$ at the front) is measured as a function of ϕ [see Fig. 11(b)]. The relation between forward and backward propagation implies

$$\tilde{I}^r(\phi) = I^b(\pi - \phi) \tag{12}$$

for the output intensities (see article III). The exchange of intensities between the two sublattices follows from the action of S_5 and applies to both bosonic and fermionic time-reversal symmetry. The phase shift $\phi \mapsto \pi - \phi$, however, appears if and only if the system possesses fermionic time-reversal symmetry.

1.4 Non-Hermitian engineering

The Hermitian Hamiltonian H_J in Eq. (9) or equivalently the unitary propagator U_J , which were exclusively used in the last section to describe the pairwise coupling in the driving protocols, omit an important property of the experimental platform: losses that the waveguide bending incurs. In the waveguide lattice in Fig. 5, each step of the driving protocol corresponds to a relative light amplitude loss of around 4% during propagation for perfect coupling [30].

To account for these losses, H_J should be replaced with

$$H_{J,\gamma} = \begin{pmatrix} -i\gamma & J \\ J & -i\gamma \end{pmatrix}, \tag{13}$$

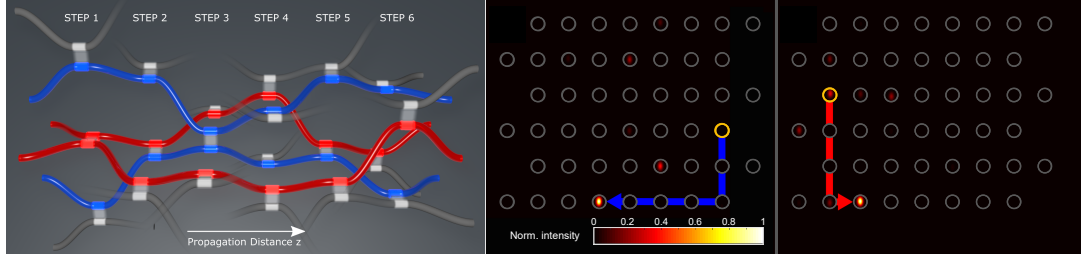


Figure 10: Left Panel: Experimental realization of Fig. 8 in waveguide lattices. Central and right panel: Output intensity distribution after light propagated for three driving periods in the waveguide lattice with non-zero sublattice coupling J' . Gray circles indicate the waveguide positions. The initial excitation site is marked in yellow. Adapted from article III, which provides the parameters for this figure.

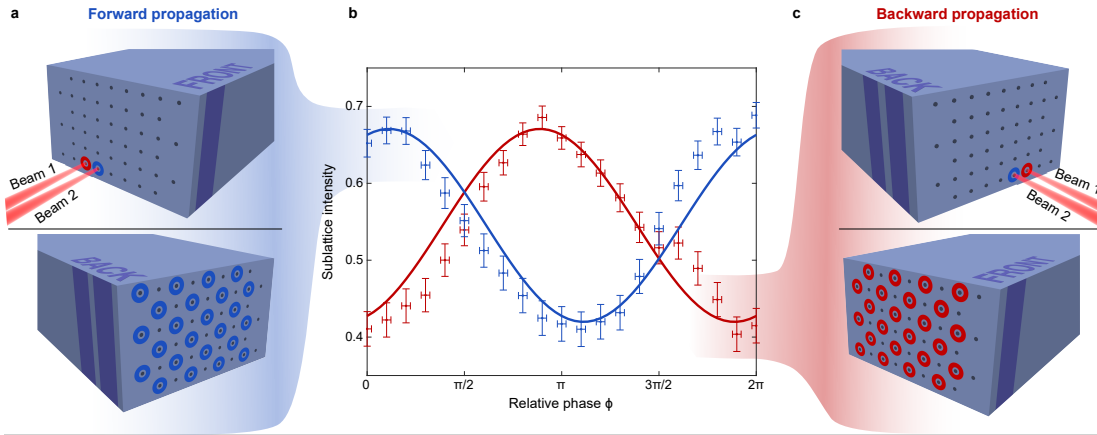


Figure 11: (a, c) Position of the two input beams and the position of the measured output intensities for forward and backward propagation after one driving period. The initial excitation is injected into the same two waveguides for both forward and backward propagation. (b) The output intensity distributions $I^b(\phi)$, $\tilde{I}^r(\phi)$ as functions of the relative phase ϕ between the two input beams (solid lines: numerical calculations, dots: measured values with error bars). Adapted from article III, which provides the parameters for this figure.

and U_J with $U_{J,\gamma} = \exp(-iH_{J,\gamma}) = (\cos(J) - i\sigma_x \sin(J))e^{-i\gamma}$. The parameter $\gamma \in \mathbb{R}$ specifies the strength of the attenuation.

If the losses are the same on each site of the lattice, they amount to an imaginary shift $H(t) \mapsto H(t) - i\gamma$ of the lattice Hamiltonian, which implies $U(T) \mapsto e^{-\gamma T}U(T)$ for the Floquet propagator of the driving protocol. Such an imaginary shift does not change the physical properties of the system. Omitting the factor $e^{-\gamma T}$, which drops out if we consider normalized intensities, of the form $I(\mathbf{r}) = |\psi(\mathbf{r})|^2 / \max_{\mathbf{r}'} |\psi(\mathbf{r}')|^2$, we recover Hermiticity. The waveguide lattices in Figs. 5, 10 were designed this way. As a direct consequence, the Hamiltonian H_{is} for the isolated sites at the boundary is set to $H_{\text{is}} = -i\gamma$. In other words, uncoupled waveguides must be bent in the exact same manner as the coupled waveguides (see Fig. 12) to guarantee that the bulk and boundary states accumulate the same losses during propagation.

Conversely, the losses of the boundary states can be manipulated independently of the bulk losses if we set $H_{\text{is}} = -i\gamma_{\text{is}} \neq -i\gamma$ for the losses γ_{is} of the isolated sites. The natural choice here is to set $\gamma_{\text{is}} = 0$ which corresponds to straight waveguides in the respective step of the protocol (see Fig. 12).

Consider now, e.g., the minimal driving protocol for this loss configuration. For perfect coupling, bulk states will be attenuated by $e^{-\gamma T}$ after one period, but the chiral boundary states only by $e^{-\gamma T/2}$. The corresponding Floquet quasienergies, which are now complex numbers, are $\varepsilon^\nu(\mathbf{k}, T) = -i\gamma T$ for the Floquet bands and $\varepsilon(k, T) = \pi + k - i\gamma T/2$ for the chiral boundary state. Note that the real part of the quasienergies is again defined only up to multiples of 2π . The boundary state is spectrally detached from the bulk bands. An imaginary gap $i\Gamma$ at $\Gamma = -3\gamma T/4$ separates the two. As Fig. 13 shows, the detachment also occurs for non-perfect coupling.

Non-Hermitian boundary state engineering We denote the process of spectrally detaching topological boundary states from the bulk bands as non-Hermitian boundary state engineering (BSE). This intrinsically non-Hermitian effect can only occur in anomalous Floquet topological insulators. To understand why, consider the spectrum $\{e^{-i\varepsilon(T)}\}$ of $U(T)$ for an ordinary and an anomalous topological phase as in Fig. 14. For a Hermitian system, the spectrum of $U(T)$ lies on the unit circle. In ordinary phases, any boundary state, viewed as a continuous curve $k \mapsto e^{-i\varepsilon(T,k)}$ parametrized by momentum k , connects two different bulk bands. In contrast, the boundary states of an anomalous Floquet topological insulator wind around the unit circle. In a non-Hermitian system,

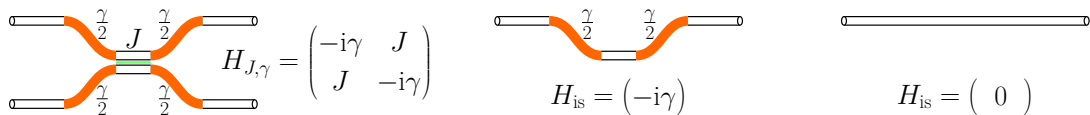


Figure 12: Left Panel: Idealized Hamiltonian of two coupled waveguides which includes the losses in the bending sections. Middle panel: Hamiltonian of an uncoupled waveguide which is bent in the same manner as the coupled waveguides. Right panel: Hamiltonian of an uncoupled straight waveguide. Adapted from article IV.

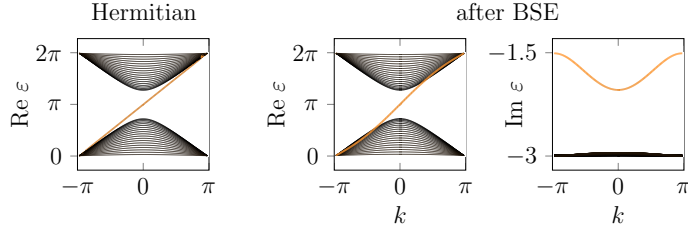


Figure 13: Bands and boundary states of the minimal driving protocol (with coupling $J = 1$) in the Hermitian case (left panel) and after BSE (central and right panel) with losses $\gamma = 0.75$, $\gamma_{\text{is}} = 0$. Adapted from article IV.

the spectrum of U can move away from the unit circle. Regular boundary states have to remain attached to the bulk bands, since otherwise the continuous dependence on momentum would be violated. Anomalous boundary states, however, can detach from the bulk bands and thus be manipulated independently. This new freedom is exploited in BSE.

Due to the invertibility of the propagator, which also holds in the non-Hermitian setting, the spectrum cannot move through the origin. Therefore, an anomalous boundary state, which winds around the origin, retains this property during BSE and remains topologically protected as a non-contractible loop. Note that this topological protection is independent of the bulk topology. The detached boundary states are no longer bound to the bulk-boundary correspondence. We will explore the implications of this statements later.

In the minimal driving protocol, BSE enables the amplification of boundary transport relative to bulk motion or vice versa. In the universal driving protocol, more sophisticated manipulations become possible due to the interplay between BSE and the symmetry protection. Here, we focus on the time-reversal symmetric variant of the protocol. Adaptation of our results to the particle-hole symmetric case is straightforward.

For notational simplicity, we assume uniform losses γ for the pairwise coupling in each step of the time-reversal symmetric protocol (see article IV for more general considerations). The two counterpropagating boundary states can be independently manipulated by varying the losses of the isolated sites on the red (γ_{is}^r) or blue (γ_{is}^b) sublattice, respectively. Upon the introduction of these non-Hermitian terms, the symmetry relation (5)



Figure 14: Conceptual sketch of the spectrum $\{e^{-i\epsilon(T)}\} \subset \mathbb{C} \setminus \{0\}$ of the Floquet propagator in the Hermitian and non-Hermitian case, with bulk bands (black dots) and boundary states (orange curves) for an ordinary and anomalous topological phase. Adapted from article IV.

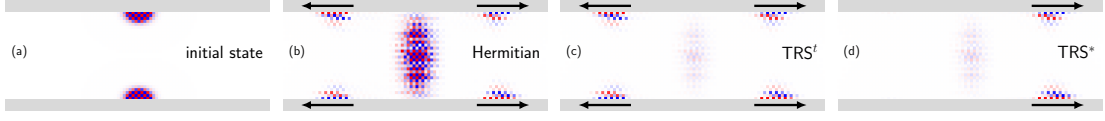


Figure 15: Real-space propagation of an initial state prepared at the boundaries of the time-reversal symmetric protocol, in the Hermitian case or after BSE. Lightness encodes the wave function intensity $I(\mathbf{r}) = |\psi(\mathbf{r})|^2$ at each lattice site, normalized to the maximum value. (a) Initial state. (b)–(d) States after $n_p = 15$ periods of the driving protocol. Adapted from article IV, which provides the parameters for this figure.

for time-reversal symmetry splits up into two separate relations (see article IV)

$$(\text{TRS}^t): \quad \theta H(t) \theta^{-1} = H^t(T - t), \quad (14a)$$

$$(\text{TRS}^*): \quad \theta H(t) \theta^{-1} = H^*(T - t) - 2i\gamma. \quad (14b)$$

Here, $(\cdot)^t$ denotes transposition and we have $\theta = S_5$ with $\theta^* \theta = -1$. Clearly, both relations agree for a Hermitian Hamiltonian with $H^*(t) = H^t(t)$, $\gamma = 0$. To satisfy Eq. (14), we have to set $\gamma_{\text{is}}^r = \gamma_{\text{is}}^b$ ($\gamma_{\text{is}}^b = -\gamma_{\text{is}}^r + 2\gamma$) for TRS^t (TRS^*). BSE is possible in both cases but leads to significantly different propagation properties. For TRS^t , we can set $\gamma_{\text{is}}^r = \gamma_{\text{is}}^b = 0$ as in the minimal driving protocol such that the helical transport carried by the two boundary states is amplified relative to the bulk motion [see Fig. 15(c)]. In the TRS^* case, setting, e.g., $\gamma_{\text{is}}^r = 0$ implies $\gamma_{\text{is}}^b = 2\gamma$. Therefore, amplification of one boundary state relative to bulk motion implies the suppression of the other boundary state, leading to chiral boundary transport. A unique feature of BSE is that we can individually choose, on each boundary of the lattice, which boundary state survives propagation. In particular, we can induce chiral transport in the same direction on opposite boundaries as in Fig. 15(d). Without BSE, this is strictly prohibited by the bulk-boundary correspondence.

Breakdown of the bulk-boundary correspondence To demonstrate that the detached boundary states are topologically protected irrespective of the bulk topology, we now consider the minimal driving on an infinite horizontal strip [see Fig. 16(a)] with a bottom and top boundary. BSE is applied exclusively to the bottom boundary such that only the boundary state on the bottom boundary is spectrally detached from the bulk bands.

The breakdown of the bulk-boundary correspondence for this configuration is shown in Fig. 17. We start with a non-zero W_3 invariant at $J = 1$ (left panel). At the bulk phase transition, $J = \pi/4$ (middle panel), the W_3 invariant changes to zero and the boundary state on the top boundary disappears as required by the bulk-boundary correspondence. On the other hand, the detached boundary state on the bottom boundary persists. Beyond the phase transition, at $J = 0.7$ (right panel), an additional boundary state is created on the bottom boundary which has opposite chirality relative to the detached boundary state. In a Hermitian system, these two counterpropagating boundary states would cancel, in agreement with the trivial bulk topology. Here, the imaginary gap prevents their mutual annihilation.

Cutting off the non-Hermitian boundary Since the spectrally detached boundary states no longer depend on the bulk topology, it stands to reason that the non-Hermitian boundary retains the transport properties associated with anomalous Floquet topological insulators when it is cut off from the rest of the lattice. In particular, quantized charge pumping can be implemented on it. Verifying this claim will be the focus of the rest of this thesis.

In Fig. 16(a), the spatial attachment or detachment of the bottom boundary is controlled by the parameter α . For $\alpha = 0$, the bottom boundary is cut off from the bulk and can be regarded as a separate one-dimensional chain. The resulting trajectories for perfect coupling are shown in Fig. 16(c). Through the spatial detachment, additional chiral modes (colored in green) emerge on both subsystems.

On the newly created Hermitian bottom boundary of the minimal driving protocol, conventional bulk-boundary correspondence is recovered (see Fig. 18). On the non-Hermitian Floquet chain, two non-contractible loops $k \mapsto \varepsilon^{1,2}(k, T)$ with opposite chirality $\varepsilon^{1,2}(k + 2\pi, T) = \varepsilon^{1,2}(k, T) \pm 2\pi$ appear in the Floquet spectrum that are separated by an imaginary gap. Here, we observe a new topological phase that occurs exclusively in non-Hermitian Floquet systems and lies outside the classification [34, 35] for static non-Hermitian systems.

Non-Hermitian Floquet chains To study this topological phase, we introduce a simple one-dimensional driving protocol which consists of two alternating steps with directional pairwise coupling $Je^{\pm\gamma}$ [see Fig. 19(a)] between the $n = 2$ adjacent sites \bullet, \circ . A similar model was recently implemented in plasmonic waveguide arrays [72]. For perfect coupling, a state starting on a \bullet (\circ) site moves two sites to the right (left) and picks up the amplitude factor $e^{2\gamma}$ ($e^{-2\gamma}$).

The driving protocol features a topological phase transition at the critical value $\gamma_c = \text{arcosh}(1/\sin|J|)$. As shown in Fig. 19, the spectrum below the transition ($|\gamma| < \gamma_c$) consists of a single contractible loop with periodicity $k \mapsto k + 4\pi$. The contraction of the loop is realized in the Hermitian limit $\gamma \rightarrow 0$. At the transition ($|\gamma| = \gamma_c$), the spectrum possesses an exceptional point [73, 74]. Starting from the exceptional point, the spectrum splits into two non-contractible loops above the transition ($|\gamma| > \gamma_c$). The loops occur with opposite chirality and are separated by an imaginary gap $i\Gamma$ at $\Gamma = 0$.

The phases are distinguished by the \mathbb{Z} -valued winding number

$$\begin{aligned} W(\Gamma) &= \frac{i}{2\pi} \sum_{e^{\Gamma} < |e^{-i\varepsilon^\nu(k, T)}|} \int_{-\pi}^{\pi} e^{i\varepsilon^\nu(k, T)} \partial_k e^{-i\varepsilon^\nu(k, T)} dk \\ &= \frac{1}{2\pi} \sum_{\Gamma < \text{Im} \varepsilon^\nu(k, T)} [\text{Re} \varepsilon^\nu(k, T)]_{k=-\pi}^{k=\pi}, \end{aligned} \tag{15}$$

which counts the number of non-contractible loops above the imaginary gap $i\Gamma$. A non-contractible loop in clockwise direction contributes with a positive integer. In the present model, we have $W = 0$ below the transition and $W = 1$ ($W = -1$) above the transition for $\gamma > 0$ ($\gamma < 0$). We also get $W = 1$ for the detached boundary of the minimal driving protocol in Fig. 18.

Hermitian chains, where loops cannot be separated by imaginary gaps, as well as static non-Hermitian chains, which have only contractible loops, necessarily have winding

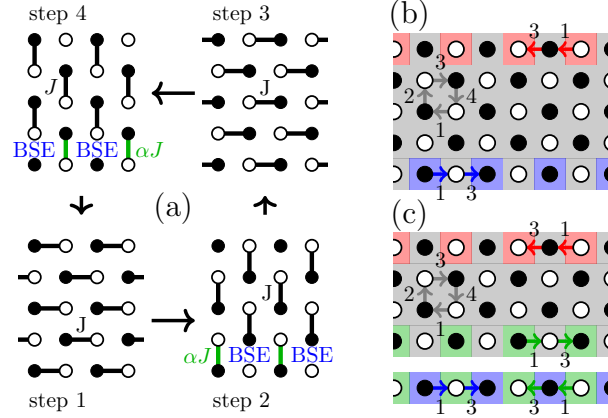


Figure 16: (a) Minimal driving protocol on a semi-infinite strip along the x -axis, with BSE only on the bottom boundary. The non-Hermitian parameter used for the BSE can be found in article VI. Panel (b) [panel (c)] shows the patterns of motion for perfect coupling and $\alpha = 1$ ($\alpha = 0$). Adapted from article VI.

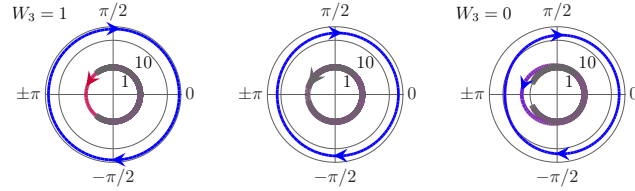


Figure 17: Spectrum $\{e^{-i\epsilon(T)}\}$ of Fig. 16 for $\alpha = 1$, showing the breakdown of bulk-boundary correspondence on the bottom boundary. We use a logarithmic radial axis in all three panels. The color of the curves indicates the amplitude distribution of the eigenvectors on the red, blue, and gray colored areas of the lattice in Fig. 16(b). The arrows indicate the chirality of the loops. Adapted from article VI.

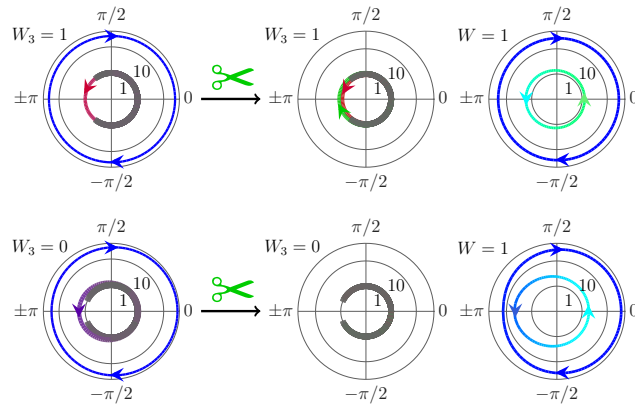


Figure 18: Same as Fig. 17, now showing the spectra before ($\alpha = 1$, left column) and after ($\alpha = 0$, central and right column) the bottom boundary has been cut off. The color of the curves now indicates the amplitude distribution on the colored areas of the lattice in Fig. 16(c). Adapted from article VI.

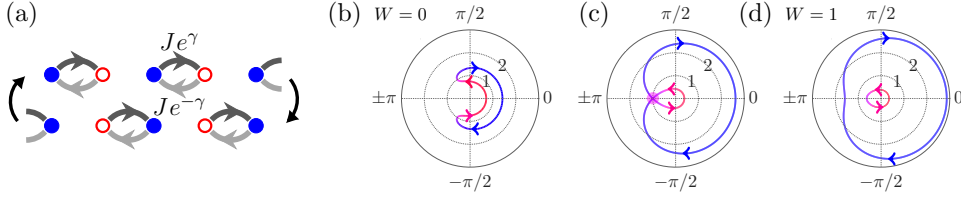


Figure 19: (a) Driving protocol for a non-Hermitian Floquet chain with directional coupling. (b-d) Spectrum of the driving protocol in (b) the trivial phase ($\gamma = 0.2$), (c) at the phase transition ($\gamma = \gamma_c \approx 0.55$), and (d) in the non-trivial phase ($\gamma = 0.6$). We set $J = \pi/3$ in all panels. The exceptional point at the phase transition is indicated by a pink dot. Adapted from article V.

number $W(\Gamma) = 0$ for all Γ .

Since non-Hermitian Floquet chains with a non-zero winding number can be constructed from the boundaries of anomalous Floquet topological insulators, we expect that they carry chiral transport. To quantify the transport, we again use Eq. (1). Note that the transferred charge \bar{C} always vanishes in a Hermitian chain (see article V). $\bar{C} \neq 0$ only becomes possible in a non-Hermitian chain. In the expression of \bar{C} , the propagation distance of each wave packet is now weighted by the non-conserved norm $\langle m|U^\dagger(T)U(T)|m\rangle$, which complicates the interpretation. After normalization $\bar{C}/\bar{\Xi}^2$ with the average norm $\bar{\Xi}^2 \sim \sum_{m=1}^n \langle m|U^\dagger(T)U(T)|m\rangle$ [see Eq. (19) in the supplemental material of article V for the full expression], we recover its original meaning as the average propagation distance.

Fig. 20 shows that the normalized transferred charge $\bar{C}/\bar{\Xi}^2$ continuously increases when we go from the trivial phase with $W = 0$ to the non-trivial phase with $W = 1$, similar to the two-dimensional case in Fig. 5. Again, the phase transition is not directly observable in the functional dependence of \bar{C} .

Probing transport by means of wave packet propagation, we observe a significant difference between the two phases: While wave packets spread out during propagation below the topological phase transition (row “(Fl <)” in Fig. 20), they propagate without spreading above the phase transition (row “(Fl >)” in Fig. 20), where $\bar{C}/\bar{\Xi}^2 \rightarrow 1$.

To relate W and \bar{C} , and thus transport and topology, the Floquet propagator must be regularized in a slightly different manner than for anomalous Floquet topological insulators. Here, the Floquet propagator is regularized if (i) the dominant eigenvalues of the Floquet propagator have modulus one, (ii) the modulus of all other eigenvalues is infinitesimally close to zero, and (iii) the eigenvectors are mutually orthogonal. If these conditions are satisfied, we obtain the fundamental relation (see article V)

$$\bar{C}_{(\text{reg})} = W(\Gamma), \quad (16)$$

which guarantees quantized charge pumping.

Conceptually, regularization of the propagator corresponds to a continuous deformation of $U(T, k)$ such that the eigenvalues $e^{-ie\nu(k, T)}$ move towards the origin or towards the unit circle, as illustrated in the left panel of Fig. 21. Physically, regularization

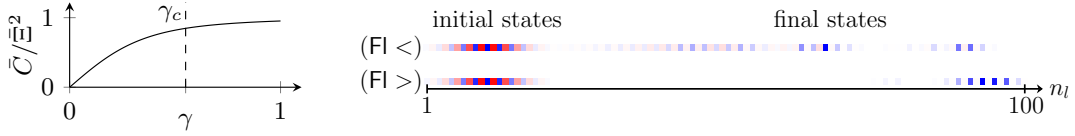


Figure 20: Left panel: Normalized transferred charge $\bar{C}/\bar{\Xi}^2$, as a function of γ with $J = \pi/3$. Right panel: Real-space propagation in the chain over $n_p = 40$ periods with $J = \pi/3$ and $\gamma = 0.08, 1.5$ from top to bottom. Adapted from article V.

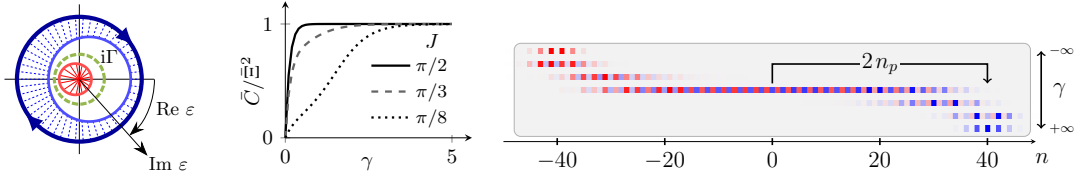


Figure 21: Left panel: Regularization of the spectrum of the Floquet propagator. The spectrum outside (inside) of the imaginary gap $i\Gamma$ (dashed green) moves to the unit circle (origin). Middle panel: Normalized transferred charge $\bar{C}/\bar{\Xi}^2$, for three different values of J . In all cases, $\bar{C}/\bar{\Xi}^2 \rightarrow 1$ in the non-Hermitian limit $\gamma \rightarrow \infty$. Right panel: Real-space propagation of an initial state, centered at site $n = 0$, over $n_p = 20$ periods. Shown is the final state for $\gamma = -\infty, -1, -0.25, 0, 0.25, 1, \infty$ from top to bottom with $J = \pi/3$. In the non-Hermitian limit, we observe quantized charge pumping. Adapted from article V.

corresponds to the Hermitian limit $\gamma \rightarrow 0$ below the phase transition, and the non-Hermitian limit $\gamma \rightarrow \pm\infty$ above the phase transition, where hopping in one direction is fully suppressed.

In contrast to anomalous Floquet topological insulators, fine-tuning to perfect coupling is not required for quantized charge pumping. In the limit $\gamma \rightarrow \pm\infty$, only the norm of the wave packets depends on the parameter J , which drops out after normalization of \bar{C} (see the middle panel of Fig. 21). Exactly half of the wave packet (on either the red or the blue sites in the right panel of Fig. 21) survives propagation and robustly moves 2 sites in each driving period, even if we add disorder to the chain (see article V).

1.5 Conclusions

In this thesis, we studied two-dimensional anomalous Floquet topological insulators with a focus on symmetry and non-Hermiticity. We developed new degeneracy-point expressions for the relevant topological invariants of the propagator which generalize the expressions given in Ref. [19]. The degeneracy-point expressions give an intuitive understanding of the bulk-boundary correspondence and provide the basis for efficient numerical evaluation of the invariants. They especially allowed us to verify that the uni-

versal driving protocol proposed here supports symmetry-protected anomalous Floquet topological phases.

An interesting property of the universal driving protocol, which was not explored in this thesis, is that the symmetry-protection can be locally broken by omitting only the red (or only the blue) lattice sites within a unit cell. In case of fermionic time-reversal symmetry, backscattering is allowed in such a symmetry-breaking unit cell. Therefore, the counterpropagating boundary state will be reflected at a symmetry-breaking unit which is placed at the boundary of the lattice. This could be used to restrict the helical transport to certain regions on the boundary.

The implementation of the time-reversal symmetric variant of the universal driving protocol in waveguide lattices demonstrates that \mathbb{Z}_2 topological phases commonly associated with fermionic condensed matter systems can also be realized in, e.g., photonic systems. Conversely, properties commonly associated with photonic systems like non-Hermitian gain and loss can now be combined with fermionic \mathbb{Z}_2 topological phases through the common framework of the universal driving protocol.

This directly leads to boundary state engineering (BSE), which is probably the most important result of this thesis. BSE and its direct consequences equip anomalous Floquet topological insulators with unprecedented possibilities to control and manipulate topological transport: Boundary states can be selectively amplified, the bulk is no longer required for topological protection, and robustly quantized charge pumping can be implemented on the boundaries even if they have been cut off from the rest of the lattice. Let us emphasize here that the spatial detachment of the boundary is an option offered by BSE, but not required for quantized charge pumping. Depending on the desired application, one may choose to implement quantized charge pumping in a one-dimensional chain, or rather at the boundary of a two-dimensional insulator. Which approach will prove most convenient is a matter of future experimental research. In this thesis, we focused on the potential implementation of BSE in photonic waveguides because the bending losses provide a natural source of non-Hermiticity. Optical lattices of ultracold atoms are another promising platform for BSE. Driving protocols [27] and the manipulation of dissipation losses [75] are both possible within optical lattices.

On the theoretical side, an obvious route for future research is further studies on the interplay between BSE and symmetries, e.g. by cutting off a boundary of the universal driving protocol, after BSE has been applied, and exploring the transport properties of the resulting chain for the two non-Hermitian flavors TRS^* , TRS^t of time-reversal symmetry. Inspection of Fig. 15 already tells us what we can expect. For TRS^* , we can expect a \mathbb{Z} topological phase with chiral transport. For TRS^t , a \mathbb{Z}_2 topological phase with helical transport should emerge, which will require a new topological invariant. Another important question waiting to be explored is whether BSE is specific to two-dimensional anomalous Floquet topological insulators or can be applied to any higher-dimensional anomalous Floquet system.

2 Thesis articles

Author Contribution

Article I:

“*Topological invariants for Floquet-Bloch systems with chiral, time-reversal, or particle-hole symmetry*”

B. Höckendorf, A. Alvermann and H. Fehske, *Phys. Rev. B* **97**, 045140 (2018).

All authors discussed the scope of the work and the strategy of the calculation. B. Höckendorf and A. Alvermann developed the theory and wrote the manuscript which was edited by all authors.

Article II:

“*Universal driving protocol for symmetry-protected Floquet topological phases*”

B. Höckendorf, A. Alvermann and H. Fehske, *Phys. Rev. B* **99**, 245102 (2019).

All authors discussed the scope of the work and the strategy of the calculation. B. Höckendorf and A. Alvermann developed the theory and wrote the manuscript which was edited by all authors.

Article III:

“*Fermionic time-reversal symmetry in a photonic topological insulator*”

L. J. Maczewsky, B. Höckendorf, M. Kremer, T. Biesenthal, M. Heinrich, A. Alvermann, H. Fehske and A. Szameit, *Nat. Mater.*, (2020).

The theory was established by B. Höckendorf, A. Alvermann, and H. Fehske. The sample design and lattice implementation was developed by L. Maczewsky, M. Heinrich and A. Szameit. The characterisation of the lattice structure was carried out by L. Maczewsky, M. Kremer and T. Biesenthal. The project was supervised by H. Fehske and A. Szameit. All authors discussed the results and co-wrote the paper.

Article IV:

“*Non-Hermitian Boundary State Engineering in Anomalous Floquet Topological Insulators*”

B. Höckendorf, A. Alvermann and H. Fehske, *Phys. Rev. Lett.* **123**, 190403 (2019).

All authors discussed the scope of the work and the strategy of the calculation. B. Höckendorf and A. Alvermann developed the theory and wrote the manuscript which was edited by all authors.

Article V:

“*Non-Hermitian Floquet Chains as Topological Charge Pumps*”

B. Höckendorf, A. Alvermann and H. Fehske, submitted to *Phys. Rev. Lett.*

All authors discussed the scope of the work and the strategy of the calculation. B. Höckendorf and A. Alvermann developed the theory and wrote the manuscript which was edited by all authors.

Article VI:

“*Cutting off the non-Hermitian boundary from an anomalous Floquet topological insulator*”

B. Höckendorf, A. Alvermann and H. Fehske, submitted to *Europhys. Lett.*

All authors discussed the scope of the work and the strategy of the calculation. B. Höckendorf developed the theory and wrote the manuscript which was edited by all authors.

Confirmed:

(Prof. Dr. Holger Fehske)

Greifswald, 30.03.2020

(Bastian Höckendorf)

Greifswald, 30.03.2020

Topological invariants for Floquet-Bloch systems with chiral, time-reversal, or particle-hole symmetry

Bastian Höckendorf, Andreas Alvermann,* and Holger Fehske

Institut für Physik, Ernst-Moritz-Arndt-Universität Greifswald, D-17487 Greifswald, Germany



(Received 23 August 2017; published 22 January 2018)

We introduce \mathbb{Z}_2 -valued bulk invariants for symmetry-protected topological phases in $2+1$ -dimensional driven quantum systems. These invariants adapt the W_3 invariant, expressed as a sum over degeneracy points of the propagator, to the respective symmetry class of the Floquet-Bloch Hamiltonian. The bulk-boundary correspondence that holds for each invariant relates a nonzero value of the bulk invariant to the existence of symmetry-protected topological boundary states. To demonstrate this correspondence we apply our invariants to a chiral Harper, time-reversal Kane-Mele, and particle-hole symmetric graphene model with periodic driving, where they successfully predict the appearance of boundary states that exist despite the trivial topological character of the Floquet bands. Especially for particle-hole symmetry, the combination of the W_3 and the \mathbb{Z}_2 invariants allows us to distinguish between weak and strong topological phases.

DOI: [10.1103/PhysRevB.97.045140](https://doi.org/10.1103/PhysRevB.97.045140)

I. INTRODUCTION

Topological states of matter [1–6] have become the subject of intensive research activities over the past decade. More recently, unconventional topological phases in periodically driven systems [7–12] have moved into focus. Driving allows for nontrivial topological phases even if each individual Floquet band is topologically trivial. These phases cannot be characterized by static invariants, such as the Chern numbers of the Floquet bands, but only through invariants that depend on the entire dynamical evolution of the system [11]. Irradiated solid-state systems [13–15] and photonic crystals [16–19], where the third spatial dimension represents the time axis, are promising candidates for the realization of these new topological phases.

The relevant topological invariant of driven $2+1$ -dimensional systems is the W_3 invariant of unitary maps [11], which is evaluated for the Floquet-Bloch propagator $U(\mathbf{k}, t)$ that solves the Schrödinger equation $i\partial_t U(\mathbf{k}, t) = H(\mathbf{k}, t)U(\mathbf{k}, t)$ with a periodic Hamiltonian $H(\mathbf{k}, t+T) = H(\mathbf{k}, t)$. The bulk-boundary correspondence for the W_3 invariant guarantees that the value of $W_3(\epsilon)$ equals the number of chiral boundary states in the gap around the quasienergy ϵ .

The situation changes again for driven systems with additional symmetries. Symmetry-protected boundary states appear in pairs of opposite chirality, such that the W_3 invariant can no longer characterize the nontrivial topological phases [20–28]. Two questions arise immediately: Can the phases be characterized by new invariants? Can these invariants be computed for complicated Hamiltonians and Floquet-Bloch propagators?

In this paper we try to answer both questions affirmatively by deriving and evaluating \mathbb{Z}_2 -valued bulk invariants for Floquet-Bloch systems with chiral, time-reversal, or particle-

hole symmetry. In each case, the symmetry is given by a relation of the form $H(\mathbf{k}, t) = \pm SH(\hat{\mathbf{k}}, \pm t)S^{-1}$ for the time-dependent Bloch Hamiltonian $H(\mathbf{k}, t)$, with a (anti-)unitary operator S and an involution $\mathbf{k} \mapsto \hat{\mathbf{k}}$ on the Brillouin zone \mathcal{B} . The symmetry relation implies a zero W_3 invariant in certain gaps, because the degeneracy points of $U(\mathbf{k}, t)$ that contribute to $W_3(\epsilon)$ occur in symmetric pairs and cancel. Conceptually, the new symmetry-adapted invariants count only one partner of each pair of degeneracy points. Since the result depends on which partner is counted, the new invariants are \mathbb{Z}_2 valued. Symmetry-protected topological boundary states appear in gaps where the symmetry relation enforces $W_3(\epsilon) = 0$, but the \mathbb{Z}_2 invariants are nonzero.

Topological invariants for Floquet-Bloch systems with and without additional symmetries have been introduced before [7, 11, 24–26, 28, 29], and our constructions resemble some of them [24–26] in various aspects. However, most constructions in the literature differ for each symmetry. One of our goals is to show that the construction of invariants in terms of degeneracy points of $U(\mathbf{k}, t)$ applies to each symmetry equally, with only the obvious minimal modifications. In this way the constructions described here constitute a unified approach to topological invariants in Floquet-Bloch systems with symmetries.

Our presentation begins in Sec. II with the discussion of an expression for the W_3 invariant that is particularly well suited for the following constructions, before the different invariants for chiral, time-reversal, and particle-hole symmetry are introduced in Sec. III. Section IV summarizes our conclusions, and the appendixes (Appendix A to Appendix D) give details on the derivations in the main text.

II. W_3 INVARIANT AND DEGENERACY POINTS

The starting point for the construction of the \mathbb{Z}_2 invariants is the expression,

$$W_3(\epsilon) = \sum_{v=1}^n \sum_{i=1}^{\text{dp}} N^v(\epsilon, \mathbf{d}_i) C^v(\mathbf{d}_i), \quad (1)$$

*Author to whom correspondence should be addressed: alvermann@physik.uni-greifswald.de

of the W_3 invariant as a sum over all degeneracy points $i = 1, \dots, \text{dp}$ of the Floquet-Bloch propagator $U(\mathbf{k}, t)$ that occur during time evolution $0 \leq t \leq T$.

Equation (1) is a modified version of an expression for $W_3(\epsilon)$ given in Ref. [30]. As explained in Appendix A, which contains a detailed derivation, it generalizes a similar expression introduced in Ref. [25]. A unique feature of Eq. (1) is the invariance of all quantities under general shifts $\epsilon(\cdot) \mapsto \epsilon(\cdot) + 2\pi m$ of the Floquet quasienergies, whereby the ambiguity of mapping eigenvalues $e^{-i\epsilon(\cdot)}$ of $U(\cdot)$ to quasienergies $\epsilon(\cdot)$ is resolved from the outset. For this reason, Eq. (1) is particularly convenient for numerical evaluation, e.g., with the algorithm from Ref. [30]. Note that for the sake of clarity of the main presentation we assume in Eq. (1) that the bands are topologically trivial for $t \rightarrow 0$. The general case is given in Appendix A.

To evaluate Eq. (1), we must decompose $U(\mathbf{k}, t) = \sum_{\nu=1}^n e^{-i\epsilon^\nu} |\mathbf{s}^\nu\rangle\langle \mathbf{s}^\nu|$ into bands $\nu = 1, \dots, n$ with quasienergies $\epsilon^\nu \equiv \epsilon^\nu(\mathbf{k}, t)$ and eigenvectors $\mathbf{s}^\nu \equiv \mathbf{s}^\nu(\mathbf{k}, t)$. Quasienergies are measured in units of $1/T$, and defined up to multiples of 2π . We assume that the $\epsilon^\nu(\mathbf{k}, t)$ are continuous functions. At $t = T$, $\epsilon^\nu(\mathbf{k}, T)$ agrees (modulo 2π) with the Floquet quasienergy derived from the eigenvalues of $U(\mathbf{k}, T)$.

A degeneracy point $\mathbf{d}_i = (\mathbf{k}_i, t_i, \epsilon_i)$ occurs whenever the quasienergies $\epsilon^\nu(\mathbf{k}_i, t_i)$, $\epsilon^\mu(\mathbf{k}_i, t_i)$ of two bands $\nu \neq \mu$ differ by a multiple of 2π , such that $e^{-i\epsilon^\nu} = e^{-i\epsilon^\mu} = e^{-i\epsilon_i}$ for two eigenvalues of $U(\mathbf{k}_i, t_i)$. With each degeneracy point, we can associate the Chern numbers $C^\nu(\mathbf{d}_i) = \oint_{S(\mathbf{d}_i)} F_\alpha^\nu dS^\alpha$, given as the integral of the Berry curvature $2\pi i F_\alpha^\nu(\mathbf{k}, t) = \epsilon_{\alpha\beta\gamma} \partial^\beta (\mathbf{s}^\nu(\mathbf{k}, t)^\dagger \partial^\gamma \mathbf{s}^\nu(\mathbf{k}, t))$ over a small surface $S(\mathbf{d}_i)$ enclosing the degeneracy point. It is $C^\nu(\mathbf{d}_i) = -C^\mu(\mathbf{d}_i) \neq 0$ only for the bands ν, μ that touch in the degeneracy point.

The contribution from each degeneracy point is multiplied by the integer $N^\nu(\epsilon, \mathbf{d}_i) = \lceil (\epsilon^\nu(\mathbf{k}_i, t_i) - \epsilon)/(2\pi) \rceil + \lceil (\epsilon - \epsilon^\nu(\mathbf{k}, T))/(2\pi) \rceil$ that counts how often band ν crosses the gap at ϵ while it evolves from the degeneracy point at $t = t_i$ to its final position at $t = T$. Here, $\lceil \cdot \rceil$ denotes rounding up to the next integer. Since ϵ lies in a gap, $N^\nu(\epsilon, \mathbf{d}_i)$ does not depend on \mathbf{k} .

Moving from one gap at ϵ to the next gap at ϵ' , both being separated by band ν , the value of $N^\nu(\epsilon, \mathbf{d}_i)$ changes by one, such that $W_3(\epsilon)$ changes by $C^\nu = \sum_{i=1}^{\text{dp}} C_i^\nu(\mathbf{d}_i)$. The value of C^ν is just the Chern number of band ν at $t = T$. Note that when we move once through the quasienergy spectrum, letting $\epsilon \mapsto \epsilon + 2\pi$, we change $W_3(\epsilon)$ by $\sum_\nu C^\nu = 0$.

In the situation sketched in Fig. 1, we have $N^\nu(\epsilon, \mathbf{d}_i) = 1$ (or $N^\nu(\epsilon, \mathbf{d}_i) = 0$) for the band directly below (or above) the gap at ϵ . Here, where the bands of $U(\mathbf{k}, t)$ do not wind around the circle independently, $W_3(\epsilon)$ is simply the sum over the degeneracy points in each gap.

III. \mathbb{Z}_2 INVARIANTS FOR FLOQUET-BLOCH SYSTEMS WITH SYMMETRIES

For the construction of the new \mathbb{Z}_2 invariants we adapt Eq. (1), essentially by including only half of the degeneracy points in the summation. We will now, for each of the three symmetries, introduce the respective invariant, formulate the bulk-boundary correspondence between the invariant and symmetry-protected topological boundary states, and present

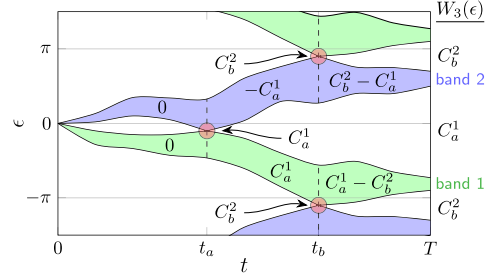


FIG. 1. Schematic illustration of two Floquet-Bloch bands $\nu = 1, 2$, which touch in two degeneracy points $i = a, b$ during the time evolution from $t = 0$ to $t = T$. At each degeneracy point, the Chern numbers of the bands and the W_3 invariant change by the integer $C_i^1(\mathbf{d}_i) = -C_i^2(\mathbf{d}_i)$ according to Eq. (1). In the situation sketched here, anomalous boundary states occur if $C_a^1 = C_b^2 \neq 0$, such that the bands are topologically trivial at $t = T$ but $W_3 \neq 0$ in each gap.

an exemplary application to a Floquet-Bloch system with the specific symmetry.

A. Chiral symmetry

The symmetry relation for chiral symmetry, realized as a sublattice symmetry on a bipartite lattice, is

$$H_{\text{ch}}(\mathbf{k}, t) = -S H_{\text{ch}}(\mathbf{k} + \mathbf{k}_\pi, T - t) S^{-1}, \quad (2)$$

with a unitary operator S , and a reciprocal lattice vector \mathbf{k}_π corresponding to the sublattice decomposition [e.g., $\mathbf{k}_\pi = (\pi, \pi)$ for a square lattice].

Note that the symmetry relation (2) differs from the standard definition of chiral symmetry [27–29], which does not contain the momentum shift \mathbf{k}_π . The inclusion of the momentum shift \mathbf{k}_π is crucial for the existence of symmetry-protected boundary states and of the \mathbb{Z}_2 invariant defined below. As detailed in Appendix B, a Hamiltonian $H_{\text{ch}}(\cdot)$ that fulfills Eq. (2) also fulfills the standard chiral symmetry relation but possesses an additional symmetry that protects the topological phases and boundary states. Without the \mathbf{k}_π shift, chiral symmetry does not allow for the symmetry-protected boundary states observed here [27–29].

Because of the $T-t$ argument on the right-hand side, the symmetry relation (2) does not extend to $U(\mathbf{k}, t)$ but only to the time-symmetrized propagator $U_\star(\mathbf{k}, t) = U(\mathbf{k}, \frac{1}{2}(t + T)) U^\dagger(\mathbf{k}, \frac{1}{2}(T - t))$, for which it implies $S U_\star(\mathbf{k} + \mathbf{k}_\pi, t) S^{-1} = U_\star^\dagger(\mathbf{k}, t)$. Therefore, degeneracy points of $U_\star(\cdot)$ occur in pairs $\mathbf{d}_i = (\mathbf{k}_i, t_i, \epsilon_i)$, $\hat{\mathbf{d}}_i = (\mathbf{k}_i + \mathbf{k}_\pi, t_i, -\epsilon_i)$ with the opposite sign of $C^\nu(\mathbf{d}_i) = -C^\nu(\hat{\mathbf{d}}_i)$. The W_3 invariant, computed from $U_\star(\cdot)$, fulfills $W_3(-\epsilon) = -W_3(\epsilon)$, especially $W_3(\epsilon) = 0$ for a gap at $\epsilon = 0, \pi$.

Note that $U_\star(\cdot)$ belongs to a family of propagators that are related to $U(\cdot)$ by the homotopy $s \mapsto U(\mathbf{k}, (1-s)t + sT) U^\dagger(\mathbf{k}, s(T-t))$. For $s = 0$, we obtain the original propagator $U(\cdot)$, for $s = 1/2$ the symmetrized propagator $U_\star(\cdot)$. Since $U_\star(\cdot)$ is homotopic to $U(\cdot)$, with fixed boundary values $U_\star(\mathbf{k}, 0) = 1$ and $U_\star(\mathbf{k}, T) = U(\mathbf{k}, T)$, we obtain the same result if $W_3(\epsilon)$ is computed with the original

propagator $U(\cdot)$. In this computation, however, the cancellation of degeneracy points would not be obvious.

We now define a \mathbb{Z}_2 invariant, for $\epsilon = 0$ or $\epsilon = \pi$, via

$$W_{\text{ch}}(\epsilon) \equiv \sum_{v=1}^n \sum_{i=1}^{\text{dp}/2} N^v(\epsilon, \mathbf{d}_i) C^v(\mathbf{d}_i) \pmod{2}, \quad (3)$$

where the upper limit $\text{dp}/2$ in the sum over i indicates that exactly one degeneracy point of each symmetric pair $\mathbf{d}_i, \hat{\mathbf{d}}_i$ is included. Depending on which points are included the sum can differ by an even number, such that $W_{\text{ch}}(\epsilon) \in \mathbb{Z}_2$. Since the degeneracy points in each pair are separated by \mathbf{k}_π , a homotopy of $H_{\text{ch}}(\cdot)$ that respects chiral symmetry cannot annihilate the degeneracy points. Therefore, $W_{\text{ch}}(\epsilon)$ is invariant under such a homotopy.

A nonzero value of $W_{\text{ch}}(\epsilon)$ indicates that an odd number of pairs of degeneracy points occur in the gap at ϵ during time evolution from 0 to T . If a boundary is introduced into the system, say along the x direction, the first pair of degeneracy points $\mathbf{d}_i, \hat{\mathbf{d}}_i$ gives rise to two boundary states B_I, B_{II} of opposite chirality that appear immediately after t_i at momenta $(\mathbf{k}_i)_x, (\mathbf{k}_i + \mathbf{k}_\pi)_x$. During the subsequent time evolution the dispersion of these boundary states is related by $\epsilon_I(k_x) = -\epsilon_{II}(k_x + \pi)$ due to chiral symmetry. Therefore, the boundary states are protected: They cannot annihilate each other, because the number of crossings through $\epsilon = 0, \pi$ is fixed by the above relation. The pair of boundary states can disappear only through the appearance of a second pair of degeneracy points at a later $t_j > t_i$. In this way, each pair flips the value of $W_{\text{ch}}(\epsilon)$ and the number of symmetry-protected boundary states in the respective gap. This consideration establishes the bulk-boundary correspondence for chiral symmetry: A nonzero bulk invariant $W_{\text{ch}}(\epsilon)$ corresponds to the existence of a pair of symmetry-protected boundary states with opposite chirality in the gap at ϵ .

Chiral symmetry is realized in the extended Harper model on a square lattice [22],

$$H_{\text{ch}}(t) = \sum_{ij} [J_x(t)(e^{2\pi i \alpha j} c_{i+1,j}^\dagger c_{ij} + \text{H.c.}) + J_y(c_{i,j+1}^\dagger c_{ij} + \text{H.c.})], \quad (4)$$

provided that $J_x(T - t) = J_x(t)$. The rational parameter $\alpha = p/n$ controls the number n of Floquet bands. Note that the (magnetic) unit cell of this model has one element in the x direction and n elements in the y direction.

For the results in Fig. 2 we set $J_x(t) = J_{x,1} + J_{x,2} \cos(2\pi t/T)$, with $\alpha = 1/3, J_{x,1} = 2, J_{x,2} = 1, J_y = 2$. Since n is odd, chiral symmetry prevents the opening of a gap at $\epsilon = 0$. In the gap at $\epsilon = \pi$, where $W_3(\pi) = 0$, a pair of symmetry-protected boundary states exists in accordance with the nonzero value of $W_{\text{ch}}(\pi)$. Note for the interpretation of Fig. 2 that according to the magnetic unit cell for $\alpha = 1/3$ the two boundary states along the y axis can coexist at three different quasienergies for a given k_y , but indeed cross the gap at $\epsilon = \pi$ only once with opposite chirality.

In summary, we see that Eq. (3) defines a \mathbb{Z}_2 -valued bulk invariant for chiral symmetry, which predicts the appearance (or absence) of a symmetry-protected topological phase and of the corresponding boundary states. A different \mathbb{Z}_2 invariant,

which is constructed for a finite system with absorbing boundaries, has been introduced in Ref. [26], where also the “weak” or “strong” nature of topological phases with chiral symmetry is addressed. To relate these results to our \mathbb{Z}_2 invariant we include in Appendix B additional data for different boundary orientations in the Harper model from Eq. (4).

B. Time-reversal symmetry

The symmetry relation for time-reversal symmetry of fermionic particles is

$$H_{\text{tr}}(\mathbf{k}, t) = \Theta H_{\text{tr}}(-\mathbf{k}, T - t) \Theta^{-1}, \quad (5)$$

with an antiunitary operator Θ for which $\Theta^2 = -1$. The symmetry relation (5) implies $\Theta U_\star(-\mathbf{k}, t) \Theta^{-1} = U_\star^\dagger(\mathbf{k}, t)$, again for the time-symmetrized propagator $U_\star(\cdot)$. Therefore, degeneracy points of $U_\star(\mathbf{k}, t)$ occur in pairs $\mathbf{d}_i = (\mathbf{k}_i, t_i, \epsilon_i)$, $\hat{\mathbf{d}}_i = (-\mathbf{k}_i, t_i, \epsilon_i)$ with the opposite sign of $C^v(\mathbf{d}_i) = -C^v(\hat{\mathbf{d}}_i)$. It is $W_3(\epsilon) = 0$ in each gap.

We now define a \mathbb{Z}_2 invariant,

$$W_{\text{tr}}(\epsilon) \equiv \sum_{v=1}^{2n} \sum_{i=1}^{\text{dp}/2} N^v(\epsilon, \mathbf{d}_i) C^v(\mathbf{d}_i) \pmod{2}, \quad (6)$$

where again only one degeneracy point from each symmetric pair is included in the sum.

Note that the bands of $U_\star(\cdot)$ appear in Kramers pairs [3] which, if arranged in this specific order, fulfill $\epsilon^{2\nu-1}(-\mathbf{k}, t) = \epsilon^{2\nu}(\mathbf{k}, t)$. The two bands of each Kramers pair are degenerate at the invariant momenta (IM) $\mathbf{k} \equiv -\mathbf{k}$ (modulo a reciprocal lattice vector). The Kramers degeneracy at the IM, which is enforced by time-reversal symmetry for all t , must be distinguished from the degeneracy points that contribute in Eq. (6): These occur only at certain t_i and involve two bands from two different Kramers pairs.

The considerations leading to a bulk-boundary correspondence are similar to those for chiral symmetry. Again, a pair of degeneracy points $\mathbf{d}_i, \hat{\mathbf{d}}_i$ gives rise to two boundary states, which now appear at momenta $(\mathbf{k}_i)_x, -(\mathbf{k}_i)_x$. Their dispersion relations are connected by $\epsilon_I(k_x) = \epsilon_{II}(-k_x)$, with Kramers degeneracy at the IM $k_x \equiv -k_x$. Because of $\Theta^2 = -1$ the boundary states are twofold degenerate at the IM, which prevents their mutual annihilation. Continuing with the reasoning as before, we conclude that a nonzero value of $W_{\text{tr}}(\epsilon)$ implies the existence of a pair of symmetry-protected boundary states with opposite chirality in the gap at ϵ .

If we move from one gap at ϵ to the next gap at ϵ' , separated by a Kramers pair of bands $2\nu - 1, 2\nu$, the value of $W_{\text{tr}}(\epsilon)$ changes by $W_{\text{tr}}(\epsilon') - W_{\text{tr}}(\epsilon) \equiv \sum_{i=1}^{\text{dp}/2} (C^{2\nu-1}(\mathbf{d}_i) + C^{2\nu}(\mathbf{d}_i)) \pmod{2}$. The right-hand side of this expression gives just the Kane-Mele invariant [3] of the respective Kramers pair (see Appendix C).

Time-reversal symmetry is realized in the extended Kane-Mele model on a graphene lattice [31],

$$H_{\text{tr}}(t) = J_1(t) \sum_{(i,j)} c_i^\dagger c_j + i J_2(t) \sum_{\langle\langle i,j \rangle\rangle} v_{ij} c_i^\dagger \sigma_z c_j + \lambda_v \sum_i \xi_i c_i^\dagger c_i + i \lambda_R \sum_{(i,j)} c_i^\dagger (\boldsymbol{\sigma} \times \mathbf{d}_{ij})_z c_j, \quad (7)$$

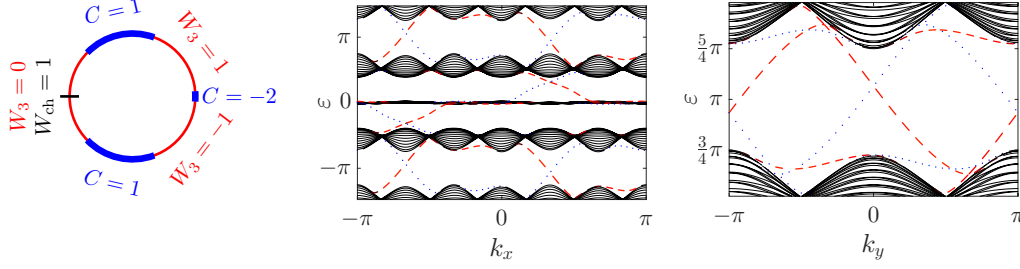


FIG. 2. Bands and boundary states for the chiral model (4) at $t = T$. (Left panel) Diagrammatic representation of the Floquet bands $\exp(-i\epsilon^v(\mathbf{k}, T))$ on the circle S^1 (indicated by thick arcs), with three gaps at quasienergies $\epsilon = \pm\pi/4$ and $\epsilon = \pi$. Included are the Chern numbers of each band, and the W_3 and W_{ch} invariants in each gap. (Central and right panels) Bands (solid) and boundary states (dashed/dotted) on a semi-infinite strip along the x or y axis, as a function of momentum k_x or k_y . Dashed red (dotted blue) curves correspond to boundary states on the top (bottom) boundary. In the right panel, we show only the gap at $\epsilon = \pi$ for better visibility. For both boundary orientations, one pair of symmetry-protected topological boundary states exists in the gap at $\epsilon = \pi$ in accordance with $W_{\text{ch}}(\pi) \neq 0$ in the left panel.

provided that $J_{1,2}(T-t) = J_{1,2}(t)$. For the results in Fig. 3 we set $J_1(t) = J_a + J_b \cos(2\pi t/T)$, $J_2(t) = J_c + J_d \cos(2\pi t/T)$ with $J_a = 0.9, J_b = 1.8, J_c = 0.6, J_d = 1.2$, and $\lambda_v = 1.8, \lambda_R = 0.3$. The W_{tr} invariant correctly predicts the appearance of symmetry-protected boundary states in the gaps at $\epsilon = 0$ and $\epsilon = \pi$, while the Kane-Mele invariants of the Floquet bands and the W_3 invariant vanish.

In summary, we see that Eq. (6) defines a \mathbb{Z}_2 -valued bulk invariant for time-reversal symmetry. The construction of this invariant closely resembles the construction from Ref. [25], to which it reduces under the additional conditions stated in Appendix A for the W_3 invariant. A different \mathbb{Z}_2 invariant has been introduced in Ref. [24], which is based on the original expression [11] for the W_3 invariant and requires a more complicated auxiliary construction [24,32] of a time-symmetrized propagator.

C. Particle-hole symmetry

The symmetry relation for particle-hole symmetry of fermionic particles is

$$H_{\text{ph}}(\mathbf{k}, t) = -\Pi H_{\text{ph}}(-\mathbf{k}, t) \Pi^{-1}, \quad (8)$$

with an antiunitary operator Π for which $\Pi^2 = 1$. The symmetry relation (8) implies $\Pi U(-\mathbf{k}, t) \Pi^{-1} = U(\mathbf{k}, t)$, for the original propagator $U(\cdot)$. If degeneracy points of $U(\mathbf{k}, t)$ occur in pairs $\mathbf{d}_i = (\mathbf{k}_i, t_i, \epsilon_i)$, $\tilde{\mathbf{d}}_i = (-\mathbf{k}_i, t_i, -\epsilon_i)$, they now occur with the same sign of $C^v(\mathbf{d}_i) = C^v(\tilde{\mathbf{d}}_i)$. We can only conclude $W_3(\epsilon) = W_3(-\epsilon)$, and in contrast to chiral and time-reversal symmetry the symmetry relation does not enforce $W_3(\epsilon) = 0$ in any gap.

Despite this difference, symmetry-protected boundary states exist also for particle-hole symmetry, because the IM $\mathbf{k} \equiv -\mathbf{k}$ again have specific significance but play the opposite role as in the case of time-reversal symmetry. There, $\Theta^2 = -1$ forbids single unpaired boundary states at the IM, while here $\Pi^2 = 1$ is compatible with their appearance. An unpaired boundary state in the gaps at $\epsilon = 0, \pi$, which is pinned at the IM, is protected by particle-hole symmetry [26,33]. These states are associated with unpaired degeneracy points of $U(\mathbf{k}, t)$ at the IM.

Let the four IM in the $2+1$ -dimensional bulk system be $\mathbf{M}_0 = 0, \mathbf{M}_1 = \mathbf{b}_1/2, \mathbf{M}_2 = \mathbf{b}_2/2, \mathbf{M}_3 = (\mathbf{b}_1 + \mathbf{b}_2)/2$, for two

primitive reciprocal lattice vectors $\mathbf{b}_1, \mathbf{b}_2$. If we introduce a boundary along a primitive lattice vector \mathbf{a} , with $\mathbf{a} \cdot \mathbf{b}_{1,2} \in \{0, 2\pi\}$, the four IM are projected onto two momenta $k_a = \mathbf{a} \cdot \mathbf{M}_m \in \{0, \pi\}$. Symmetry-protected boundary states, with dispersion relation $\epsilon(-k_a) = -\epsilon(k_a)$, can exist at both momenta.

To capture this situation, we need a total of four \mathbb{Z}_2 invariants, defined for $\alpha = 0, \pi$ and $\epsilon = 0, \pi$ as

$$W_{\text{ph}}^\alpha(\epsilon) = \sum_{v=1}^n \sum_{\substack{\mathbf{k}_i \in \{\mathbf{M}_m\} \\ \mathbf{a} \cdot \mathbf{k}_i = \alpha}} N^v(\epsilon, \mathbf{d}_i) C^v(\mathbf{d}_i) \pmod{2}. \quad (9)$$

In Eq. (9) only unpaired degeneracy points at the two IM \mathbf{M}_m with $\mathbf{a} \cdot \mathbf{M}_m = \alpha$ contribute. Therefore, a nonzero W_{ph} invariant implies the existence of a symmetry-protected boundary state that is pinned at the respective momentum $k_a = \alpha$. For example, $W_{\text{ph}}^\pi(0) \neq 0$ corresponds to a symmetry-protected boundary state with $\epsilon(k_a = \pi) = 0$ in the gap at $\epsilon = 0$. Note that we assume here the absence of boundary states for $t = 0$ (but see Appendix D for an extended discussion).

The W_{ph} invariants only count unpaired degeneracy points, which necessarily occur at IM. The W_3 invariant also counts paired degeneracy points with opposite momenta $\pm\mathbf{k}$; that occur away from the IM. Since paired degeneracy points change the W_3 invariant by an even number, we have $W_{\text{ph}}^0(\epsilon) + W_{\text{ph}}^\pi(\epsilon) \equiv W_3(\epsilon) \pmod{2}$.

According to the summation in Eq. (9) the W_{ph} invariants depend on the boundary orientation given by \mathbf{a} . Especially if $W_3(\epsilon) = 0$ a “weak” topological phase can occur [33], where two symmetry-protected boundary states exist on some boundaries where $W_{\text{ph}}^0 = W_{\text{ph}}^\pi = 1$, but not on other boundaries where $W_{\text{ph}}^0 = W_{\text{ph}}^\pi = 0$. If, on the other hand, $W_3(\epsilon) \neq 0$ in a “strong” topological phase, boundary states occur on each boundary. Especially for odd $W_3(\epsilon)$, we must have nonzero W_{ph} invariants for each boundary orientation, and thus a symmetry-protected boundary state at either $k_a = 0$ or $k_a = \pi$.

Particle-hole symmetry is realized in the graphene lattice model [7,26],

$$H_{\text{ph}}(t) = \sum_{\mathbf{r}} \sum_{l=1}^3 J_l(t) c_{B,\mathbf{r}}^\dagger c_{A,\mathbf{r}+\delta_l} + \text{H.c.}, \quad (10)$$

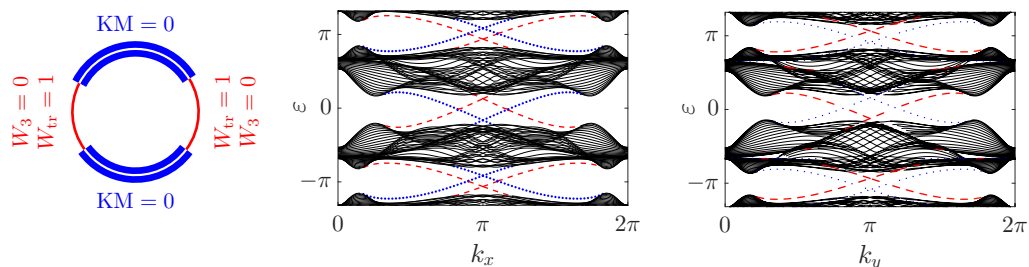


FIG. 3. Same as Fig. 2, now for the time-reversal model (7). (Left panel) Included are the Kane-Mele invariants (KM) of each Kramers pair, and the W_3 and W_{tr} invariants in the two gaps at $\epsilon = 0, \pi$. (Central and right panels) Bands and boundary states on a semi-infinite strip along the x and y axes. For both boundary configurations, one pair of symmetry-protected topological boundary states exists in the two gaps in accordance with $W_{tr}(\epsilon) \neq 0$ in the left panel.

without further constraints on the $J_l(t)$. The $J_l(t)$ are periodically varied according to the protocol in Ref. [26]. For the results in Fig. 4 we set $J_{s,1} = -3\pi/2, J_{s,2} = -3\pi/2, J_{s,3} = 3\pi/2, J_{u,1} = 0, J_{u,2} = -1.2, J_{u,3} = 0.9$.

In Fig. 4 we recognize the weak topological phase just discussed: On a zigzag boundary along a lattice vector \mathbf{a}_3 , with invariants $W_{ph}^0(\epsilon) = W_{ph}^\pi(\epsilon) \neq 0$, we observe in each gap two symmetry-protected boundary states with opposite chirality at momenta $k_3^z = 0, \pi$. On an armchair boundary along a nearest-neighbor vector δ_1 , with invariants $W_{ph}^0(\epsilon) = W_{ph}^\pi(\epsilon) = 0$, no boundary states cross $\epsilon = 0$ or $\epsilon = \pi$. The W_{ph} invariants, together with the zero W_3 invariant, correctly describe this situation.

Note that for a hexagonal lattice, with three inequivalent orientations for each boundary type, an exhaustive analysis is significantly more complicated than suggested by Fig. 4. For details we refer the reader to Appendix D.

In summary, we see that Eq. (9) defines four \mathbb{Z}_2 -valued bulk invariants for particle-hole symmetry, which predict the appearance of symmetry-protected boundary states at $k_a = 0, \pi$ in dependence on the boundary orientation. Since nonzero W_{ph} invariants are compatible with both $W_3(\epsilon) = 0$ and $W_3(\epsilon) \neq 0$, weak and strong topological phases can be distinguished. The possible combinations of the four invariants for fixed $W_3(\epsilon)$ are given by the summation rule stated above. Different \mathbb{Z}_2 invariants have been introduced in Ref. [26], in the form of scattering invariants for finite systems.

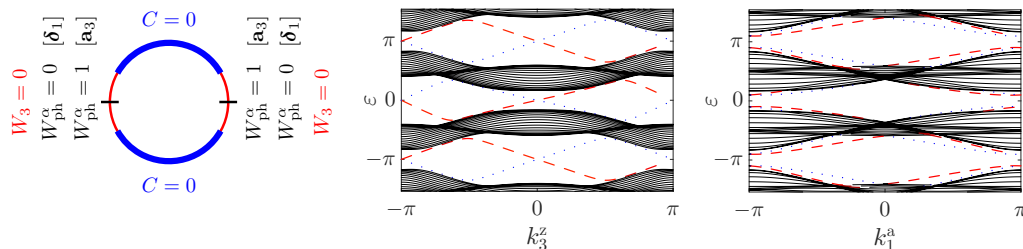


FIG. 4. Same as Figs. 2 and 3, now for the particle-hole symmetric model (10). (Left panel) Included are the Chern numbers of each band, and the W_3 and W_{ph} invariants in the two gaps at $\epsilon = 0, \pi$. [Central (right) panel] Bands and boundary states on a semi-infinite strip with boundaries along the \mathbf{a}_3 (or δ_1) direction, as a function of the respective momentum k_3^z (or k_1^a) parallel to the zigzag (or armchair) boundary. In both gaps, symmetry-protected boundary states exist at $k_3^z = 0, \pi$ (or are absent at $k_1^a = 0, \pi$) in accordance with $W_{ph}^0 = W_{ph}^\pi \neq 0$ for \mathbf{a}_3 (or $W_{ph}^0 = W_{ph}^\pi = 0$ for δ_1) in the left panel.

IV. CONCLUSIONS

The \mathbb{Z}_2 invariants introduced here allow for the classification of topological phases in driven systems with chiral, time-reversal, or particle-hole symmetry. In this way, they complement the W_3 invariant for driven systems without additional symmetries. The \mathbb{Z}_2 invariants are related to previous constructions for symmetry-protected topological phases [24–26,32], but they combine two substantial aspects. First, they are bulk invariants of driven systems, and a bulk-boundary correspondence holds for each invariant. Second, they are given by simple and explicit expressions that involve the (time-symmetrized) Floquet-Bloch propagator, but require no complicated auxiliary constructions. Quite intuitively, the invariants are defined through counting of half of the degeneracy points that appear in symmetric pairs. Note that the invariants depend on the entire time evolution of $U(\mathbf{k}, t)$ over one period $0 \leq t \leq T$, as required for driven systems with the possibility of anomalous boundary states [7,11,24–26]. Once the degeneracy points are known computation of the invariants according to Eqs. (3), (6), and (9) is straightforward. Particularly efficient computation of the \mathbb{Z}_2 invariants is possible with the algorithm from Ref. [30].

These aspects should make the \mathbb{Z}_2 invariants viable tools in the analysis of driven systems with symmetries. For the three generic models considered here, the invariants correctly predict the appearance of symmetry-protected topological boundary

states, even if the static invariants and the W_3 invariant vanish. Concerning the nature of these states, chiral and time-reversal symmetry are set apart from particle-hole symmetry. In the latter case, the existence of symmetry-protected states depends on the orientation of the boundary, similar to the situation for three-dimensional weak topological insulators [6] or quantum Hall systems [34]. It will be interesting to study the different impact of symmetries on topological phases, and on the anomalous boundary states that are unique to driven systems, in nature. One way towards realization of the proper symmetries should be offered by photonic crystals [18,19].

ACKNOWLEDGMENTS

This work was financed in part by Deutsche Forschungsgemeinschaft through SFB 652. B.H. was funded by the federal state of Mecklenburg-West Pomerania through a postgraduate scholarship within the International Helmholtz Graduate School for Plasma Physics.

APPENDIX A: DERIVATION OF EXPRESSION Eq. (1) FOR THE W_3 INVARIANT

We here give the details of the derivation of Eq. (1). In slightly different notation, Eqs. (3.18) and (5.4) in Ref. [30] yield the expression,

$$W_3(\epsilon) = \frac{1}{2\pi} \sum_{v=1}^n \left[\int_0^T \iint_{\mathcal{B}} (\partial^\alpha F_\alpha^v(\mathbf{k}, t)) \epsilon^v(\mathbf{k}, t) dk_1 dk_2 dt \right. \\ \left. + \iint_{\mathcal{B}} F_3^v(\mathbf{k}, T) (i \log_\epsilon e^{-i\epsilon^v(\mathbf{k}, T)} - \epsilon^v(\mathbf{k}, T)) dk_1 dk_2 \right. \\ \left. + \iint_{\mathcal{B}} F_3^v(\mathbf{k}, 0) \epsilon^v(\mathbf{k}, 0) dk_1 dk_2 \right], \quad (\text{A1})$$

for the W_3 invariant from Ref. [11]. It is written as an integral of the Berry curvature,

$$F_\alpha^v(\mathbf{k}, t) = \frac{1}{2\pi i} \epsilon_{\alpha\beta\gamma} \partial^\beta (s^v(\mathbf{k}, t)^\dagger \partial^\gamma s^v(\mathbf{k}, t)), \quad (\text{A2})$$

which involves the eigenvectors $s^v(\mathbf{k}, t)$ and the quasienergies $\epsilon^v(\mathbf{k}, t)$ of the different bands of the Floquet-Bloch propagator $U(\mathbf{k}, t)$. Both quantities are obtained from diagonalization of $U(\mathbf{k}, t)$ as

$$U(\mathbf{k}, t) = \sum_{v=1}^n e^{-i\epsilon^v(\mathbf{k}, t)} |s^v(\mathbf{k}, t)\rangle \langle s^v(\mathbf{k}, t)|. \quad (\text{A3})$$

For the above expression to make sense, we assume continuous quasienergies $\epsilon^v(\mathbf{k}, t)$.

In Eq. (A2), $\epsilon_{\alpha\beta\gamma}$ is the antisymmetric Levi-Civita tensor, the indices α, β, γ run over permutations of the parameters k_1, k_2, t of $U(\cdot)$, and summation over repeated indices is implied. In all expressions, e.g., for F_3^v , we choose t as the third coordinate. The integration is over one period $0 \leq t \leq T$ and over the two-dimensional Brillouin zone \mathcal{B} . The invariant $W_3(\epsilon)$ depends on the quasienergy ϵ within a gap through the second term, the boundary term at $t = T$, where the branch cut of the complex logarithm $\log_\epsilon(\cdot)$ is chosen along the line from zero through $e^{-i\epsilon}$.

The above expression, which is the starting point for the construction of the algorithm in Ref. [30], is not fully suitable for the present study because it is formulated with respect to an absolute reference point $\epsilon = 0$. Instead, we seek an expression where all quantities are computed relative to the quasienergy ϵ of the gap under consideration.

To obtain this expression, note that the divergence of the Berry curvature $F_\alpha^v(\mathbf{k}, t)$ is nonzero only [35] at a degeneracy point \mathbf{d}_i of $U(\mathbf{k}, t)$. At such a point, it is $\partial^\alpha F_\alpha^v(\mathbf{k}_i, t_i) = C^v(\mathbf{d}_i) \delta(\mathbf{k} - \mathbf{k}_i, t - t_i)$, where $C^v(\mathbf{d}_i) = \oint_{\mathcal{S}(\mathbf{d}_i)} F_\alpha^v dS^\alpha$ with a small surface around \mathbf{d}_i . The quantity $C^v(\mathbf{d}_i)$ is an integer, which can be interpreted as the topological charge of the degeneracy point in band v (cf. Ref. [25]). The net charge of a degeneracy point is zero, that is $C^v(\mathbf{d}_i) = -C^\mu(\mathbf{d}_i)$ for the two bands μ, v that touch at \mathbf{d}_i .

We can now replace the first term in Eq. (A1) by a sum over all degeneracy points i . Each degeneracy point gives a contribution of the form,

$$C^v(\mathbf{d}_i) (\epsilon^v(\mathbf{k}_i, t_i) + \Delta_i) + C^\mu(\mathbf{d}_i) (\epsilon^\mu(\mathbf{k}_i, t_i) + \Delta_i), \quad (\text{A4})$$

where we can include a shift Δ_i that cancels because of $C^v(\mathbf{d}_i) = -C^\mu(\mathbf{d}_i)$. We choose Δ_i such that $\epsilon^v(\mathbf{k}_i, t_i) + \Delta_i = \lceil (\epsilon^v(\mathbf{k}_i, t_i) - \epsilon) / (2\pi) \rceil$, with the ceiling function $\lceil \cdot \rceil$ (i.e., rounding up to the next integer). Then, it is also $\epsilon^\mu(\mathbf{k}_i, t_i) + \Delta_i = \lceil (\epsilon^\mu(\mathbf{k}_i, t_i) - \epsilon) / (2\pi) \rceil$ because at a degeneracy point $\epsilon^v(\mathbf{k}_i, t_i)$ and $\epsilon^\mu(\mathbf{k}_i, t_i)$ differ by a multiple of 2π .

For the second term in Eq. (A1), we note that the factor involving the quasienergies does not depend on \mathbf{k} when ϵ is in a gap. Therefore, it can be pulled out of the integral. Evaluation of the complex logarithm, with the branch cut at the right position, gives

$$\frac{i \log_\epsilon e^{-i\epsilon^v(\mathbf{k}, T)} - \epsilon^v(\mathbf{k}, T)}{2\pi} = \left\lceil \frac{\epsilon - \epsilon^v(\mathbf{k}, T)}{2\pi} \right\rceil. \quad (\text{A5})$$

For the third term in Eq. (A1), we have similarly that $\epsilon^v(\mathbf{k}, 0)$ does not depend on \mathbf{k} and, because of $U(\mathbf{k}, 0) = 1$, is in fact a multiple of 2π .

Now we can sum the contribution of all degeneracy points to one band v , and find

$$C^v - C_0^v = \iint_{\mathcal{B}} F_3^v(\mathbf{k}, T) - F_3^v(\mathbf{k}, 0) dk_1 dk_2 = \sum_{i=1}^{\text{dp}} C^v(\mathbf{d}_i), \quad (\text{A6})$$

where $C^v = \iint_{\mathcal{B}} F_3^v(\mathbf{k}, T) dk_1 dk_2$ and $C_0^v = \iint_{\mathcal{B}} F_3^v(\mathbf{k}, 0) dk_1 dk_2$ are the Chern numbers of band v at the final time $t = T$ and initial time $t = 0$.

Putting everything together, we arrive at

$$W_3(\epsilon) = \sum_{v=1}^n \left[\sum_{i=1}^{\text{dp}} N^v(\epsilon, \mathbf{d}_i) C^v(\mathbf{d}_i) \right. \\ \left. + \left\lceil \frac{\epsilon - \epsilon^v(\mathbf{k}, T) + \epsilon^v(\mathbf{k}, 0)}{2\pi} \right\rceil C_0^v \right], \quad (\text{A7})$$

with

$$N^v(\epsilon, \mathbf{d}_i) = \left\lceil \frac{\epsilon^v(\mathbf{k}_i, t_i) - \epsilon}{2\pi} \right\rceil + \left\lceil \frac{\epsilon - \epsilon^v(\mathbf{k}, T)}{2\pi} \right\rceil. \quad (\text{A8})$$

Note that these expressions are invariant under shifts $\epsilon^v(\cdot) \mapsto \epsilon^v(\cdot) + 2\pi m$ of the quasienergies of a band by multiples of 2π , as it should. We can especially choose $\epsilon^v(\mathbf{k}, 0) = 0$, if we prefer, for example, as in Fig. 1 in the main text. For the sake of brevity, we also drop the last term and set $C_0^v = 0$ in the main text, as if all bands were topologically trivial at $t = 0$.

One might want to note the similarity of Eq. (A7) to Eq. (4.4) in Ref. [30], which is the basis of the algorithm presented there. Owing to this similarity, evaluation of the above expression, and also of the \mathbb{Z}_2 invariants defined in the main text, is possible with that algorithm.

Let us finally remark that the expression for the W_3 invariant given in Eq. (9) of Ref. [25] can be recovered from our Eq. (A7) if we adopt the same ordering of the Floquet bands in a “natural quasienergy Brillouin zone.” Specifically, we have to (a) set $\epsilon^v(\mathbf{k}, 0) = 0$, (b) impose the ordering condition, $\epsilon^v(\mathbf{k}, t) \leq \epsilon^{v'}(\mathbf{k}, t)$ for $v < v'$, and (c) assume that $\epsilon^n(\mathbf{k}, t) - \epsilon^1(\mathbf{k}, t) \leq 2\pi$.

Now suppose that the gap at ϵ separates Floquet bands $m, m+1$, that is $\epsilon^m(\mathbf{k}, T) < \epsilon < \epsilon^{m+1}(\mathbf{k}, T)$. In this case, Eq. (A7) reduces to

$$W_3(\epsilon) = \sum_{v=1}^m C^v + \sum_{v=1}^n \sum_{i=1}^{\text{dp}} \left[\frac{\epsilon^v(\mathbf{k}_i, t_i) - \epsilon}{2\pi} \right] C^v(\mathbf{d}_i). \quad (\text{A9})$$

In this expression, the contributions from a degeneracy point \mathbf{d}_i that occurs between two bands $1 \leq \mu < \mu+1 \leq n$, that is for $\epsilon^\mu(\mathbf{k}_i, t_i) = \epsilon^{\mu+1}(\mathbf{k}_i, t_i)$, cancel: The ceiling function $\lceil \cdot \rceil$ has the same value for $v \in \{\mu, \mu+1\}$, but $C^\mu(\mathbf{d}_i) = -C^{\mu+1}(\mathbf{d}_i)$. Only the degeneracy points that occur between bands 1, n , which fulfill $\epsilon^1(\mathbf{k}_i, t_i) = \epsilon^n(\mathbf{k}_i, t_i) - 2\pi$, contribute: Now $\lceil \cdot \rceil = 0$ for $v = 1$, but $\lceil \cdot \rceil = 1$ for $v = n$. In Ref. [25], these degeneracy points are called “zone-edge singularities.” We thus obtain, under the above assumptions, an expression of the form,

$$W_3(\epsilon) = \sum_{v=1}^m C^v + \sum_{i=1}^{\text{dp}} C^n(\mathbf{d}_i), \quad (\text{A10})$$

which is, up to notational differences, Eq. (9) from Ref. [25]. We can thus recognize this equation as a special case of the more general Eq. (A7).

APPENDIX B: CHIRAL SYMMETRY WITH A MOMENTUM SHIFT \mathbf{k}_π

In Eq. (2) chiral symmetry is defined with a $\mathbf{k} \mapsto \mathbf{k} + \mathbf{k}_\pi$ momentum shift, which differs from the standard definition in the literature [27–29],

$$\tilde{H}_{\text{ch}}(\mathbf{k}, t) = -S \tilde{H}_{\text{ch}}(\mathbf{k}, T - t) S^{-1}, \quad (\text{B1})$$

that does not involve a momentum shift.

The origin of the momentum shift in Eq. (2) is a bipartite even-odd sublattice symmetry assumed there. Specifically, we consider the original lattice, whose unit cells are enumerated by two indices (i, j) , as being composed of the sublattices of even $(i + j \equiv 0 \pmod{2})$ and odd $(i + j \equiv 1 \pmod{2})$ unit cells. If the chiral symmetry operator includes an alternating sign flip for every second unit cell of the lattice, say for the odd unit cells, the sign flip translates into the shift $\mathbf{k} \mapsto \mathbf{k} + \mathbf{k}_\pi$ for the Bloch Hamiltonian.

We can now consider the Bloch Hamiltonian for a 2×2 unit cell that comprises four unit cells of the original lattice. If we enumerate these four unit cells in the obvious way, say in the order $(2i, 2j), (2i+1, 2j), (2i, 2j+1), (2i+1, 2j+1)$, the new Bloch Hamiltonian has the 4×4 block form,

$$\hat{H}(\mathbf{k}, t) = \begin{pmatrix} H_{\text{loc}} & H_x & H_y & H_d \\ H_x & H_{\text{loc}} & H_d & H_y \\ H_y & H_d & H_{\text{loc}} & H_x \\ H_d & H_y & H_x & H_{\text{loc}} \end{pmatrix}. \quad (\text{B2})$$

It contains diagonal blocks $H_{\text{loc}} \equiv H_{\text{loc}}(t)$ for terms within a unit cell, and the off-diagonal blocks $H_{x/y} \equiv H_{x/y}(\mathbf{k}, t)$ for hopping along the two lattice axes and $H_d \equiv H_d(\mathbf{k}, t)$ for diagonal hopping. For a Hamiltonian with only nearest-neighbor hopping, the blocks $H_d \equiv 0$ vanish. The equality of the diagonal and off-diagonal blocks incorporated into Eq. (B2) follows from the translational symmetry of the original Hamiltonian. Note that we do not assume additional geometric symmetries, and allow for $H_x \neq H_y$.

The chiral symmetry operator for $\hat{H}(\mathbf{k}, t)$,

$$\hat{S} = \begin{pmatrix} S & & & \\ & -S & & \\ & & -S & \\ & & & S \end{pmatrix}, \quad (\text{B3})$$

is block diagonal. The plus and minus signs of the entries correspond to the alternating sign flip on the even-odd sublattice structure. If the original Hamiltonian $H(\mathbf{k}, t)$ satisfies Eq. (2), we have $\hat{S} \hat{H}(\mathbf{k}, t) \hat{S}^{-1} = -\hat{H}(\mathbf{k}, T - t)$ for the new Hamiltonian. Therefore, $\hat{H}(\mathbf{k}, t)$ fulfills the standard chiral symmetry relation (B1).

To obtain $\hat{H}(\mathbf{k}, t)$ we have considered only translations by an even number of sites on the original lattice. $\hat{H}(\mathbf{k}, t)$ inherits additional symmetries from translations by an odd number of sites. The two symmetry operators are

$$\hat{T}_x = \begin{pmatrix} 0 & \mathbb{1} & 0 & 0 \\ \mathbb{1} & 0 & 0 & 0 \\ 0 & 0 & 0 & \mathbb{1} \\ 0 & 0 & \mathbb{1} & 0 \end{pmatrix}, \quad \hat{T}_y = \begin{pmatrix} 0 & 0 & \mathbb{1} & 0 \\ 0 & 0 & 0 & \mathbb{1} \\ \mathbb{1} & 0 & 0 & 0 \\ 0 & \mathbb{1} & 0 & 0 \end{pmatrix}. \quad (\text{B4})$$

Since $[\hat{T}_x, \hat{T}_y] = 0$, only one of the two symmetry operators is needed below. Note that if we want to interpret $\hat{T}_{x/y}$ as a translation on the original lattice some prefactors $\sim e^{ik_i}$ must be included, but since the prefactors cancel trivially in all relations we have dropped them here. We have $[\hat{T}_{x/y}, \hat{H}(\mathbf{k}, t)] = 0$, but $\hat{S} \hat{T}_{x/y} \hat{S}^{-1} = -\hat{T}_{x/y}$.

The above relations carry over to the Floquet-Bloch propagator $\hat{U}(\mathbf{k}, t)$ associated with $\hat{H}(\mathbf{k}, t)$. We have $S \hat{U}_*(\mathbf{k}, t) S^{-1} = \hat{U}_*^\dagger(\mathbf{k}, t)$, and $[\hat{T}_{x/y}, \hat{U}_*(\mathbf{k}, t)] = 0$.

Now let us assume that $|\psi\rangle$ is an eigenstate of $\hat{U}_*(\mathbf{k}, t)$, to the quasienergy ϵ . The state $|\zeta\rangle = \hat{S}|\psi\rangle$ is an eigenstate of $\hat{U}_*(\mathbf{k}, t)$ to the negative quasienergy $-\epsilon$. Now if $\epsilon = 0, \pi$ the states $|\psi\rangle, |\zeta\rangle$ are degenerate. For the original Hamiltonian, with symmetry relation (2), degenerate quasienergies occur at momenta $\mathbf{k}, \mathbf{k} + \mathbf{k}_\pi$. For the Hamiltonian \hat{H} , with symmetry relation (B1), degeneracies occur at the same momentum \mathbf{k} .

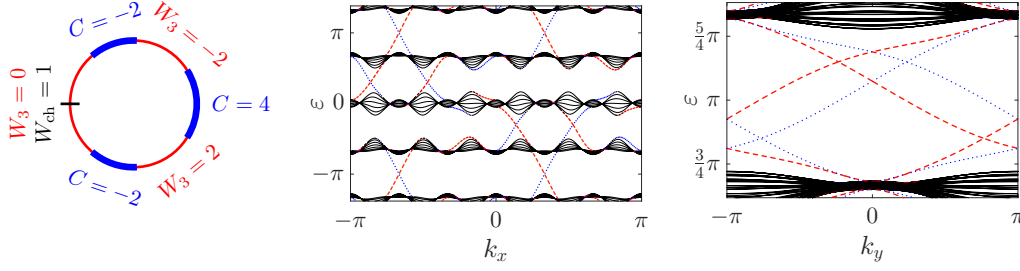


FIG. 5. Same as Fig. 2, now for the periodically kicked version of the Harper model (4) as in Ref. [26] with $\tilde{J}_x = \pi$. (Left panel) Included are the Chern numbers of each band, and the W_3 and W_{ch} invariants in each gap. (Central and right panel) Bands and boundary states on a semi-infinite strip along the x and y axes. In the right panel, we show only the gap at $\epsilon = \pi$ for better visibility. For both boundary configurations, one pair of symmetry-protected topological boundary states exists in the gap at $\epsilon = \pi$ in accordance with $W_{\text{ch}}(\pi) \neq 0$ in the left panel.

For time-reversal symmetry, where a similar situation occurs at the IM, Kramers' theorem implies the orthogonality of the two degenerate states, and thus the symmetry protection of the corresponding topological phases. For chiral symmetry, the eigenstates can be classified by means of the symmetry operator \hat{T}_x (or \hat{T}_y), as $\hat{T}_x|\psi\rangle = \pm|\psi\rangle$. Now $|\zeta\rangle$ is also an eigenstate of \hat{T}_x , with the negative eigenvalue $\hat{T}_x|\zeta\rangle = \mp|\zeta\rangle$. This observation implies the orthogonality of $|\psi\rangle$ and $|\zeta\rangle$.

Therefore, the situation for chiral symmetry is, although for different reasons, analogous to the situation for time-reversal symmetry: In both cases symmetry-protected topological phases exist because degenerate states occur only in orthogonal pairs. We repeat that without the momentum shift \mathbf{k}_π no such argument is possible, and we should not expect that a symmetry-protected topological phase exists in $2+1$ -dimensional systems with that type of chiral symmetry.

To support these findings with additional numerical evidence we show in Figs. 5 and 6 invariants and boundary states of the periodically kicked Harper model introduced in Ref. [26] for the study of topological phases with chiral symmetry. This model is equal to the Harper model of Eq. (4), now with the time dependence $J_x(t) = \tilde{J}_x \sum_{m=-\infty}^{\infty} \delta(t - mT/2)$.

In Fig. 5, with parameters $\alpha = 1/3$, $\tilde{J}_x = \pi$, $J_y = \pi/3$ that correspond to the central panel of Fig. 1 in Ref. [26], we observe one pair of boundary states with opposite chirality in

accordance with the nonzero value $W_{\text{ch}}(\pi)$ of the W_{ch} invariant. This pair exists independently of the boundary orientation. Note that in the gaps between $\epsilon = 0, \pi$, which have no special significance for chiral symmetry, the number of unpaired boundary states is given by the W_3 invariant.

Having changed the parameter \tilde{J}_x to $\tilde{J}_x = 3/2\pi$ in Fig. 6, which corresponds to the right panel of Fig. 1 in Ref. [26], gaps have closed and reopened. The values of the invariants have changed, and now $W_{\text{ch}}(\pi) = 0$. Since $W_{\text{ch}}(\pi)$ is a \mathbb{Z}_2 invariant we expect an even number of pairs of boundary states with opposite chirality. Indeed, we observe two pairs on a boundary along the x axis (central panel), and zero pairs on a boundary along the y axis (right panel). The two pairs are not protected, and could be annihilated by variation of additional model parameters [26].

These results agree with Ref. [26], and with our statements in the main text. In particular, we observe the existence or absence of symmetry-protected boundary states in dependence on the value of the \mathbb{Z}_2 invariant $W_{\text{ch}}(\epsilon)$, but independently of the boundary orientation.

APPENDIX C: DEGENERACY POINTS AND THE KANE-MELE INVARIANT

In the time-reversal symmetric case we can define an effective Brillouin zone \mathcal{E} such that either $\mathbf{k} \in \mathcal{E}$ or $-\mathbf{k} \in \mathcal{E}$. Then, the sum over half of the degeneracy points in Eq. (6) for

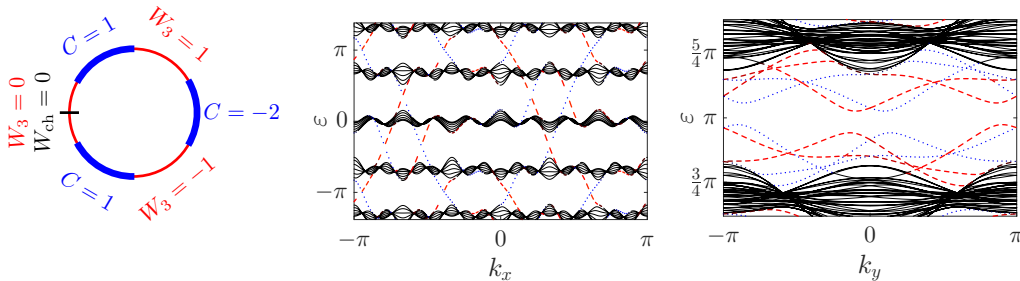


FIG. 6. Same as Fig. 5, now for $\tilde{J}_x = 3/2\pi$. (Central panel) On a boundary along the x axis, two pairs of boundary states with opposite chirality exist in the gap at $\epsilon = \pi$. The two pairs are not symmetry protected and can annihilate each other. (Right panel) On a boundary along the y axis, no boundary state crossing the gap at $\epsilon = \pi$ exists. For both boundary configurations, the number of boundary states (taken modulo 2) agrees with the value $W_{\text{ch}}(\pi) = 0$ in the left panel.

the W_{tr} invariant in the main text can be performed by counting exactly the degeneracy points \mathbf{d}_i with $\mathbf{k}_i \in \mathcal{E}$. Including the time coordinate, these degeneracy points lie in the box $\mathcal{B}\mathcal{X} = \mathcal{E} \times [0, T]$.

Now consider a single Kramers pair of bands $2\nu - 1$, 2ν . The sum over all degeneracy points of this pair can be written as

$$\begin{aligned} & \sum_{i=1}^{\text{dp}/2} C^{2\nu-1}(\mathbf{d}_i) + C^{2\nu}(\mathbf{d}_i) \\ &= \iiint_{\mathcal{B}\mathcal{X}} \partial^\alpha F_\alpha^{2\nu-1}(\mathbf{k}, t) + \partial^\alpha F_\alpha^{2\nu}(\mathbf{k}, t) dk_1 dk_2 dt. \end{aligned} \quad (\text{C1})$$

With Gauss's theorem we can convert this integral into an integral over the surface of the box $\mathcal{B}\mathcal{X}$, which is the union of the two faces $\mathcal{F}_0 = \mathcal{E} \times \{0\}$, $\mathcal{F}_T = \mathcal{E} \times \{T\}$ and the cylinder $\mathcal{C} = \partial\mathcal{E} \times [0, T]$ that contains the points on the boundary curve $\partial\mathcal{E}$ of \mathcal{E} .

With Stokes' theorem, the integral of the Berry curvature $F_\alpha^{2\nu-1}$, $F_\alpha^{2\nu}$ over \mathcal{C} can be converted further into a line integral of the Berry connection $A^{\alpha, 2\nu-1}$, $A^{\alpha, 2\nu}$ over the two curves $\partial\mathcal{E} \times \{0\}$, $\partial\mathcal{E} \times \{T\}$. Recall that in terms of the eigenvectors of $U_\star(\cdot)$, it is $A^{\alpha, \nu}(\mathbf{k}, t) = \frac{1}{2\pi i} [\mathbf{s}^\nu(\mathbf{k}, t)]^\dagger \partial^\alpha \mathbf{s}^\nu(\mathbf{k}, t)$. Since the Berry connection is gauge dependent, we here have to impose a time-reversal constraint on $\partial\mathcal{E}$, namely,

$$\begin{aligned} \mathbf{s}^{2\nu-1}(-\mathbf{k}, t) &= \Theta \mathbf{s}^{2\nu}(\mathbf{k}, t), \\ \mathbf{s}^{2\nu}(-\mathbf{k}, t) &= -\Theta \mathbf{s}^{2\nu-1}(\mathbf{k}, t), \end{aligned} \quad (\text{C2})$$

to obtain the Kane-Mele invariants in a manner analogously to Ref. [36]. Note that the $\mathbf{s}(\cdot)$ in this expression are the eigenvectors of the time-symmetrized propagator $U_\star(\cdot)$, such that the time argument t is unchanged while \mathbf{k} is flipped.

We arrive at the relation (everything taken modulo two),

$$\begin{aligned} & \sum_{i=1}^{\text{dp}/2} C^{2\nu-1}(\mathbf{d}_i) + C^{2\nu}(\mathbf{d}_i) \\ & \equiv \iint_{\mathcal{E}} F_\alpha^{2\nu-1}(\mathbf{k}, T) + F_\alpha^{2\nu}(\mathbf{k}, T) dk_1 dk_2 \\ & \quad - \int_{\partial\mathcal{E}} A^{\alpha, 2\nu-1}(\mathbf{k}, T) + A^{\alpha, 2\nu}(\mathbf{k}, T) dk_\alpha \\ & \quad - \iint_{\mathcal{E}} F_\alpha^{2\nu-1}(\mathbf{k}, 0) + F_\alpha^{2\nu}(\mathbf{k}, 0) dk_1 dk_2 \\ & \quad + \int_{\partial\mathcal{E}} A^{\alpha, 2\nu-1}(\mathbf{k}, 0) + A^{\alpha, 2\nu}(\mathbf{k}, 0) dk_\alpha \\ & \equiv \text{KM}^\nu(T) - \text{KM}^\nu(0), \end{aligned} \quad (\text{C3})$$

and recognize [36] the Kane-Mele invariants $\text{KM}^\nu(0)$ and $\text{KM}^\nu(T)$ of the Kramers pair $2\nu - 1$, 2ν at $t = 0$ and $t = T$. Therefore, the Kane-Mele invariants can be expressed as the sum over half of the degeneracy points of each Kramers pair. This observation justifies the corresponding statements in the main text. For the sake of brevity of the presentation, we there assume $\text{KM}^\nu(0) = 0$, as if the Kramers pairs were topologically trivial at $t = 0$.

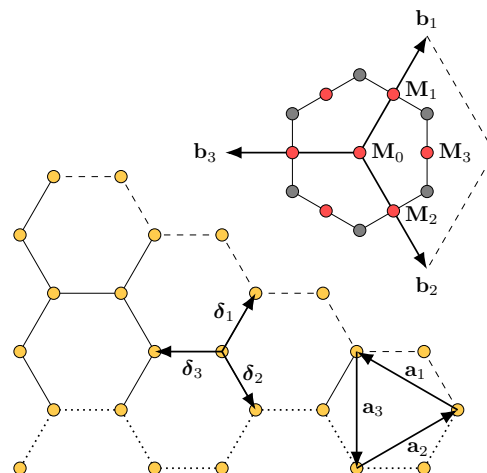


FIG. 7. Primitive lattice vectors \mathbf{a}_i and nearest-neighbor vectors δ_i on a hexagonal lattice. Primitive lattice vectors point along the direction of zigzag boundaries (dashed, along \mathbf{a}_1), and nearest-neighbor vectors along the direction of armchair boundaries (dotted, along δ_3). Also shown are the primitive reciprocal lattice vectors \mathbf{b}_i , together with red circles that indicate the IM $\mathbf{M}_0, \dots, \mathbf{M}_3$ in the Brillouin zone.

APPENDIX D: PARTICLE-HOLE SYMMETRIC BOUNDARY STATES ON A HEXAGONAL LATTICE

For a hexagonal lattice as in Fig. 7, zigzag boundaries occur along directions given by primitive lattice vectors $\mathbf{a}_1, \mathbf{a}_2, \mathbf{a}_3$. Armchair boundaries occur along directions given by nearest-neighbor vectors $\delta_1, \delta_2, \delta_3$. Note that the primitive translation vector for an armchair boundary is $3\delta_i$. In contrast to, say, the situation for a square lattice, both boundary types exist in three inequivalent orientations. This necessitates the more detailed analysis provided here.

To evaluate Eq. (9) for each boundary, we first need to project the IM $\mathbf{M}_1, \mathbf{M}_2, \mathbf{M}_3$ onto the boundary direction (the projection of \mathbf{M}_0 results in zero). For zigzag boundaries, we have $\mathbf{a}_i \cdot \mathbf{M}_i = 0$, and $\mathbf{a}_i \cdot \mathbf{M}_m = \pi$ for the remaining two IM with $m \neq i$. For armchair boundaries we obtain essentially the same result: $3\delta_i \cdot \mathbf{M}_i = 0$, and $3\delta_i \cdot \mathbf{M}_m = \pi$ for $m \neq i$. Note that all values are given modulo 2π . We recognize that for each boundary orientation two IM will contribute in Eq. (9) for given momentum $k_a = 0, \pi$.

To evaluate Eq. (9) we further need to determine the contribution $N^\nu(\epsilon, \mathbf{d}_i) C^\nu(\mathbf{d}_i)$ from unpaired degeneracy points at each IM $\mathbf{M}_0, \dots, \mathbf{M}_3$. For the model from Eq. (10), in the situation of Fig. 4 and Figs. 8 and 9, these values are given in Table I. They have been determined from the propagator $U(\mathbf{k}, t)$ for $0 \leq t \leq T$, using the algorithm from Ref. [30].

With the information from Table I we can now immediately evaluate Eq. (9). In the gap at $\epsilon = \pi$ we obtain the W_{ph} invariants given in the first column of Table II. Note that because of $W_3(\pi) = 0$ we have $W_{\text{ph}}^0(\pi) = W_{\text{ph}}^\pi(\pi)$. Comparison with Figs. 8 and 9, where the boundary states are shown explicitly, confirms the correctness of the W_{ph} invariants.

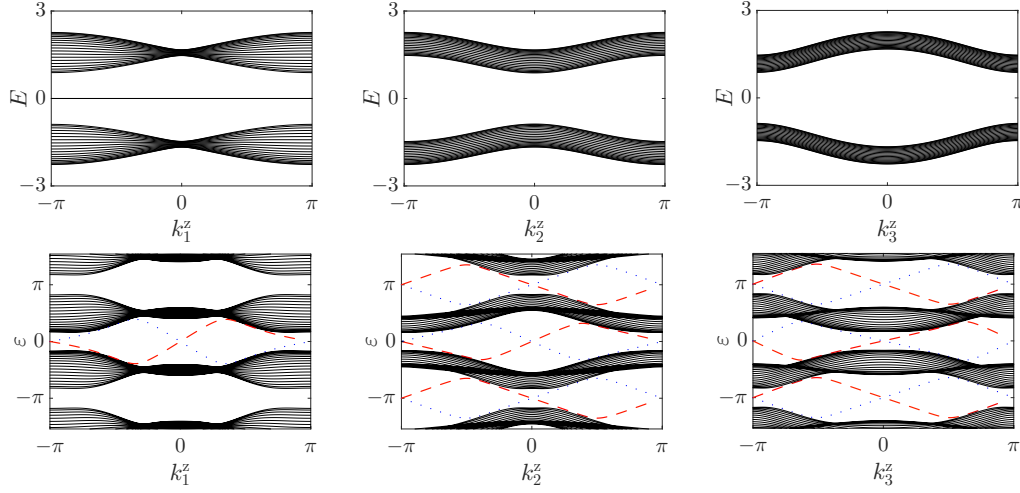


FIG. 8. Initial boundary states of $H_{\text{ph}}(t=0)$ (top row) and Floquet-Bloch boundaries states at $t=T$ (bottom row) for the particle-hole symmetric model (10), on zigzag boundaries along the lattice vectors $\mathbf{a}_1, \mathbf{a}_2, \mathbf{a}_3$ (from left to right). Shown are the energies $E(k_i^z)$ or the quasienergies $\epsilon(k_i^z)$ as a function of the respective momentum k_1^z, k_2^z, k_3^z .

In the gap at $\epsilon=0$ another complication arises due to the possibility of boundary states for $t=0$. In the upper rows of Figs. 8 and 9 we show the boundary spectrum of the initial Hamiltonian $H_{\text{ph}}(t=0)$, which is the starting point for the subsequent evolution described by $U(\cdot)$. Depending on the boundary orientation, $H_{\text{ph}}(t=0)$ can possess a boundary state at $\epsilon=0$. In the present situation, where $H_{\text{ph}}(t=0)$ is particle-hole and (as a real-valued Hamiltonian) time-reversal symmetric, the dispersion of the boundary state is perfectly flat. Recall that $U(\mathbf{k}, t)$, on the other hand, is not time-reversal symmetric according to Eq. (5).

The initial boundary states must be included in Eq. (9), just as we had to do for the W_3 invariant in Eq. (A7) if the bands are not topologically trivial at $t=0$. Any initial boundary

state changes the corresponding W_{ph} invariant by one, that is, through counting modulo two, flips its value between zero and one.

The number of initial boundary states $N(t=0)$ in Table II can be taken from the upper rows in Figs. 8 and 9. The contribution from the degeneracy points of $U(\mathbf{k}, t)$ is given in the third column of this table. Summation of both numbers now gives the W_{ph} invariants for the gap at $\epsilon=0$. Note that because of $W_3(0)=0$ we have again $W_{\text{ph}}^0(0)=W_{\text{ph}}^\pi(0)$. Comparison with Figs. 8 and 9 confirms the correctness of the W_{ph} invariants, also in cases where initial boundary states have to be taken into account.

In the main text, for Fig. 4, we have selected two boundaries without initial boundary states (namely, the third column from

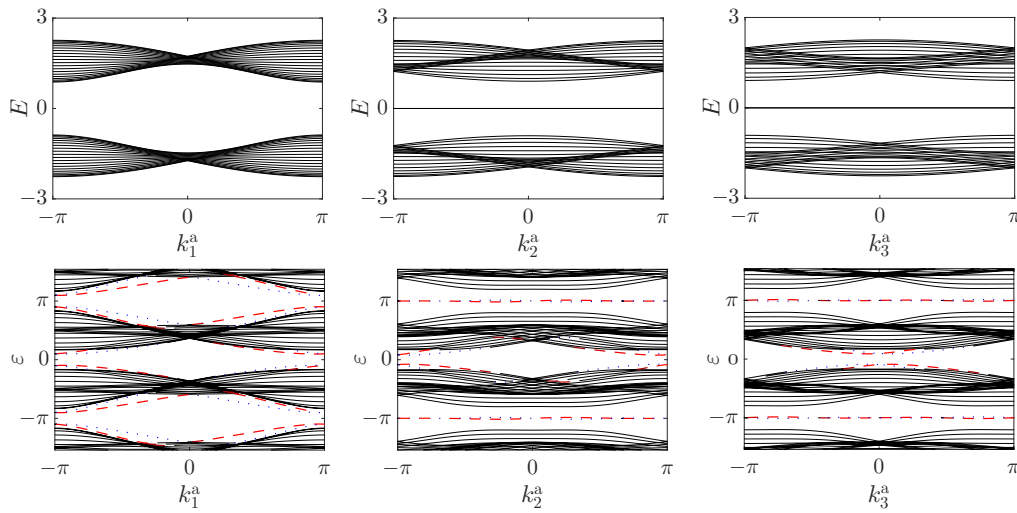


FIG. 9. Same as Fig. 8, now for armchair boundaries along the nearest-neighbor vectors $\delta_1, \delta_2, \delta_3$, and momenta k_1^a, k_2^a, k_3^a .

TABLE I. Values of $N^v(\epsilon, \mathbf{d}_i) C^v(\mathbf{d}_i)$ for Figs. 8 and 9.

ϵ	\mathbf{M}_0	\mathbf{M}_1	\mathbf{M}_2	\mathbf{M}_3
0	0	0	1	1
π	0	0	1	1

Fig. 8 and the first column in Fig. 9), which allowed for a straightforward discussion. With the present results for all boundaries, we recognize the full complexity associated with the “weak” topological phase.

For the gap at $\epsilon = \pi$, initial boundary states do not play a role [they simply do not exist outside of the spectrum of $H_{\text{ph}}(t = 0)$]. According to the $0-\pi$ pattern of the projections $\mathbf{a}_i \cdot \mathbf{M}_m$ or $\delta_i \cdot \mathbf{M}_m$, we expect that in a “weak” phase symmetry-protected boundary states exist for two out of three boundary orientations. This is true for both zigzag and armchair boundaries in Figs. 8 and 9.

For the gap at $\epsilon = 0$, the “two-out-of-three” rule does not apply because of the initial boundary states. For arm-

TABLE II. W_{ph} invariants for Figs. 8 and 9.


	$W_{\text{ph}}^{0,\pi}(\pi)$	$N(t = 0)$	$\sum N^v C^v$	$W_{\text{ph}}^{0,\pi}(0)$
\mathbf{a}_1	0	1	0	0
\mathbf{a}_2	1	0	1	1
\mathbf{a}_3	1	0	1	1
$3\delta_1$	0	0	0	0
$3\delta_2$	1	1	1	0
$3\delta_3$	1	1	1	0

chair boundaries, symmetry-protected boundary states do not occur for any boundary orientation. For zigzag boundaries, symmetry-protected boundary states occur for every boundary orientation. We like to stress that this effect is not a simple consequence of the different geometry of armchair and zigzag boundaries. In particular, as Figs. 8 and 9 show, no immediate relation between the appearance of boundary states at $t = 0$ and at $t = T$ exists. Unless one computes the full W_{ph} invariants, which keep track of the creation and annihilation of symmetry-protected states during time evolution, the entire situation remains obscure.

- [1] K. v. Klitzing, G. Dorda, and M. Pepper, *Phys. Rev. Lett.* **45**, 494 (1980).
- [2] D. J. Thouless, M. Kohmoto, M. P. Nightingale, and M. den Nijs, *Phys. Rev. Lett.* **49**, 405 (1982).
- [3] C. L. Kane and E. J. Mele, *Phys. Rev. Lett.* **95**, 146802 (2005).
- [4] M. Z. Hasan and C. L. Kane, *Rev. Mod. Phys.* **82**, 3045 (2010).
- [5] M. König, S. Wiedmann, C. Brüne, A. Roth, H. Buhmann, L. W. Molenkamp, X.-L. Qi, and S.-C. Zhang, *Science* **318**, 766 (2007).
- [6] L. Fu, C. L. Kane, and E. J. Mele, *Phys. Rev. Lett.* **98**, 106803 (2007).
- [7] T. Kitagawa, E. Berg, M. Rudner, and E. Demler, *Phys. Rev. B* **82**, 235114 (2010).
- [8] N. H. Lindner, G. Refael, and V. Galitski, *Nat. Phys.* **7**, 490 (2011).
- [9] T. Kitagawa, T. Oka, A. Brataas, L. Fu, and E. Demler, *Phys. Rev. B* **84**, 235108 (2011).
- [10] N. Fläschner, B. S. Rem, M. Tarnowski, D. Vogel, D.-S. Lühmann, K. Sengstock, and C. Weitenberg, *Science* **352**, 1091 (2016).
- [11] M. S. Rudner, N. H. Lindner, E. Berg, and M. Levin, *Physical Review X* **3**, 031005 (2013).
- [12] J. Klinovaja, P. Stano, and D. Loss, *Phys. Rev. Lett.* **116**, 176401 (2016).
- [13] Y. H. Wang, H. Steinberg, P. Jarillo-Herrero, and N. Gedik, *Science* **342**, 453 (2013).
- [14] H. L. Calvo, L. E. F. Foa Torres, P. M. Perez-Piskunow, C. A. Balseiro, and G. Usaj, *Phys. Rev. B* **91**, 241404 (2015).
- [15] Y. Wang, Y. Liu, and B. Wang, *Sci. Rep.* **7**, 41644 (2017).
- [16] L. Lu, J. D. Joannopoulos, and M. Soljacic, *Nat. Photon.* **8**, 821 (2014).
- [17] M. C. Rechtsman, J. M. Zeuner, Y. Plotnik, Y. Lumer, D. Podolsky, F. Dreisow, S. Nolte, M. Segev, and A. Szameit, *Nature (London)* **496**, 196 (2013).
- [18] L. J. Maczewsky, J. M. Zeuner, S. Nolte, and A. Szameit, *Nat. Comm.* **8**, 13756 (2017).
- [19] S. Mukherjee, A. Spracklen, M. Valiente, E. Andersson, P. Öhberg, N. Goldman, and R. R. Thomson, *Nat. Comm.* **8**, 13918 (2017).
- [20] M. Lababidi, I. I. Satija, and E. Zhao, *Phys. Rev. Lett.* **112**, 026805 (2014).
- [21] D. Y. H. Ho and J. Gong, *Phys. Rev. B* **90**, 195419 (2014).
- [22] Z. Zhou, I. I. Satija, and E. Zhao, *Phys. Rev. B* **90**, 205108 (2014).
- [23] L. Zhou, H. Wang, Y. D. Ho, and J. Gong, *Eur. Phys. J. B* **87**, 1 (2014).
- [24] D. Carpentier, P. Delplace, M. Fruchart, and K. Gawędzki, *Phys. Rev. Lett.* **114**, 106806 (2015).
- [25] F. Nathan and M. S. Rudner, *New J. Phys.* **17**, 125014 (2015).
- [26] I. C. Fulga and M. Maksymenko, *Phys. Rev. B* **93**, 075405 (2016).
- [27] R. Roy and F. Harper, *Phys. Rev. B* **96**, 155118 (2017).
- [28] S. Yao, Z. Yan, and Z. Wang, *Phys. Rev. B* **96**, 195303 (2017).
- [29] M. Fruchart, *Phys. Rev. B* **93**, 115429 (2016).
- [30] B. Höckendorf, A. Alvermann, and H. Fehske, *J. Phys. A* **50**, 295301 (2017).
- [31] Z. Yan, B. Li, X. Yang, and S. Wan, *Sci. Rep.* **5**, 16197EP (2015).
- [32] D. Carpentier, P. Delplace, M. Fruchart, K. K. Gawędzki, and C. Tauber, *Nucl. Phys. B* **896**, 779 (2015).
- [33] I. Seroussi, E. Berg, and Y. Oreg, *Phys. Rev. B* **89**, 104523 (2014).
- [34] M. Kohmoto, B. I. Halperin, and Y.-S. Wu, *Phys. Rev. B* **45**, 13488 (1992).
- [35] M. V. Berry, *Proc. R. Soc. London, Ser. A* **392**, 45 (1984).
- [36] L. Fu and C. L. Kane, *Phys. Rev. B* **74**, 195312 (2006).

Universal driving protocol for symmetry-protected Floquet topological phases

Bastian Höckendorf, Andreas Alvermann,^{*} and Holger Fehske
Institut für Physik, Universität Greifswald, 17487 Greifswald, Germany

 (Received 2 March 2019; published 3 June 2019)

We propose a universal driving protocol for the realization of symmetry-protected topological phases in $2 + 1$ -dimensional Floquet systems. Our proposal is based on the theoretical analysis of the possible symmetries of a square lattice model with pairwise nearest-neighbor coupling terms. Among the eight possible symmetry operators we identify the two relevant choices for topological phases with either time-reversal, chiral, or particle-hole symmetry. From the corresponding symmetry conditions on the protocol parameters, we obtain the universal driving protocol where each of the symmetries can be realized or broken individually. We provide specific parameter values for the different cases, and demonstrate the existence of symmetry-protected copropagating and counterpropagating topological boundary states. The driving protocol especially allows us to switch between bosonic and fermionic time-reversal symmetry, and thus between a trivial and nontrivial symmetry-protected topological phase, through continuous variation of a parameter.

DOI: [10.1103/PhysRevB.99.245102](https://doi.org/10.1103/PhysRevB.99.245102)

I. INTRODUCTION

Topological phases have become a central topic of condensed matter research over the last few decades [1–6]. Recently, topological phases in periodically driven systems [7–13] have attracted increasing interest, including the anomalous Floquet topological insulators that exhibit a nontrivial topological phase although each of the individual Floquet bands is topologically trivial [14]. Photonic lattices of evanescently coupled waveguides are especially well suited for the realization of these new topological phases [15,16]. In photonic lattices, periodic driving is replaced by spatially periodic modulation of the interwaveguide distance, and thus of the coupling between adjacent waveguides, such that one spatial coordinate represents the time axis of a $2 + 1$ -dimensional Floquet system [17,18]. In this way, direct implementation of driving protocols for (anomalous) Floquet topological insulators becomes possible [19,20].

In this paper, we propose a universal driving protocol for symmetry-protected Floquet topological phases. Presently, most of the theoretical proposals for the realization of such phases [21–32] focus on solid state applications and utilize mechanisms that are not well-suited for a photonic lattice implementation, involving, e.g., spin degrees of freedom [25,30], complicated driving schemes [26,27], or complex gauge potentials [21–24,27]. The driving protocol proposed here, in contrast, has minimal complexity: With only six steps per period and simple pairwise couplings between adjacent sites of a square lattice it can realize Floquet topological phases with time-reversal, chiral, or particle-hole symmetry. Given its minimal complexity, the protocol is not only of intrinsic theoretical value, but allows for immediate experimental observation of these symmetry-protected topological phases in photonic systems.

The starting point for our construction is the analysis of the possible symmetry operators for a driving protocol with only pairwise couplings. On a square lattice, eight distinct symmetry operators have to be considered, but only two of them can lead to driving protocols with symmetry-protected topological phases.

The symmetry analysis provides us with the general form of the driving protocol, which appears in two types: a protocol **A** that supports time-reversal symmetry, and a protocol **B** that supports particle-hole symmetry. These two types of the universal driving protocol cover all four symmetry combinations with nontrivial $2 + 1$ -dimensional topological phases. To verify the universality of the protocol we provide specific parameter sets according to the conditions enforced by the different symmetries. The symmetry-protected Floquet topological phases realized with these parameters are analyzed by means of symmetry-adapted topological bulk invariants [25,26,32], and transport via counterpropagating boundary states is demonstrated numerically.

The structure of the paper is as follows. In Sec. II, we define the square lattice model that is the basis of the present study. In Sec. III, we identify the eight types of symmetry operators that are compatible with the assumptions made in the construction of the square lattice model, analyze which of these operators can be used to implement time-reversal, chiral, or particle-hole symmetry, and determine the resulting constraints on the driving protocol. The universal driving protocol is then introduced and investigated in Secs. IV–VII, once with a focus on time-reversal symmetry (protocol **A** in Secs. V and VI), once for particle-hole symmetry (protocol **B** in Sec. VII). We conclude in Sec. VIII. The appendices detail the pseudospin interpretation of our construction (Appendix A), explore the differences between parallel and antiparallel diagonal couplings (Appendices B and C), and explain why a universal driving protocol with a two-site unit cell should not exist (Appendix D).

^{*}Author to whom any correspondence should be addressed; alvermann@physik.uni-greifswald.de

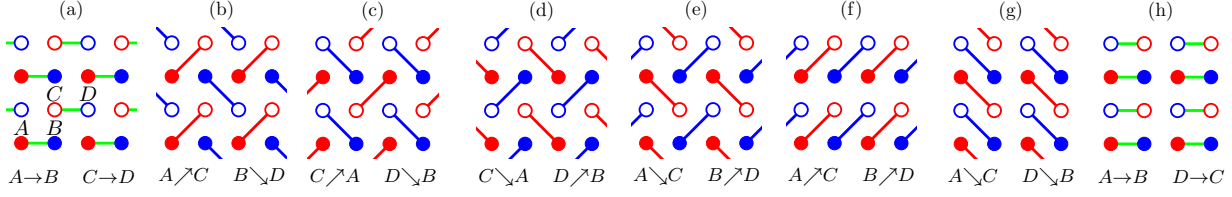


FIG. 1. Eight examples of patterns of compatible pairwise couplings in the square lattice model. The couplings are indicated by lines between adjacent sites. The labels below each pattern follow the notation in the text, with the four sites A (filled red), B (filled blue), C (open red), and D (open blue) as shown in the leftmost pattern.

II. SQUARE LATTICE MODEL

For the construction of the driving protocol, we start with a square lattice with a four-element unit cell, which is the minimal choice for the realization of topological phases with, e.g., time-reversal symmetry (see Appendix D for the case of a two-element unit cell). The lattice sites are located at positions $\mathbf{r} = i\mathbf{a}_x + j\mathbf{a}_y + \delta_s$, with $i, j \in \mathbb{Z}$ and $s \in \{A, B, C, D\}$. Here, $\mathbf{a}_x = (2, 0)^t$, $\mathbf{a}_y = (0, 2)^t$ are the primitive vectors of lattice translations, and $\delta_A = (0, 0)^t$, $\delta_B = (1, 0)^t$, $\delta_C = (1, 1)^t$, $\delta_D = (2, 1)^t$ enumerate the four sites in the unit cell (see Fig. 1). This enumeration is purely a matter of convention, but the present choice will prove useful later. All vectors are measured as multiples of some unspecified unit of length.

On the square lattice, pairwise coupling of neighboring lattice sites can occur along four directions: horizontal [$\delta_{\rightarrow} = (1, 0)$], vertical [$\delta_{\uparrow} = (0, 1)$], diagonal [$\delta_{\nearrow} = (1, 1)$], and antidiagonal [$\delta_{\searrow} = (1, -1)$]. This gives $4 \times 4 = 16$ translational invariant pairwise coupling terms $\hat{t}_{s\circ s'} = \sum_{\mathbf{r}=i\mathbf{a}_x+j\mathbf{a}_y} |\mathbf{r} + \delta_s + \delta_{\circ}\rangle \langle \mathbf{r} + \delta_{s'}|$, with $s \in \{A, B, C, D\}$ and $\circ \in \{\searrow, \rightarrow, \nearrow, \uparrow\}$. In essence, $\hat{t}_{s\circ s'}$ moves a particle (representing, e.g., light in a waveguide) from sites of type s along direction \circ to sites of type s' . The Hermitian conjugate $\hat{t}_{s\circ s'}^\dagger$ operates in the opposite direction, from s' to s . Note that s' is determined by s and \circ , and included for notational clarity only. In addition to the pairwise coupling terms, there are four on-site terms $\hat{n}_s = \sum_{\mathbf{r}=i\mathbf{a}_x+j\mathbf{a}_y} |\mathbf{r} + \delta_s\rangle \langle \mathbf{r} + \delta_s|$, which involve a single type s of lattice sites.

Note that we do not use the language of second quantization but the simpler bra-ket notation. In particular, we do not fix the particle statistics, as encoded by the (anti) commutation relations of creation and annihilation operators in second quantization, and consider both fermionic and bosonic symmetries for the driving protocol.

The general square lattice Hamiltonian reads

$$H(t) = \sum_{\substack{s \in \{A, B, C, D\} \\ \circ \in \{\searrow, \rightarrow, \nearrow, \uparrow\}}} J_{s\circ s'}(t) \hat{t}_{s\circ s'} + J_{s\circ s'}^*(t) \hat{t}_{s\circ s'}^\dagger + \sum_{s \in \{A, B, C, D\}} \Delta_s(t) \hat{n}_s. \quad (1)$$

It includes $4 \times 4 + 4 = 20$ time-dependent parameters $J_{s\circ s'}(t)$ (for pairwise couplings) and $\Delta_s(t)$ (for on-site potentials). All parameters, and so $H(t)$ itself, will be periodic in time, with period T .

In the Hamiltonian (1), not all parameter combinations are admissible. Instead, we impose a compatibility constraint on

the pairwise couplings: terms that involve the same lattice site cannot occur together at the same time. Therefore $J_{s\circ s'}(t) \neq 0$ requires $J_{p\circ p'}(t) = 0$ for any other coupling with $\{p, p'\} \cap \{s, s'\} \neq \emptyset$. Note that this compatibility condition is fulfilled precisely if the two operators $\hat{t}_{s\circ s'}$, $\hat{t}_{p\circ p'}$ commute. A further restriction concerns pairwise couplings that “cross each other” on the lattice, which occurs only for diagonal couplings. For example, $J_{A\nearrow C}(t)$, $J_{D\searrow B}(t)$ cannot both be nonzero at the same t . The on-site potentials $\Delta_s(t)$ are not restricted, and can occur together with any pairwise coupling.

The combination of compatible pairwise couplings gives a total of 12 diagonal + 4 horizontal + 4 vertical = 20 coupling patterns, eight of which are depicted in Fig. 1. For every coupling pattern, at most two parameters $J_{s\circ s'}(t)$ of the Hamiltonian are nonzero. The driving protocol will consist of a cyclic sequence of these coupling patterns, which are selected according to the symmetry analysis in the next section.

In the introduction, we have motivated the universal driving protocol also with the possibility of a photonic lattice implementation. In such an implementation, lattice sites correspond to waveguides. Since coupling of waveguides is achieved by reducing their distance locally [18], spatially complex coupling patterns are not easily realized experimentally and thus should be avoided in the driving protocol. This includes the coupling of more than two or of nonadjacent waveguides, and results in the constraints imposed on the Hamiltonian above.

III. SYMMETRY OPERATORS AND SYMMETRY CONDITIONS

The symmetry relations of time-reversal, chiral, and particle-hole symmetry, as specified further below, involve a transformation $SH(t)S^{-1}$ of the Hamiltonian with a translational-invariant operator S . The symmetry relations can only hold if the transformed Hamiltonian has the same structure as the original Hamiltonian, and is again composed only of pairwise couplings and on-site potentials.

This observation restricts the possible symmetry operators S in a similar way to the coupling patterns in Fig. 1. In particular, every operator can only be composed of nonoverlapping pairwise terms $\hat{t}_{s\circ s'}$ or on-site terms \hat{n}_s . Otherwise, with overlapping terms, the transformed Hamiltonian $SH(t)S^{-1}$ would contain couplings between three or more lattice sites. We do not, however, have the restriction that pairwise terms cannot cross.

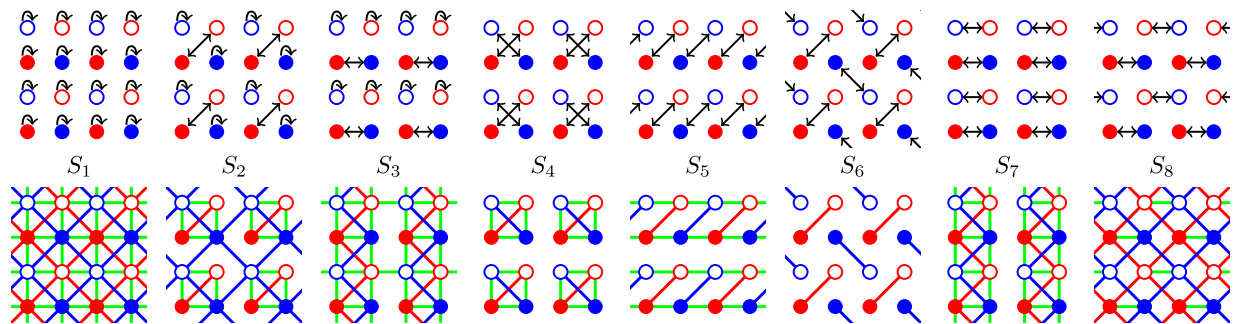


FIG. 2. Graphical representation of the eight symmetry operators S_1, \dots, S_8 for the Hamiltonian (1). The arrows in the upper row indicate how each symmetry operator maps a site onto itself, or onto one of its eight neighbors. The lines in the lower row indicate the compatible pairwise coupling terms.

In total, there are the eight possible symmetry operators S_1, \dots, S_8 shown in Fig. 2, not counting rotations, reflections, or translations. These operators map every lattice site onto exactly one other lattice site, either the same (e.g., for S_1) or a different one (e.g., for S_8).

Each symmetry operator is compatible with the pairwise couplings shown in the lower half of Fig. 2. Exactly these couplings are mapped again to couplings between adjacent sites in the transformation $SH(t)S^{-1}$ with the respective symmetry operator. The remaining pairwise couplings are mapped onto coupling terms that do not occur in the Hamiltonian, and must be excluded.

Two observations are immediate. First, if the graph spanned by the compatible pairwise couplings in Fig. 2 is disconnected, such that propagation is restricted to a lower-dimensional subset of the lattice, nontrivial $2 + 1$ -dimensional topological phases cannot exist. The symmetry operators S_5 and S_7 restrict propagation to quasi-one-dimensional stripes, S_4 and S_6 to finite regions. Only the operators S_1, S_2, S_3, S_8 allow for propagation on the entire two-dimensional lattice. Second, among these four operators, S_1, S_2, S_3 involve isolated on-site terms \hat{n}_s . Such terms necessarily square to $(\xi \hat{n}_s)(\xi \hat{n}_s)^* = |\xi|^2 \hat{n}_s$ for any $\xi \in \mathbb{C}$, which is incompatible with nonunitary symmetries that require $SS^* = -1$ (e.g., fermionic time-reversal symmetry with $\Theta^2 = -1$). These two observations leave us with the operator S_8 for the construction of the universal driving protocol. Note that S_8 is compatible with the symmetry operator S_1 , which will allow us to implement an additional particle-hole symmetry once the protocol has been constructed with S_8 .

The unitary operators S_1 and S_8 can be specified by two 2×2 unitary matrices σ, τ in the form

$$S_{1,8} = \sigma_{AA} \hat{n}_A + \sigma_{BB} \hat{n}_B + \sigma_{BA} \hat{t}_{A \rightarrow B} + \sigma_{AB} \hat{t}_{A \rightarrow B}^\dagger + \tau_{CC} \hat{n}_C + \tau_{DD} \hat{n}_D + \tau_{DC} \hat{t}_{C \rightarrow D} + \tau_{CD} \hat{t}_{C \rightarrow D}^\dagger, \quad (2)$$

where σ, τ have only diagonal (for S_1) or only off-diagonal (for S_8) entries. The mnemonic form of this equation is

$$“S_{1,8} = \begin{pmatrix} |A\rangle \\ |B\rangle \end{pmatrix} \cdot \sigma \begin{pmatrix} \langle A| \\ \langle B| \end{pmatrix} + \begin{pmatrix} |C\rangle \\ |D\rangle \end{pmatrix} \cdot \tau \begin{pmatrix} \langle C| \\ \langle D| \end{pmatrix}” \quad (3)$$

This expression suggests a pseudospin interpretation of the “red” and “blue” sublattice structure depicted in Figs. 1 and 2,

which is detailed in Appendix A. For the following considerations, this interpretation is not needed.

The operator S_8 is compatible with ten pairwise coupling terms, as depicted in Fig. 2, and all diagonal terms \hat{n}_s . These fourteen terms change according to Table I under a transformation with the operator S_1 or S_8 . These transformation rules, together with the symmetry conditions specified next, determine the constraints on the parameters of the Hamiltonian for the respective symmetry, and thus the structure of the driving protocol.

Inspection of Figs. 1 and 2 shows how a transformation with the symmetry operators S_1 and S_8 affects different coupling patterns. The symmetry operator S_1 maps every pattern onto itself. For horizontal couplings, the symmetry operator S_8 leaves pattern (a) invariant but is not compatible with pattern (h). The remaining two horizontal patterns not shown in Fig. 1, as well as all four patterns with vertical couplings, are also incompatible with S_8 . For patterns with perpendicular diagonal couplings, S_8 swaps patterns (b) \leftrightarrow (e) and (c) \leftrightarrow (d). For patterns with parallel diagonal couplings, S_8 leaves pattern (f) invariant while pattern (g) is mapped onto

TABLE I. Transformation $T \mapsto S_1 T S_1^{-1}$ and $T \mapsto S_8 T S_8^{-1}$ of the fourteen terms T used in the construction of the driving protocol.

T	$S_1 T S_1^{-1}$	$S_8 T S_8^{-1}$
$\hat{t}_{A \rightarrow B}$	$\sigma_{AA}^* \sigma_{BB} \hat{t}_{A \rightarrow B}$	$\sigma_{BA}^* \sigma_{AB} \hat{t}_{A \rightarrow B}^\dagger$
$\hat{t}_{C \rightarrow D}$	$\tau_{CC}^* \tau_{DD} \hat{t}_{C \rightarrow D}$	$\tau_{DC}^* \tau_{CD} \hat{t}_{C \rightarrow D}^\dagger$
$\hat{t}_{A \nearrow C}$	$\sigma_{AA}^* \tau_{CC} \hat{t}_{A \nearrow C}$	$\sigma_{BA}^* \tau_{DC} \hat{t}_{B \nearrow D}$
$\hat{t}_{A \searrow C}$	$\sigma_{AA}^* \tau_{CC} \hat{t}_{A \searrow C}$	$\sigma_{BA}^* \tau_{DC} \hat{t}_{B \searrow D}$
$\hat{t}_{C \nearrow A}$	$\sigma_{AA} \tau_{CC}^* \hat{t}_{C \nearrow A}$	$\sigma_{BA} \tau_{DC}^* \hat{t}_{D \nearrow B}$
$\hat{t}_{C \searrow A}$	$\sigma_{AA} \tau_{CC}^* \hat{t}_{C \searrow A}$	$\sigma_{BA} \tau_{DC}^* \hat{t}_{D \searrow B}$
$\hat{t}_{B \nearrow D}$	$\sigma_{BB}^* \tau_{DD} \hat{t}_{B \nearrow D}$	$\sigma_{AB}^* \tau_{CD} \hat{t}_{A \nearrow C}$
$\hat{t}_{B \searrow D}$	$\sigma_{BB}^* \tau_{DD} \hat{t}_{B \searrow D}$	$\sigma_{AB}^* \tau_{CD} \hat{t}_{A \searrow C}$
$\hat{t}_{D \nearrow B}$	$\sigma_{BB} \tau_{DD}^* \hat{t}_{D \nearrow B}$	$\sigma_{AB} \tau_{CD}^* \hat{t}_{C \nearrow A}$
$\hat{t}_{D \searrow B}$	$\sigma_{BB} \tau_{DD}^* \hat{t}_{D \searrow B}$	$\sigma_{AB} \tau_{CD}^* \hat{t}_{C \searrow A}$
\hat{n}_A	\hat{n}_A	\hat{n}_B
\hat{n}_B	\hat{n}_B	\hat{n}_A
\hat{n}_C	\hat{n}_C	\hat{n}_D
\hat{n}_D	\hat{n}_D	\hat{n}_C

TABLE II. Conditions on pairwise couplings and on-site potentials for time-reversal, chiral, and particle-hole symmetry, which follow from Eqs. (4), (6), and (8) and the corresponding choice of the S_8 or S_1 operator. The top and bottom row of each segment of the table must be identical. The sign in the first two relations for time-reversal and particle-hole symmetry with $\Pi = KS_8$ coincides with the sign of the relations $\Theta^2 = \pm 1$, $\Pi^2 = \pm 1$. Note that we allow for $J_{s\leftrightarrow s'}(t) \in \mathbb{C}$ but, due to Hermiticity of the Hamiltonian, have $\Delta_s(t) \in \mathbb{R}$.

time-reversal symmetry							
$J_{A \rightarrow B}(T-t)$	$J_{C \rightarrow D}(T-t)$	$J_{B \nearrow D}(T-t)$	$J_{B \searrow D}(T-t)$	$J_{D \nearrow B}(T-t)$	$J_{D \searrow B}(T-t)$	$\Delta_B(T-t)$	$\Delta_D(T-t)$
$\pm J_{A \rightarrow B}(t)$	$\pm J_{C \rightarrow D}(t)$	$J_{A \nearrow C}^*(t)$	$J_{A \searrow C}^*(t)$	$J_{C \nearrow A}^*(t)$	$J_{C \searrow A}^*(t)$	$\Delta_A(t)$	$\Delta_C(t)$
chiral symmetry							
$J_{A \rightarrow B}(T-t)$	$J_{C \rightarrow D}(T-t)$	$J_{B \nearrow D}(T-t)$	$J_{B \searrow D}(T-t)$	$J_{D \nearrow B}(T-t)$	$J_{D \searrow B}(T-t)$	$\Delta_B(T-t)$	$\Delta_D(T-t)$
$J_{A \rightarrow B}^*(t)$	$J_{C \rightarrow D}^*(t)$	$-J_{A \nearrow C}(t)$	$J_{A \searrow C}(t)$	$-J_{C \nearrow A}(t)$	$J_{C \searrow A}(t)$	$-\Delta_A(t)$	$-\Delta_C(t)$
particle-hole symmetry with $\Pi = KS_1$							
$J_{A \rightarrow B}(t)$	$J_{C \rightarrow D}(t)$	$J_{s \nearrow s'}(t)$	$J_{s \searrow s'}(t)$	$\Delta_A(t)$	$\Delta_B(t)$	$\Delta_C(t)$	$\Delta_D(t)$
$J_{A \rightarrow B}^*(t)$	$J_{C \rightarrow D}^*(t)$	$J_{s' \nearrow s}^*(t)$	$J_{s' \searrow s}^*(t)$	0	0	0	0
particle-hole symmetry with $\Pi = KS_8$							
$J_{A \rightarrow B}(t)$	$J_{C \rightarrow D}(t)$	$J_{B \nearrow D}(t)$	$J_{B \searrow D}(t)$	$J_{D \nearrow B}(t)$	$J_{D \searrow B}(t)$	$\Delta_B(t)$	$\Delta_D(t)$
$\mp J_{A \rightarrow B}(t)$	$\mp J_{C \rightarrow D}(t)$	$-J_{A \nearrow C}^*(t)$	$-J_{A \searrow C}^*(t)$	$-J_{C \nearrow A}^*(t)$	$-J_{C \searrow A}^*(t)$	$-\Delta_A(t)$	$-\Delta_C(t)$

a different pattern with parallel couplings (cf. Appendix B). Note that this behavior concerns only the geometric structure of the coupling patterns. For the mapping of the coupling parameters, Table I has to be consulted.

A. Time-reversal symmetry

The symmetry relation for time-reversal symmetry is

$$H_{\text{tr}}(T-t) = \Theta H_{\text{tr}}(t) \Theta^{-1}, \quad (4)$$

with an antiunitary symmetry operator Θ for which $\Theta^2 = \pm 1$. For our purposes, the operator Θ can be written in the form $\Theta = KS_8$, with the unitary symmetry operator S_8 from the previous section and complex conjugation K . Then, the condition $\Theta^2 = \pm 1$ is equivalent to $\sigma^* \sigma = \tau^* \tau = \pm 1$.

For fermionic time-reversal symmetry with $\Theta^2 = -1$, the only choice is $\sigma = \alpha \sigma_y$ and $\tau = \beta \sigma_y$, with the Pauli matrix σ_y and two phases $\alpha, \beta \in \mathbb{C}$, $|\alpha| = |\beta| = 1$. Without loss of generality, we set $\alpha = \beta = 1$ such that the transformation of (anti)diagonal couplings in Table I involves the same sign. The relevant operator S_8 thus is

$$S_8 = i(\hat{t}_{A \rightarrow B} - \hat{t}_{A \rightarrow B}^\dagger) + i(\hat{t}_{C \rightarrow D} - \hat{t}_{C \rightarrow D}^\dagger), \quad (5)$$

that is $\sigma_{AB} = -\sigma_{BA} = \tau_{CD} = -\tau_{DC} = -i$. Note that the operator does not involve on-site terms \hat{n}_s . The resulting conditions on the parameters of the Hamiltonian following from Eq. (4) are given in Table II. For bosonic time-reversal symmetry with $\Theta^2 = 1$, we must have $\sigma^* \sigma = \tau^* \tau = 1$, and choose $\sigma = \tau = \sigma_x$ with the Pauli matrix σ_x .

B. Chiral symmetry

The symmetry relation for chiral symmetry is

$$H_{\text{ch}}(T-t) = -\Gamma H_{\text{ch}}(t) \Gamma^{-1} \quad (6)$$

with a unitary operator Γ and, by convention, $\Gamma^2 = 1$. Note that, in difference to unitarily-realized symmetries, this relation contains a minus sign: the Hamiltonian anticommutes with Γ .

In the universal driving protocol, which will be constructed based on the symmetry operator S_8 , chiral symmetry can be

implemented either by means of S_1 or S_8 . Here, we deliberately choose the operator S_8 because of its overall significance in the present constructions.

In order to obtain a symmetry-protected phase, chiral symmetry must be realized as a bipartite even-odd sublattice symmetry, where the operator Γ includes a minus sign on every second unit cell [27,32]. With this alternating sign, we have

$$\Gamma = \left[\sum_{\substack{\mathbf{r} = i\mathbf{a}_1 + j\mathbf{a}_2 \\ s \in \{A, B, C, D\}}} (-1)^{i+j} |\mathbf{r} + \delta_s\rangle \langle \mathbf{r} + \delta_s| \right] S_8 \quad (7)$$

as a modification of the translational-invariant operator S_8 . The alternating sign depends on our choice of the unit cell of the square lattice, which here consists of the sites A, B, C , and D in Fig. 1. This is the natural choice when dealing with the symmetry operator S_8 .

The condition $\Gamma^2 = 1$ is equivalent to $S_8^2 = 1$, that is $\sigma^2 = \tau^2 = 1$, since the alternating sign cancels. As for fermionic time-reversal symmetry, we choose $\sigma = \tau = \sigma_y$ with the Pauli matrix σ_y . Note that this choice gives $\Gamma^2 = 1$ here, but $\Theta^2 = -1$ for time-reversal symmetry due to the antiunitarity of Θ . The resulting conditions on the parameters of the Hamiltonian following from Eq. (6) are again given in Table II.

C. Particle-hole symmetry

The symmetry relation for particle-hole symmetry is

$$H_{\text{ph}}(t) = -\Pi H_{\text{ph}}(t) \Pi^{-1}, \quad (8)$$

with an antiunitary operator Π for which $\Pi^2 = \pm 1$. Note that the same time argument t appears on both sides of the relation.

For $\Pi^2 = 1$, use of the operator S_8 (with $\sigma = \tau = \sigma_x$) forbids the appearance of horizontal pairwise couplings $A \rightarrow B$ and $C \rightarrow D$ in the driving protocol according to the constraints listed in Tab. II. Then, the lattice decouples into two independent (“red” and “blue”) sublattices. To avoid this

situation, we use the operator S_1 for particle-hole symmetry with $\Pi^2 = 1$.

We now choose $\sigma = -\tau = \sigma_z$ with the Pauli matrix σ_z , such that

$$S_1 = n_A - n_B - n_C + n_D, \quad (9)$$

or $\sigma_{AA} = -\sigma_{BB} = -\tau_{CC} = \tau_{DD} = 1$. The resulting conditions on the parameters of the Hamiltonian following from Eq. (8), especially $\Delta_s(t) = 0$ for all on-site potentials, are given in Table II.

For $\Pi^2 = -1$, we have to use the operator S_8 according to the analysis in Sec. III. We can choose $\sigma = \tau = \sigma_y$ as for fermionic time-reversal symmetry. Now, however, the symmetry relation (8) contains the same time argument. The resulting conditions on the parameters of the Hamiltonian are again given in Table II.

IV. UNIVERSAL DRIVING PROTOCOL: PRINCIPAL CONSIDERATIONS

The driving protocols considered here consist of n consecutive steps during which the Hamiltonian is constant. Since we can always multiply the Hamiltonian in one step by a number proportional to the step length, we can assume that all steps have equal length $\delta t = T/n$, where T is the period of the driving protocol.

Due to the constraints imposed on the Hamiltonian in Sec. II, each step of the driving protocol is given by one pattern of compatible pairwise couplings, several of which are shown in Fig. 1. While there remains some ambiguity in the construction of the protocol, the selection of the coupling patterns, and their arrangement into the n -step sequence, has to be carried out according to the symmetry analysis from Sec. III. In particular, only coupling patterns that are compatible with the symmetry operator S_8 can be chosen in the construction.

The principal distinction between the two protocols that will be introduced in Secs. V and VII arises from the time argument in the symmetry relations (4) and (8). For time-reversal symmetry, where different time arguments t and $T-t$ appear on either sides of the symmetry relation (4), in principal any pattern “(p)” compatible with S_8 can be used in the protocol if its counterpart “ $S_8(p)S_8^{-1}$ ” appears at $T-t$. Exploration of the different combinations quickly shows that only the four patterns (b)–(e) with perpendicular diagonal couplings give rise to a nontrivial driving protocol with a small number of steps. In fact, it is not surprising that perpendicular couplings should be used since the protocol has to support counter-propagating boundary states for time-reversal symmetry (see also Appendix B). Therefore the driving protocol for time-reversal symmetry (“protocol A”) will be constructed out of the four patterns (b)–(e) in Fig. 1 with perpendicular diagonal couplings, in combination with the horizontal pattern (a).

For particle-hole symmetry, where the same time argument t appears on both sides of the symmetry relation (8), only patterns that are mapped onto themselves by S_8 can be used. Therefore the driving protocol for particle-hole symmetry (“protocol B”) will be constructed out of patterns with parallel diagonal couplings (pattern (f) in Fig. 1, or patterns

(f1)–(f4) in Fig. 12 in the Appendix), in combination with the horizontal pattern (a).

V. UNIVERSAL DRIVING PROTOCOL A: TIME-REVERSAL SYMMETRY

A. Construction of the protocol

According to the previous section, we construct the driving protocol A for time-reversal symmetry out of the four perpendicular diagonal coupling patterns (b)–(e) from Fig. 1. How these patterns should be arranged into a sequence can now be deduced from the mappings induced by the operator S_8 . If we start the sequence with, say, pattern (b), the sequence has to end with pattern (e) since S_8 swaps (b) \leftrightarrow (e). If the second step in the sequence is pattern (c), the penultimate step in the sequence must be pattern (d) since S_8 swaps (c) \leftrightarrow (d). Therefore only two different four-step sequences qualify for driving protocol A: (b) \rightarrow (c) \rightarrow (d) \rightarrow (e) and (b) \rightarrow (d) \rightarrow (c) \rightarrow (e). Starting with different patterns results in equivalent sequences.

In these two four-step sequences, the “red” and “blue” sublattice of the square lattice remain decoupled, as can be deduced from Fig. 1. Therefore a horizontal (or, equivalently, vertical) coupling pattern has to be added to the sequence. The only pattern of this type compatible with S_8 is pattern (a) in Fig. 1. In order to allow for time-reversal or chiral symmetry, pattern (a) has to appear in symmetric position in the sequence: (i) as the central step 3 of a five-step sequence, (ii) as steps 1, 6 or (iii) steps 2, 4 of a six-step sequence. Taking into account that according to Table I fermionic time-reversal symmetry changes the sign of the parameters $J_{A \rightarrow B}$, $J_{C \rightarrow D}$ of pattern (a), only the last possibility (iii) results in a nontrivial addition to the sequence.

To summarize, we have the two variants of driving protocol A shown in Fig. 3. The protocol is constructed out of the first five coupling patterns in Fig. 1, and according to our construction will be able to support either time-reversal, chiral, or particle-hole symmetry. In each step, the coupling patterns can be combined with arbitrary on-site potentials $\Delta_s(t)$ without changing the structure of the driving protocol or violating the constraints on the Hamiltonian. This gives a total of $6 \times (2 + 4) = 36$ parameters, which are further restricted by the conditions in Table II if the respective symmetry is enforced.

B. Perfect coupling

“Perfect coupling” denotes the situation where all on-site potentials $\Delta_s \equiv 0$, and the pairwise couplings in a given step are either both $J_{s_0 s'} \equiv 0$ or $|J_{s_0 s'}| \equiv J_p$, with $J_p = \pi/(2\delta t)$ (here, for six steps, $J_p = 3\pi/T$). The sign of the $J_{s_0 s'}$ parameters must be chosen according to Table II for the respective symmetry.

At perfect coupling, pairwise coupling fully transfers the amplitude on one lattice site to an adjacent lattice site. The driving protocol reduces to a sequence of jumps that follow the geometric shapes of the coupling patterns.

The resulting patterns of motion for the two variants of driving protocol A are shown in Fig. 4. The difference between the two variants is only the coupling in the horizontal steps

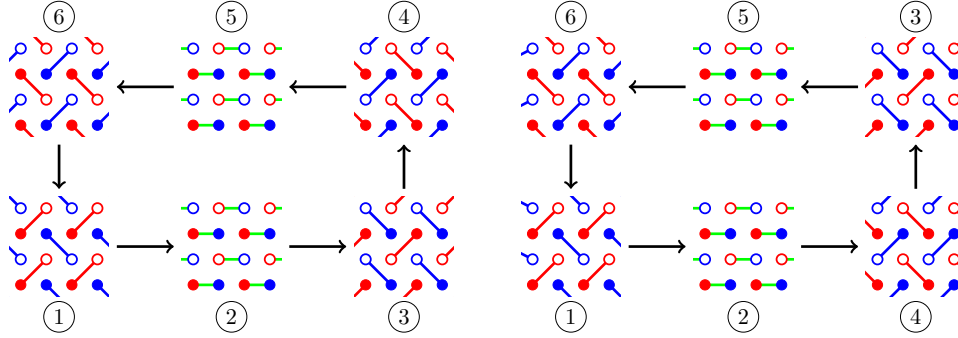


FIG. 3. Two variants of the driving protocol A, which consist of a cyclic six-step sequence of the first five coupling patterns (a)—(e) from Fig. 1. (Left) In this variant, the protocol consists of the sequence (b) \rightarrow (a) \rightarrow (c) \rightarrow (d) \rightarrow (a) \rightarrow (e). (Right) In this variant, the protocol consists of the sequence (b) \rightarrow (a) \rightarrow (d) \rightarrow (c) \rightarrow (a) \rightarrow (e). As shown in the text, both variants are equivalent.

2 and 5, which is equal to $\pm J_p$ for the “left” variant and equal to zero for the “right” variant. A particle in the bulk moves in a closed loop, while a particle at the boundary is transported by two sites in one cycle. The direction of motion depends on the starting site (“red” or “blue”). This pattern of motion gives rise to a nontrivial topological phase, and to a symmetry-protected pair of boundary states with opposite chirality.

Note that when we introduce boundaries, either here or for Figs. 5–9 below, we always choose boundaries that do not separate sites within one unit cell, and thus are compatible with the symmetry operators S_1 and S_8 . As in Fig. 4, boundaries along the x direction (y direction) are parallel to the translation vector \mathbf{a}_x (\mathbf{a}_y).

For perfect coupling, scattering between boundary states with opposite chirality is strictly forbidden by the construction of the protocol, rather than by a topological constraint. In particular, a state starting on a “red” (“blue”) site always ends up on a “red” (“blue”) site after a full cycle. Fully developed symmetry-protected phases require general parameters in the driving protocol, and will be studied in the next section.

C. Equivalence of driving protocols

The patterns of motion in Fig. 4 suggest that the two variants of the driving protocol A are in fact equivalent. As we show now, the equivalence holds not only at perfect coupling but in general.

The Floquet propagator $U(T)$, over one period of the driving protocol, is a simple product

$$U(T) = U_6 U_5 U_4 U_3 U_2 U_1 \quad (10)$$

of the Floquet propagators $U_k = \exp[-i\delta t H_k]$ for each of the steps $k = 1, \dots, 6$, with constant Hamiltonian $H(t) \equiv H_k$ for $(k-1)\delta t \leq t \leq k\delta t$ in step k .

Now let $S = \hat{t}_{A \rightarrow B} + \hat{t}_{A \rightarrow B}^\dagger + \hat{t}_{C \rightarrow D} + \hat{t}_{C \rightarrow D}^\dagger$ be the unitary operator that swaps the “red” and “blue” sublattice (we have $S = S^\dagger$ and $S^2 = 1$). In fact, S is a special case of the symmetry operator S_8 , and $S = -iU_2 = -iU_5$ at perfect coupling $J_{A \rightarrow B} = J_{C \rightarrow D} = J_p$.

Inserting S into the Floquet propagator, we have the alternative expression

$$U(T) = U_6 (U_5 S^\dagger) (S U_4 S^\dagger) (S U_3 S^\dagger) (S U_2) U_1. \quad (11)$$

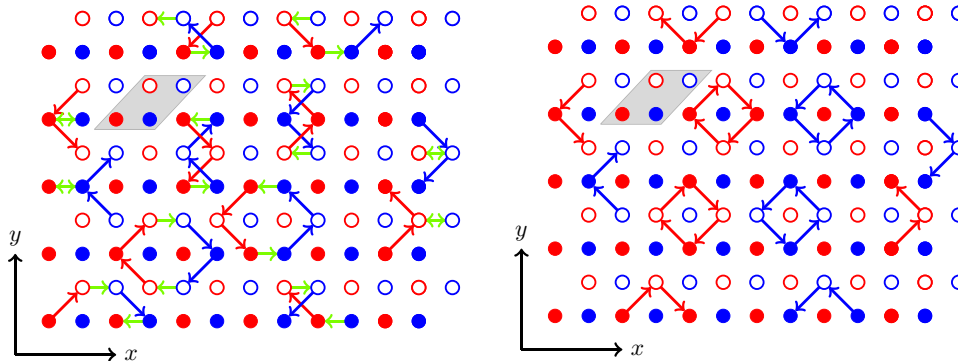


FIG. 4. Patterns of motion during one cycle of driving protocol A at perfect coupling, on a finite lattice of 6×4 unit cells (one unit cell is shown as a gray rhomboid). The lattice comprises only entire unit cells, such that the boundaries are compatible with the symmetry operators S_1 and S_8 . The left and right panel correspond to the two variants of the protocol in Fig. 3. For the “left” variant, the coupling in the horizontal steps 2, 5 is equal to $\pm J_p$, for the “right” variant it is equal to zero.

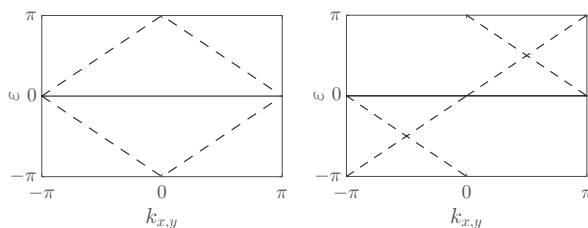


FIG. 5. Dispersion of bulk (solid) and boundary (dashed) states for perfect coupling with fermionic time-reversal (left) or chiral (right) symmetry. Parameter values can be deduced from the corresponding columns in Table III, setting $J = J_p$ and $\Delta = 0$. Here and in Figs. 6–8, we show the states on one boundary of a semi-infinite ribbon, and do not include the states on the opposite boundary.

Since S swaps the “red” and “blue” sublattice, it effectively exchanges steps 3 and 4. On the other hand, the product SU_2 can be combined into a horizontal coupling step 2 with modified parameters, as in

$$SU_2 \begin{bmatrix} J_{A \rightarrow B} \\ J_{C \rightarrow D} \end{bmatrix} = -i U_2 \begin{bmatrix} J_{A \rightarrow B} - J_p \\ J_{C \rightarrow D} - J_p \end{bmatrix}, \quad (12)$$

where we include the coupling parameters explicitly.

Therefore the Floquet propagator $U(T)$, over one driving period of the protocol, is identical (up to a sign $(-i)^2 = -1$) for both variants if the parameters of the horizontal coupling steps 2, 5 are modified by $\pm J_p$ according to the above transformation. Especially at perfect coupling, the parameters are either J_p (“left” variant) or zero (“right” variant), as in Fig. 4.

Note that the “right” variant in Fig. 4 has a close connection to the driving protocol from Ref. [14], which realizes Floquet topological insulators without additional symmetries. Essentially, two copies of this protocol have to be combined to obtain our driving protocol with symmetries. The details of the combination, as well as the conditions on the protocol parameters, follow from the symmetry analysis provided here.

D. Equivalence of coupling steps

Similar to the entire driving protocol, also the individual steps can be written in different equivalent ways. To see how, assume that the Hamiltonian in one step of duration δt is of the form $H_{\text{step}} = J(\hat{t}_{s\oslash s'} + \hat{t}_{s\oslash s'}^\dagger) + \Delta(\hat{n}_s - \hat{n}_{s'})$, with $J, \Delta \in \mathbb{R}$. The propagator for this step evaluates to

$$U_{\text{step}}(J, \Delta) = \exp[-i \delta t H_{\text{step}}] \\ = \cos(\delta t \xi) \mathbb{1} - i \frac{\sin(\delta t \xi)}{\xi} H_{\text{step}}, \quad (13)$$

with $\xi = (J^2 + \Delta^2)^{1/2}$. Essentially, this propagator is an $SU(2)$ rotation.

The right-hand side of Eq. (13) is periodic in the quantity ξ . Therefore

$$U_{\text{step}}(J, \Delta) = (-1)^m U_{\text{step}}(\alpha_m J, \alpha_m \Delta) \quad (14)$$

for every $\alpha_m = 1 + (2mJ_p)/(J^2 + \Delta^2)^{1/2}$ with $m \in \mathbb{Z}$.

This relation becomes especially clear for $\Delta = 0$, where $U_{\text{step}}(J, 0) = (-1)^m U_{\text{step}}(J + 2mJ_p, 0)$. In particular, for perfect coupling $|J| = J_p = \pi/(2\delta t)$, where $U(\pm J_p, 0) = \mp i(\hat{t}_{s\oslash s'} + \hat{t}_{s\oslash s'}^\dagger)$, negative and positive couplings $J = \pm J_p$ are equivalent.

The equivalence of coupling steps with different parameters has important consequences, both conceptually (see Sec. VIB) as well as practically for a photonic lattice implementation. Implementation of negative couplings between waveguides is a challenging procedure [33], but depending on the symmetry negative couplings cannot be avoided in the driving protocol (cf. Table II). Fortunately, any negative coupling $J < 0$ can be replaced by an equivalent positive coupling $\alpha_m J$ from Eq. (14). This argument shows that negative couplings are not a principal obstacle against a photonic lattice implementation of the universal driving protocol.

VI. SYMMETRY-PROTECTED FLOQUET TOPOLOGICAL PHASES

In $2 + 1$ dimensions [28], fermionic time-reversal symmetry ($\Theta^2 = -1$) leads to a symmetry-protected \mathbb{Z}_2 topological phase with counterpropagating boundary states. Bosonic time-reversal symmetry ($\Theta^2 = 1$) does not lead to a nontrivial topological phase. Particle-hole symmetry with $\Pi^2 = 1$ allows for generic Chern insulators without additional symmetry protection, while particle-hole symmetry with $\Pi^2 = -1$ features a $2\mathbb{Z}$ topological phase with an even number of copropagating chiral boundary states.

TABLE III. Parameter sets for driving protocol A with time-reversal (TRS), chiral (CS), or particle-hole symmetry (PHS). TRS and CS have the two free parameters J, Δ . PHS with $\Pi^2 = 1$ has two free parameters J, J' . Perfect coupling corresponds to $\Delta = 0$ and $J = J' = J_p$, where $J_p = 3\pi/T$ for a six-step protocol. Unspecified parameters are zero, and the sign in step 5 of the TRS column is + for bosonic and— for fermionic time-reversal symmetry. In Figs. 6–9, we use the values of Δ, J, J' specified under “this work.”

	TRS	CS	PHS $\Pi^2 = 1$
step 1	$J_{A \nearrow C} = J_p$ $J_{B \searrow D} = J_p$ $\Delta_A = \Delta_B = \Delta$ $\Delta_C = \Delta_D = -\Delta$	$J_{A \nearrow C} = J_p$ $J_{B \searrow D} = J_p$ $\Delta_B = -\Delta$ $\Delta_D = \Delta$	$J_{A \nearrow C} = J_p$ $J_{B \searrow D} = J_p$
step 2	$J_{A \rightarrow B} = J$ $J_{C \rightarrow D} = J$	$J_{A \rightarrow B} = J$ $J_{C \rightarrow D} = J$	$J_{A \rightarrow B} = J$ $J_{C \rightarrow D} = J$
step 3	$J_{C \nearrow A} = J_p$ $J_{D \searrow B} = J_p$ $\Delta_A = \Delta_B = \Delta$ $\Delta_C = \Delta_D = -\Delta$	$J_{C \nearrow A} = J_p$ $J_{D \searrow B} = J_p$	$J_{C \nearrow A} = J_p$ $J_{D \searrow B} = J_p$
step 4	$J_{C \searrow A} = J_p$ $J_{D \nearrow B} = J_p$ $\Delta_A = \Delta_B = \Delta$ $\Delta_C = \Delta_D = -\Delta$	$J_{C \searrow A} = J_p$ $J_{D \nearrow B} = -J_p$	$J_{C \searrow A} = J_p$ $J_{D \nearrow B} = -J_p$
step 5	$J_{A \rightarrow B} = \pm J$ $J_{C \rightarrow D} = \pm J$	$J_{A \rightarrow B} = J$ $J_{C \rightarrow D} = J$	$J_{A \rightarrow B} = J'$ $J_{C \rightarrow D} = J'$
step 6	$J_{A \searrow C} = J_p$ $J_{B \nearrow D} = J_p$ $\Delta_A = \Delta_B = \Delta$ $\Delta_C = \Delta_D = -\Delta$	$J_{A \searrow C} = J_p$ $J_{B \nearrow D} = -J_p$ $\Delta_A = \Delta$ $\Delta_C = -\Delta$	$J_{A \searrow C} = J_p$ $J_{B \nearrow D} = -J_p$
this work	$J = 2\pi/T$ $\Delta = 3/T$	$J = 2\pi/T$ $\Delta = 9/T$	$J = 2\pi/T$ $J' = \pi/T$

The symmetry-protected \mathbb{Z}_2 phase with fermionic time-reversal symmetry is realized in the driving protocol **A**. Since this constitutes the most interesting situation, we start with an extended discussion of topological phases and boundary states in this protocol. The $2\mathbb{Z}$ phase with particle-hole symmetry will be discussed after the introduction of protocol **B** in Sec. **VII**.

At perfect coupling, the driving protocol **A** realizes a non-trivial topological phase with counterpropagating boundary states that follow the patterns of motion in Fig. 4. The bulk bands and boundary state dispersions are shown in Fig. 5, where we plot the Floquet quasienergies ε as a function of momentum k_x or k_y along a boundary in x or y direction. The quasienergies are computed from the eigenvalues $e^{-i\varepsilon}$ of the Floquet propagator after one driving period. At perfect coupling, the bulk bands are flat at $\varepsilon = 0$ and a gap exists at $\varepsilon = \pi$. The boundary states have linear dispersion, which does not depend on the orientation of the boundary. Due to symmetry, they occur in pairs of opposite chirality. Furthermore, with zero potential $\Delta_s \equiv 0$, time-reversal or chiral symmetry appears together with particle-hole symmetry.

To realize symmetry-protected Floquet topological phases away from perfect coupling, we use the parameter values listed in Table **III**. Of the 36 parameters of the protocol, at most 28 parameters are assigned nonzero values. Steps 2 and 5 do not involve on-site potentials, and all parameters are real. It is straightforward to check that the three parameter sets fulfill either the conditions of time-reversal, chiral, or particle-hole symmetry in Table **II**. Each set depends on two free parameters, and includes the perfect coupling case in Fig. 5. For the remainder of this section, we use the parameters listed under “this work” and the “left” variant of driving protocol **A** in Fig. 3.

A. Time-reversal symmetry

In Fig. 6, we show the Floquet bands and boundary states for fermionic and bosonic time-reversal symmetry. Both cases differ only by the sign of the parameters in step 5 of the driving protocol (cf. Table **III**), such that the gap is either at $\varepsilon = \pi$ (fermionic) or $\varepsilon = 0$ (bosonic).

For fermionic time-reversal symmetry (top row in Fig. 6), two boundary states with opposite chirality traverse the gap. The crossing of the boundary states at the invariant momentum $k_{x,y} = 0$ is protected by Kramers degeneracy. Since the two boundary states are mapped onto each other by the symmetry operator S_8 , they can be described as helical boundary states in the pseudospin interpretation of the driving protocol given in Appendix **A**.

Because of time-reversal symmetry, the boundary states have to appear in pairs of opposite chirality. In this situation, the W_3 invariant [14], which counts the net chirality of boundary states in a gap of a Floquet system, necessarily vanishes. Therefore the topological phase observed here is not protected against general deformations of the Floquet Hamiltonian, but only against deformations that preserve time-reversal symmetry.

To characterize this symmetry-protected topological phase, we can compute the relevant \mathbb{Z}_2 -valued bulk invariant [25,26,32]. In the present situation, we get a nonzero invariant ($W_{\text{tr}} \neq 0$ in the notation of Ref. [32], computed with the algorithm from Ref. [34]). This confirms that the driving protocol indeed supports a nontrivial time-reversal symmetric topological phase, with a pair of counterpropagating boundary states.

Additionally, we find that the Kane-Mele invariants [3,35,36] of the individual Floquet bands are zero. We recognize the signature of an anomalous Floquet topological

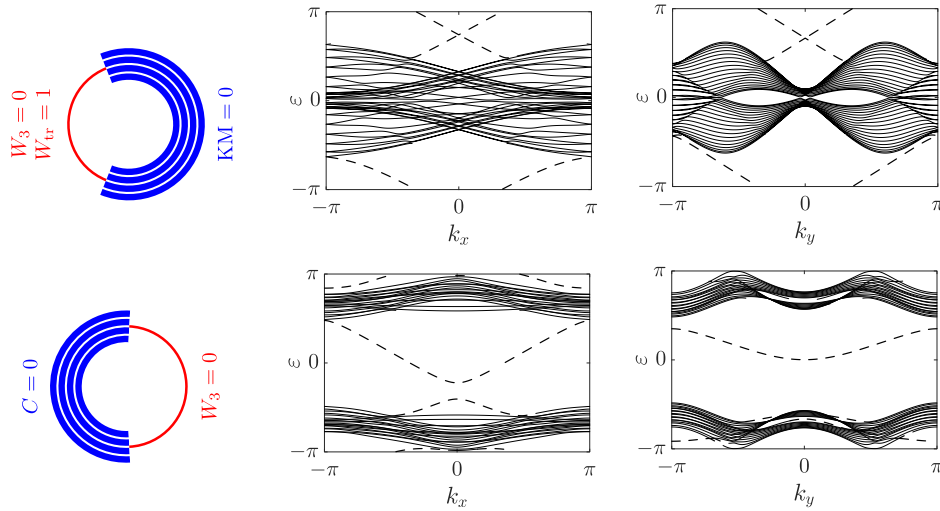


FIG. 6. Floquet bands and boundary states for fermionic (top row) and bosonic (bottom row) time-reversal symmetry, using the parameters from Table **III**. (Left column) Blue arcs indicate the (fourfold degenerate) Floquet bands, red arcs the gaps. Quasienergies ε are plotted on the circle $\varepsilon \mapsto e^{-i\varepsilon}$. Included are the respective (Kane-Mele KM or Chern number C) invariants of the bands, and the W_{tr} invariant or the W_3 invariant associated with the gap. (Central and right columns) Floquet bands (solid) and boundary state dispersion (dashed), as a function of momentum k_x or k_y for a boundary along the x or y direction.

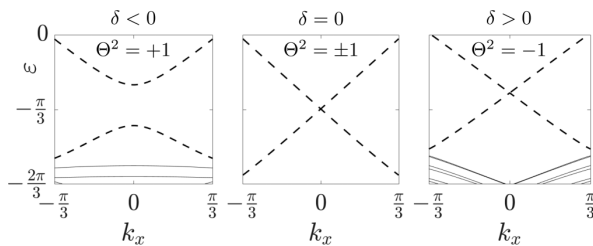


FIG. 7. Switching between bosonic (left and central) and fermionic (central and right) time-reversal symmetry through continuous variation of the parameter δ (see text). The panels show the boundary state dispersion. The protocol parameters for the negative and positive $\delta = \pm\pi/T$ used here agree with Fig. 6.

phase [14,26], which exists although all Floquet bands are topologically trivial.

For bosonic time-reversal symmetry (bottom row in Fig. 6), the W_3 invariant still has to be zero. Now, however, crossing of the boundary states is not protected by Kramers degeneracy. The boundary states do not have to traverse the gap and can be deformed continuously to merge with the Floquet bands, without breaking the symmetry. Consequently, the system is topologically trivial.

B. Continuous switching between fermionic and bosonic time-reversal symmetry

Since fermionic and bosonic time-reversal symmetry differ by the sign of the parameters in step 5 of the driving protocol, they are realized in separate regions of the parameter space. Especially at perfect coupling ($J = \pm J_p$), the conditions for fermionic or bosonic time-reversal symmetry in Table II are mutually exclusive. However, considering the argument in Sec. V D, the cases $J = J_p$ and $J = -J_p$ are in fact equivalent. The Floquet propagators in both cases differ only by a minus sign, which shifts the quasienergies by π but affects neither the topological invariants nor the existence of boundary states.

Building on this observation, we can switch continuously between fermionic and bosonic time-reversal symmetry: Set

$J_{A \rightarrow B} = J_{C \rightarrow D} = J_p - |\delta|$ in step 2 and $J_{A \rightarrow B} = J_{C \rightarrow D} = J_p + \delta$ in step 5. For $\delta \leq 0$, the driving protocol has bosonic time-reversal symmetry. For $\delta \geq 0$, the parameter value $J_p + \delta$ in step 5 is equivalent to the parameter value $J_p + \delta - 2J_p = -(J_p - |\delta|)$, up to a minus sign of the Floquet propagator. The driving protocol has fermionic time-reversal symmetry. At perfect coupling $\delta = 0$ in steps 2 and 5, both fermionic and bosonic time-reversal symmetry are realized simultaneously.

In Fig. 7, we show the change of the boundary state dispersion if the parameter δ is varied through $\delta = 0$, and we switch continuously from bosonic to fermionic time-reversal symmetry. Note that since the propagator acquires a minus sign for $\delta > 0$, if compared to Fig. 6, the position of the gap remains at $\varepsilon = 0$. Because of time-reversal symmetry, the boundary dispersion is invariant under the mapping $k_x \mapsto -k_x$. While the boundary states are separated for $\delta < 0$, they are gapless for $\delta > 0$. Only in the latter parameter regime, the crossing at the invariant momentum $k_x = 0$ is protected by Kramers degeneracy. In this way, continuous variation of δ switches between a trivial (bosonic) and nontrivial (fermionic) time-reversal symmetric topological phase, without the bulk gap closing at $\delta = 0$.

C. Chiral and particle-hole symmetry

In Fig. 8, we show the Floquet bands and boundary states for chiral and particle-hole symmetry, with two gaps at quasienergies $\varepsilon = 0, \pi$. For both symmetries, we are interested in “weak” topological phases, where protected boundary states occur in the gap, but transport in real space is not necessarily topologically protected.

For chiral symmetry, the W_3 invariant has to be zero in both gaps (at $\varepsilon = 0, \pi$). Similar to time-reversal symmetry, this implies that the boundary states are not stable under general deformations of the Floquet Hamiltonian. However, with the alternating sign of Eq. (6), chiral symmetry gives rise to a symmetry-protected \mathbb{Z}_2 phase that is visible in the dispersion $\varepsilon(k_{x,y})$ of boundary states in momentum space [27,32]. The reason is that the dispersion fulfills the constraint $\varepsilon(k_{x,y} + \pi) \equiv -\varepsilon(k_{x,y}) \pmod{2\pi}$, such that chiral symmetry protects

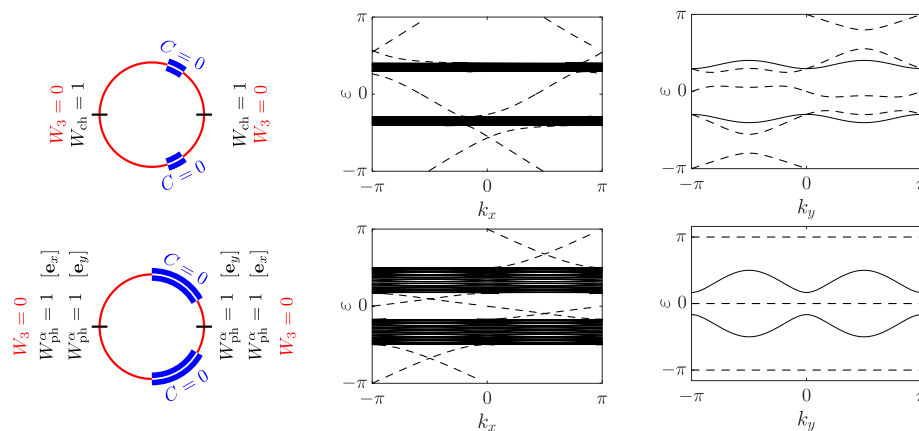


FIG. 8. Same as Fig. 6, now for chiral (top) and particle-hole symmetry (bottom) and parameters from Table III. The relevant bulk invariants are here the Chern numbers C of the Floquet bands, and the symmetry-adapted W_{ch} and W_{ph}^α invariants from Ref. [32].

the crossings of $\varepsilon(k_{x,y})$ through the quasienergy $\varepsilon = 0$ or $\varepsilon = \pi$. The crossings have to occur in pairs that are separated by momentum π (see Appendix B of Ref. [32] for an extended argument). Note that inclusion of the alternating sign in the symmetry relation (6) is essential for this momentum-space protection, otherwise chiral symmetry does not protect any nontrivial phase [28,29,31].

In Fig. 8, exactly two crossings exist in each gap and on each boundary, which agrees with the nonzero value $W_{\text{ch}} \neq 0$ of the \mathbb{Z}_2 -valued invariant W_{ch} that is adapted to chiral symmetry [32]. The above momentum-space constraint on $\varepsilon(k_{x,y})$ does not enforce that the boundary states traverse the band gap. Therefore the chiral symmetric phase seen here does not necessarily exhibit counterpropagating boundary states with opposite chirality, and with the concomitant transport properties.

For particle-hole symmetry with $\Pi^2 = 1$, topological phases are still characterized by the Chern number or, for Floquet systems, the W_3 invariant. Weak topological phases, where the number of boundary states depends on the boundary orientation [27], arise for vanishing W_3 invariant. Several \mathbb{Z}_2 -valued invariants W_{ph}^α are required in this situation [32]. In Fig. 8, all W_{ph}^α invariants are nonzero and boundary states exist in each gap and on each (x or y) boundary. Particle-hole symmetry does not enforce a zero W_3 invariant, but here it is $W_3 = 0$ in Fig. 8, such that the net chirality of the boundary states in each gap is zero.

Similar to chiral symmetry, in these weak phases the appearance of boundary states in momentum space does not imply topologically protected transport in real space. In Fig. 8, the boundary state dispersion is perfectly flat on the boundary in y direction while the bulk bands are dispersive (this is a particular property of the parameter set in Table III, not of particle-hole symmetry). In this situation, states propagate along the y direction only in the bulk but not on the boundary.

In contrast to time-reversal symmetry, which requires the Kane-Mele invariant of the Floquet bands, the Chern number remains a relevant invariant for chiral and particle-hole symmetry. In Fig. 8, the Chern numbers of all Floquet bands are zero. Therefore the boundary states observed here belong to anomalous Floquet topological phases, and appear although the individual Floquet bands are topologically trivial.

D. Propagation of boundary states

In Fig. 9, we show the real-space propagation of boundary states in the vicinity of a corner. At $t = 0$, an initial state is prepared either on a “red” A site of the horizontal boundary in the x direction or on a “blue” B site of the vertical boundary in the y direction, and then observed after three ($t = 3T$) and eight ($t = 8T$) periods of the driving protocol A.

Since the parameter values in Table III are sufficiently close to perfect coupling such that the essential patterns of motion from Fig. 4 still survive, the “red” (or “blue”) state propagates mainly counterclockwise (or clockwise). Note that the amplitude at the boundary decreases over time since the state propagates partially into the bulk. Also, since the boundary state dispersion is not perfectly linear (see Figs. 6 and 8), the state is distributed over several lattice sites at later propagation times.

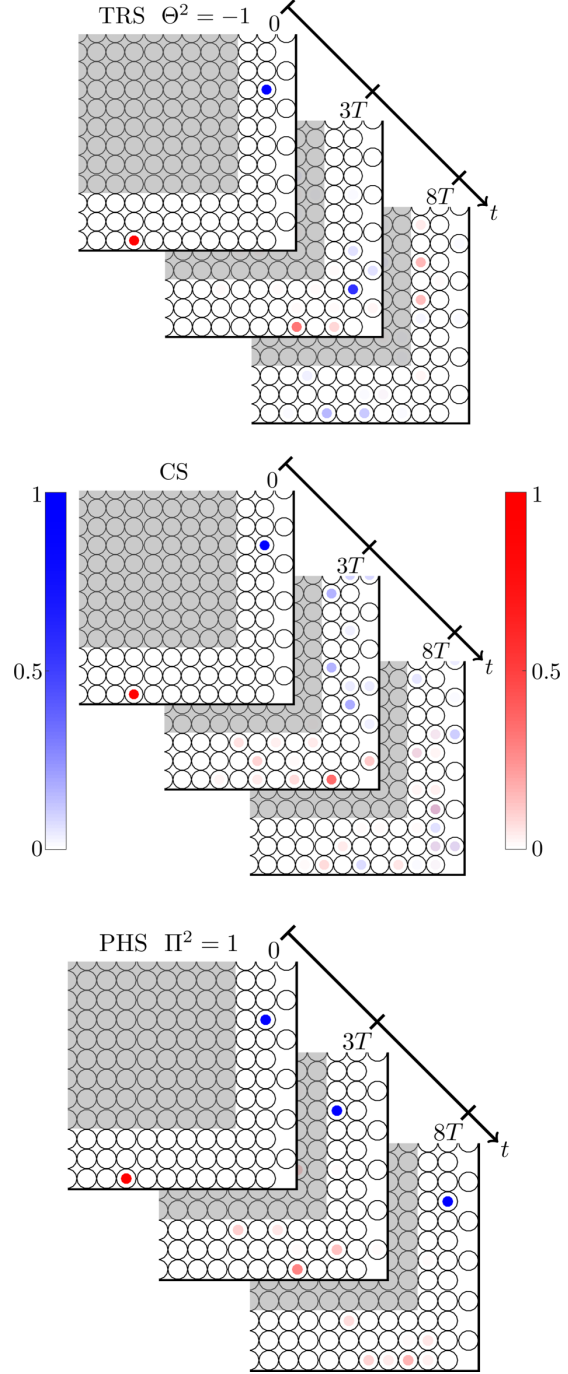


FIG. 9. Propagation of boundary states in the vicinity of a corner, starting from a “red” A site or a “blue” B site. Open black circles indicate the lattice sites. Shown is the (squared) wave function amplitude, with colors according to the two color bars, after zero ($t = 0$), three ($t = 3T$), or eight cycles ($t = 8T$) of driving protocol A.

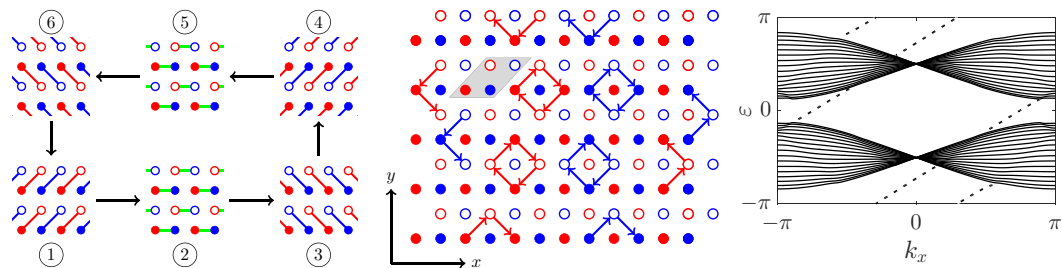


FIG. 10. (Left) Six-step driving protocol **B** for particle-hole symmetry $\Pi^2 = -1$. (Central) Patterns of motion during one cycle at perfect coupling. (Right) Floquet bands and boundary states for the set of parameters from Table IV.

As soon as the state hits the corner, it either propagates around the corner without backscattering (for fermionic time-reversal symmetry), or partially (for chiral symmetry) or totally (for particle-hole symmetry) reflected. This behavior can be attributed to the different nature of the (weak) topological phases for the different symmetries: For fermionic time-reversal symmetry, transport is topologically protected. For chiral symmetry, the boundary states are still protected in momentum space but the dispersion along the y boundary does not traverse the band gap, which leads to partial reflection. For particle-hole symmetry, the boundary state dispersion along the y direction is perfectly flat, which leads to total reflection of states starting on the x boundary. States on the y boundary stay within one unit cell, moving back and forth between the initial B site and the adjacent A site with each period of the driving protocol.

VII. UNIVERSAL DRIVING PROTOCOL B: PARTICLE-HOLE SYMMETRY

For particle-hole symmetry with $\Pi^2 = -1$, again the symmetry operator S_8 has to be used for construction of the driving protocol. Now, the symmetry relation (8) contains the same time argument on both sides, and according to Sec. IV, we have to use the parallel diagonal coupling patterns (f1)–(f4) from Fig. 12 in Appendix B.

TABLE IV. Similar to Tab. III, parameter set for driving protocol **B** with particle-hole symmetry $\Pi^2 = -1$. In Fig. 10, we use the values of the free parameters Δ , J , and J' specified under “this work.”

PHS $\Pi^2 = -1$			
step 1	$J_{A \nearrow C} = J_p$ $J_{B \nearrow D} = -J_p$ $\Delta_A = \Delta_D = \Delta$ $\Delta_B = \Delta_C = -\Delta$	step 4	$J_{C \nearrow A} = J_p$ $J_{D \nearrow B} = -J_p$ $\Delta_A = \Delta_D = \Delta$ $\Delta_B = \Delta_C = -\Delta$
step 2	$J_{A \rightarrow B} = J$ $J_{C \rightarrow D} = J$	step 5	$J_{A \rightarrow B} = J'$ $J_{C \rightarrow D} = J'$
step 3	$J_{C \searrow A} = J_p$ $J_{D \searrow B} = -J_p$ $\Delta_A = \Delta_D = \Delta$ $\Delta_B = \Delta_C = -\Delta$	step 6	$J_{A \searrow C} = J_p$ $J_{B \searrow D} = -J_p$ $\Delta_A = \Delta_D = \Delta$ $\Delta_B = \Delta_C = -\Delta$
this work	$J = 2\pi/T$ $\Delta = 3/T$		$J' = \pi/T$

Repetition of the procedure from Sec. V leads to the driving protocol **B** in Fig. 10. The considerations from Sec. V C can be adapted to construct two variants of the protocol, and the strategy from Sec. V D allows for replacement of negative by positive couplings.

The patterns of motion for perfect coupling ($J_{s_0 s'} = J_p$ in steps 1, 3, 4, 6 and $J_{s_0 s'} = 0$ in steps 2 and 5) are shown in the central panel of Fig. 10. Comparison with Fig. 4 shows that now states on the “red” and “blue” sublattice propagate in the same direction. This explains, quite intuitively, why parallel (perpendicular) diagonal coupling patterns are used for particle-hole (time-reversal) symmetry with copropagating (counterpropagating) boundary states.

For the general case, we use the parameter values in Table IV. The corresponding Floquet bands and boundary states are shown in the right panel of Fig. 10. Two boundary states with the same chirality exist in the two gaps at quasienergies $\varepsilon = 0$ and $\varepsilon = \pi$. This phase is characterized by the conventional Chern number C and W_3 invariant, which are restricted to even values ($2\mathbb{Z}$) by the particle-hole symmetry. In accordance with the appearance of two copropagating boundary states, we have $W_3 = 2$ for both gaps. Consequently, we have $C = 0$ for the individual Floquet bands, which is the signature of an anomalous Floquet topological phase with $C = 0$ but $W_3 \neq 0$.

VIII. CONCLUSIONS

The universal driving protocol introduced in the present paper allows for the realization of Floquet topological phases with time-reversal, chiral, or particle-hole symmetry. Switching between the different symmetries only requires adjustment of a few parameters, or the replacement of parallel (protocol **B**) with perpendicular (protocol **A**) diagonal couplings. The general structure of the driving protocol, which follows from the analysis of the possible symmetry operators for the underlying square lattice Hamiltonian, remains unchanged. In fact, if we allow for coupling of three or more lattice sites, the two types **A** and **B** of the universal driving protocol are continuously connected, and appear as special cases of the slightly generalized universal driving model depicted in Appendix C.

Due to the minimal complexity of the universal driving protocol, which is a result of the constraints accounted for in its construction, it is not only of theoretical value but can be implemented by extension of previous experimental

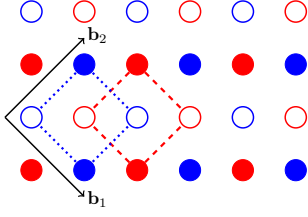


FIG. 11. The square lattice can be viewed as a centered square lattice, or the union of a “red” and “blue” square lattice.

work [19,20]. Reference [37] documents the photonic lattice implementation of the driving protocol with fermionic time-reversal symmetry, and reports the observation of a topological phase with scatter-free counterpropagating boundary states. These states are protected by the fermionic time-reversal symmetry prescribed by the protocol, even though the underlying photonic system is of bosonic nature.

A novel aspect yet to be explored in more detail is the possibility of switching between fermionic and bosonic time-reversal symmetry by continuous variation of a parameter. Normally, without symmetries, switching between nontrivial and trivial topological phases requires that a gap closes and reopens. The driving protocol allows us to switch between a nontrivial and trivial symmetry-protected topological phase without directly affecting the topological nature of the system (the gap stays open), and without breaking time-reversal symmetry. Instead, only the type of time-reversal symmetry changes, and that even in a continuous manner.

ACKNOWLEDGMENTS

The authors would like to thank L. Maczewsky, M. Kremer, A. Szameit, and A. Fritzsche for useful discussions on time-reversal symmetric Floquet insulators.

APPENDIX A: PSEUDOSPIN INTERPRETATION

The pseudospin interpretation of the “red” and “blue” sublattice structure depicted in Figs. 1–4 is suggested by the geometric structure of the operator S_8 in Fig. 2. A natural way to represent the pseudospin is to understand the original lattice as a centered square lattice (see Fig. 11), and associate the “red” (“blue”) sublattice with the “up” (“down”) component of a spin $\frac{1}{2}$.

Technically, the pseudospin interpretation is obtained through a Hilbert space isomorphism \mathcal{I}_S , which is defined by

the mapping

$$\begin{aligned} \mathcal{I}_S |i\mathbf{b}_1 + j\mathbf{b}_2\rangle \otimes |\uparrow\rangle &= |i\mathbf{b}_1 + j\mathbf{b}_2\rangle, \\ \mathcal{I}_S |i\mathbf{b}_1 + j\mathbf{b}_2\rangle \otimes |\downarrow\rangle &= |i\mathbf{b}_1 + j\mathbf{b}_2 + \mathbf{e}_x\rangle, \end{aligned} \quad (\text{A1})$$

for $i, j \in \mathbb{Z}$. Here, $\mathbf{b}_1 = (1, -1)^t$, $\mathbf{b}_2 = (1, 1)^t$ are the translation vectors of the centered square lattice, and $\mathbf{e}_x = (1, 0)^t$, $\mathbf{e}_y = (0, 1)^t$ the unit vectors of the original square lattice. In terms of the vectors $\mathbf{a}_x, \mathbf{a}_y, \delta_s$ used in Sec. II, we have

$$\mathcal{I}_S |i\mathbf{b}_1 + j\mathbf{b}_2\rangle \otimes |S\rangle = \lfloor \frac{i+j}{2} \rfloor \mathbf{a}_x + \lfloor \frac{j-i}{2} \rfloor \mathbf{a}_y + \delta_s, \quad (\text{A2})$$

where $\lfloor \cdot \rfloor$ denotes the floor function (rounding down to the next integer), and s is chosen according to

$$\begin{aligned} i+j \text{ even} & \quad S = \uparrow & \quad S = \downarrow \\ & \quad s = A & \quad s = B \\ i+j \text{ odd} & \quad s = C & \quad s = D \end{aligned} \quad (\text{A3})$$

Within the pseudospin interpretation, diagonal pairwise couplings correspond to translations along the vectors \mathbf{b}_1 and \mathbf{b}_2 that preserve the pseudospin, as in

$$\begin{aligned} (\mathcal{I}_S^{-1} \hat{t}_{A \nearrow C} \mathcal{I}_S) |i\mathbf{b}_1 + j\mathbf{b}_2\rangle \otimes |\uparrow\rangle &= |(i+1)\mathbf{b}_1 + j\mathbf{b}_2\rangle \otimes |\uparrow\rangle, \\ (\mathcal{I}_S^{-1} \hat{t}_{A \nearrow C} \mathcal{I}_S) |i\mathbf{b}_1 + j\mathbf{b}_2\rangle \otimes |\downarrow\rangle &= 0. \end{aligned} \quad (\text{A4})$$

The horizontal coupling pattern (a) in Fig. 1, which appears in steps 2 and 5 of the universal driving protocol, corresponds to a spin transformation

$$\mathcal{I}_S^{-1} (\hat{t}_{A \rightarrow B} + \hat{t}_{A \rightarrow B}^\dagger + \hat{t}_{C \rightarrow D} + \hat{t}_{C \rightarrow D}^\dagger) \mathcal{I}_S = \sigma_x \quad (\text{A5})$$

with the Pauli matrix σ_x that preserves the i, j index of the centered square lattice. Note that here the parameters $J_{A \rightarrow B}$, $J_{C \rightarrow D}$ of the two pairwise couplings are equal (cf. Table III). The remaining horizontal and vertical couplings, which are not compatible with the symmetry operator S_8 , have no such simple representation.

The operator S_8 itself allows for a simple representation if the matrices σ, τ in Eq. (2) are given by a common 2×2 matrix Σ , i.e., $\sigma = \tau = \Sigma$. Then, we simply have

$$\mathcal{I}_S^{-1} S_8 \mathcal{I}_S = \Sigma. \quad (\text{A6})$$

At least for fermionic time-reversal symmetry, this form of S_8 is mandatory (with $\Sigma = \sigma_y$), up to phase factors in σ, τ . Note that these phase factors could be absorbed into the mapping \mathcal{I}_S , preserving the simple form of S_8 even in the general case.

The pseudospin interpretation of the square lattice allows us to reuse familiar notions such as “helicity” of boundary states in the present context. Conversely, the existence of this interpretation, as well as the precise form of the mapping

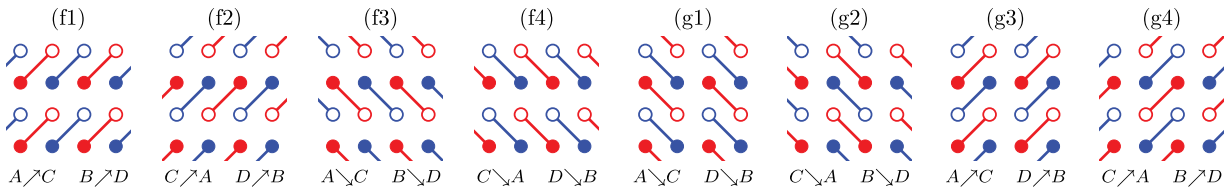


FIG. 12. The eight coupling patterns with parallel diagonal pairwise couplings. Patterns (f1) and (g1) correspond to patterns (f) and (g) in Fig. 1.

\mathcal{I}_S of the (pseudo) spin onto the square lattice, is a natural consequence of the symmetry analysis provided in the present paper.

APPENDIX B: PARALLEL DIAGONAL COUPLINGS

On the square lattice with a four-element unit cell, $4 \times 4 = 16$ diagonal coupling patterns exist in total. Four of them contain pairwise couplings that cross each other, and are not allowed due to the constraints imposed in Sec. II. Out of the allowed twelve patterns, the four perpendicular diagonal coupling patterns (b)–(e) in Fig. 1 constitute the main steps of the driving protocol A with time-reversal symmetry from Sec. V. Out of the remaining eight parallel diagonal coupling patterns depicted in Fig. 12, patterns (f1)–(f4) constitute the main steps of the driving protocol B with particle-hole symmetry in Sec. VII. The latter choice is mandatory, because only these patterns are mapped onto themselves by the symmetry operator S_8 , while patterns (g1) \leftrightarrow (g2) and (g3) \leftrightarrow (g4) are swapped.

That leaves open the question why the parallel diagonal coupling patterns are not used for the driving protocol A with time-reversal symmetry. Intuitively, this question is answered by comparison of the patterns of motion in Figs. 4 and 10: parallel diagonal couplings give rise to copropagating states, while time-reversal symmetry requires counterpropagating states, hence the perpendicular diagonal coupling patterns.

For a more exhaustive argument, consider the situation that the driving protocol should support time-reversal symmetry, but has to be composed only out of parallel diagonal coupling patterns. We can then try to repeat the construction from Sec. V A and focus on the two central steps, e.g., steps 3, 4 in a six-step protocol. These two steps must be exchanged under a mapping with S_8 .

If the two steps involve patterns (f1)–(f4), they are mapped onto each other by S_8 , and can be combined into a single step. In this way, nothing is gained for the construction of the driving protocol. If the two steps involve patterns (g1)–(g4), possible combinations are pattern (g1) followed by pattern (g2), or patterns (g3) followed by pattern (g4), etc. Visual inspection of these patterns in Fig. 12 shows that such

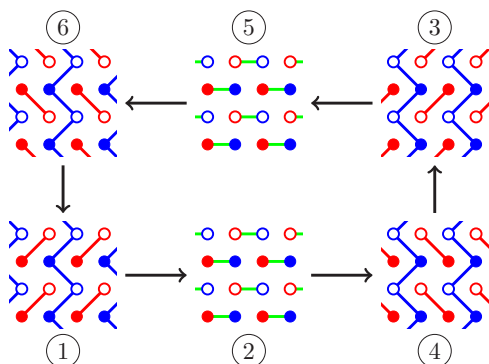


FIG. 13. A universal driving protocol that contains protocol A (right variant in Fig. 3) and protocol B, but violates the constraints from Sec. II.

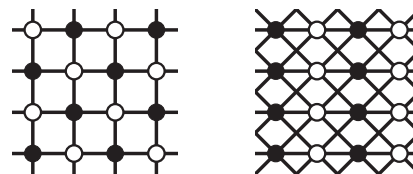


FIG. 14. Pairwise couplings (solid lines) on a square lattice with a two-element (a filled and an open circle) unit cell, and two choices for translation symmetry.

combinations transport states by two lattice sites in diagonal direction, but not on a closed loop as required for our driving protocol (see Fig. 4). Nothing is gained for the construction of the driving protocol in this way, either.

We conclude that a driving protocol with time-reversal symmetry has to use the perpendicular diagonal coupling patterns (b)–(e) from Fig. 1, instead of the parallel diagonal coupling patterns (f1)–(g4) from Fig. 12.

APPENDIX C: JOINT A AND B DRIVING PROTOCOL

In the main text, the two types A (in Fig. 3) and B (in Fig. 10) of the driving protocol appear as disjoint cases, with either perpendicular or parallel diagonal couplings. In fact, both types of the protocol are just special cases of the combined driving protocol shown in Fig. 13. However, continuous interpolation between protocol A and protocol B requires inclusion of couplings between three or more lattice sites, as is evident from the zigzag “blue” couplings in Fig. 13. The inclusion of such couplings is perfectly valid, unless we impose the very restrictive constraints of Sec. II. Only because of these constraints, we had to discuss protocol A and protocol B separately in the main text.

APPENDIX D: PROTOCOLS WITH A TWO-SITE UNIT CELL

Translational symmetry on a square lattice with a two-element unit cell can be implemented in two ways (see Fig. 14): either with primitive translation vectors $\mathbf{a}_x = (2, 0)$, $\mathbf{a}_y = (1, 1)$ (left panel), or $\mathbf{a}_x = (2, 0)$, $\mathbf{a}_y = (1, 0)$ (right panel). With the constraint that pairwise couplings are allowed only between neighboring lattice sites, only the couplings

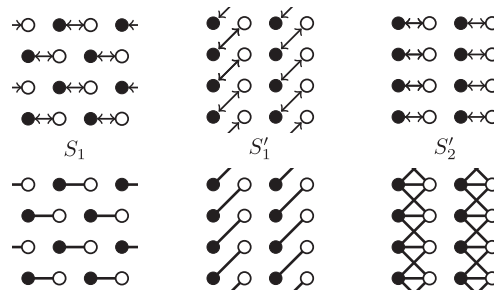


FIG. 15. Options for a symmetry operator for fermionic time-reversal symmetry on the square lattice from Fig. 14 (top row) and the compatible pairwise couplings (bottom row).

depicted in Fig. 14 are possible. In the two cases, either (anti)diagonal (left panel) or vertical (right panel) coupling terms are forbidden.

A symmetry analysis in the spirit of Sec. III leaves us with only three options for a symmetry operator that could be used to implement fermionic time-reversal symmetry (see Fig. 15).

For all options, the pairwise couplings compatible with the symmetry do not connect the entire lattice. We conclude that, under the constraints imposed here, a nontrivial $2 + 1$ -dimensional topological phase with time-reversal symmetry cannot be realized with a two-element unit cell, but requires at least a four-element unit cell.

-
- [1] K. v. Klitzing, G. Dorda, and M. Pepper, *Phys. Rev. Lett.* **45**, 494 (1980).
 - [2] D. J. Thouless, M. Kohmoto, M. P. Nightingale, and M. den Nijs, *Phys. Rev. Lett.* **49**, 405 (1982).
 - [3] C. L. Kane and E. J. Mele, *Phys. Rev. Lett.* **95**, 146802 (2005).
 - [4] M. Z. Hasan and C. L. Kane, *Rev. Mod. Phys.* **82**, 3045 (2010).
 - [5] M. König, S. Wiedmann, C. Brüne, A. Roth, H. Buhmann, L. W. Molenkamp, X.-L. Qi, and S.-C. Zhang, *Science* **318**, 766 (2007).
 - [6] L. Fu, C. L. Kane, and E. J. Mele, *Phys. Rev. Lett.* **98**, 106803 (2007).
 - [7] T. Kitagawa, E. Berg, M. Rudner, and E. Demler, *Phys. Rev. B* **82**, 235114 (2010).
 - [8] N. H. Lindner, G. Refael, and V. Galitski, *Nat. Phys.* **7**, 490 (2011).
 - [9] T. Kitagawa, T. Oka, A. Brataas, L. Fu, and E. Demler, *Phys. Rev. B* **84**, 235108 (2011).
 - [10] N. Fläschner, B. S. Rem, M. Tarnowski, D. Vogel, D.-S. Lühmann, K. Sengstock, and C. Weitenberg, *Science* **352**, 1091 (2016).
 - [11] Y. H. Wang, H. Steinberg, P. Jarillo-Herrero, and N. Gedik, *Science* **342**, 453 (2013).
 - [12] H. L. Calvo, L. E. F. Foa Torres, P. M. Perez-Piskunow, C. A. Balseiro, and G. Usaj, *Phys. Rev. B* **91**, 241404(R) (2015).
 - [13] Y. Wang, Y. Liu, and B. Wang, *Sci. Rep.* **7**, 41644 (2017).
 - [14] M. S. Rudner, N. H. Lindner, E. Berg, and M. Levin, *Phys. Rev. X* **3**, 031005 (2013).
 - [15] M. C. Rechtsman, J. M. Zeuner, Y. Plotnik, Y. Lumer, D. Podolsky, F. Dreisow, S. Nolte, M. Segev, and A. Szameit, *Nature (London)* **496**, 196 (2013).
 - [16] T. Ozawa, H. M. Price, A. Amo, N. Goldman, M. Hafezi, L. Lu, M. C. Rechtsman, D. Schuster, J. Simon, O. Zilberberg, and I. Carusotto, *Rev. Mod. Phys.* **91**, 015006 (2019).
 - [17] L. Lu, J. D. Joannopoulos, and M. Soljacic, *Nat. Photon.* **8**, 821 (2014).
 - [18] A. Szameit and S. Nolte, *J. Phys. B* **43**, 163001 (2010).
 - [19] L. J. Maczewsky, J. M. Zeuner, S. Nolte, and A. Szameit, *Nat. Comm.* **8**, 13756 (2017).
 - [20] S. Mukherjee, A. Spracklen, M. Valiente, E. Andersson, P. Öhberg, N. Goldman, and R. R. Thomson, *Nat. Comm.* **8**, 13918 (2017).
 - [21] M. Lababidi, I. I. Satija, and E. Zhao, *Phys. Rev. Lett.* **112**, 026805 (2014).
 - [22] D. Y. H. Ho and J. Gong, *Phys. Rev. B* **90**, 195419 (2014).
 - [23] Z. Zhou, I. I. Satija, and E. Zhao, *Phys. Rev. B* **90**, 205108 (2014).
 - [24] L. Zhou, H. Wang, Y. D. Ho, and J. Gong, *Eur. Phys. J. B* **87**, 1 (2014).
 - [25] D. Carpentier, P. Delplace, M. Fruchart, and K. Gawędzki, *Phys. Rev. Lett.* **114**, 106806 (2015).
 - [26] F. Nathan and M. S. Rudner, *New J. Phys.* **17**, 125014 (2015).
 - [27] I. C. Fulga and M. Maksymenko, *Phys. Rev. B* **93**, 075405 (2016).
 - [28] R. Roy and F. Harper, *Phys. Rev. B* **96**, 155118 (2017).
 - [29] S. Yao, Z. Yan, and Z. Wang, *Phys. Rev. B* **96**, 195303 (2017).
 - [30] Z. Yan, B. Li, X. Yang, and S. Wan, *Sci. Rep.* **5**, 16197 (2015).
 - [31] M. Fruchart, *Phys. Rev. B* **93**, 115429 (2016).
 - [32] B. Höckendorf, A. Alvermann, and H. Fehske, *Phys. Rev. B* **97**, 045140 (2018).
 - [33] R. Keil, C. Poli, M. Heinrich, J. Arkininstall, G. Weihs, H. Schomerus, and A. Szameit, *Phys. Rev. Lett.* **116**, 213901 (2016).
 - [34] B. Höckendorf, A. Alvermann, and H. Fehske, *J. Phys. A* **50**, 295301 (2017).
 - [35] L. Fu and C. L. Kane, *Phys. Rev. B* **74**, 195312 (2006).
 - [36] F. Takahiro and H. Yasuhiro, *J. Phys. Soc. Jpn.* **76**, 053702 (2007).
 - [37] L. J. Maczewsky, B. Höckendorf, M. Kremer, T. Biesenthal, M. Heinrich, A. Alvermann, H. Fehske, and A. Szameit, [arXiv:1812.07930](https://arxiv.org/abs/1812.07930).



Fermionic time-reversal symmetry in a photonic topological insulator

Lukas J. Maczewsky^{1,3}, Bastian Höckendorf^{2,3}, Mark Kremer¹, Tobias Biesenthal¹,
Matthias Heinrich¹, Andreas Alvermann²✉, Holger Fehske² and Alexander Szameit¹✉

Much of the recent attention directed towards topological insulators is motivated by their hallmark feature of protected chiral edge states. In electronic (or fermionic) topological insulators, these states originate from time-reversal symmetry and allow carriers with opposite spin-polarization to propagate in opposite directions at the edge of an insulating bulk. By contrast, photonic (or bosonic) systems are generally assumed to be precluded from supporting edge states that are intrinsically protected by time-reversal symmetry. Here, we experimentally demonstrate counter-propagating chiral states at the edge of a time-reversal-symmetric photonic waveguide structure. The pivotal step in our approach is the design of a Floquet driving protocol that incorporates effective fermionic time-reversal symmetry, enabling the realization of the photonic version of an electronic topological insulator. Our findings allow for fermionic properties to be harnessed in bosonic systems, thereby offering alternative opportunities for photonics as well as acoustics, mechanical waves and cold atoms.

Since their original theoretical proposals^{1,2}, topological insulators (TIs) have been experimentally investigated in a large number of different platforms and materials^{3–15}. Remarkably, solid-state TIs prohibit electrons from traversing their interior, while simultaneously supporting chiral surface currents that are protected by fermionic time-reversal symmetry (TRS)^{3,4,6}. Due to this symmetry, pairs of counter-propagating edge states exist, while scattering between them is strongly suppressed. As a result, a TI's surface may be highly conductive while the bulk remains insulating. This phase of a material can be characterized by an appropriate topological invariant^{1,2}, which is specific to fermionic (electronic) systems and closely related to fermionic TRS. Therefore, one would not expect bosonic systems to be able to accommodate such a TI phase with its unique feature of counter-propagating unidirectional edge states¹⁶.

Nevertheless, bosonic systems are still able to exhibit topological phases by breaking the TRS. These so-called Chern-type^{17,18} or driven anomalous TIs¹⁹, as depicted in Fig. 1a, feature unidirectional, robust edge transport in only one specific direction. They are characterized by an integer-valued topological invariant, indicated by \mathbb{Z} . Such systems have been reported across a broad range of physical platforms, such as microwave systems⁷, photonic lattices^{7,20,21}, matter waves²², acoustics¹⁰ and even mechanical waves¹¹.

Recently, several works demonstrated the superposition of two TIs with opposite chirality^{8,11,23–26} (see Fig. 1b), each of which can independently support edge states that, in the combined system, happen to be counter-propagating with respect to one another. The absence of a physical coupling mechanism then prevents the scattering of these counter-propagating states into each other. Such systems are topologically characterized by two independent \mathbb{Z} invariants, and therefore realize a topological phase denoted by $\mathbb{Z} + \mathbb{Z}$. Any non-zero coupling between the subsystems of these bipartite lattices destroys the topological protection and reduces the arrangement to a conventional insulator, regardless of bosonic TRS or its absence (see Fig. 1c). However, despite the presence of a subsystem coupling (for example, a Rashba term¹), a topological phase

can exist, protected by a fermionic TRS²⁷. This is the case in a fermionic (electronic) TI, where the counter-propagating edge states cannot scatter into each other (see Fig. 1d). This different topology is characterized by a \mathbb{Z}_2 invariant¹, which displays counter-propagating topological edge states. Due to their reliance on fermionic TRS, these systems are typically restricted to solid-state physics.

Our approach overcomes this limitation, as it is capable of enforcing effectively fermionic behaviour in photonic systems despite their inherently bosonic character. Taking inspiration from solid-state \mathbb{Z}_2 TIs^{1,2,28}, where the desired topological properties originate from the fermionic spin degree of freedom, we exploit the bipartite substructure of the underlying photonic lattice to encode a pseudo-spin 1/2, and design a driving protocol that implements effective fermionic TRS (corresponds to Fig. 1d). We experimentally realize this type of lattice in photonic waveguide arrays, directly observe the resulting counter-propagating edge states and confirm the presence of fermionic TRS in the system by interferometric measurements.

Theoretical model

To establish the desired topological phase, we subject the couplings in a discrete lattice to a time-dependent modulation scheme, called a driving protocol. This driving protocol is implemented across two intertwined sublattices (marked with either red (R) or blue (B) sites in Fig. 2a), which correspond to the 'up' and 'down' states of the fermionic (pseudo-) spin 1/2. A full driving cycle comprises a sequence of six individual steps, each of which couples two different nearest-neighbour sites as indicated by the solid lines in Fig. 2a. These steps represent two fundamental types of operation^{28,29}: steps 1, 3, 4 and 6 realize spin-preserving translations through interactions between sites of the same sublattice, whereas steps 2 and 5 manifest spin rotations by bringing sites from different sublattices into contact. The symmetric placement of these inter-sublattice couplings within the overall driving period is crucial for the desired TRS. In these two steps, partial hopping represents general spin rotations, whereas a spin flip corresponds to a total exchange of populations between the sublattices.

¹Institut für Physik, Universität Rostock, Rostock, Germany. ²Institut für Physik, Universität Greifswald, Greifswald, Germany. ³These authors contributed equally: Lukas J. Maczewsky, Bastian Höckendorf. ✉e-mail: alvermann@physik.uni-greifswald.de; alexander.szameit@uni-rostock.de

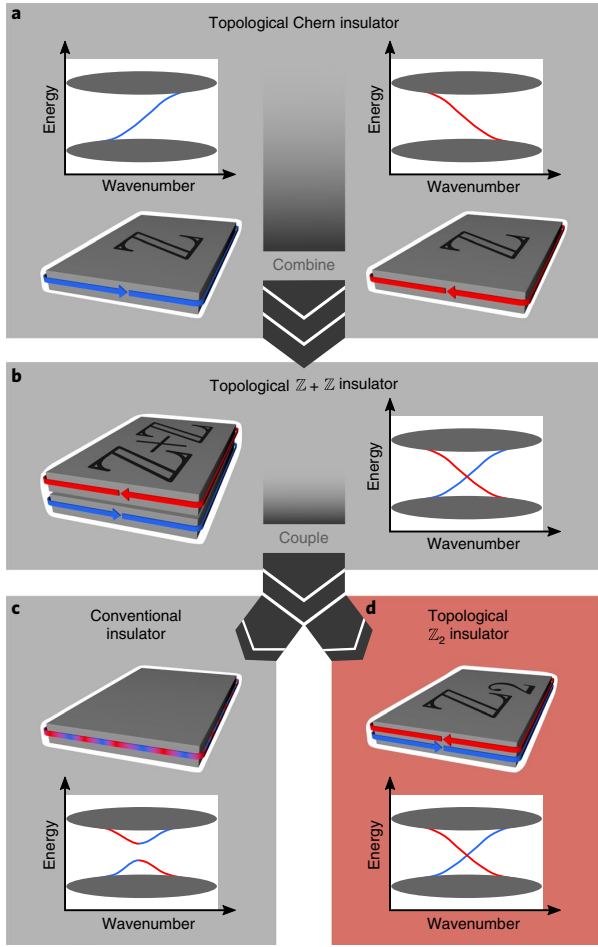


Fig. 1 | Conceptual idea. **a**, A topological Chern insulator supports topologically protected chiral edge states (marked red and blue, respectively), whose energies lie between the two bulk bands (marked grey in the band diagrams). The real-space propagation is indicated by red and blue arrows around the perimeter of the schematic two-dimensional systems. **b**, The non-interacting superposition of two Chern insulators from **a** form a $\mathbb{Z} + \mathbb{Z}$ TI that supports two independent sets (red, blue) of chiral edge states. **c**, Upon the introduction of any sublattice coupling, a band gap is opened, such that the topological phase, and with it the unidirectional character of the edge states, vanishes. Regardless of bosonic TRS or its absence, any non-zero coupling yields a conventional insulator. **d**, By contrast, coupled Chern insulators that obey fermionic TRS exhibit topologically protected counter-propagating edge states. We experimentally realize such a topological \mathbb{Z}_2 insulator in a photonic (that is, bosonic) system.

For the sake of brevity, the explicit formulation of the associated lattice Hamiltonian $H(t)$ has been relegated to the Supplementary Information. Here, we will instead highlight its fundamental properties: being of the Floquet type, the Hamiltonian is periodic in time, $H(t+T)=H(t)$, with the driving period T . Moreover, $H(t)$ obeys the fermionic TRS relation

$$\Theta H(t) \Theta^{-1} = H(T-t) \quad (1)$$

where Θ is an anti-unitary operator with $\Theta^2 = -1$. Note that TRS inverts the direction of time, that is $t \mapsto -t$, which is equivalent to

$t \mapsto T-t$ for the time-periodic Hamiltonian³⁰. In the (pseudo-) spin interpretation of the two sublattices, we have $\Theta = \sigma_y \mathcal{K}$, with the Pauli matrix σ_y and the operator \mathcal{K} that represents complex conjugation. This symmetry brings about Kramers degeneracy and, in turn, the desired counter-propagating photonic edge states and their topological protection. Note that the considered effective (Floquet) fermionic TRS should be distinguished from the pseudo TRS, which is implemented by combining a crystal symmetry with bosonic TRS and therefore is instantaneous but not local^{31,32}. Floquet TRS depends on a full driving cycle (that is, a temporal unit cell). In this non-instantaneous fashion, we can establish topologically protected counter-propagating edge states even in the general case of coupled subsystems. To understand the basic mechanism behind the driving protocol, Fig. 2b illustrates the evolution of single-site excitations in the spin flip case. Note how, depending on the initially excited sublattice, the sequence of alternating nearest-neighbour couplings prescribed by the driving protocol gives rise to two distinct edge states, moving either counter-clockwise (red arrow) or clockwise (blue arrow). By contrast, all excitations in the bulk of the lattice follow closed loops such that no transport occurs. In the spin flip case, the red/blue sublattices are still uncoupled. The crucial feature of our driving protocol, which clearly distinguishes it from previously realized Chern-type bosonic insulators, is that TRS-protected edge states are preserved even with coupling between the two sublattices, that is, in the general spin rotation case (see Fig. 2d). This situation can no longer be described as the independent propagation in two uncoupled Chern insulators (with $\mathbb{Z} + \mathbb{Z}$ topological phases), but requires a finer topological characterization.

Topological characterization

Neither the Chern number \mathcal{C} (ref. 33) nor the Kane–Mele \mathbb{Z}_2 invariant ν_{KM} (refs. 1,34) is an appropriate topological invariant for Floquet systems³⁵. Instead, the existence of Floquet topological phases is linked to the \mathcal{W} invariant¹⁹. The \mathcal{W} invariant counts the net topological charge of degeneracy points of the propagator $U(t) = \mathcal{T} \exp(-i \int_0^t H(\tau) d\tau)$ (\mathcal{T} denotes time-ordering, and \hbar is set to one)^{32,36,37}. With fermionic TRS, the topological charges cancel and the \mathcal{W} invariant vanishes even if the Floquet system supports edge states, just as the Chern number in a conventional \mathbb{Z}_2 insulator does. Instead, Floquet topological phases with fermionic TRS are characterized by a \mathbb{Z}_2 invariant ν_{TR} (refs. 28,32,37), which is related to the Kane–Mele invariant in a similar way as the \mathcal{W} invariant is related to the Chern number (a detailed overview is given in the Supplementary Information). The \mathbb{Z}_2 photonic TI introduced in this work exhibits an anomalous ($\mathcal{C} = \nu_{\text{KM}} = 0$) topological phase³⁵ with counter-propagating edge states ($\nu_{\text{TR}} = 1$). This phase is protected by fermionic TRS, and would be absent without TRS, since $\mathcal{W} = 0$ (a detailed consideration of this statement is provided in the Supplementary Information).

Observation of counter-propagating edge modes

As a testbed for the practical implementation and experimental verification of our protocol, we chose an optical platform: lattices of evanescently coupled laser-written waveguides³⁸. Light evolves in these structures according to the paraxial Helmholtz equation, which reads,

$$i \frac{d}{dz} \psi_m(z) = \epsilon_m(z) \psi_m(z) + \sum_{k \in \langle m \rangle} c_{k,m}(z) \psi_k(z) \quad (2)$$

in the tight-binding approximation. Here, $\epsilon_m(z)$ is the on-site potential of waveguide m , ψ_m represents the field amplitude of its guided mode, $c_{k,m}(z)$ denotes the coupling to the nearest neighbour k and the propagation distance z serves as the evolution coordinate. In the summation, $\langle m \rangle$ denotes the nearest neighbours of the m th

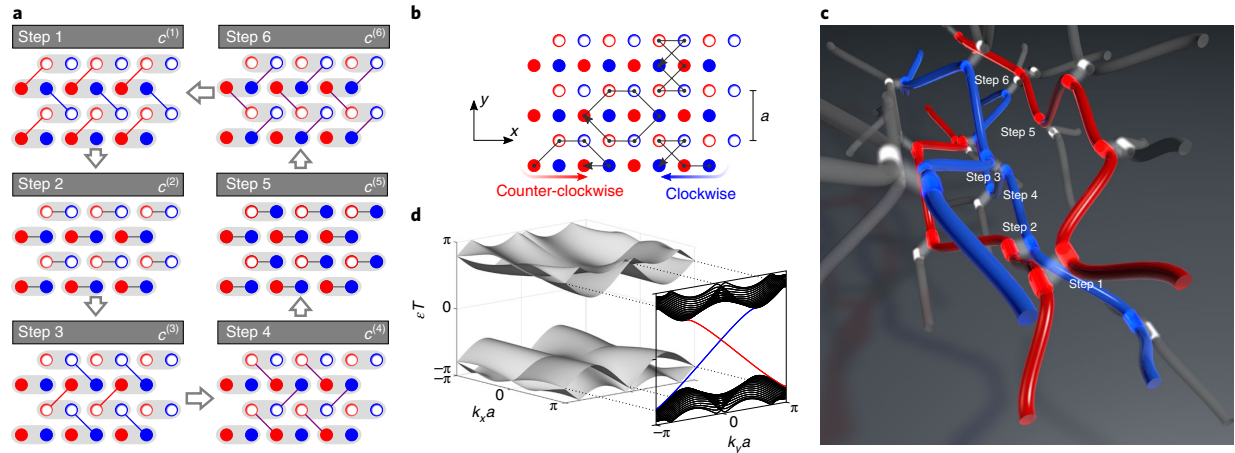


Fig. 2 | Schematic of the driving protocol. **a**, Over the course of one full driving period T , adjacent lattice sites of the two sublattices (marked by red and blue circles) are selectively coupled with identical coefficients $c^{(j)}$ (indicated by solid lines) in a sequence of six distinct steps $j = 1, \dots, 6$. In addition to the coupling, an on-site detuning $e^{(j)}$ can be introduced. **b**, For a full transfer ($c^{(j)} = 3\pi/T$), bulk transport is entirely suppressed. The chiral edge states travel along the lattice perimeter (illustrated in the Supplementary Information) in the clockwise and counter-clockwise directions. Blue and red arrows indicate the displacement of the edge states. The lattice constant a denotes the size of the unit cell. **c**, Schematic of the implementation of the driving protocol in a waveguide structure. The unit cell geometry (red/blue) is embedded within the surrounding waveguide lattice (grey). The interaction region of each step is highlighted by semi-transparent ribbons. **d**, The three-dimensional band structure (grey) of our photonic TI in the general spin rotation case. The band structure, which is periodic in the quasi-momenta k_x, k_y and the quasi-energy ϵ , reveals the insulating gap of the bulk system. The two counter-propagating edge modes (shown in front in blue and red) cross the band gap and intersect at the invariant momentum $k_y = 0$ as a consequence of Kramers degeneracy.

waveguide. Since equation (2) is mathematically equivalent to the Schrödinger equation, where the propagation distance acts as the time coordinate in our setting, the longitudinal modulation of the waveguide structure can mimic the temporal evolution of a Hamiltonian. This enables the implementation of a time-dependent Hamiltonian with a static photonic system^{20,21}. It is in this sense that we adopt temporal terminology such as ‘driving protocol’ or ‘period’ for the description of our concept and its implementation.

In the system under consideration, the values of the couplings $c_{i,m}(z)$ differ in each step of the full sequence: as illustrated in Fig. 2a, interactions have to be avoided except for steps that necessitate hopping between two given waveguides. For simplicity, we refer to the couplings and potentials in step j as $c^{(j)}$ and $e^{(j)}$. The purpose of the potentials $e^{(j)}$ is to explicitly break particle–hole and chiral symmetry (see the Supplementary Information). The structure depicted in Fig. 2c schematically presents our experimental realization of the driving protocol. Here, a single unit cell is shown in a transverse cross-section. Each waveguide corresponds to one lattice site. The discrete coupling steps are implemented by regions of reduced separation between the waveguides, where the desired amount of evanescent coupling occurs. For our experiments, we fabricated a lattice spanning four by three unit cells in the x – y plane and three driving cycles along the z direction. In real-world units, the unit cell transversely extends over $a^2 = 80 \times 80 \mu\text{m}^2$ (see Fig. 2b), and $T = 4.44 \text{ cm}$ along the propagation direction z . Further details of the fabrication, in particular the explicit values of the couplings $c^{(j)}$ and potentials $e^{(j)}$, are given in the Methods section.

Our samples were characterized by recording the output intensity distributions resulting from single-site excitations after three driving periods (see Fig. 3a,b). In the spin flip case, where the bulk bands exhibit no dispersion (Fig. 3c), we observe an edge state moving clockwise (in blue) and another one moving counter-clockwise (in red) as shown in Fig. 3d,e. (Extended sets of experimental images are provided in the Supplementary Information.) These states follow the patterns of motion from Fig. 2b. Crucially for our

demonstration of a \mathbb{Z}_2 photonic TI, the edge states survive in the general spin rotation case, where they remain protected by fermionic TRS against the coupling between the two sublattices. Note that the bulk bands have acquired some dispersion (Fig. 3f–h). The experimental data shown in Fig. 3d,e,g,h exhibit cross-correlation similarities of 0.9687, 0.9334, 0.9147 and 0.9196, respectively, with respect to the theoretical simulations. Additionally, we investigated the robustness of these edge states theoretically and experimentally. In particular, the stability of the chiral edge channels has been confirmed by our analysis of symmetry restrictions and perturbed excitations (see Supplementary Information).

Direct measurement of TRS

Whereas the observation of such protected counter-propagating edge states is already a strong indication of Kramers degeneracy, a direct demonstration of fermionic TRS is within the scope of this experiment. Our line of reasoning relies on the fact that via TRS, forward propagation through the waveguides (in the positive z direction) is linked to backward propagation (along $-z$). It should be emphasized that backward propagation by itself is not identical to time reversal, which cannot be achieved by merely exciting the opposite end of the sample. However, if the system obeys fermionic TRS ($\Theta = \sigma_y \mathcal{K}$), the backward propagator $\tilde{U}(T)$ is related to the previously defined forward propagator $U(T)$ via $\tilde{U}(T) = \sigma_y U(T) \sigma_y^{-1}$ (the tilde denotes quantities related to backward propagation). The mathematical details behind this argument are provided in the Supplementary Information.

Now consider the output states $|\psi_{\text{out}}(\phi)\rangle = U(T)|\psi_{\text{in}}(\phi)\rangle$ and $|\tilde{\psi}_{\text{out}}(\phi)\rangle = \tilde{U}(T)|\psi_{\text{in}}(\phi)\rangle$ that evolve from either forward or backward propagation of an input state $|\psi_{\text{in}}(\phi)\rangle$. In our experiments, a suitable input state $|\psi_{\text{in}}(\phi)\rangle$ spanning two adjacent (‘red’ and ‘blue’) waveguides with the same amplitude but a relative phase ϕ is synthesized with a spatial light modulator (SLM) as illustrated in Fig. 4. Note that the same corresponding waveguides are excited in both forward and backward propagation (see Fig. 4a,c). For both

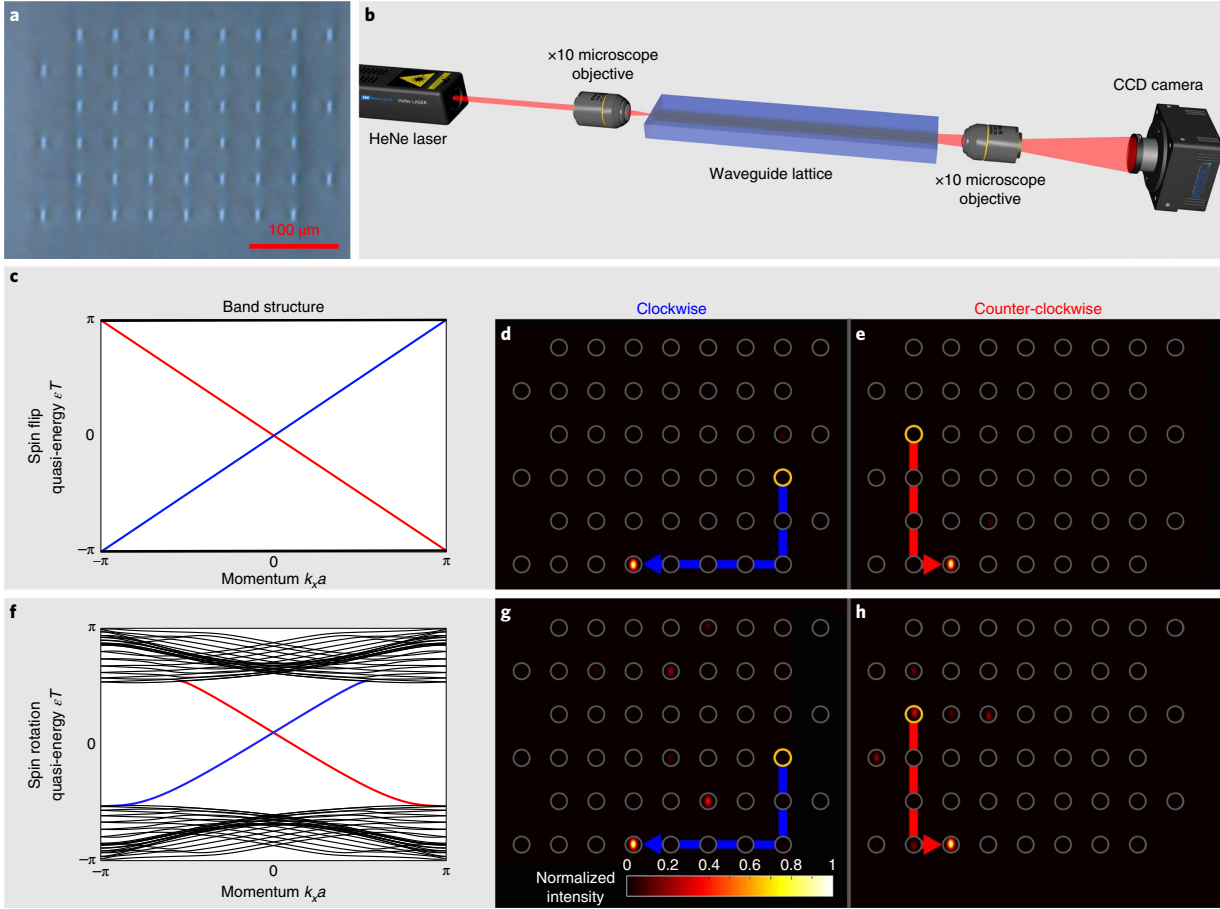


Fig. 3 | Experimental demonstration of TRS-protected counter-propagating edge modes. **a**, Microscope image of the cross-section of the inscribed waveguide lattice. The experimental lattice constant is $a = 80 \mu\text{m}$. **b**, Experimental setup for a single-site excitation. A HeNe laser is focused into the glass sample by a microscope objective. Another microscope objective is used to image the output facet onto a coupled charged device (CCD) camera. **c**, Band structure in the spin flip case. **d, e**, The output intensity distribution after three full driving periods for a single-site excitation associated with the spin flip case. Grey circles indicate the waveguide positions, whereas the excited sites are marked in yellow. The effective trajectories of the propagating modes are visualized by broad blue/red arrows. **f**, Band structure in the spin rotation case. **g, h**, The output intensity distribution after three full driving periods for a single-site excitation associated with the spin rotation case.

directions, we extract an intensity distribution from the observed output states $|\psi_{\text{out}}(\phi)\rangle$, $|\tilde{\psi}_{\text{out}}(\phi)\rangle$, either on the blue or red sublattice ($I^{\text{B}}(\phi)$ or $\tilde{I}^{\text{R}}(\phi)$, respectively), and track their dependence on the relative phase ϕ of the input state. The relation between the forward and backward propagator given above then readily translates into

$$\tilde{I}^{\text{R}}(\phi) = I^{\text{B}}(\pi - \phi) \quad (3)$$

for the output intensities. Notably, this expression is unique to fermionic TRS (see the Supplementary Information for a detailed discussion). As our experiment indeed faithfully reproduces the characteristic phase shift $\phi \rightarrow \pi - \phi$ as well as the exchange of intensities between the two sublattices predicted by equation (3) (see Fig. 4b), it unequivocally confirms the presence of fermionic TRS in our system.

Conclusion and outlook

In summary, we have shown that fermionic TRS can be effectively realized even in an intrinsically bosonic system. The resulting structure is described by a \mathbb{Z}_2 -type topological invariant and, as such,

exhibits counter-propagating chiral edge states that are topologically protected by Kramers degeneracy. While we chose an optical platform for our proof of principle, the presented protocol is general and can be readily adopted in any bosonic wave system. In this vein, we expect the experimental realization of a photonic system with fermionic TRS to stimulate fruitful theoretical and experimental efforts to illuminate the role of \mathbb{Z}_2 -type invariants in bosonic topological systems in greater detail. There are various fascinating questions waiting to be explored by experiments. One is the impact of interactions and non-linearity or the quantum many-body regime on topological phases in systems with fermionic TRS, as topology in experimentally available condensed matter systems is considered to be intrinsically a linear single-particle effect³⁹. Another is the role of TRS in non-Hermitian topological systems⁴⁰, including but not limited to those with parity-time (\mathcal{PT}) symmetry^{41,42}, which promise even broader opportunities for the manipulation of edge states. Equally intriguing is the potential interplay with supersymmetric notions, since these notions describe a global symmetry that became accessible only recently in photonic systems^{43,44}. The answers to these questions, and many more, are now within the reach of experiment.

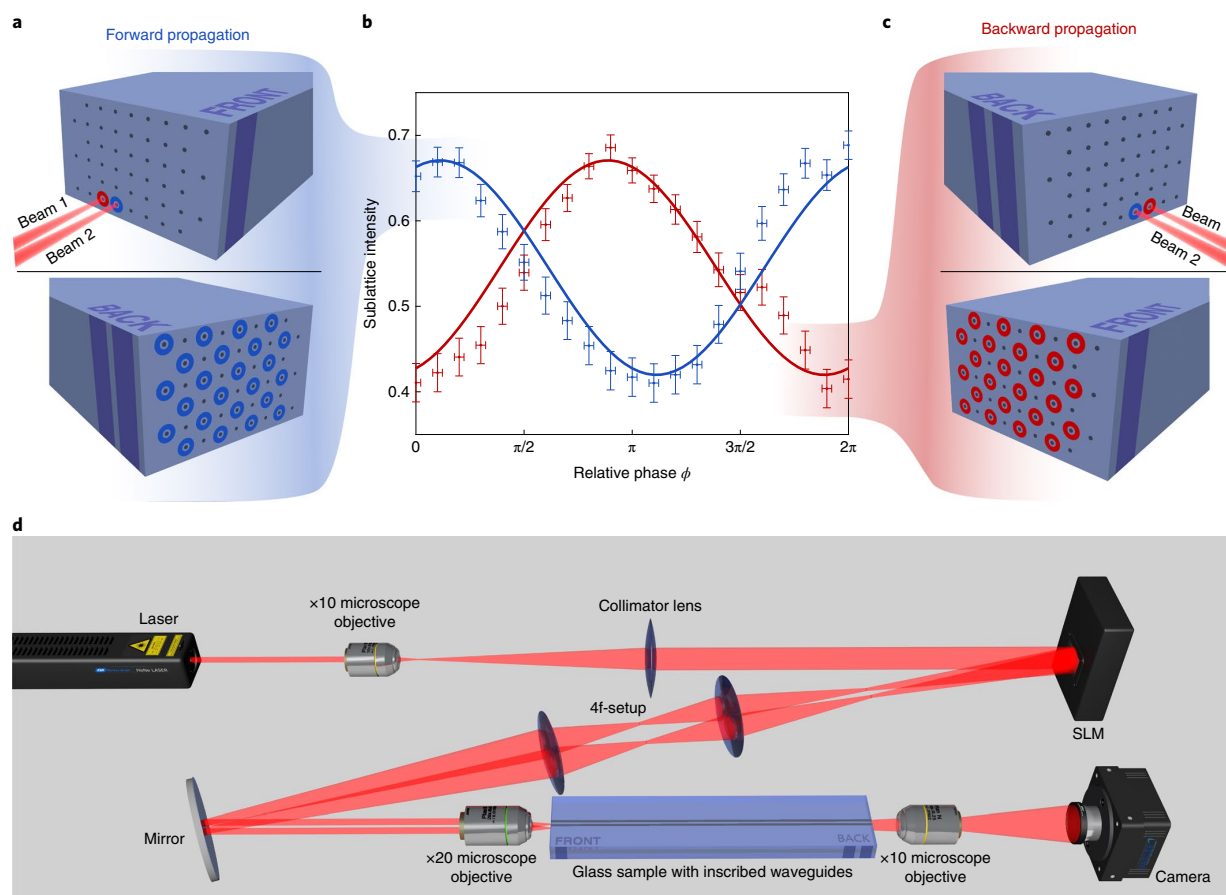


Fig. 4 | Experimental verification of fermionic TRS. **a**, Excitation and measurement scheme for forward propagation. The lattice is excited at two sites corresponding to different sublattices (indicated by red and blue circles in the upper panel) by two beams with a relative phase ϕ . The intensity of all blue sublattice sites is measured (marked by blue circles in the lower panel). **b**, Dependence of the sublattice population on the relative phase of a dual-site excitation (solid lines, numerical calculations; dots, measured values with error bars). The comparison between forward and backward propagation confirms the predicted characteristic phase shift between the behaviour of the output intensities in the red and blue sublattices, respectively. The horizontal error bars represent the uncertainty associated with the beam preparation, whereas the vertical error bars take the fabrication deviations of the lattice into account. **c**, Excitation and measurement scheme for backward propagation. The lattice is identically excited at the same lattice sites (compare with **a**). The intensity of all red sublattice sites is measured (marked by red circles in the lower panel). **d**, Schematic of the experimental setup. The light from a HeNe laser, collimated by a microscope objective and a lens, illuminates an SLM. The SLM synthesizes two phase-shifted beams, which are subsequently rescaled by a 4f-setup and another microscope objective and imaged onto the sample. The resulting output intensity distributions are recorded by a CCD camera via a third microscopic objective.

Online content

Any methods, additional references, Nature Research reporting summaries, source data, extended data, supplementary information, acknowledgements, peer review information; details of author contributions and competing interests; and statements of data and code availability are available at <https://doi.org/10.1038/s41563-020-0641-8>.

Received: 6 March 2019; Accepted: 14 February 2020;

Published online: 23 March 2020

References

- Kane, C. L. & Mele, E. J. Z_2 topological order and the quantum spin Hall effect. *Phys. Rev. Lett.* **95**, 146802 (2005).
- Bernevig, B. A. & Zhang, S.-C. Quantum spin Hall effect. *Phys. Rev. Lett.* **96**, 106802 (2006).
- König, M. et al. Quantum spin Hall insulator state in HgTe quantum wells. *Science* **318**, 766–770 (2007).
- Hsieh, D. et al. A topological Dirac insulator in a quantum spin Hall phase. *Nature* **452**, 970–974 (2008).
- Wang, Z., Chong, Y., Joannopoulos, J. D. & Soljačić, M. Observation of unidirectional backscattering-immune topological electromagnetic states. *Nature* **461**, 772–775 (2009).
- Hasan, M. Z. & Kane, C. L. Colloquium: topological insulators. *Rev. Mod. Phys.* **82**, 3045 (2010).
- Rechtsman, M. C. et al. Photonic Floquet topological insulators. *Nature* **496**, 196–200 (2013).
- Hafezi, M., Mittal, S., Fan, J., Migdall, A. & Taylor, J. M. Imaging topological edge states in silicon photonics. *Nat. Photon.* **7**, 1001–1005 (2013).
- Lu, L., Joannopoulos, J. D. & Soljačić, M. Topological photonics. *Nat. Photon.* **8**, 821–829 (2014).
- Yang, Z. et al. Topological acoustics. *Phys. Rev. Lett.* **114**, 114301 (2015).
- Süsstrunk, R. & Huber, S. D. Observation of phononic helical edge states in a mechanical topological insulator. *Science* **349**, 47–50 (2015).
- Bandres, M. A. et al. Topological insulator laser: experiments. *Science* **359**, eaar4005 (2018).
- Stützer, S. et al. Photonic topological Anderson insulators. *Nature* **560**, 461–465 (2018).

14. Klemmt, S. et al. Exciton–polariton topological insulator. *Nature* **562**, 552–556 (2018).
15. Blanco-Redondo, A., Bell, B., Oren, D., Eggleton, B. J. & Segev, M. Topological protection of biphoton states. *Science* **362**, 568–571 (2018).
16. Ozawa, T. et al. Topological photonics. *Rev. Mod. Phys.* **91**, 015006 (2019).
17. Haldane, F. D. M. Model for a quantum Hall effect without Landau levels: condensed-matter realization of the ‘parity anomaly’. *Phys. Rev. Lett.* **61**, 2015 (1988).
18. Haldane, F. D. M. & Raghu, S. Possible realization of directional optical waveguides in photonic crystals with broken time-reversal symmetry. *Phys. Rev. Lett.* **100**, 013904 (2008).
19. Rudner, M. S., Lindner, N. H., Berg, E. & Levin, M. Anomalous edge states and the bulk-edge correspondence for periodically driven two-dimensional systems. *Phys. Rev. X* **3**, 031005 (2013).
20. Maczewsky, L. J., Zeuner, J. M., Nolte, S. & Szameit, A. Observation of photonic anomalous Floquet topological insulators. *Nat. Commun.* **8**, 13756 (2017).
21. Mukherjee, S. et al. Experimental observation of anomalous topological edge modes in a slowly driven photonic lattice. *Nat. Commun.* **8**, 13918 (2017).
22. Jotzu, G. et al. Experimental realization of the topological Haldane model with ultracold fermions. *Nature* **515**, 237–240 (2014).
23. Ningyuan, J., Owens, C., Sommer, A., Schuster, D. & Simon, J. Time- and site-resolved dynamics in a topological circuit. *Phys. Rev. X* **5**, 021031 (2015).
24. Cheng, X. et al. Robust reconfigurable electromagnetic pathways within a photonic topological insulator. *Nat. Mater.* **15**, 542–548 (2016).
25. Slobozhanyuk, A. P. et al. Experimental demonstration of topological effects in bianisotropic metamaterials. *Sci. Rep.* **6**, 22270 (2016).
26. He, C. et al. Photonic topological insulator with broken time-reversal symmetry. *Proc. Natl Acad. Sci. USA* **113**, 4924–4928 (2016).
27. Schnyder, A. P., Ryu, S., Furusaki, A. & Ludwig, A. W. Classification of topological insulators and superconductors in three spatial dimensions. *Phys. Rev. B* **78**, 195125 (2008).
28. Carpentier, D., Delplace, P., Fruchart, M. & Gawędzki, K. Topological index for periodically driven time-reversal invariant 2D systems. *Phys. Rev. Lett.* **114**, 106806 (2015).
29. Kitagawa, T., Rudner, M. S., Berg, E. & Demler, E. Exploring topological phases with quantum walks. *Phys. Rev. A* **82**, 033429 (2010).
30. Roy, R. & Harper, F. Periodic table for Floquet topological insulators. *Phys. Rev. B* **96**, 155118 (2017).
31. Wu, L.-H. & Hu, X. Scheme for achieving a topological photonic crystal by using dielectric material. *Phys. Rev. Lett.* **114**, 223901 (2015).
32. Nathan, F. & Rudner, M. S. Topological singularities and the general classification of Floquet-Bloch systems. *New J. Phys.* **17**, 125014 (2015).
33. Thouless, D. J., Kohmoto, M., Nightingale, M. P. & den Nijs, M. Quantized Hall conductance in a two-dimensional periodic potential. *Phys. Rev. Lett.* **49**, 405 (1982).
34. Fu, L. & Kane, C. L. Time reversal polarization and a Z_2 adiabatic spin pump. *Phys. Rev. B* **74**, 195312 (2006).
35. Kitagawa, T., Berg, E., Rudner, M. & Demler, E. Topological characterization of periodically driven quantum systems. *Phys. Rev. B* **82**, 235114 (2010).
36. Höckendorf, B., Alvermann, A. & Fehske, H. Efficient computation of the W_3 topological invariant and application to Floquet-Bloch systems. *J. Phys. A* **50**, 295301 (2017).
37. Höckendorf, B., Alvermann, A. & Fehske, H. Topological invariants for Floquet-Bloch systems with chiral, time-reversal, or particle-hole symmetry. *Phys. Rev. B* **97**, 045140 (2018).
38. Szameit, A. & Nolte, S. Discrete optics in femtosecond-laser-written photonic structures. *J. Phys. B* **43**, 163001 (2010).
39. Rachel, S. Interacting topological insulators: a review. *Rep. Prog. Phys.* **81**, 116501 (2018).
40. Poli, C., Bellec, M., Kuhl, U., Mortessagne, F. & Schomerus, H. Selective enhancement of topologically induced interface states in a dielectric resonator chain. *Nat. Commun.* **6**, 6710 (2015).
41. Weimann, S. et al. Topologically protected bound states in photonic parity-time-symmetric crystals. *Nat. Mater.* **16**, 433–438 (2017).
42. Kremer, M. et al. Demonstration of a two-dimensional \mathcal{PT} -symmetric crystal. *Nat. Commun.* **10**, 435 (2019).
43. Heinrich, M. et al. Supersymmetric mode converters. *Nat. Commun.* **5**, 3698 (2014).
44. Queraltó, G. et al. Topological state engineering via supersymmetric transformations. *Commun. Phys.* **3**, 49 (2020).

Publisher’s note Springer Nature remains neutral with regard to jurisdictional claims in published maps and institutional affiliations.

© The Author(s), under exclusive licence to Springer Nature Limited 2020

Methods

Sample fabrication. The waveguide lattices used in our experiments were fabricated by means of the femtosecond-laser direct-writing technique³⁸. Pulses from a Ti:sapphire amplifier system (Coherent Mira 900/RegA 9000, wavelength 800 nm, repetition rate 100 kHz, pulse energy 250 nJ) are focused into the bulk of a fused silica wafer (Corning 7980, dimensions $1 \times 20 \times 150$ mm³) by means of a $\times 20$ microscopy objective (numerical aperture, 0.35). A three-axis positioning system (Aerotech ALS 130) was used to inscribe extended lines of permanent refractive index modifications on the order of 7×10^{-4} by translating the sample with respect to the focal spot. At the probe wavelength of 633 nm, these waveguides exhibit a mode field diameter of $10.4 \mu\text{m} \times 8 \mu\text{m}$ and anisotropic coupling in the x - y plane. The discrete hopping steps were implemented via dedicated directional couplers (length 6 mm) connected by sinusoidal fan-in/fan-out branches mediating the transitions (length 1.4 mm) of subsequent steps. Moreover, we made use of the fact that the trajectories of these transition sections can readily be fashioned with precisely defined differences in their overall optical path lengths, which in turn allows propagating light to accumulate the same additional phases that a detuned coupler would produce. In this vein, we are able to selectively include diagonal terms in the discrete Hamiltonian without having to physically change the on-site potential. The spin flip case was achieved with a coupling separation of $11.6 \mu\text{m}$ (diagonal interactions, $c^{(1,3,4,6)} = 3\pi/T$) and $10.9 \mu\text{m}$ (horizontal interactions, $c^{(2,5)} = 3\pi/T$). The spin rotation case was in turn realized with separations of $11.6 \mu\text{m}$, $12.5 \mu\text{m}$ and $10.2 \mu\text{m}$ for $c^{(1,3,4,6)} = 5\pi/2T$, $c^{(2)} = 2\pi/T$ and $c^{(5)} = 4\pi/T$, respectively, and an effective on-site potential $e^{(1,3,4,6)} = 3/2T$. The lattice for the probing of the TRS was manufactured with only one driving period and the parameters $c^{(1,3,4,6)} = 9\pi/4T$, $c^{(2)} = 2\pi/T$, $c^{(5)} = 4\pi/T$ and $e^{(1,3,4,6)} = 4/T$. The suppression of undesirable interactions was ensured by increasing the waveguide separation to $40 \mu\text{m}$ in the inert regions.

Probing the lattice dynamics. The samples were illuminated by 633-nm light from a helium–neon laser (Melles Griot, 35 mW). For the demonstration of the counter-propagating modes, a single lattice site was excited with a $\times 10$ microscope objective (numerical aperture 0.25). Another $\times 10$ microscope objective was used to image the output facet onto a CCD camera (Basler Aviator). The recorded images were post-processed to reduce noise and filtered to extract the actual modal intensities while reducing the influence of background light.

The two-site excitations for the verification of TRS were synthesized by means of a spatial light modulator (Hamamatsu LCOS-SLM X0468-02) with a holographic pattern comprising two separated Fresnel lenses. Additionally, these patterns were offset to impart a relative phase onto these two beams. A 4f-setup (focal lengths 1,000 mm and 125 mm) and a $\times 20$ microscope objective (numerical aperture 0.40) served to scale down the beam diameters and separation to excite two adjacent waveguides. The resulting output intensity distributions were similarly recorded and post-processed to extract the data plotted in Fig. 4b. Note that to achieve a non-zero contrast from the sine/cosine-shaped intensity-phase dependences, coupling steps 1, 3, 4 and 6 necessarily require non-zero diagonal entries in the Hamiltonian. In line with the approach described above, these were implemented via geometric path differences of $9.6 \mu\text{m}$ (transitions from step 1 \rightarrow 2 and 2 \rightarrow 3) and $9.9 \mu\text{m}$ (4 \rightarrow 5 and 5 \rightarrow 6), which would in the conventional realization correspond to a detuning of $4/T$ within the couplers of steps 1, 2, 3 and 4.

Numerical calculations. The band structures in Figs. 2 and 3 were obtained by diagonalizing the Floquet–Bloch propagator $U(\mathbf{k}, T)$ after one driving period T , which provides the quasi-energies ϵ as a function of momentum k_x and k_y . The propagator $U(\mathbf{k}, T)$ was calculated numerically with the Bloch Hamiltonian $H(\mathbf{k}, t)$ of the driving protocol in momentum space (the explicit expression for $H(\mathbf{k}, t)$ is given in the Supplementary Information). To derive the dispersion of the edge states in Figs. 2 and 3, the Floquet propagator on a semi-infinite ribbon was computed as a function of momentum k_x or k_y , parallel to the edges. The width of the ribbon was chosen as 15 unit cells, and only the edge states on one edge of the ribbon were included in the figures. Further details on the ribbon geometry are provided in the Supplementary Information. For the numerical results in Fig. 4b (solid curves for $I^B(\phi)$, $I^R(\phi)$) the Floquet propagators $U(T)$ of forward and $\tilde{U}(T)$ of backward propagation were obtained from the lattice Hamiltonian $H(t)$ of the driving protocol on a finite lattice with 4×3 unit cells in the x - y plane, as in Figs. 2 and 3. In all computations, the parameters $c^{(j)}$ and $e^{(j)}$ of the driving protocol have been set to the relevant experimental values specified previously for the spin rotation case (for Figs. 2d and 3f) and spin flip case (for Fig. 3c), or for the probing of TRS (for Fig. 4b).

Data availability

The data represented in Figs. 3d,e,g,h and 4b are provided with the paper as source data. All other data that support results in this Article are available from the corresponding author upon reasonable request.

Code availability

The numerical codes that support the plots within this paper and other findings of this study are available from the corresponding author upon reasonable request.

Acknowledgements

A.S. gratefully acknowledges financial support from the Deutsche Forschungsgemeinschaft (grants SZ 276/9-1, SZ 276/19-1, SZ 276/20-1, BL 574/13-1) and the Alfred Krupp von Bohlen und Halbach Foundation. We thank C. Otto for preparing the high-quality fused silica samples used in all experiments presented here.

Author contributions

The theory was established by B.H., A.A. and H.F. The sample design and lattice implementation were developed by L.M., M.H. and A.S. The characterization of the lattice structure was carried out by L.M., M.K. and T.B. The project was supervised by H.F. and A.S. All authors discussed the results and co-wrote the paper.

Competing interests

The authors declare no competing interests.

Additional information









Supplementary information is available for this paper at <https://doi.org/10.1038/s41563-020-0641-8>.

Correspondence and requests for materials should be addressed to A.A. or A.S.

Reprints and permissions information is available at www.nature.com/reprints.

In the format provided by the authors and unedited.

Fermionic time-reversal symmetry in a photonic topological insulator

Lukas J. Maczewsky ^{1,3}, Bastian Höckendorf^{2,3}, Mark Kremer ¹, Tobias Biesenthal¹,
Matthias Heinrich ¹, Andreas Alvermann ² , Holger Fehske ² and Alexander Szameit ¹ 

¹Institut für Physik, Universität Rostock, Rostock, Germany. ²Institut für Physik, Universität Greifswald, Greifswald, Germany. ³These authors contributed equally: Lukas J. Maczewsky, Bastian Höckendorf. [✉]e-mail: alvermann@physik.uni-greifswald.de; alexander.szameit@uni-rostock.de

Supplementary Information for
**Fermionic time-reversal symmetry
in a photonic topological insulator**

Lukas J. Maczewsky^{1,*}, Bastian Höckendorf^{2,*}, Mark Kremer¹,
Tobias Biesenthal¹, Matthias Heinrich¹, Andreas Alvermann²,
Holger Fehske², and Alexander Szameit¹

¹ Institut für Physik, Universität Rostock, Albert-Einstein-Str. 23,
18059 Rostock, Germany.

² Institut für Physik, Universität Greifswald, Felix-Hausdorff-Str. 6,
17489 Greifswald, Germany.

* These authors contributed equally.

alvermann@physik.uni-greifswald.de; alexander.szameit@uni-rostock.de

Contents

I Experimental techniques	2
I.1 Implementation of on-site potentials	2
I.2 Estimation of the experimental data correlation	4
I.3 Additional edge state measurements	4
II Theory	7
II.1 Construction of the driving protocol	7
II.2 Time-reversal symmetry	11
II.3 Negative coupling	13
II.4 Particle-hole and chiral symmetry	14
II.5 Bulk invariants and symmetry-protected topological phases	14
II.5.1 Chern number \mathcal{C}	14
II.5.2 Kane-Mele invariant ν_{KM}	15
II.5.3 Winding Number \mathcal{W}	15
II.5.4 TRS invariant ν_{TR}	16
II.6 Topological consideration of a ribbon geometry	16
II.7 Probing fermionic time-reversal symmetry	18
III Stability of the \mathbb{Z}_2 topological insulator	21
III.1 Experimental study of multi wavelength excitation	21
III.2 Bandstructure analysis under the influence of specific perturbations	22
References	23

I Experimental techniques

I.1 Implementation of on-site potentials

While the femtosecond laser inscription technique is capable of directly and precisely modulating the effective index of the fabricated waveguides via the exposure parameters (pulse energy, writing velocity) [1], we followed a different approach in this work to selectively implement diagonal terms in the discrete Hamiltonian. Instead of writing detuned couplers, i.e., evanescently interacting waveguides with different effective refractive indices, we designed the trajectories of the transition sections between subsequent steps such that precisely defined differences in their overall optical path lengths allow propagating light to accumulate the same additional phases that physically detuned couplers would produce (see Fig. S1). In this vein, our method separates the couplings terms from the detunings/on-site terms, since one is realized during the steps, while the other implementation occurs in between (see Fig. S2). The technique is of particular importance for the verification of time reversal symmetry (TRS), since in order to obtain a non-zero contrast of the sine/cosine shaped intensity-phase-dependences, coupling steps 1, 3, 4 and 6 necessarily require detuning via non-zero diagonal entries of the Hamiltonian. In line with the approach described above, these were implemented via geometric path differences of $9.6\ \mu\text{m}$ (transitions from step $1 \rightarrow 2$ and $2 \rightarrow 3$) and $9.9\ \mu\text{m}$ ($4 \rightarrow 5$ and $5 \rightarrow 6$), which would in the conventional realisation correspond to a detuning of $4/T$ within the couplers of steps 1, 2, 3 and 4 (see Fig. S2).

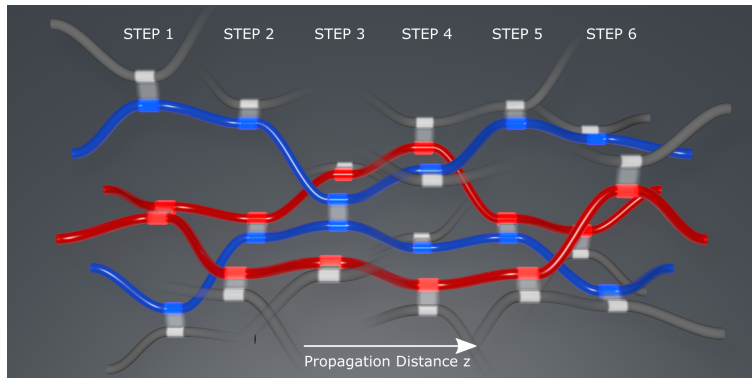


Figure S1: **Three dimensional representation of a unit cell (red/blue)** of the implemented waveguide structure. The unit cell is embedded in the surrounding waveguides (grey). The coupling regions are highlighted by semi-transparent ribbons. The different path lengths of the waveguides between the coupling regions are visible.

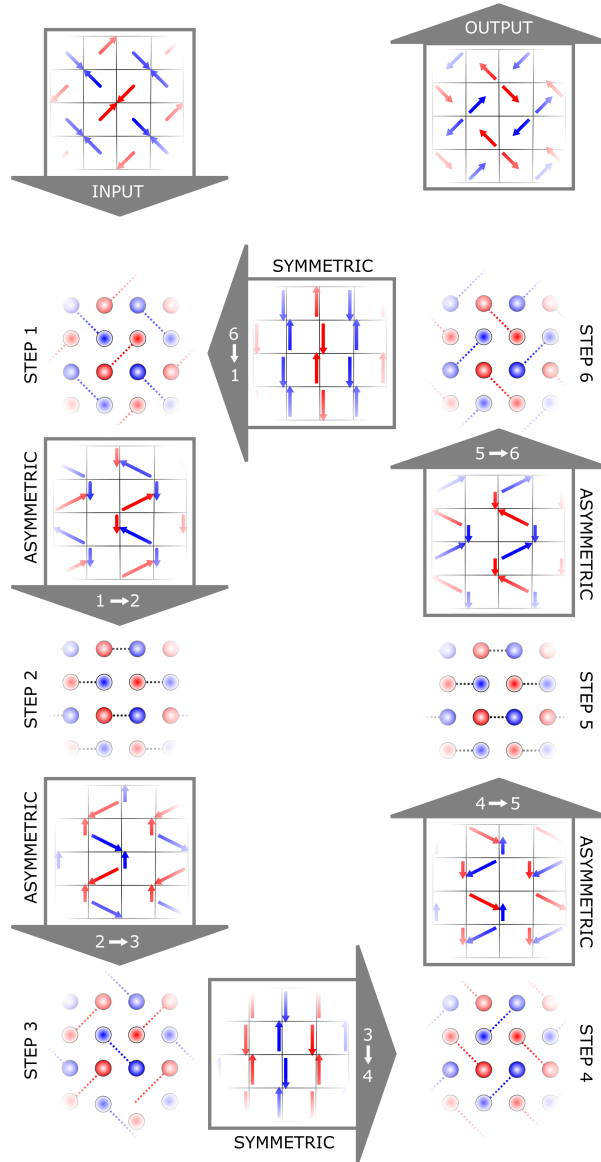


Figure S2: **Implementation of the on-site potential.** The discrete driving protocol of Fig. 2a of the main text is combined with trajectories of the waveguides between the hopping steps. The trajectories are marked by the red and blue arrows. The length of these arrows corresponds to the optical path length of the light guided by the waveguides. The asymmetric path lengths are clearly visible in the transitions from step $1 \rightarrow 2$ and $2 \rightarrow 3$.

I.2 Estimation of the experimental data correlation

The experimental data, which we presented in Fig. 3d,e,g,h of the main text, can be compared to theoretical simulations of the proposed driving protocol. The experimental images are mapped into a 8×6 matrix, by integrating over the area of the lattice sites. We determine the *image normalized cross-correlation* of the simulations and these reduced experimental data [2] (using $\sigma = 2$, since our edge typically has the size of 1 – 2 lattice sites). The extracted values, given in the main text, demonstrate the excellent agreement of experiment and theory.

I.3 Additional edge state measurements

As further evidence for the predicted edge state behaviour in our system, Fig. S4 and Fig. S5 show the output intensity profiles for additional single-site excitations beyond the ones shown in Fig. 3. Note that the spin flip case (Fig. S4) is characterised both by chiral edge transport (panels a/e, b/f), as well as a flat bulk band (Fig. 3c). The latter is responsible for the localised bulk excitations (panels c/g and d/h). The more general spin-rotation case (Fig. S5) continues to support the edge states. However, owing to the non-zero curvature of their trajectories through the band diagram (Fig. 3f), these edge states exhibit non-uniform transverse (along the edge) velocities. As a result, edge state excitations remain decoupled from the bulk, but are subject to a certain degree of dispersive broadening (along the edge) as they propagate along the edges. Due to the rhomboidal unit cell, some lattice sites belong to the edge, yet are not in direct contact with the environment. Figure S3 explicitly displays the edge location for clockwise and counterclockwise edge states.

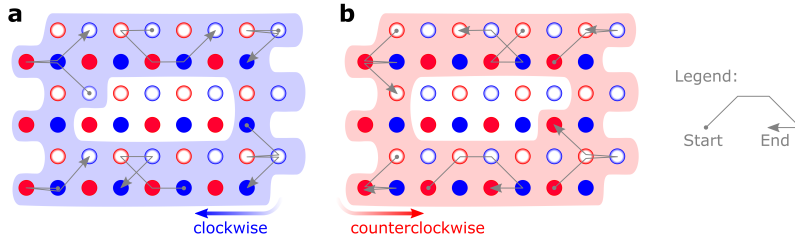


Figure S3: **Edge locations.** The black arrows pointing out the path of light during one driving period in the spin flip case. The colored background indicates the lattices sites which belong to the edge for **a** clockwise and **b** counterclockwise moving edge states, respectively.

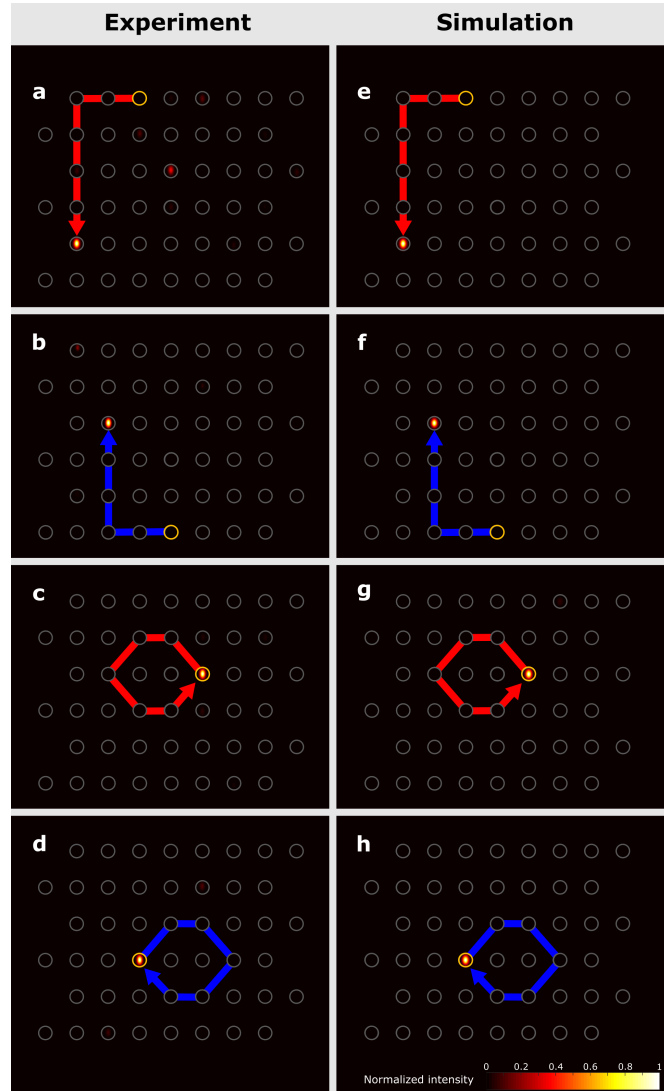


Figure S4: **Additional data for the spin-flip case.** Shown are the output intensity distributions resulting from excitations of the orange-outlined lattice sites after three full driving periods. The effective wave packet trajectories are indicated by blue and red arrows for clockwise and counter-clockwise propagation, respectively. **a,b**, Edge excitations exhibit chiral transport, **c,d**, bulk excitations remain effectively localised after each driving period. **e–h** Corresponding numerical simulations. In comparison with the simulations **a,b,c,d** the experimental data **e,f,g,h** coincide to 0.9093, 0.9966, 0.9903, 0.9919, respectively (based on [2]).

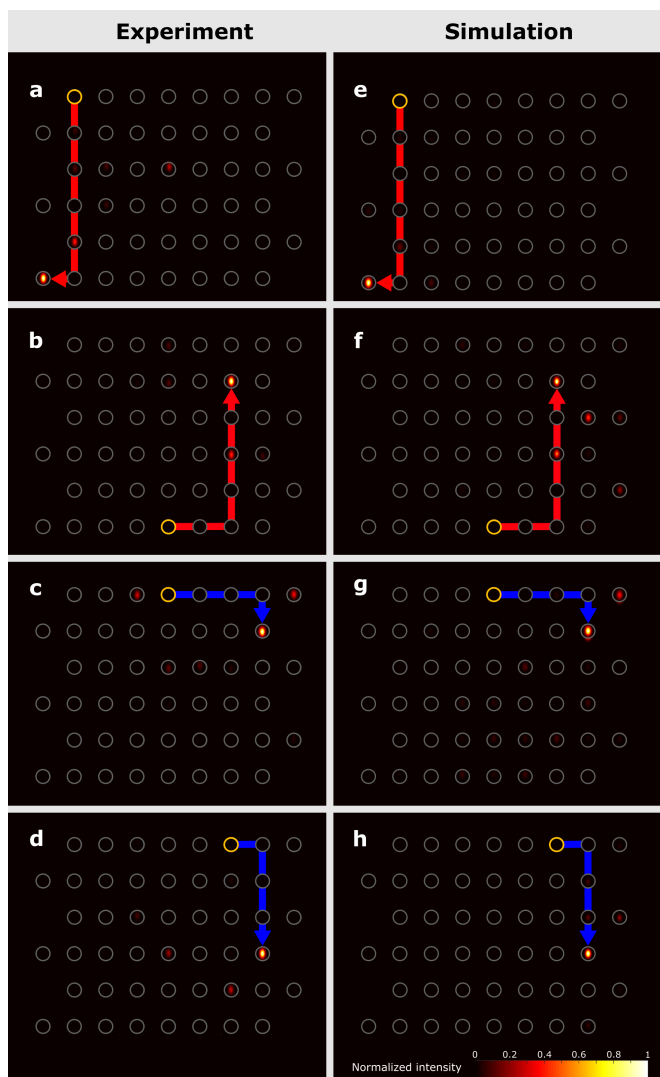


Figure S5: **Additional data for the spin-rotation case.** Shown are the output intensity distributions resulting from edge excitations of the orange-outlined lattice sites after three full driving periods. The effective wave packet trajectories are indicated by blue and red arrows for clockwise and counter-clockwise propagation, respectively. The edge states associated with both sublattices R (panels **a,b**) and B (panels **c,d**) now exhibit non-uniform transverse velocities, as indicated by a certain amount of wave packet broadening. **e–h** Corresponding numerical simulations. In comparison with the simulations **a,b,c,d** the experimental data **e,f,g,h** coincide to 0.9345, 0.8111, 0.9321, 0.8917, respectively (based on [2]).

II Theory

II.1 Construction of the driving protocol

Our construction of a driving protocol with fermionic time-reversal symmetry (TRS) follows the conceptual idea depicted in Fig. S6. The driving protocol is based on the square lattice model proposed in Ref. [3], which combines the four elementary coupling patterns between adjacent lattice sites defined in Fig. S7. To denote these patterns in the real-space Hamiltonian $H(t)$ of the driving protocol, we use the shorthand graphical notation

$$\begin{array}{c} \circ \\ \vdots \\ \circ \end{array}, \begin{array}{c} \bullet \\ \vdots \\ \bullet \end{array}, \begin{array}{c} \circ \\ \vdots \\ \bullet \end{array}, \begin{array}{c} \bullet \\ \vdots \\ \circ \end{array} \quad (\text{SI.1})$$

introduced in Fig. S7. Similarly, we write

$$\begin{array}{c} \circ \\ \vdots \\ \circ \end{array} = \sum_{k,l} (-1)^{k+l} |k, l\rangle \langle k, l| \quad (\text{SI.2})$$

for a term with alternating on-site potentials. In this notation, the ket vector $|k, l\rangle$, for $k, l \in \mathbb{Z}$, denotes the state at the k th and l th lattice site in horizontal and vertical direction, respectively. Lattice sites with even $k + l$ are identified with filled circles, sites with odd $k + l$ with hollow circles.

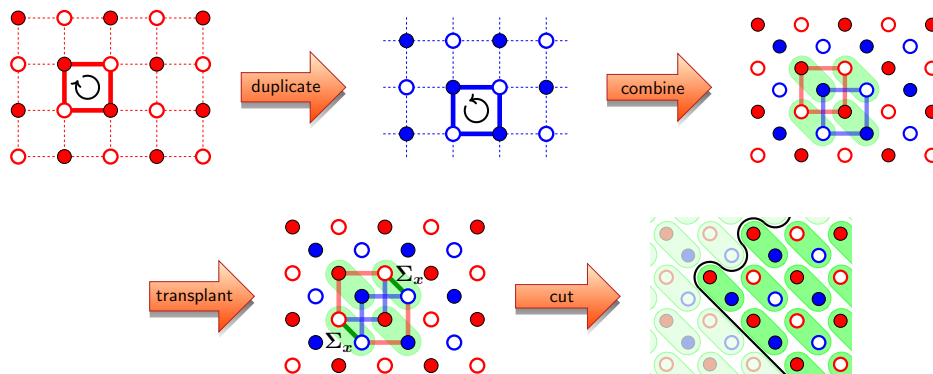


Figure S6: Construction of the driving protocol with TRS: Two copies (“red” and “blue”) of a driving protocol with opposite chirality are combined into a centred square lattice. The red/blue sublattice structure can be associated with a pseudo-spin $1/2$, where two neighbouring lattice sites are paired (“green” oval). After rotation by 45° , this construction gives the protocol depicted in Fig. 2 in the main text.

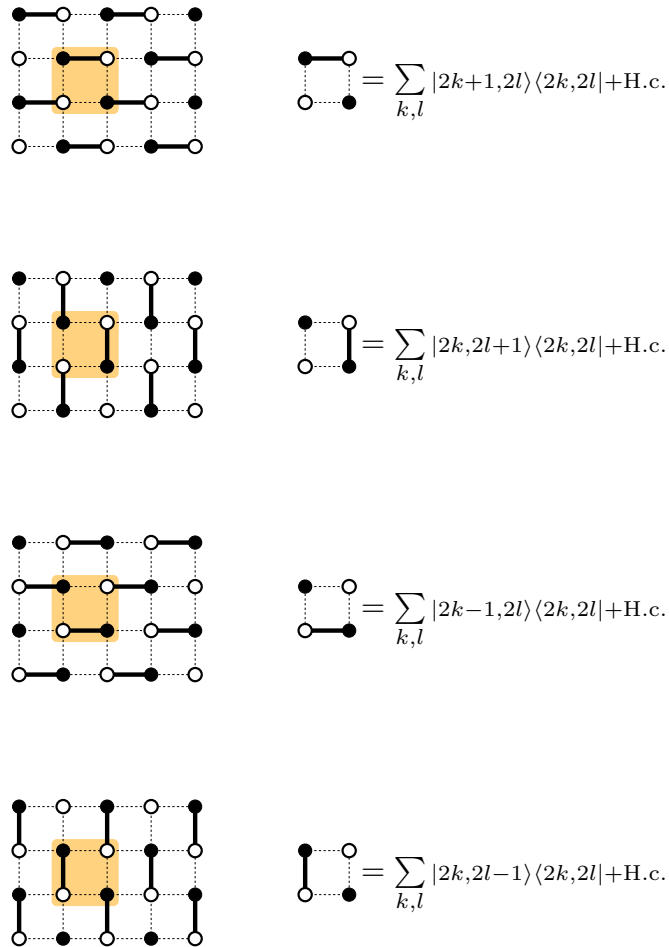


Figure S7: Shorthand graphical notation for the four elementary coupling patterns on the square lattice.

If the four coupling patterns are arranged in a periodic sequence, as in the model from Ref. [3], the resulting driving protocol implements a Floquet topological insulator with chiral edge states, but non-trivial symmetries cannot be enforced without modification of the protocol [4].

Therefore, to construct a driving protocol with TRS, we *duplicate* the previous non-symmetric model and *combine* the two copies, as shown in Fig. S6. One copy is the mirror image of the other, such that they implement opposite chirality for states on equivalent lattice sites. For the theoretical analysis, it is convenient to associate the two copies with a pseudo-spin $1/2$, where we identify the “red” and “blue” sublattice of the centred square lattice in Fig. S6 with the “up” spin state $|\uparrow\rangle$ and “down” spin state $|\downarrow\rangle$, respectively. In this way, the coupling patterns become associated with the two spin directions. We have, for example,

$$\begin{array}{c} \text{red} \\ \text{red} \end{array} = \sum_{k,l} |2k+1, 2l\rangle \langle 2k, 2l| \otimes |\uparrow\rangle \langle \uparrow| + \text{H.c.}, \quad (\text{SI.3})$$

$$\begin{array}{c} \text{blue} \\ \text{blue} \end{array} = \sum_{k,l} |2k+1, 2l\rangle \langle 2k, 2l| \otimes |\downarrow\rangle \langle \downarrow| + \text{H.c.}, \quad (\text{SI.4})$$

and similarly

$$\begin{array}{c} \text{blue} \\ \text{red} \end{array} = \sum_{k,l} (-1)^{k+l} |k, l\rangle \langle k, l| \otimes |\downarrow\rangle \langle \downarrow| + \text{H.c.} \quad (\text{SI.5})$$

for the potential terms. These terms preserve the pseudo-spin direction, as expressed by the projections $|\uparrow\rangle \langle \uparrow| = \frac{1}{2}(1 + \sigma_z)$ and $|\downarrow\rangle \langle \downarrow| = \frac{1}{2}(1 - \sigma_z)$.

To connect the two pseudo-spin directions, or sublattices, steps with a pseudo-spin transformation

$$\sigma_x = |\uparrow\rangle \langle \downarrow| + |\downarrow\rangle \langle \uparrow|, \quad (\text{SI.6})$$

need to be included in the driving protocol. In order to preserve TRS, these steps have to appear pairwise in symmetric position, in our case as steps 2 and 5 of the protocol.

The entire construction results in the driving protocol specified by the time-dependent Hamiltonian

$$H(t) = H_j, \quad \text{for } \left(n + \frac{j-1}{6}\right)T \leq t < \left(n + \frac{j}{6}\right)T \quad \text{with } n \in \mathbb{N}, \quad (\text{SI.7})$$

where the Hamiltonians H_j of each step $j \in \{1, \dots, 6\}$ are listed in Tab. S1. By construction, the Hamiltonian is Hermitian and periodic, $H(t+T) = H(t)$. Each period consists of six steps of equal duration $T/6$. Steps 1, 3, 4 and 6 leave the pseudo-spin unchanged, while steps 2, 5 involve a pseudo-spin rotation. To allow for breaking of particle-hole and chiral symmetry, steps 1, 3, 4 and 6 contain additional on-site potentials. In summary, the driving protocol has ten parameters: six couplings $c^{(j)}$, for $j \in \{1, \dots, 6\}$, and four on-site potentials $\epsilon^{(j)}$, for $j \in \{1, 3, 4, 6\}$. All parameters, hence also the entire Hamiltonian, are real-valued. The Hamiltonian in Eq. (SI.7) has been used in all numerical calculations presented in this work, and is the basis of the experimental implementation.

From this Hamiltonian, the Floquet propagator

$$U(T) = U_6 U_5 U_4 U_3 U_2 U_1 \quad (\text{SI.8})$$

Table S1: Hamiltonian $H(t)$ of the driving protocol in pseudo-spin representation, using the graphical notation from Fig. S7.

Driving protocol		$H(t)$
Step 1: $0 \leq t < \frac{1}{6}T$	$H_1 = c^{(1)} \left(\begin{array}{c} \text{red circle} \text{---} \text{red circle} \\ \uparrow \\ \text{red circle} \end{array} + \begin{array}{c} \text{blue circle} \text{---} \text{blue circle} \\ \downarrow \\ \text{blue circle} \end{array} \right) + \epsilon^{(1)} \left(\begin{array}{c} \text{red circle} \text{---} \text{red circle} \\ \uparrow \\ \text{red circle} \\ \text{---} \\ \text{red circle} \end{array} + \begin{array}{c} \text{blue circle} \text{---} \text{blue circle} \\ \downarrow \\ \text{blue circle} \\ \text{---} \\ \text{blue circle} \end{array} \right)$	
Step 2: $\frac{1}{6}T \leq t < \frac{2}{6}T$	$H_2 = c^{(2)} \mathbb{1} \otimes \sigma_x$	
Step 3: $\frac{2}{6}T \leq t < \frac{3}{6}T$	$H_3 = c^{(3)} \left(\begin{array}{c} \text{red circle} \text{---} \text{red circle} \\ \uparrow \\ \text{red circle} \end{array} + \begin{array}{c} \text{blue circle} \text{---} \text{blue circle} \\ \downarrow \\ \text{blue circle} \end{array} \right) + \epsilon^{(3)} \left(\begin{array}{c} \text{red circle} \text{---} \text{red circle} \\ \uparrow \\ \text{red circle} \\ \text{---} \\ \text{red circle} \end{array} + \begin{array}{c} \text{blue circle} \text{---} \text{blue circle} \\ \downarrow \\ \text{blue circle} \\ \text{---} \\ \text{blue circle} \end{array} \right)$	
Step 4: $\frac{3}{6}T \leq t < \frac{4}{6}T$	$H_4 = c^{(4)} \left(\begin{array}{c} \text{red circle} \text{---} \text{red circle} \\ \uparrow \\ \text{red circle} \end{array} + \begin{array}{c} \text{blue circle} \text{---} \text{blue circle} \\ \downarrow \\ \text{blue circle} \end{array} \right) + \epsilon^{(4)} \left(\begin{array}{c} \text{red circle} \text{---} \text{red circle} \\ \uparrow \\ \text{red circle} \\ \text{---} \\ \text{red circle} \end{array} + \begin{array}{c} \text{blue circle} \text{---} \text{blue circle} \\ \downarrow \\ \text{blue circle} \\ \text{---} \\ \text{blue circle} \end{array} \right)$	
Step 5: $\frac{4}{6}T \leq t < \frac{5}{6}T$	$H_5 = c^{(5)} \mathbb{1} \otimes \sigma_x$	
Step 6: $\frac{5}{6}T \leq t < T$	$H_6 = c^{(6)} \left(\begin{array}{c} \text{red circle} \text{---} \text{red circle} \\ \uparrow \\ \text{red circle} \end{array} + \begin{array}{c} \text{blue circle} \text{---} \text{blue circle} \\ \downarrow \\ \text{blue circle} \end{array} \right) + \epsilon^{(6)} \left(\begin{array}{c} \text{red circle} \text{---} \text{red circle} \\ \uparrow \\ \text{red circle} \\ \text{---} \\ \text{red circle} \end{array} + \begin{array}{c} \text{blue circle} \text{---} \text{blue circle} \\ \downarrow \\ \text{blue circle} \\ \text{---} \\ \text{blue circle} \end{array} \right)$	

is obtained, where the six propagators for each step are defined by $U_j = \exp(-iH_j T/6)$. For full coupling ($c^{(j)} = \pm 3\pi/T$, $\epsilon^{(j)} = 0$) the Floquet propagator in the bulk is trivial ($U(T) = \pm \mathbb{1}$). Especially, steps 2 and 5 correspond to a spin flip $U_{2,5} = \pm i\sigma_x$ and thus *transplant* states from one to the other pseudo-spin direction (see Fig. S6). The introduction of edges gives rise to pairs of edge states with opposite chirality, which move along the trajectories depicted in Fig. 2b in the main text. Note that an edge must result from a *cut* that preserves TRS, and does not separate lattice sites that are paired in the pseudo-spin (or red and blue sublattice) representation (see last panel in Fig. S6).

From the real-space Hamiltonian $H(t)$, one obtains the Bloch-Hamiltonian $H(\mathbf{k}, t)$ in momentum space given in Table S2. With this Hamiltonian, computation of the bulk band structures in Fig. 2d and Fig. S8 (below) is straightforward.

Pseudo-spin to lattice mapping As mentioned before, we map the up spin state $|\uparrow\rangle$ onto the “red” and the down spin state $|\downarrow\rangle$ onto the “blue” sublattice to obtain a pure lattice model without pseudo-spin degrees of freedom, which is suitable for a photonic waveguide implementation. Now, the ket vector $|k, l, R/B\rangle$ carries the sublattice information R/B in addition to the lattice site position k, l ,

Table S2: Same as Tab. S1, now for the Bloch Hamiltonian $H(\mathbf{k}, t)$ of the driving protocol. We use the abbreviations $k_1 = (a/2)(k_x + k_y)$ and $k_2 = (a/2)(-k_x + k_y)$, with the quasi-momentum $\mathbf{k} = (k_x, k_y)^t$ given in the x, y coordinates of Fig. 2b in the main text.

Driving protocol	$H(\mathbf{k}, t)$
Step 1: $0 \leq t < \frac{1}{6}T$	$H_1(\mathbf{k}) = \begin{pmatrix} \epsilon^{(1)} & c^{(1)}e^{ik_1} \\ c^{(1)}e^{-ik_1} & -\epsilon^{(1)} \end{pmatrix} \otimes \uparrow\rangle\langle\uparrow + \begin{pmatrix} \epsilon^{(1)} & c^{(1)}e^{-ik_2} \\ c^{(1)}e^{ik_2} & -\epsilon^{(1)} \end{pmatrix} \otimes \downarrow\rangle\langle\downarrow $
Step 2: $\frac{1}{6}T \leq t < \frac{2}{6}T$	$H_2(\mathbf{k}) = c^{(2)} \mathbb{1}_2 \otimes \sigma_x$
Step 3: $\frac{2}{6}T \leq t < \frac{3}{6}T$	$H_3(\mathbf{k}) = \begin{pmatrix} \epsilon^{(3)} & c^{(3)}e^{-ik_1} \\ c^{(3)}e^{ik_1} & -\epsilon^{(3)} \end{pmatrix} \otimes \uparrow\rangle\langle\uparrow + \begin{pmatrix} \epsilon^{(3)} & c^{(3)}e^{ik_2} \\ c^{(3)}e^{-ik_2} & -\epsilon^{(3)} \end{pmatrix} \otimes \downarrow\rangle\langle\downarrow $
Step 4: $\frac{3}{6}T \leq t < \frac{4}{6}T$	$H_4(\mathbf{k}) = \begin{pmatrix} \epsilon^{(4)} & c^{(4)}e^{ik_2} \\ c^{(4)}e^{-ik_2} & -\epsilon^{(4)} \end{pmatrix} \otimes \uparrow\rangle\langle\uparrow + \begin{pmatrix} \epsilon^{(4)} & c^{(4)}e^{-ik_1} \\ c^{(4)}e^{ik_1} & -\epsilon^{(4)} \end{pmatrix} \otimes \downarrow\rangle\langle\downarrow $
Step 5: $\frac{4}{6}T \leq t < \frac{5}{6}T$	$H_5(\mathbf{k}) = c^{(5)} \mathbb{1}_2 \otimes \sigma_x$
Step 6: $\frac{5}{6}T \leq t < T$	$H_6(\mathbf{k}) = \begin{pmatrix} \epsilon^{(6)} & c^{(6)}e^{-ik_2} \\ c^{(6)}e^{ik_2} & -\epsilon^{(6)} \end{pmatrix} \otimes \uparrow\rangle\langle\uparrow + \begin{pmatrix} \epsilon^{(6)} & c^{(6)}e^{ik_1} \\ c^{(6)}e^{-ik_1} & -\epsilon^{(6)} \end{pmatrix} \otimes \downarrow\rangle\langle\downarrow $

and the coupling and potential terms read,

$$\begin{array}{c} \text{---} \circ \text{---} \circ \text{---} \\ | \\ \text{---} \circ \text{---} \circ \text{---} \end{array} \text{R} = \sum_{k,l} |2k+1, 2l, R\rangle\langle 2k, 2l, R| + \text{H.c.}, \quad (\text{SI.9})$$

$$\begin{array}{c} \text{---} \circ \text{---} \circ \text{---} \\ | \\ \text{---} \circ \text{---} \circ \text{---} \end{array} \text{B} = \sum_{k,l} |2k+1, 2l, B\rangle\langle 2k, 2l, B| + \text{H.c.}, \quad (\text{SI.10})$$

or

$$\begin{array}{c} \text{---} \circ \text{---} \circ \text{---} \\ | \\ \text{---} \circ \text{---} \circ \text{---} \end{array} \text{B} = \sum_{k,l} (-1)^{k+l} |k, l, B\rangle\langle k, l, B| + \text{H.c.}, \quad (\text{SI.11})$$

and similarly for the remaining terms. The pseudo-spin transformation σ_x in steps 2 and 5 is replaced by the operator

$$\begin{array}{c} \text{---} \circ \text{---} \circ \text{---} \\ | \\ \text{---} \circ \text{---} \circ \text{---} \end{array} \simeq \Sigma_x = \sum_{k,l} |k, l, R\rangle\langle k, l, B| + \text{H.c.}, \quad (\text{SI.12})$$

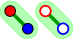
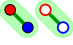
which swaps the red and blue sublattice (see Fig. S6). In this way, we obtain the Hamiltonian of the pure lattice model specified explicitly in Table S3.

II.2 Time-reversal symmetry

TRS is defined by the relation

$$\Theta H(t) \Theta^{-1} = H(T - t) \quad (\text{SI.13})$$

Table S3: Hamiltonian $H(t)$ of the driving protocol in “red” and “blue” sublattice representation of the pseudo-spin.

Driving protocol		$H(t)$
Step 1:	$0 \leq t < \frac{1}{6}T$	$H_1 = c^{(1)} \left(\begin{array}{ c c } \hline \bullet & \circ \\ \hline \circ & \bullet \\ \hline \end{array} \text{R} + \begin{array}{ c c } \hline \bullet & \circ \\ \hline \circ & \bullet \\ \hline \end{array} \text{B} \right) + \epsilon^{(1)} \left(\begin{array}{ c c } \hline + & - \\ \hline - & + \\ \hline \end{array} \text{R} + \begin{array}{ c c } \hline + & - \\ \hline - & + \\ \hline \end{array} \text{B} \right)$
Step 2:	$\frac{1}{6}T \leq t < \frac{2}{6}T$	$H_2 = c^{(2)} \begin{array}{ c c } \hline \bullet & \circ \\ \hline \circ & \bullet \\ \hline \end{array}$ 
Step 3:	$\frac{2}{6}T \leq t < \frac{3}{6}T$	$H_3 = c^{(3)} \left(\begin{array}{ c c } \hline \bullet & \circ \\ \hline \circ & \bullet \\ \hline \end{array} \text{R} + \begin{array}{ c c } \hline \bullet & \circ \\ \hline \circ & \bullet \\ \hline \end{array} \text{B} \right) + \epsilon^{(3)} \left(\begin{array}{ c c } \hline + & - \\ \hline - & + \\ \hline \end{array} \text{R} + \begin{array}{ c c } \hline + & - \\ \hline - & + \\ \hline \end{array} \text{B} \right)$
Step 4:	$\frac{3}{6}T \leq t < \frac{4}{6}T$	$H_4 = c^{(4)} \left(\begin{array}{ c c } \hline \bullet & \circ \\ \hline \circ & \bullet \\ \hline \end{array} \text{R} + \begin{array}{ c c } \hline \bullet & \circ \\ \hline \circ & \bullet \\ \hline \end{array} \text{B} \right) + \epsilon^{(4)} \left(\begin{array}{ c c } \hline + & - \\ \hline - & + \\ \hline \end{array} \text{R} + \begin{array}{ c c } \hline + & - \\ \hline - & + \\ \hline \end{array} \text{B} \right)$
Step 5:	$\frac{4}{6}T \leq t < \frac{5}{6}T$	$H_5 = c^{(5)} \begin{array}{ c c } \hline \bullet & \circ \\ \hline \circ & \bullet \\ \hline \end{array}$ 
Step 6:	$\frac{5}{6}T \leq t < T$	$H_6 = c^{(6)} \left(\begin{array}{ c c } \hline \bullet & \circ \\ \hline \circ & \bullet \\ \hline \end{array} \text{R} + \begin{array}{ c c } \hline \bullet & \circ \\ \hline \circ & \bullet \\ \hline \end{array} \text{B} \right) + \epsilon^{(6)} \left(\begin{array}{ c c } \hline + & - \\ \hline - & + \\ \hline \end{array} \text{R} + \begin{array}{ c c } \hline + & - \\ \hline - & + \\ \hline \end{array} \text{B} \right)$

(cf. Eq. (1) in the main text), where Θ is an anti-unitary operator with $\Theta^2 = \mathbb{1}$ for bosonic TRS and $\Theta^2 = -\mathbb{1}$ for fermionic TRS.

For fermionic TRS we choose $\Theta = \sigma_y \mathcal{K}$, with the second Pauli matrix σ_y and the operator of complex conjugation \mathcal{K} . Then, the symmetry relation (SI.13) reads

$$\sigma_y H(t) \sigma_y^{-1} = H(T - t)^* \quad (\text{SI.14})$$

(and we have $\sigma_y^{-1} = \sigma_y$). Note that the operator σ_y only acts on the pseudo-spin degrees of freedom of $H(t)$.

The transformation of terms in the Hamiltonian $H(t)$ is straightforward, for example, $\sigma_y \begin{array}{|c|c|} \hline \bullet & \circ \\ \hline \circ & \bullet \\ \hline \end{array} \uparrow \sigma_y^{-1} = \begin{array}{|c|c|} \hline \bullet & \circ \\ \hline \circ & \bullet \\ \hline \end{array} \downarrow$, or generally

$$\sigma_y |\uparrow\rangle \langle \uparrow| \sigma_y^{-1} = |\downarrow\rangle \langle \downarrow|. \quad (\text{SI.15})$$

On the other hand, we have $\sigma_y \sigma_x \sigma_y^{-1} = -\sigma_x$ for the spin flip σ_x . Therefore, the driving protocol obeys the relation (SI.14) if and only if the conditions

$$c^{(1)} = c^{(6)}, \quad c^{(3)} = c^{(4)}, \quad \epsilon^{(1)} = \epsilon^{(6)}, \quad \epsilon^{(3)} = \epsilon^{(4)}, \quad c^{(2)} = -c^{(5)} \quad (\text{SI.16})$$

are fulfilled. Then, we have

$$\Theta H_j \Theta^{-1} = H_{7-j} \quad (j = 1, \dots, 6) \quad (\text{SI.17})$$

for each of the steps, or equivalently

$$\sigma_y H_j \sigma_y^{-1} = H_{7-j} \quad (j = 1, \dots, 6) \quad (\text{SI.18})$$

since all H_j are real-valued. If all parameters are non-zero, the protocol does not possess additional particle-hole or chiral symmetry, see Sec. II.4.

For the present work, we choose the parameters (spin flip case)

$$c^{(1,2,3,4,6)} = 3\pi/T, \quad c^{(5)} = -3\pi/T, \quad \epsilon^{(1,3,4,6)} = 0, \quad (\text{SI.19})$$

and (spin rotation case)

$$\begin{aligned} c^{(1,3,4,6)} &= 5\pi/(2T), \quad \epsilon^{(1,3,4,6)} = 3/(2T), \\ c^{(2)} &= 2\pi/T, \quad c^{(5)} = -2\pi/T. \end{aligned} \quad (\text{SI.20})$$

II.3 Negative coupling

The condition (SI.16) implies that either the coupling $c^{(2)}$ in step 2 or $c^{(5)}$ in step 5 has to be negative, unless trivially $c^{(2)} = c^{(5)} = 0$. Negative couplings can indeed be implemented experimentally [5, 6], but we decided to circumvent the additional complexity involved in their implementation. To avoid negative couplings, we make the following observation: In steps 2,5 of the driving protocol, of duration δt (here $\delta t = T/6$) and with the spin matrix $c^{(2,5)}\sigma_x$, we have

$$\exp(-i\delta t c^{(2,5)}\sigma_x) = \exp\left[in\pi\sigma_x - i\delta t \left(\frac{n\pi}{\delta t} + c^{(2,5)}\right)\sigma_x\right] \quad (\text{SI.21})$$

$$= (-1)^n \exp\left[-i\delta t \left(\frac{n\pi}{\delta t} + c^{(2,5)}\right)\sigma_x\right] \quad (\text{SI.22})$$

for every $n \in \mathbb{Z}$. Therefore, negative couplings $c^{(2,5)} < 0$ in these steps can be replaced by positive couplings $\frac{n\pi}{\delta t} + c^{(2,5)} > 0$ for sufficiently large n , without changing the driving protocol implemented in the experiment. For odd n , the modified protocol contains an irrelevant global phase.

In the experiment (cf. Methods section), we realise the parameters (spin flip case)

$$c^{(1,2,3,4,5,6)} = 3\pi/T, \quad \epsilon^{(1,3,4,6)} = 0, \quad (\text{SI.23})$$

and (spin rotation case)

$$\begin{aligned} c^{(1,3,4,6)} &= 5\pi/(2T), \quad \epsilon^{(1,3,4,6)} = 3/(2T), \\ c^{(2)} &= 2\pi/T, \quad c^{(5)} = 4\pi/T, \end{aligned} \quad (\text{SI.24})$$

having replaced the negative coupling $c^{(5)}$ by the positive value $c^{(5)} + 6\pi/T$ in step 5 of the driving protocol. Due the global phase introduced by this replacement the Floquet quasi-energies are shifted by $\varepsilon \mapsto \varepsilon + \pi/T$, but the real space propagation remains unchanged.

II.4 Particle-hole and chiral symmetry

Particle-hole symmetry is defined by the relation

$$\Pi H(t) \Pi^{-1} = -H(t), \quad (\text{SI.25})$$

where Π is an anti-unitary operator for which $\Pi^2 = \pm \mathbb{1}$. Note that the same time argument t appears on both sides of the relation, so the symmetry relation maps each step of the driving protocol

$$\Pi H_j \Pi^{-1} = -H_j \quad (j = 1, \dots, 6) \quad (\text{SI.26})$$

onto itself.

While particle-hole symmetry with $\Pi^2 = -\mathbb{1}$ would require a modified version of our driving protocol [7], particle-hole symmetry with $\Pi^2 = \mathbb{1}$ is satisfied if the on-site potentials are set to zero. To see this, we choose

$$\Pi = \left(\begin{array}{c} \uparrow \\ \circ \\ \downarrow \\ \uparrow \end{array} - \begin{array}{c} \uparrow \\ \circ \\ \downarrow \\ \uparrow \end{array} \right) \mathcal{K}. \quad (\text{SI.27})$$

The coupling terms in the Hamiltonian transform as

$$\Pi \begin{array}{c} \uparrow \\ \circ \\ \downarrow \\ \uparrow \end{array} \Pi^{-1} = - \begin{array}{c} \uparrow \\ \circ \\ \downarrow \\ \uparrow \end{array}, \quad \Pi \begin{array}{c} \uparrow \\ \circ \\ \downarrow \\ \uparrow \end{array} \Pi^{-1} = - \begin{array}{c} \uparrow \\ \circ \\ \downarrow \\ \uparrow \end{array}, \quad \text{or} \quad \Pi \sigma_x \Pi^{-1} = -\sigma_x. \quad (\text{SI.28})$$

Comparison with Eq. (SI.26) indicates that all of them trivially satisfy particle-hole symmetry without any restriction on the values of $c^{(j)}$. On the other hand, we have

$$\Pi \begin{array}{c} \uparrow \\ \circ \\ \downarrow \\ \uparrow \end{array} \Pi^{-1} = \begin{array}{c} \uparrow \\ \circ \\ \downarrow \\ \uparrow \end{array}, \quad \text{and} \quad \Pi \begin{array}{c} \uparrow \\ \circ \\ \downarrow \\ \uparrow \end{array} \Pi^{-1} = \begin{array}{c} \uparrow \\ \circ \\ \downarrow \\ \uparrow \end{array} \quad (\text{SI.29})$$

for the on-site terms. Therefore, the driving protocol fulfills the symmetry relation (SI.26) if and only if the on-site potentials $\epsilon^{(j)} = 0$ vanish. In the present work, we want to exclusively probe the effects that fermionic time-reversal symmetry has on the driving protocols. For this reason, we include on-site terms to break particle-hole symmetry.

Since the driving protocol has time-reversal symmetry, but no particle-hole symmetry, the product of the two, which is chiral symmetry, is also broken [8].

II.5 Bulk invariants and symmetry-protected topological phases

In order to clearly separate the four topological invariants discussed in the main text, Chern number \mathcal{C} , Kane-Mele invariant ν_{KM} , Floquet winding number \mathcal{W} and Floquet TRS invariant ν_{TR} , we give an overview of their definition and relevance for (symmetry-protected) topological edge states. For a brief summary, see Tab. S4.

II.5.1 Chern number \mathcal{C}

The topological classification of time-independent systems without additional symmetries employs the integer-valued Chern number [15]

$$\mathcal{C} = \frac{1}{2\pi i} \int_{\text{BZ}} d\mathbf{k}^2 \nabla_{\mathbf{k}} \times \langle \psi | \nabla_{\mathbf{k}} | \psi \rangle. \quad (\text{SI.30})$$

Table S4: Overview of the discussed topological invariants.

Invariant	System type		Values	Occurrence	This work
\mathcal{C}	Static	No symmetry	\mathbb{Z}	[9, 10]	$\mathcal{C} = 0$
ν_{KM}	Static	Fermionic TRS	\mathbb{Z}_2	[11, 12]	$\nu_{\text{KM}} = 0$
\mathcal{W}	Floquet	No symmetry	\mathbb{Z}	[13, 14]	$\mathcal{W} = 0$
ν_{TR}	Floquet	Fermionic TRS	\mathbb{Z}_2	This work	$\nu_{\text{TR}} = 1$

The abbreviation BZ denotes integration over the entire Brillouin zone. The value of the Chern number corresponds to the net-chirality of edge states. When evaluated for the individual bands of a Floquet system, the Chern number is calculated from the eigenvectors $|\psi(\mathbf{k})\rangle$ of the Floquet-Bloch propagator $U(\mathbf{k}, T)$. In Floquet systems, it usually fails to correctly predict the number of edge states [3, 16] due to the periodicity of the quasi-energy. For the numerical computation of the Chern number, we use the algorithm from Ref. [17].

II.5.2 Kane-Mele invariant ν_{KM}

The topological classification of time-independent systems with fermionic TRS employs the \mathbb{Z}_2 -valued Kane-Mele invariant [18]

$$\nu_{\text{KM}} = \frac{1}{2\pi i} \left[\int_{\text{BZ}_{1/2}} d\mathbf{k}^2 (\nabla_{\mathbf{k}} \times \langle \psi | \nabla_{\mathbf{k}} | \psi \rangle) - \int_{\partial \text{BZ}_{1/2}} d\mathbf{k} \langle \psi | \nabla_{\mathbf{k}} | \psi \rangle \right] \pmod{2}. \quad (\text{SI.31})$$

The abbreviations $\text{BZ}_{1/2}$ or $\partial \text{BZ}_{1/2}$ now denote integration over half of the Brillouin zone or over its boundary, respectively. A non-zero value of this invariant implies the existence of a pair of symmetry-protected edge states with opposite chirality. Again, when evaluated for the individual bands of a Floquet system, the Kane-Mele invariant is calculated from the eigenvectors of the Floquet-Bloch propagator. Now, symmetry-protected edge states can appear even when the Kane-Mele invariant is zero [4, 19, 20], which is indeed the case for our driving protocol. For the numerical computation of the Kane-Mele invariant, we use the algorithm from Ref. [21].

II.5.3 Winding Number \mathcal{W}

The topological classification of Floquet systems without additional symmetries employs the integer-valued winding number [3]

$$\mathcal{W}(\varepsilon) = \frac{1}{8\pi^2} \int_0^T dt \int_{\text{BZ}} d\mathbf{k}^2 \text{Tr} (U_\varepsilon^\dagger \partial_t U_\varepsilon [U_\varepsilon^\dagger \partial_{k_x} U_\varepsilon, U_\varepsilon^\dagger \partial_{k_y} U_\varepsilon]) . \quad (\text{SI.32})$$

This invariant counts the net-chirality of edge states in the band gap at quasi-energy ε . Conceptually, it replaces the Chern number of time-independent systems

as the relevant invariant for Floquet systems. The modified propagator $U_\varepsilon(\mathbf{k}, t)$ is constructed from the Floquet-Bloch propagator $U(\mathbf{k}, t)$ as follows:

$$U_\varepsilon(\mathbf{k}, t) = \begin{cases} U(\mathbf{k}, 2t) & \text{if } 0 \leq t \leq \frac{T}{2} \\ V_\varepsilon(\mathbf{k}, 2T - 2t) & \text{if } \frac{T}{2} < t \leq T \end{cases},$$

where $V_\varepsilon(\mathbf{k}, t) = \exp(t \log_\varepsilon U(\mathbf{k}, T))$. The branch cut of the complex logarithm is chosen along the line from zero to $\exp(-i\varepsilon T)$, i.e., the eigenvalues of $i \log_\varepsilon U(\mathbf{k}, T)$ are elements of the interval $(T\varepsilon - 2\pi, T\varepsilon]$.

Alternatively, the winding number \mathcal{W} may be expressed as the sum

$$\mathcal{W}(\varepsilon) = \sum_{i=1}^p N_i(\varepsilon) \hat{\mathcal{C}}_i \quad (\text{SI.33})$$

over all degeneracy points $i = 1, \dots, p$ of the Floquet-Bloch propagator $U(\mathbf{k}, t)$ that occur during time-evolution [19, 20]. To each degeneracy point, we assign a topological charge $\hat{\mathcal{C}}_i$, given as a Chern number, and a weight factor $N_i(\varepsilon)$ that ensures that only the degeneracy points in the gap ε contribute to the sum. Now, the Chern numbers $\hat{\mathcal{C}}_i$ and weight factors $N_i(\varepsilon)$ are calculated from the eigenvectors and eigenvalues of the Floquet-Bloch propagator $U(\mathbf{k}, t)$ for all $0 \leq t \leq T$. For the numerical evaluation of the \mathcal{W} -invariant, we use the algorithm from Ref. [22].

II.5.4 TRS invariant ν_{TR}

In Floquet systems with fermionic TRS, the degeneracy points of the Bloch propagator appear in pairs with opposite topological charge, and cancel each other in the expression for the \mathcal{W} -invariant (SI.33). The appropriate \mathbb{Z}_2 -valued invariant for these systems [19, 20],

$$\nu_{\text{TR}}(\varepsilon) = \sum_{i=1}^{p/2} N_i(\varepsilon) \hat{\mathcal{C}}_i \pmod{2}, \quad (\text{SI.34})$$

counts only one partner of each symmetric pair of degeneracy points, as indicated by the upper summation limit $p/2$. A non-zero value of $\nu_{\text{TR}}(\varepsilon)$ implies the existence of symmetry-protected edge states with opposite chirality in the band gap at quasi-energy ε . Conceptually, this invariant serves the same role for Floquet systems as the Kane-Mele invariant for time-independent systems. For the numerical evaluation of the ν_{TR} -invariant, we use the algorithm from Ref. [22].

II.6 Topological consideration of a ribbon geometry

In a finite sample, symmetry-protected topological phases manifest themselves through chiral edge states. In our experiment, as well as in the numerical simulations, the edges of the sample run along either -45° (“ x -axis”) or $+45^\circ$ (“ y -axis”) on the centred square lattice, as indicated in Fig. 3 and Fig. S6. Note that the edges have to preserve TRS and thus may not separate lattice sites that are paired in the pseudo-spin representation.

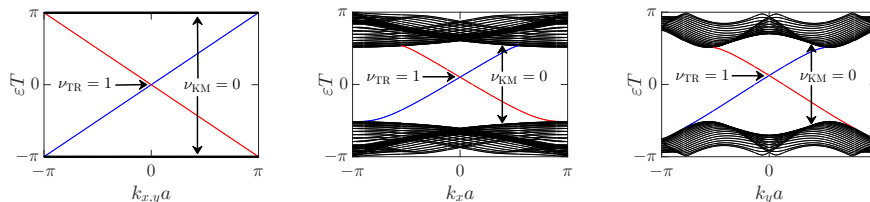


Figure S8: Floquet bands and symmetry-protected counter-propagating topological edge states for the spin flip (left panel) and spin rotation (central and right panel) case. Included are the values of the Kane-Mele invariant of the Floquet bands and the ν_{TR} -invariant in the central gap.

Figure S8 shows the edge states on a semi-infinite ribbon, together with the Floquet bands of the bulk, using the parameters of our driving protocol in Eq. (SI.23) (spin flip case) or Eq. (SI.24) (spin rotation case). In Fig. S8, the ribbon is 15 unit cells wide, and we only show the edge states on one of the two edges. Numerically, the edge states and bulk bands are computed from diagonalisation of the Floquet propagator on the ribbon after one driving period T , evaluated as a function of the momentum $k_{x/y}$ parallel to the edges along the x -axis or y -axis. Note that we include the shift $\varepsilon \mapsto \varepsilon + \pi/T$ of Floquet quasi-energies that appears through the replacement $c^{(5)} \mapsto c^{(5)} + 6\pi/T$ of the negative parameter $c^{(5)}$ by a positive value as we switch from the parameters in Eqs. (SI.20), (SI.19) to the experimental parameters in Eqs. (SI.24), (SI.23) (see Sec. II.3). Accordingly, the gap appears at quasi-energy $\varepsilon = 0$.

Through the bulk-edge correspondence the existence of chiral edge states coincides with a non-zero value of the respective bulk invariants, as collected in Sec. II.5. The present situation is characterised by the values listed in Table S4. Since $\mathcal{C} = 0$ and $\mathcal{W} = 0$ by TRS, edge states have to appear in counter-propagating pairs. Since $\nu_{\text{KM}} = 0$ but $\nu_{\text{TR}} \neq 0$ an odd number of counter-propagating pairs of edge states has to be present in the gap between the Floquet bands. Note that this combination of invariants corresponds to an anomalous Floquet topological phase [3, 16].

Counter-propagating edge states are indeed observed in Fig. S8 (here, a single pair). In both cases, the edge states exist independently of the direction of the edge, as required for (symmetry-protected) topological states. In the spin flip case, the Floquet bands are perfectly flat and the dispersion of the edge states is linear. Changing the parameters of the driving protocol from the spin flip to the spin rotation case, the Floquet bands acquire dispersion but the topological invariants do not change since the gap does not close. Alternatively, we could note that the number of crossings of the edge state dispersion at the invariant momenta $k_{x,y} = 0, \pi/a$, and hence the number of counter-propagating edge states, is protected by TRS through Kramers degeneracy. Indeed, these two viewpoints are equivalent due to the bulk-edge correspondence. The pair of counter-propagating edge states observed here in momentum space gives rise to the propagating modes observed in real space in the experiment (see Figs. 3, S4, S5).

II.7 Probing fermionic time-reversal symmetry

To check the TRS relation (SI.13) experimentally, we reverse the sample as described in the main text. As we derive now, this allows us to probe fermionic and bosonic TRS.

Reversing the sample does not correspond to reversing time, but to reversing the order of steps of the driving protocol. Therefore, if the forward propagator is given by Eq. (SI.8), the backward propagator is

$$\tilde{U}(T) = U_1 U_2 U_3 U_4 U_5 U_6 . \quad (\text{SI.35})$$

Here, we consider only one period of the driving protocol. Generalisation to several periods is straightforward.

In the present situation, a general TRS operator can be written as $\Theta = \sigma \mathcal{K}$, with a unitary spin-1/2 matrix σ such that $\sigma \sigma^* = \pm \mathbb{1}_2$. For such a general operator, the TRS relation (SI.13) is valid if and only if

$$\sigma H_j \sigma^{-1} = H_{7-j} \quad (j = 1, \dots, 6) \quad (\text{SI.36})$$

for the Hamiltonians H_j of each step (cf. Eqs. (SI.17), (SI.18)). Here, we use that the H_j are real-valued in our driving protocol, which allows us to drop the complex conjugation \mathcal{K} . Equivalently, we have

$$\sigma U_j \sigma^{-1} = \exp(-i(T/6) \sigma H_j \sigma^{-1}) \quad (\text{SI.37})$$

$$= \exp(-i(T/6) H_{7-j}) = U_{7-j} \quad (\text{SI.38})$$

for the propagators $U_j = \exp(-iH_j T/6)$ of each step. Therefore, the TRS relation for the backward propagator reads

$$\sigma U(T) \sigma^{-1} = (\sigma U_6 \sigma^{-1}) \cdots (\sigma U_1 \sigma^{-1}) = U_1 \cdots U_6 = \tilde{U}(T) . \quad (\text{SI.39})$$

Now suppose we use in the experiment the input state

$$|\psi_{\text{in}}(\phi)\rangle = |k_0, l_0, \text{R}\rangle + e^{i\phi} |k_0, l_0, \text{B}\rangle , \quad (\text{SI.40})$$

with finite amplitude on an adjacent red (R) and blue (B) site and a relative phase ϕ . If the state propagates through the sample, with forward propagation illustrated in Fig. 4a, the intensities of the waveguides measured at the output facet are given by the state

$$|\psi_{\text{out}}(\phi)\rangle = U(T) |\psi_{\text{in}}(\phi)\rangle = \sum_{k,l} (\psi_{k,l,\text{R}}(\phi) |k, l, \text{R}\rangle + \psi_{k,l,\text{B}}(\phi) |k, l, \text{B}\rangle) . \quad (\text{SI.41})$$

The amplitudes $\psi_{k,l,\text{R/B}}(\phi)$ occurring here could be computed with the Hamiltonian $H(t)$. Summing over the red or blue sites, respectively, we obtain the output intensities

$$I^{\text{R}}(\phi) = \sum_{k,l} |\psi_{k,l,\text{R}}(\phi)|^2 , \quad I^{\text{B}}(\phi) = \sum_{k,l} |\psi_{k,l,\text{B}}(\phi)|^2 , \quad (\text{SI.42})$$

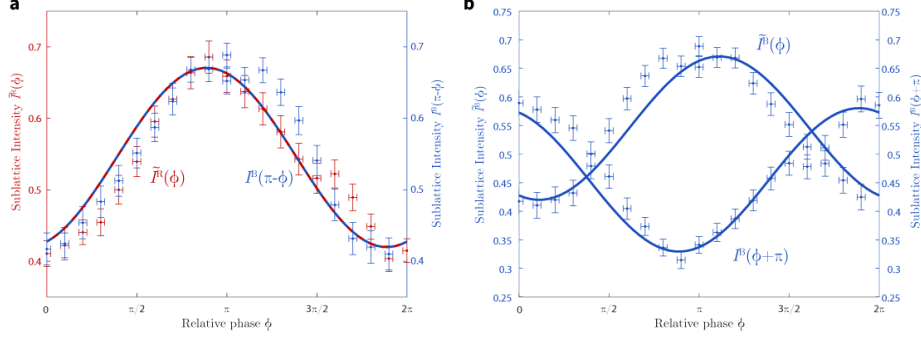


Figure S9: Probing the output intensities from Fig. 4b for fermionic TRS with $\sigma = \sigma_y$ (panel **a**) or bosonic TRS with $\sigma = \sigma_z$ (panel **b**). According to Table S5, it should hold $\tilde{I}^R(\phi) = I^B(\pi - \phi)$ in case **a** and $\tilde{I}^B(\phi) = I^B(\pi + \phi)$ in case **b** if the respective TRS is realised. Clearly, the relation for case **a** is satisfied but for case **b** is not.

shown in Fig. 4b and Fig. S9.

If, alternatively, the input state propagates through the reversed sample, i.e. with backward propagation illustrated in Fig. 4c, the output is given by the state

$$|\tilde{\psi}_{\text{out}}(\phi)\rangle = \tilde{U}(T)|\psi_{\text{in}}(\phi)\rangle = \Sigma U(T)\Sigma^{-1}|\psi_{\text{in}}(\phi)\rangle, \quad (\text{SI.43})$$

now with different output intensities $\tilde{I}^R(\phi)$, $\tilde{I}^B(\phi)$. The operator Σ that appears here is the mapping of the pseudo-spin operator σ onto the red/blue sublattice structure of the waveguide implementation (cf. Eq. (SI.12)). In bra-ket notation, it is

$$\Sigma = \sum_{k,l} (\sigma_{\uparrow\uparrow}|k,l,R\rangle\langle k,l,R| + \sigma_{\downarrow\uparrow}|k,l,B\rangle\langle k,l,R| + \quad (\text{SI.44})$$

$$\sigma_{\uparrow\downarrow}|k,l,R\rangle\langle k,l,B| + \sigma_{\downarrow\downarrow}|k,l,B\rangle\langle k,l,B|) \quad (\text{SI.45})$$

for

$$\sigma = \begin{pmatrix} \sigma_{\uparrow\uparrow} & \sigma_{\uparrow\downarrow} \\ \sigma_{\downarrow\uparrow} & \sigma_{\downarrow\downarrow} \end{pmatrix}. \quad (\text{SI.46})$$

From Eq. (SI.43) we see that the relation between the output intensities $I^R(\phi)$, $I^B(\phi)$ for forward propagation and $\tilde{I}^R(\phi)$, $\tilde{I}^B(\phi)$ for backward propagation depends entirely on the operator σ that determines Σ . Conversely, if the relation between the output intensities is known from the experiment, the possible choices of σ can be deduced.

The relevant possibilities are listed in Table S5. Note that a global phase of the operator σ drops out of the TRS relation (SI.13) due to complex conjugation, and is therefore not included in the table. For example, with $\sigma \equiv \sigma_y$ we have

$$\Sigma \equiv \Sigma_y = \sum_{k,l} (i|k,l,B\rangle\langle k,l,R| - i|k,l,R\rangle\langle k,l,B|), \quad (\text{SI.47})$$

Table S5: Relation between output intensities in forward and backward propagation for the four relevant choices of the operator σ in the general TRS relation.

σ	$\tilde{I}^{\text{R}}(\phi)$	$\tilde{I}^{\text{B}}(\phi)$
$\mathbb{1}$	$I^{\text{R}}(\phi)$	$I^{\text{B}}(\phi)$
σ_x	$I^{\text{B}}(\phi)$	$I^{\text{R}}(\phi)$
σ_y	$I^{\text{B}}(\pi - \phi)$	$I^{\text{R}}(\pi - \phi)$
σ_z	$I^{\text{R}}(\pi + \phi)$	$I^{\text{B}}(\pi + \phi)$

and thus

$$\Sigma_y^{-1}|\psi_{\text{in}}(\phi)\rangle = -ie^{i\phi}|\psi_{\text{in}}(-\phi + \pi)\rangle \quad (\text{SI.48})$$

for the input state while, according to Eq. (SI.43),

$$\begin{aligned} |\tilde{\psi}_{\text{out}}(\phi)\rangle &= -ie^{i\phi}\Sigma_y|\psi_{\text{out}}(-\phi + \pi)\rangle \\ &= e^{i\phi}\sum_{k,l}(\psi_{k,l,\text{R}}(-\phi + \pi)|k, l, \text{B}\rangle - \psi_{k,l,\text{B}}(-\phi + \pi)|k, l, \text{R}\rangle) \end{aligned} \quad (\text{SI.49})$$

for the output state. The phases $\pm e^{i\phi}$ drop out, but the output intensities on the red and blue sublattice are swapped by Σ_y . Therefore, we get the relations $\tilde{I}^{\text{R}}(\phi) = I^{\text{B}}(-\phi + \pi)$, $\tilde{I}^{\text{B}}(\phi) = I^{\text{R}}(-\phi + \pi)$ given in Table S5.

Now, the type of TRS realised by the driving protocol can be determined conclusively from the experimental data in Fig. 4b in the main text. In the experimental data we observe that (i) the output intensities on the red and blue sublattice are swapped and (ii) a phase shift $\phi \mapsto \pm\phi + \pi$ occurs when reversing the probe. Observation (i) rules out all possibilities for TRS apart from the choices $\sigma = \sigma_x$ or $\sigma = \sigma_y$, which are the only operators with purely off-diagonal elements as required for the swapping of intensities. Observation (ii) rules out all possibilities for TRS apart from the choices $\sigma = \sigma_y$ or $\sigma = \sigma_z$, which are the only operators leading to a phase shift $\phi \mapsto \pm\phi + \pi$. In combination, we are left with the choice $\sigma = \sigma_y$ of fermionic TRS.

For a final check of fermionic TRS, the experimental data are reproduced in Fig. S9 in direct correspondence to the relations from Table S5. Note that we have $I^{\text{R}}(\phi) = 1 - I^{\text{B}}(\phi)$ and $\tilde{I}^{\text{R}}(\phi) = 1 - \tilde{I}^{\text{B}}(\phi)$ for the normalised output intensities, such that the data in Fig. 4b fully determine the four functions entering these relations. Fig. S9 clearly shows that (only) the choice $\sigma = \sigma_y$ is compatible with the experimental data: Within the limit of experimental uncertainties, we have $\tilde{I}^{\text{R}}(\phi) = I^{\text{B}}(\pi - \phi)$ (hence also $\tilde{I}^{\text{B}}(\phi) = I^{\text{R}}(\pi - \phi)$ for normalised output intensities). Therefore, probing fermionic TRS results in a positive result: The experimental data for the output intensities are compatible with – and only with – fermionic TRS.

III Stability of the \mathbb{Z}_2 topological insulator

III.1 Experimental study of multi wavelength excitation

The coupling coefficient of evanescently coupled waveguides depends crucially on the excitation wavelength [1]. All of the samples discussed in this work are designed at an operation wavelength of 633 nm. By using a white light laser source (NKT SUPERK EXTREME) and a narrow wavelength filter (PHOTON ETC LLTF-SR-VIS-HP8), we are able to excite the structures in the wavelength range 600 – 670 nm. Hence, perturbing the photonic structure around the designed operating wavelength. We study the influence of the wavelength on two edge states at the lower x -edge of our structure, one clockwise and one counterclockwise (see Fig. S10a). When operated at an off-design wavelength (as shown for 626 nm in Fig. S10b), the efficiency with which the protocol confines light to the chiral edge channels systematically drops, and a certain fraction of the initial excitation can escape to the bulk. Nevertheless, more than 70 % confinement is achieved over a range of 20 nm (see Fig. S10c), corresponding to a bandwidth of more than 3 % of the carrier wavelength 633 nm. For comparison, the well established C-band in infrared telecommunications (1530–1565 nm) spans approximately 2.3 % of its carrier wavelength [23]. This is another indication that the underlying topology indeed provides robustness to the counterpropagating edge states.

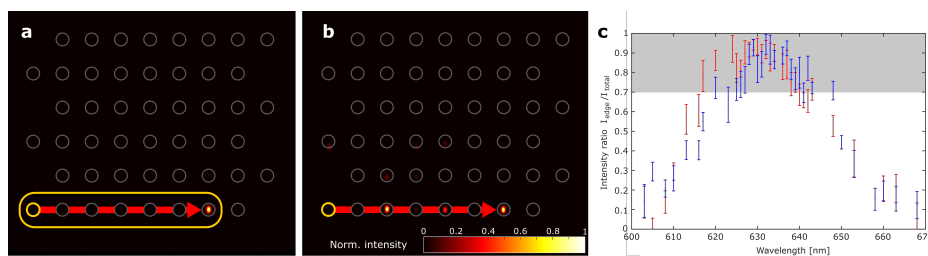


Figure S10: **Probing the stability of the edge states by exciting the lattice with off-design wavelength.** **a**, Evolution of a counterclockwise moving edge state after three driving periods at designed wavelength 633 nm. **b**, Edge state of the same lattice at the same single site excitation, for a wavelength of 626 nm. The intensity is spread over the edge, but remains at the edge. **c**, Intensity ratio of light at the edge (orange encircled region in **a**) as a function of the excitation wavelength. The blue/red data points indicate the excitation of a clockwise/counter-clockwise moving edge state, respectively. The grey bar indicates the region, where more than 70 % remains confined at the edge. The error bars are estimated by using the signal-to-noise ratio of the experimental image.

III.2 Bandstructure analysis under the influence of specific perturbations

The key ingredient for the \mathbb{Z}_2 topological insulator is the presence of fermionic TRS. If this symmetry is broken, the topological protection is lost, as illustrated in the bottom left panel of Fig. 1 in the main text. In order to highlight how such symmetry breaking affects the topological phase of our system (compare Fig. 3 in the main text), we change the system parameters and either preserve (see Figs. S11a,b) or break (see Figs. S11c,d) fermionic TRS. Since our driving protocol mainly depends on two parameters, the coupling and the detuning, we illustrate the effects of symmetry preservation/breaking for both cases. We choose the parameters in accordance to the experimental realisation (see Eq. (SI.20)) and add changes in steps one and six.

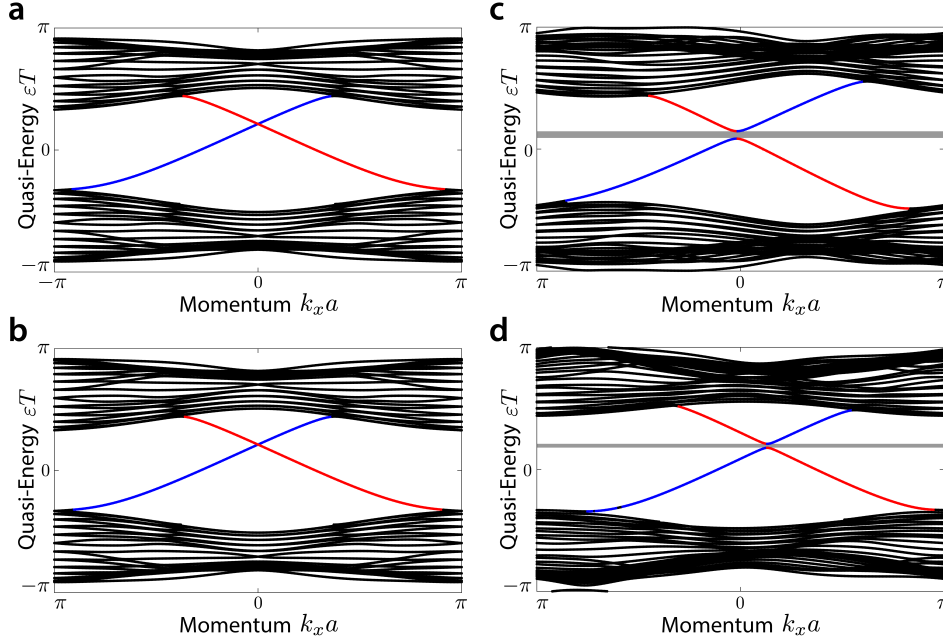


Figure S11: Analysis of the stability of the \mathbb{Z}_2 topological insulator with counter-propagating edge states under changes that preserve or break fermionic TRS. The band structure shows the stability of edge states under **a**, a symmetric offset in the coupling and **b** a symmetric offset in the detuning, which are both changes that preserve the symmetry. If the **c** coupling or **d** detuning is changed only in step one of the driving protocol, which breaks any TRS symmetry, a gap (marked in gray) is visible in the edge state dispersion.

In order to preserve fermionic TRS it is crucial that parameter changes are symmetric with respect to the steps of the driving protocol (see Eq. (SI.16)). The resulting band structures are displayed in Figs. S11a,b, where we add a constant offset to the coupling

$$c^{(1)} \rightarrow c^{(1)} + \frac{\pi}{T} \quad \text{and} \quad c^{(6)} \rightarrow c^{(6)} + \frac{\pi}{T}, \quad (\text{SI.50})$$

as shown in Fig. S11a, or a constant offset to the detuning (see Fig. S11b)

$$\epsilon^{(1)} \rightarrow \epsilon^{(1)} + \frac{3}{T} \quad \text{and} \quad \epsilon^{(6)} \rightarrow \epsilon^{(6)} + \frac{3}{T}. \quad (\text{SI.51})$$

Here, the counter-propagating edge states are still present, due to the protection by fermionic TRS.

In order to break fermionic TRS symmetry we change the parameters only in the first step, hence destroying any TRS. The resulting effect on the edge states is displayed in Figs. S11c,d, where we add a constant offset to the coupling in the first step

$$c^{(1)} \rightarrow c^{(1)} + \frac{\pi}{T}, \quad (\text{SI.52})$$

as shown in Fig. S11c, or to the detuning in the first step (see Fig. S11d)

$$\epsilon^{(1)} \rightarrow \epsilon^{(1)} + \frac{3}{T}. \quad (\text{SI.53})$$

Now, the edge states do no longer traverse the band gap (emphasised by a gray box), but return into the band they originated from. Hence, they do not give rise to scatter-free transport anymore, which is a direct consequence of the loss of symmetry protection. As expected, the \mathbb{Z}_2 topological phase with counter-propagating edge states is only protected as long as the fermionic TRS is preserved.

References


- [1] Szameit, A. & Nolte, S. Discrete optics in femtosecond-laser-written photonic structures. *J. Phys. B* **43**, 163001 (2010). URL <http://stacks.iop.org/0953-4075/43/i=16/a=163001>.
- [2] Nakhmani, A. & Tannenbaum, A. A new distance measure based on generalized image normalized cross-correlation for robust video tracking and image recognition. *Pattern Recognit. Lett.* **34**, 315–321 (2013). URL <https://www.sciencedirect.com/science/article/pii/S0167865512003558>.
- [3] Rudner, M. S., Lindner, N. H., Berg, E. & Levin, M. Anomalous Edge States and the Bulk-Edge Correspondence for Periodically Driven Two-Dimensional Systems. *Phys. Rev. X* **3**, 031005 (2013). URL <http://link.aps.org/doi/10.1103/PhysRevX.3.031005>.

- [4] Carpentier, D., Delplace, P., Fruchart, M. & Gawędzki, K. Topological Index for Periodically Driven Time-Reversal Invariant 2D Systems. *Phys. Rev. Lett.* **114**, 106806 (2015). URL <https://link.aps.org/doi/10.1103/PhysRevLett.114.106806>.
- [5] Keil, R. *et al.* Universal Sign Control of Coupling in Tight-Binding Lattices. *Phys. Rev. Lett.* **116**, 213901 (2016). URL <https://link.aps.org/doi/10.1103/PhysRevLett.116.213901>.
- [6] Kremer, M. *et al.* Non-quantized square-root topological insulators: a realization in photonic Aharonov-Bohm cages. *arXiv preprint* arXiv:1805.05209 (2018). URL <https://arxiv.org/abs/1805.05209>.
- [7] Höckendorf, B., Alvermann, A. & Fehske, H. Universal driving protocol for symmetry-protected Floquet topological phases. *Phys. Rev. B* **99**, 245102 (2019). URL <https://link.aps.org/doi/10.1103/PhysRevB.99.245102>.
- [8] Roy, R. & Harper, F. Periodic table for Floquet topological insulators. *Phys. Rev. B* **96**, 155118 (2017). URL <https://link.aps.org/doi/10.1103/PhysRevB.96.155118>.
- [9] Klitzing, K. v., Dorda, G. & Pepper, M. New Method for High-Accuracy Determination of the Fine-Structure Constant Based on Quantized Hall Resistance. *Phys. Rev. Lett.* **45**, 494–497 (1980). URL <https://link.aps.org/doi/10.1103/PhysRevLett.45.494>.
- [10] Rechtsman, M. C. *et al.* Photonic Floquet topological insulators. *Nature* **496**, 196–200 (2013). URL <http://dx.doi.org/10.1038/nature12066>.
- [11] König, M. *et al.* Quantum Spin Hall Insulator State in HgTe Quantum Wells. *Science* **318**, 766–770 (2007). URL <http://science.sciencemag.org/content/318/5851/766>.
- [12] Hsieh, D. *et al.* A topological Dirac insulator in a quantum spin Hall phase. *Nature* **452**, 970–974 (2008). URL <http://dx.doi.org/10.1038/nature06843>.
- [13] Maczewsky, L. J., Zeuner, J. M., Nolte, S. & Szameit, A. Observation of photonic anomalous Floquet topological insulators. *Nature Commun.* **8**, 13756 (2017). URL <http://dx.doi.org/10.1038/ncomms13756>.
- [14] Mukherjee, S. *et al.* Experimental observation of anomalous topological edge modes in a slowly driven photonic lattice. *Nature Commun.* **8**, 13918 (2017). URL <http://dx.doi.org/10.1038/ncomms13918>.
- [15] Thouless, D. J., Kohmoto, M., Nightingale, M. P. & den Nijs, M. Quantized Hall Conductance in a Two-Dimensional Periodic Potential. *Phys. Rev. Lett.* **49**, 405–408 (1982). URL <https://link.aps.org/doi/10.1103/PhysRevLett.49.405>.

-
- [16] Kitagawa, T., Berg, E., Rudner, M. & Demler, E. Topological characterization of periodically driven quantum systems. *Phys. Rev. B* **82**, 235114 (2010). URL <http://link.aps.org/doi/10.1103/PhysRevB.82.235114>.
- [17] Fukui, T., Hatsugai, Y. & Suzuki, H. Chern Numbers in Discretized Brillouin Zone: Efficient Method of Computing (Spin) Hall Conductances. *J. Phys. Soc. Jpn.* **74**, 1674–1677 (2005). URL <https://doi.org/10.1143/JPSJ.74.1674>. <https://doi.org/10.1143/JPSJ.74.1674>.
- [18] Fu, L. & Kane, C. L. Time reversal polarization and a Z_2 adiabatic spin pump. *Phys. Rev. B* **74**, 195312 (2006). URL <http://link.aps.org/doi/10.1103/PhysRevB.74.195312>.
- [19] Höckendorf, B., Alvermann, A. & Fehske, H. Topological invariants for Floquet-Bloch systems with chiral, time-reversal, or particle-hole symmetry. *Phys. Rev. B* **97**, 045140 (2018). URL <https://link.aps.org/doi/10.1103/PhysRevB.97.045140>.
- [20] Nathan, F. & Rudner, M. S. Topological singularities and the general classification of Floquet–Bloch systems. *New J. Phys.* **17**, 125014 (2015). URL <http://stacks.iop.org/1367-2630/17/i=12/a=125014>.
- [21] Fukui, T. & Hatsugai, Y. Quantum spin hall effect in three dimensional materials: Lattice computation of Z_2 topological invariants and its application to Bi and Sb. *J. Phys. Soc. Jpn.* **76**, 053702 (2007). URL <https://doi.org/10.1143/JPSJ.76.053702>. <https://doi.org/10.1143/JPSJ.76.053702>.
- [22] Höckendorf, B., Alvermann, A. & Fehske, H. Efficient computation of the W_3 topological invariant and application to Floquet-Bloch systems. *J. Phys. A* **50**, 295301 (2017). URL <http://stacks.iop.org/1751-8121/50/i=29/a=295301>.
- [23] Winzer, P. J., Neilson, D. T. & Chraplyvy, A. R. Fiber-optic transmission and networking: the previous 20 and the next 20 years. *Opt. Express* **26**, 24190–24239 (2018). URL <https://www.osapublishing.org/oe/abstract.cfm?uri=oe-26-18-24190>.

Non-Hermitian Boundary State Engineering in Anomalous Floquet Topological Insulators

Bastian Höckendorf, Andreas Alvermann^{✉,*} and Holger Fehske
Institut für Physik, Universität Greifswald, Felix-Hausdorff-Str. 6, 17489 Greifswald, Germany

 (Received 28 July 2019; published 7 November 2019)

In Hermitian topological systems, the bulk-boundary correspondence strictly constrains boundary transport to values determined by the topological properties of the bulk. We demonstrate that this constraint can be lifted in non-Hermitian Floquet insulators. Provided that the insulator supports an anomalous topological phase, non-Hermiticity allows us to modify the boundary states independently of the bulk, without sacrificing their topological nature. We explore the ensuing possibilities for a Floquet topological insulator with non-Hermitian time-reversal symmetry, where the helical transport via counterpropagating boundary states can be tailored in ways that overcome the constraints imposed by Hermiticity. Non-Hermitian boundary state engineering specifically enables the enhancement of boundary transport relative to bulk motion, helical transport with a preferred direction, and chiral transport in the same direction on opposite boundaries. We explain the experimental relevance of our findings for the example of photonic waveguide lattices.

DOI: [10.1103/PhysRevLett.123.190403](https://doi.org/10.1103/PhysRevLett.123.190403)

Topological states of matter have proven to be a research topic where fundamental theoretical insights lead almost inevitably to state-of-the-art practical applications [1–3]. A key feature of topological systems is directional transport via chiral boundary states, which is protected by topological invariants and thus impervious to the imperfections of real-world implementations [4–8]. In combination with fundamental symmetries [9–12], especially time-reversal symmetry (TRS) in topological insulators [13,14], topology even protects bidirectional helical transport via counterpropagating boundary states [6,15]. Such symmetry-protected topological phases emerge in a variety of physical systems [16–25], where they give rise to a wide spectrum of experimentally observable phenomena [26–30]. The recent discovery of anomalous topological phases in periodically driven (i.e., Floquet) insulators demonstrates the singular relevance of topological concepts also in systems far from equilibrium [31–36].

Only very recently has the notion of topological phases been extended to non-Hermitian systems [37–39]. The perception of the role of topology in this context is still changing rapidly through theoretical investigation and classification [40–50] as well as experimental exploration [29,51–54] of non-Hermitian topological phases, which includes investigation of the interplay of non-Hermiticity and Floquet dynamics [55,56]. Intriguingly, topology is expected to protect transport even against damping and dissipation [46].

In the present Letter we introduce the topological concept of boundary state engineering (BSE) that combines the specific aspects of non-Hermitian and anomalous

Floquet topological phases, and has no counterpart in systems with a Hermitian or static Hamiltonian. The concept underlying BSE is illustrated in Fig. 1, where we sketch the spectrum of the Floquet propagator $U \equiv U(T)$, obtained as the solution of the Schrödinger equation $i\partial_t U(t) = H(t)U(t)$ after one period of a time-periodic Hamiltonian $H(t) = H(t+T)$.

For a Hermitian system, with real Floquet quasienergies ϵ , the spectrum $\{e^{-i\epsilon}\}$ of U lies on the unit circle [57]. In regular topological phases, as they appear in systems with a static Hamiltonian, any boundary state, viewed as a continuous curve $k \mapsto e^{-ie(k)}$ parametrized by momentum k , connects two different bulk bands. Anomalous Floquet topological phases, in contrast, possess boundary states that wind around the unit circle [32]. Thinking in terms of the quasienergy ϵ , this possibility results from the periodicity $\epsilon \mapsto \epsilon + 2\pi$.

In a non-Hermitian system, the spectrum of U can move away from the unit circle. Regular boundary states have to remain attached to the bulk bands, since otherwise the continuous dependence on momentum would be violated.

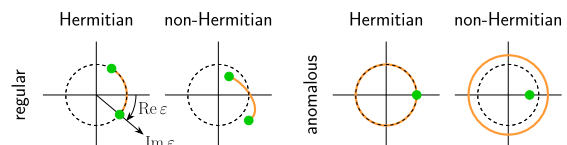


FIG. 1. Conceptual sketch of the spectrum $\{e^{-i\epsilon}\} \subset \mathbb{C}$ of the Floquet propagator in the Hermitian and non-Hermitian case, with bulk bands (green dots) and boundary states (orange curves) of a regular and anomalous topological phase.

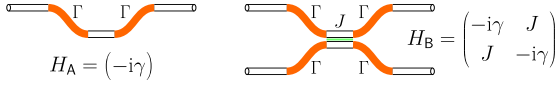


FIG. 2. Idealized Hamiltonians for an uncoupled (H_A) and two coupled (H_B) lossy waveguides, as they might appear in the experimental realization of a non-Hermitian driving protocol.

Anomalous boundary states, however, can detach from the bulk bands and thus be manipulated independently. This new freedom is exploited in BSE.

BSE is indeed a topological concept: Since the propagator U is invertible, its spectrum cannot move through the origin, and the winding number is preserved. Therefore, an anomalous boundary state, which winds around the origin, retains this property during non-Hermitian BSE and remains topologically protected.

From our discussion it is evident that BSE requires the combination of non-Hermiticity with anomalous Floquet topological phases. Non-Hermiticity arises naturally in optical settings such as photonic waveguide systems [29], since coupling involves losses due to the bending of the waveguides (see Fig. 2). The idealized Hamiltonian for the symmetric coupling of two lossy waveguides,

$$H_B = \begin{pmatrix} -i\gamma & J \\ J & -i\gamma \end{pmatrix}, \quad (1)$$

involves a coupling parameter J and damping γ . The associated propagator $U_B = \exp[-iH_B]$, over a time step $\delta t \equiv 1$, is an $SU(2)$ rotation, modified by the attenuation ($\gamma > 0$) or amplification ($\gamma < 0$) factor $e^{-\gamma}$. At perfect coupling $J = \pi/2$ we have $U_B = -ie^{-\gamma}\hat{\sigma}_x$, with the Pauli matrix $\hat{\sigma}_x$. Amplitude is swapped between the two coupled sites, but changes as $e^{-\gamma}$.

Regarding the experimental relevance of our theoretical considerations, it is useful to allow for a shift $\sigma(t) \in \mathbb{C}$ of the Hamiltonian, where we map $H(t) \mapsto H(t) + \sigma(t)$, and thus $U \mapsto \Gamma U$ with $\Gamma = \exp[-i \int_0^T \sigma(t) dt]$. Through the shift, loss and gain become relative terms, and weak loss can be interpreted as (pseudo) gain relative to strong loss. The physical content of $H(t)$ or U remains unchanged: measuring normalized intensities, of the form $I(\mathbf{r}) = |\psi(\mathbf{r})|^2 / \max_{\mathbf{r}'} |\psi(\mathbf{r}')|^2$, the factor Γ in U cancels.

Concerning the second aspect of BSE, the anomalous Floquet topological phases, we resort to the idea of a driving protocol [32]. To critically assess the potential of BSE in complex situations, we will use a driving protocol with fermionic TRS that supports counterpropagating boundary states. This protocol belongs to a class of universal protocols for symmetry-protected topological phases, which are investigated in Ref. [25].

One period of the protocol concatenates $n = 6$ steps, as given in Fig. 3 in a pictorial representation. The protocol takes place on a (finite or infinite) square lattice, which is composed of a red and blue sublattice. Because of

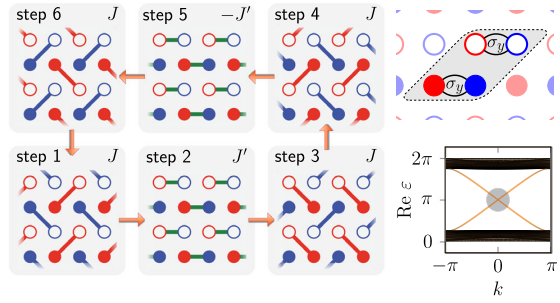


FIG. 3. Driving protocol for a Floquet insulator with TRS: Six steps of alternating interactions (left) between neighboring lattice sites (representing, e.g., photonic waveguides) lead to a \mathbb{Z}_2 topological phase with counterpropagating boundary states (bottom right), which is protected by fermionic TRS with the symmetry operator $S \equiv \hat{\sigma}_y \otimes \hat{\sigma}_y$ (top right).

fermionic TRS, the Hamiltonian obeys the relation $SH(t)S^{-1} = H(T-t)^*$, with a unitary symmetry operator S that fulfills $SS^* = -1$ [10]. Here, it is $S = \hat{\sigma}_y \otimes \hat{\sigma}_y$ if we identify the “red” and “blue” sublattice with the up and down component of a pseudospin $1/2$.

Fermionic TRS is essential for the \mathbb{Z}_2 phases of topological insulators [13]. As can be seen in Fig. 3, the driving protocol indeed supports a symmetry-protected \mathbb{Z}_2 topological phase, with counterpropagating boundary states whose intersection at momentum $k = 0$ is protected by Kramers degeneracy. This phase is an anomalous Floquet phase, since the boundary states connect the same bulk band at quasienergies separated by 2π . This phase has been explored experimentally in Ref. [15].

In general, the driving protocol supports topological phases on a continuous parameter manifold. Here, we consider a minimal parameter set, with the two parameters J (for diagonal couplings in steps 1,3,4,6) and J' (for horizontal couplings in steps 2,5). We use $J = 1.5, J' = 0.4$ in all plots. The minus sign $\pm J'$ between steps 2,5 shown in Fig. 3 is required for fermionic TRS, but negative couplings can be replaced by positive couplings to facilitate the experimental implementation [15].

Since the \mathbb{Z}_2 phase in Fig. 3 is an anomalous topological phase, it is a candidate for BSE. To understand the possibilities arising in this situation we first address the analytically tractable case of perfect coupling ($J = \pi/2, J' = 0$), before returning to general parameters.

At perfect coupling, the red and blue sublattice are decoupled (since $J' = 0$). As depicted in Fig. 4, states in the bulk move in a circular clockwise (counterclockwise) orbit on the red (blue) sublattice. At a boundary, which in Fig. 4 is oriented horizontally with respect to Fig. 3 and lies at the bottom of the (half-infinite) lattice, states propagate either to the right (red sublattice) or the left (blue sublattice). The propagation direction does not depend on the precise position of the boundary but is prescribed by the

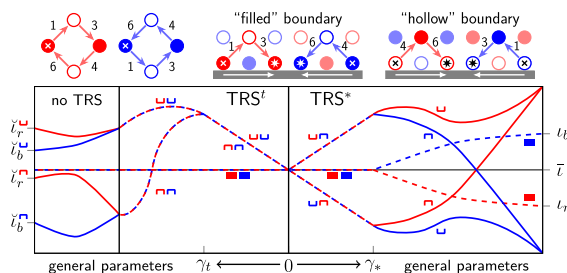


FIG. 4. Top row: motion at perfect coupling in the bulk (left) and at two boundaries (center and right), starting from a site marked with a cross (\times). Lower panel: schematic plot of the imaginary quasienergy $i \equiv \text{Im}\epsilon$ [relative to $\bar{i} = -2(\gamma_r + \gamma_b)$] for the parametrization in Eq. (7) and with general parameters. The plot shows the values in the bulk (filled rectangles) and on two different boundaries (marked with \square , \blacksquare), colored according to the starting site as in the top row.

bulk-boundary correspondence. Here, with counterpropagating boundary states, transport is protected by topology *and* fermionic TRS.

According to these patterns of motion, perfect coupling gives rise to a fourfold degenerate dispersionless bulk band at quasienergy $\epsilon = 0$, and two counterpropagating boundary states with linear dispersion $\epsilon_r(k) = \pi + k$, $\epsilon_b(k) = \pi - k$. As has been seen in Fig. 3, these features survive qualitatively for general parameters.

Non-Hermiticity is now introduced into the driving protocol in the following way. In the bulk, we assume uniform losses (as in the H_B configuration in Fig. 2) for the diagonal couplings of the red (losses with γ_r) or blue (losses with γ_b) sublattice in steps 1,3,4,6. The bulk bands thus acquire imaginary quasienergies

$$i_r = -4\gamma_r, \quad i_b = -4\gamma_b. \quad (2)$$

Here and below, a i variable denotes the imaginary part $i \equiv \text{Im}\epsilon$ of a quasienergy. Positive (negative) i implies gain (loss) according to $e^{-i\epsilon t} = e^{it} \times e^{-i\text{Re}\epsilon t}$. For the horizontal couplings in steps 2,5 we may assume identical losses, which can be absorbed into the shift of the Hamiltonian and will not be listed explicitly.

At the boundaries, losses $\check{\gamma}_r, \check{\gamma}_b$ occur at the isolated sites that, in the respective step of the protocol, do not couple to other sites (as in the H_A configuration in Fig. 2). For example, consider the state starting at a “filled red” site in the central top panel in Fig. 4. Through one period of the protocol, this state moves by two sites in steps 1,3 (incurring bulk losses $-2\gamma_r$), and remains at an isolated red site during steps 4,6 (incurring boundary losses $-2\check{\gamma}_r$). Working out the respective patterns for all four states depicted in the top row of Fig. 4, we see that the boundary states acquire imaginary quasienergies

$$\check{i}_r = i_r/2 - 2\check{\gamma}_r, \quad \check{i}_b = i_b/2 - 2\check{\gamma}_b. \quad (3)$$

Free choice of the four loss parameters $\gamma_r, \gamma_b, \check{\gamma}_r, \check{\gamma}_b$ allows for free placement of boundary states relative to the

bulk, as we had anticipated with the concept of BSE introduced in Fig. 1. In particular, the boundary states are detached from the bulk bands if $i_r \neq \check{i}_r$ or $i_b \neq \check{i}_b$.

The free assignment of losses γ (or imaginary parts i) is not compatible with TRS. To restore TRS, we can now impose two independent conditions in extension of the Hermitian case, namely

$$(\text{TRS}^*): SH(t)S^{-1} = H(T-t)^* + \xi_*(t), \quad (4a)$$

$$(\text{TRS}^{\prime}): SH(t)S^{-1} = H(T-t)^t + \xi_t(t). \quad (4b)$$

In comparison to, e.g., Ref. [39], these conditions incorporate the shift of the Hamiltonian through the functions $\xi_*(t) = \sigma(t) - \sigma(T-t)^*$, $\xi_t(t) = \sigma(t) - \sigma(T-t)$. For a constant shift $\sigma(t) \equiv \sigma$, we have $\xi_* \equiv i\text{Im}\sigma$ and $\xi_t \equiv 0$.

Similar to the coupling parameters J, J' , where fermionic TRS requires a minus sign between steps 2,5, non-Hermitian TRS imposes constraints

$$(\text{TRS}^*): \gamma_r + \gamma_b = \check{\gamma}_b + \check{\gamma}_r, \quad (5a)$$

$$(\text{TRS}^{\prime}): \gamma_r = \gamma_b, \quad \check{\gamma}_b = \check{\gamma}_r, \quad (5b)$$

on the loss parameters, which are equivalent to

$$(\text{TRS}^*): i_r + i_b = \check{i}_b + \check{i}_r, \quad (6a)$$

$$(\text{TRS}^{\prime}): i_r = i_b, \quad \check{i}_b = \check{i}_r. \quad (6b)$$

Note that TRS^{\prime} , but not TRS^* , implies equal damping of counterpropagating boundary states.

While in a uniform system the parameters $\gamma_{r,b}$ can be assumed to be identical throughout the bulk, it is essential for BSE that the losses $\check{\gamma}_{r,b}$ may very well depend on the boundary. For the schematic plot in the lower part of Fig. 4, we consider an infinite horizontal strip with different losses at the “top” ($\check{\gamma}_r^{\square}, \check{\gamma}_b^{\square}$) and “bottom” ($\check{\gamma}_r^{\blacksquare}, \check{\gamma}_b^{\blacksquare}$) boundary. The central part of this plot, along the γ_* and γ_t abscissa, uses a parametrization that results in

$$(\text{TRS}^*): i_{r,b} = -4\gamma_*, \quad (7a)$$

$$\check{i}_r^{\square} = \check{i}_b^{\square} = -2\gamma_*, \quad \check{i}_r^{\blacksquare} = \check{i}_b^{\blacksquare} = -6\gamma_*, \quad (7b)$$

$$(\text{TRS}^{\prime}): i_{r,b} = -4\gamma_t, \quad \check{i}_{r,b}^{\square} = \check{i}_{r,b}^{\blacksquare} = -2\gamma_t \quad (7c)$$

for the bulk and boundary states. TRS^* or TRS^{\prime} symmetry is preserved for all values of the respective parameter γ_* or γ_t , and bulk motion is suppressed in favor of boundary transport for $\gamma_{*,t} > 0$. The remaining figures will use this parametrization of the infinite horizontal strip.

General assignment of losses allows for more complex manipulation of boundary states, as schematically depicted along the “general parameters” abscissae. As long as TRS is preserved, the i values in Fig. 4 obey the relations of

Eq. (6). Without TRS, boundary states can be manipulated freely and independently on each boundary, as shown towards the left axis of the plot.

The schematic plot in Fig. 4 illustrates a few particularly noteworthy features of BSE. First, without TRS, the damping of bulk and boundary states can be chosen entirely freely. Second, even with TRS, the damping of boundary states relative to bulk states can be chosen freely, suppressing or enhancing either boundary transport or bulk motion. Third, the properties of boundary transport are not dictated by the properties of the bulk, as a strict bulk-boundary correspondence would demand. For example at the right axis of the plot, boundary transport occurs predominantly via red states, opposite to the predominant motion in the bulk via blue states.

In the general situation, away from perfect coupling, both the real and imaginary part of the quasienergies depend on momentum. TRS implies the constraints (see Supplemental Material [58] for a detailed derivation)

$$(\text{TRS}^{*t}): \text{Re}\{\varepsilon(\mathbf{k})\} = \text{Re}\{\varepsilon(-\mathbf{k})\}, \quad (8a)$$

$$(\text{TRS}^*): \text{Im}\{\varepsilon(\mathbf{k})\} = -\text{Im}\{\varepsilon(-\mathbf{k})\} + 2\text{Im}\sigma, \quad (8b)$$

$$(\text{TRS}^t): \text{Im}\{\varepsilon(\mathbf{k})\} = \text{Im}\{\varepsilon(-\mathbf{k})\} \quad (8c)$$

on the quasienergy spectrum $\{\varepsilon(\mathbf{k})\}$ at momentum \mathbf{k} , which generalize Eq. (6). Here, Eq. (8b) includes an imaginary shift, which drops out of Eq. (8c).

In Fig. 5, we observe the Kramers-like crossing of $\text{Re}\varepsilon(k)$ according to Eq. (8a). For TRS^t the two boundary states have to cross at the same $\text{Im}\varepsilon(k)$ and are thus truly degenerate, while for TRS^* they are separated by their imaginary part. This difference suggests that in the first case TRS^t is required to protect the boundary states, while in the second case they are robust against breaking of TRS^* . Indeed, if we break TRS by adding detunings (see Supplemental Material [58] for details on TRS breaking

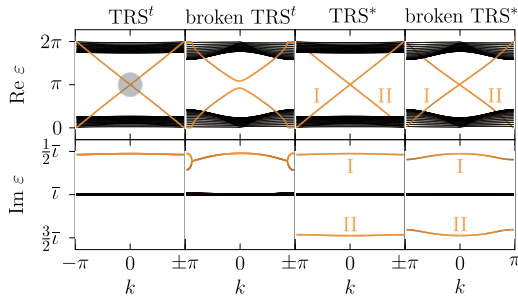


FIG. 5. Floquet quasienergy $\varepsilon(k)$ as a function of momentum k , with and without TRS as indicated, and non-Hermitian losses $\gamma_{t,*} = 1.2$ according to Eq. (7). Boundary states (on a “bottom” boundary) are shown in orange (as in Fig. 3). The gray circle indicates the Kramers-like degeneracy for TRS^t .

and preserving detunings), we observe an avoided crossing in Fig. 5 only for broken TRS^t but not for broken TRS^* .

Evidently, when counterpropagating boundary states have been separated via BSE, TRS is no longer required for their protection. However, now a preferred direction of transport exists due to the different damping of the boundary states. Only if the damping is equal, as in the TRS^t case in Fig. 5, true bidirectional transport without a preferred direction can be observed. In this scenario, TRS is still required for the protection of transport.

The new freedom introduced by BSE is thus twofold: It allows us to modify boundary transport relative to the bulk motion, and to selectively modify transport on different boundaries. Figure 6 provides a visual demonstration of the potential of such modifications. The point of reference is the Hermitian case in Fig. 6(b), with bidirectional helical transport via symmetry-protected counterpropagating boundary states (cf. Fig. 3). When protected by TRS^t , the counterpropagating boundary states survive the transition into the non-Hermitian regime, but now BSE allows us to suppress bulk motion in favor of boundary transport [Fig. 6(c)]. In the TRS^* case, we can additionally suppress either one of the two states on each boundary, which we do in such a way that transport on opposite boundaries takes place in the same (and not opposite) direction [Fig. 6(d)]. Such modifications are a unique feature of BSE: In a Hermitian system, they are prohibited by the bulk-boundary correspondence, while in a non-Floquet system boundary states remain attached to the bulk bands

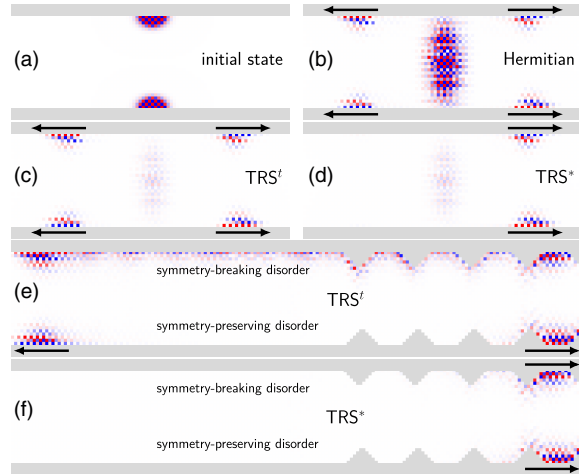


FIG. 6. Real-space propagation of an initial state prepared at the boundaries of a semi-infinite strip (height 30 sites), in the Hermitian case (b) or with non-Hermitian losses $\gamma_{t,*} = 0.1$ according to Eq. (7) (c)–(f). Lightness encodes the wave function intensity $I(r) = |\psi(r)|^2$ at each lattice site, normalized to the maximum value. (b)–(d) States after 15 periods of the driving protocol. (e),(f) States after 45 periods, with a partly serrated boundary and additional disorder that preserves or breaks TRS.

(cf. Fig. 1) and thus cannot be selectively amplified or suppressed.

To assess the full extent of topological protection in the present situation we have to examine the robustness of transport for imperfect boundaries and under the influence of disorder. In Figs. 6(e) and 6(f) we use serrated boundaries, and include disorder that preserves (breaks) TRS in the lower (upper) half of each strip. Disorder is both spatial and temporal; the exact form is specified in the Supplemental Material [58]. The disorder strength amounts to 0.2, or $\approx 13\%$ of the coupling J .

In Fig. 6(e), TRS' indeed protects the scatter-free bidirectional boundary transport, while breaking TRS' leads to visible backscattering. In Fig. 6(f), even disorder that breaks TRS* does not lead to appreciable backscattering because of the suppression of one of the two boundary states. Effectively, this situation realizes chiral transport with a preferred direction, which, in contrast to helical bidirectional transport, is protected by topology but does no longer require TRS.

In conclusion, BSE opens up new avenues to control topological transport in non-Hermitian Floquet systems. In conjunction with fermionic TRS to protect counterpropagating boundary states, BSE enables the selective enhancement of individual topological transport channels, and thus the effective manipulation of (bi)directional boundary transport. The potential for applications is immediate, and photonic waveguides, which are intrinsically non-Hermitian systems, are a natural platform to explore this potential. Experiments should also investigate the robustness of the different transport phenomena described here, thereby extending our analysis of the influence of disorder and symmetry breaking. Not least, the surprising new possibilities of BSE highlight the importance of further theoretical research regarding the status of topological invariants and the bulk-boundary correspondence in non-Hermitian Floquet systems.

*Corresponding author.

alvermann@physik.uni-greifswald.de

- [1] M. Z. Hasan and C. L. Kane, *Rev. Mod. Phys.* **82**, 3045 (2010).
- [2] X.-L. Qi and S.-C. Zhang, *Rev. Mod. Phys.* **83**, 1057 (2011).
- [3] T. Ozawa, H. M. Price, A. Amo, N. Goldman, M. Hafezi, L. Lu, M. C. Rechtsman, D. Schuster, J. Simon, O. Zilberberg, and I. Carusotto, *Rev. Mod. Phys.* **91**, 015006 (2019).
- [4] K. v. Klitzing, G. Dorda, and M. Pepper, *Phys. Rev. Lett.* **45**, 494 (1980).
- [5] D. J. Thouless, M. Kohmoto, M. P. Nightingale, and M. den Nijs, *Phys. Rev. Lett.* **49**, 405 (1982).
- [6] M. König, S. Wiedmann, C. Brüne, A. Roth, H. Buhmann, L. W. Molenkamp, X.-L. Qi, and S.-C. Zhang, *Science* **318**, 766 (2007).
- [7] Z. Wang, Y. Chong, J. D. Joannopoulos, and M. Soljacic, *Nature (London)* **461**, 772 (2009).
- [8] S. Stützer, Y. Plotnik, Y. Lumer, P. Titum, N. H. Lindner, M. Segev, M. C. Rechtsman, and A. Szameit, *Nature (London)* **560**, 461 (2018).
- [9] C.-K. Chiu, J. C. Y. Teo, A. P. Schnyder, and S. Ryu, *Rev. Mod. Phys.* **88**, 035005 (2016).
- [10] A. P. Schnyder, S. Ryu, A. Furusaki, and A. W. W. Ludwig, *Phys. Rev. B* **78**, 195125 (2008).
- [11] R. Roy and F. Harper, *Phys. Rev. B* **96**, 155118 (2017).
- [12] S. Yao, Z. Yan, and Z. Wang, *Phys. Rev. B* **96**, 195303 (2017).
- [13] C. L. Kane and E. J. Mele, *Phys. Rev. Lett.* **95**, 146802 (2005).
- [14] L. Fu and C. L. Kane, *Phys. Rev. B* **74**, 195312 (2006).
- [15] L. J. Maczewsky, B. Höckendorf, M. Kremer, T. Biesenthal, M. Heinrich, A. Alvermann, H. Fehske, and A. Szameit, [arXiv:1812.07930](https://arxiv.org/abs/1812.07930).
- [16] F. D. M. Haldane and S. Raghu, *Phys. Rev. Lett.* **100**, 013904 (2008).
- [17] G. Jotzu, M. Messer, R. Desbuquois, M. Lebrat, T. Uehlinger, D. Greif, and T. Esslinger, *Nature (London)* **515**, 237 (2014).
- [18] A. P. Slobozhanyuk, A. B. Khanikaev, D. S. Filonov, D. A. Smirnova, A. E. Miroshnichenko, and Y. S. Kivshar, *Sci. Rep.* **6**, 22270 (2016).
- [19] J. Ningyuan, C. Owens, A. Sommer, D. Schuster, and J. Simon, *Phys. Rev. X* **5**, 021031 (2015).
- [20] Z. Yang, F. Gao, X. Shi, X. Lin, Z. Gao, Y. Chong, and B. Zhang, *Phys. Rev. Lett.* **114**, 114301 (2015).
- [21] Z. Yan, B. Li, X. Yang, and S. Wan, *Sci. Rep.* **5**, 16197 (2015).
- [22] C. H. Lee, S. Imhof, C. Berger, F. Bayer, J. Brehm, L. W. Molenkamp, T. Kiessling, and R. Thomale, *Commun. Phys.* **1**, 39 (2018).
- [23] S. Klembt, T. H. Harder, O. A. Egorov, K. Winkler, R. Ge, M. A. Bandres, M. Emmerling, L. Worschech, T. C. H. Liew, M. Segev, C. Schneider, and S. Höfling, *Nature (London)* **562**, 552 (2018).
- [24] B. Höckendorf, A. Alvermann, and H. Fehske, *Phys. Rev. B* **97**, 045140 (2018).
- [25] B. Höckendorf, A. Alvermann, and H. Fehske, *Phys. Rev. B* **99**, 245102 (2019).
- [26] D. Hsieh, D. Qian, L. Wray, Y. Xia, Y. S. Hor, R. J. Cava, and M. Z. Hasan, *Nature (London)* **452**, 970 (2008).
- [27] H. Zhang, C.-X. Liu, X.-L. Qi, X. Dai, Z. Fang, and S.-C. Zhang, *Nat. Phys.* **5**, 438 (2009).
- [28] M. C. Rechtsman, J. M. Zeuner, Y. Plotnik, Y. Lumer, D. Podolsky, F. Dreisow, S. Nolte, M. Segev, and A. Szameit, *Nature (London)* **496**, 196 (2013).
- [29] J. M. Zeuner, M. C. Rechtsman, Y. Plotnik, Y. Lumer, S. Nolte, M. S. Rudner, M. Segev, and A. Szameit, *Phys. Rev. Lett.* **115**, 040402 (2015).
- [30] E. Lustig, S. Weimann, Y. Plotnik, Y. Lumer, M. A. Bandres, A. Szameit, and M. Segev, *Nature (London)* **567**, 356 (2019).
- [31] T. Kitagawa, E. Berg, M. Rudner, and E. Demler, *Phys. Rev. B* **82**, 235114 (2010).
- [32] M. S. Rudner, N. H. Lindner, E. Berg, and M. Levin, *Phys. Rev. X* **3**, 031005 (2013).
- [33] F. Nathan and M. S. Rudner, *New J. Phys.* **17**, 125014 (2015).

- [34] L. J. Maczewsky, J. M. Zeuner, S. Nolte, and A. Szameit, *Nat. Commun.* **8**, 13756 (2017).
- [35] S. Mukherjee, A. Spracklen, M. Valiente, E. Andersson, P. Öhberg, N. Goldman, and R. R. Thomson, *Nat. Commun.* **8**, 13918 (2017).
- [36] B. Höckendorf, A. Alvermann, and H. Fehske, *J. Phys. A* **50**, 295301 (2017).
- [37] Z. Gong, Y. Ashida, K. Kawabata, K. Takasan, S. Higashikawa, and M. Ueda, *Phys. Rev. X* **8**, 031079 (2018).
- [38] H. Zhou and J. Y. Lee, *Phys. Rev. B* **99**, 235112 (2019).
- [39] K. Kawabata, K. Shiozaki, M. Ueda, and M. Sato, *Phys. Rev. X* **9**, 041015 (2019).
- [40] H. Shen, B. Zhen, and L. Fu, *Phys. Rev. Lett.* **120**, 146402 (2018).
- [41] S. Yao and Z. Wang, *Phys. Rev. Lett.* **121**, 086803 (2018).
- [42] S. Yao, F. Song, and Z. Wang, *Phys. Rev. Lett.* **121**, 136802 (2018).
- [43] F. K. Kunst, E. Edvardsson, J. C. Budich, and E. J. Bergholtz, *Phys. Rev. Lett.* **121**, 026808 (2018).
- [44] C. H. Lee and R. Thomale, *Phys. Rev. B* **99**, 201103(R) (2019).
- [45] G. Harari, M. A. Bandres, Y. Lumer, M. C. Rechtsman, Y. D. Chong, M. Khajavikhan, D. N. Christodoulides, and M. Segev, *Science* **359**, eaar4003 (2018).
- [46] W. B. Rui, Y. X. Zhao, and A. P. Schnyder, *Phys. Rev. B* **99**, 241110(R) (2019).
- [47] J. Y. Lee, J. Ahn, H. Zhou, and A. Vishwanath, [arXiv:1906.08782](https://arxiv.org/abs/1906.08782).
- [48] A. Ghatak and T. Das, *J. Phys. Condens. Matter* **31**, 263001 (2019).
- [49] D. S. Borgnia, A. Jura Kruchkov, and R.-J. Slager, [arXiv:1902.07217](https://arxiv.org/abs/1902.07217).
- [50] T. Yoshida, R. Peters, N. Kawakami, and Y. Hatsugai, *Phys. Rev. B* **99**, 121101(R) (2019).
- [51] M. A. Bandres, S. Wittek, G. Harari, M. Parto, J. Ren, M. Segev, D. N. Christodoulides, and M. Khajavikhan, *Science* **359**, eaar4005 (2018).
- [52] S. Weimann, M. Kremer, Y. Plotnik, Y. Lumer, S. Nolte, K. G. Makris, M. Segev, M. C. Rechtsman, and A. Szameit, *Nat. Mater.* **16**, 433 (2017).
- [53] T. Helbig, T. Hofmann, S. Imhof, M. Abdelghany, T. Kiessling, L. W. Molenkamp, C. H. Lee, A. Szameit, M. Greiter, and R. Thomale, [arXiv:1907.11562](https://arxiv.org/abs/1907.11562).
- [54] S. Lin, L. Jin, and Z. Song, *Phys. Rev. B* **99**, 165148 (2019).
- [55] L. Zhou and J. Gong, *Phys. Rev. B* **98**, 205417 (2018).
- [56] L. Zhou and J. Pan, [arXiv:1908.02066](https://arxiv.org/abs/1908.02066).
- [57] Note that we measure quasienergies normalized to time step unity.
- [58] See Supplemental Material at <http://link.aps.org/supplemental/10.1103/PhysRevLett.123.190403> for additional details on the driving protocol and on the equations in the main text, and three additional examples of non-Hermitian boundary state engineering.

**Supplemental material for:
Non-Hermitian boundary state engineering
in anomalous Floquet topological insulators**

Bastian Höckendorf, Andreas Alvermann, and Holger Fehske
Institut für Physik, Universität Greifswald, Felix-Hausdorff-Str. 6, 17489 Greifswald, Germany

The supplemental material contains (i) a detailed derivation of Eq. (8) in the main text, (ii) the explicit specification of the non-Hermitian driving protocol, (iii) the explicit constraints on the protocol parameters from time-reversal symmetry, (iv) the specification of detunings and disorder to break time-reversal symmetry in Figs. 5, 6 in the main text, and (v) three additional examples of non-Hermitian boundary state engineering, including the application to the Kane-Mele model.

**I. TIME-REVERSAL SYMMETRY
AND ITS CONSEQUENCES**

The standard relation for time-reversal symmetry (TRS) reads $SHS^{-1} = H^* = H^t$ for a static Hamiltonian, with a unitary operator S . One can distinguish bosonic TRS with $SS^* = 1$ from fermionic TRS with $SS^* = -1$. The TRS relations generalize to

$$SH(t)S^{-1} = H(T-t)^* = H(T-t)^t \quad (1)$$

for a Floquet system with period T , where $H(t+T) = H(t)$. This relation generalizes even further for a non-Hermitian Floquet system, where we have the two separate relations [1]

$$(\text{TRS}^*) : SH(t)S^{-1} = H(T-t)^*, \quad (2a)$$

$$(\text{TRS}^t) : SH(t)S^{-1} = H(T-t)^t. \quad (2b)$$

Clearly, both relations agree for a Hermitian Hamiltonian with $H(t)^* = H(t)^t$.

TRS implies relations on the propagator $U(t)$ that lead, eventually, to the relations in Eq. (8) in the main text. To obtain these relations it is useful to consider the symmetrized propagator

$$U_*(t) = U\left(\frac{T+t}{2}, \frac{T-t}{2}\right). \quad (3)$$

It is $U_*(0) = 1$ and $U_*(T) = U(T)$. By applying $S \dots S^{-1}$ on both sides of the equation of motion

$$2i \partial_t U_*(t) = H\left(\frac{T+t}{2}\right) U_*(t) + U_*(t) H\left(\frac{T-t}{2}\right), \quad (4)$$

replacing terms according to the symmetry relations (2), and using the additional equations of motion

$$\begin{aligned} -2i \partial_t U_*(t)^{-1} &= H\left(\frac{T-t}{2}\right) U_*(t)^{-1} \\ &+ U_*(t)^{-1} H\left(\frac{T+t}{2}\right), \end{aligned} \quad (5a)$$

$$\begin{aligned} 2i \partial_t U_*(t)^t &= U_*(t)^t H\left(\frac{T+t}{2}\right)^t \\ &+ H\left(\frac{T-t}{2}\right)^t U_*(t)^t, \end{aligned} \quad (5b)$$

we see that

$$(\text{TRS}^*) : SU_*(t)S^{-1} = (U_*(t)^{-1})^*, \quad (6a)$$

$$(\text{TRS}^t) : SU_*(t)S^{-1} = U_*(t)^t. \quad (6b)$$

Therefore, we have

$$(\text{TRS}^*) : SUS^{-1} = (U^{-1})^*, \quad (7a)$$

$$(\text{TRS}^t) : SUS^{-1} = U^t \quad (7b)$$

for the Floquet propagator $U \equiv U(T) = U_*(T)$.

The TRS relations (2) are somewhat too restrictive for non-Hermitian systems, where we want to be able to freely interpret the meaning of “gain” and “loss” in relative terms. A simple modification suffices to achieve that freedom, namely, we allow for a (time-dependent) shift $\sigma(t) \in \mathbb{C}$ of the Hamiltonian

$$H(t) \mapsto H(t) + \sigma(t) \quad (8)$$

and demand that the modified TRS relations are invariant under such shifts. Replacing $H(t)$ by $H(t) + \sigma(t)$ in Eq. (2), these modified relations are obtained as

$$(\text{TRS}^*) : SH(t)S^{-1} = H(T-t)^* + \xi_*(t), \quad (9a)$$

$$(\text{TRS}^t) : SH(t)S^{-1} = H(T-t)^t + \xi_t(t), \quad (9b)$$

with arbitrary complex valued functions $\xi_*(t), \xi_t(t) \in \mathbb{C}$ that fulfill $\xi_*(T-t) = -\xi_*(t)^*$ and $\xi_t(T-t) = -\xi_t(t)$. These functions are related to the specific shift $\sigma(t)$ introduced in Eq. (8) through

$$(\text{TRS}^*) : \xi_*(t) = \sigma(t) - \sigma(T-t)^*, \quad (10a)$$

$$(\text{TRS}^t) : \xi_t(t) = \sigma(t) - \sigma(T-t). \quad (10b)$$

If $H(t)$ is modified by the shift in Eq. (8), the Floquet propagator is modified as

$$U \mapsto \Gamma U \quad (11)$$

with the scalar factor

$$\Gamma = \exp\left(-i \int_0^T \sigma(t) dt\right). \quad (12)$$

With this modification, the TRS relations for the Floquet propagator read

$$(\text{TRS}^*) : \quad SUS^{-1} = (\Gamma\Gamma^*U^*)^{-1}, \quad (13a)$$

$$(\text{TRS}^t) : \quad SUS^{-1} = U^t \quad (13b)$$

in generalization of Eq. (7). Note that the scalar factor Γ drops out of the TRS^t relation.

Both the complex conjugation in TRS^* and the transposition in TRS^t map momentum $\mathbf{k} \mapsto -\mathbf{k}$. Therefore, the above relations give

$$(\text{TRS}^*) : \quad SU(\mathbf{k}, T)S^{-1} = (\Gamma\Gamma^*U(-\mathbf{k}, T)^*)^{-1}, \quad (14a)$$

$$(\text{TRS}^t) : \quad SU(\mathbf{k}, T)S^{-1} = U(-\mathbf{k}, T)^t. \quad (14b)$$

for the Floquet-Bloch propagator $U(\mathbf{k}, T)$ that depends also on momentum \mathbf{k} .

Thinking in term of the Floquet quasienergy $\varepsilon = i \log \lambda$ to eigenvalue $\lambda = e^{-i\varepsilon}$ of U , we have that $\text{Re} \varepsilon$ is preserved but $\text{Im} \varepsilon$ changes sign under the mapping $\lambda \mapsto (\lambda^*)^{-1}$. From this, we immediately obtain the relations on the spectrum of the Floquet-Bloch propagator in Eq. (8) in the main text.

For a driving protocol with discrete steps $k = 1, \dots, n$, where the propagator of each step is $U_k = \exp[-iH_k \delta t]$ for the time step $\delta t = T/n$, the above TRS relations can be stated more explicitly. With a shift

$$H_k \mapsto H_k + \sigma_k \quad (15)$$

in the k -th step, and the associated scalar factor $\Gamma_k = e^{-i\sigma_k \delta t}$, we have

$$(\text{TRS}^*) : \quad SU_k S^{-1} = (\Gamma_k \Gamma_{n-k+1}^* U_{n-k+1}^*)^{-1}, \quad (16a)$$

$$(\text{TRS}^t) : \quad SU_k S^{-1} = (\Gamma_{n-k+1} / \Gamma_k) U_{n-k+1}^t, \quad (16b)$$

for the propagators U_k of each step. If we multiply these equations for all n steps, we see again that the propagator $U \equiv U(T) = U_n \cdots U_1$ of one period of the driving protocol obeys the relations (13), now with $\Gamma = \Gamma_1 \cdots \Gamma_n$.

II. EXPLICIT FORM OF THE NON-HERMITIAN DRIVING PROTOCOL

In the general case, the six-step protocol has $6 \times 2 \times 2^2 = 48$ complex parameters. Hermiticity reduces the number to 24 real and 12 complex parameters, which have been tabulated in Ref. [2] together with the constraints resulting from (fermionic or bosonic) TRS.

For the present study, we choose a restricted set of parameters, with two coupling parameters (J for diagonal couplings and J' for horizontal couplings), two parameters for uniform losses in the bulk (γ_r for red and γ_b for blue sites) and individual losses for isolated boundary sites ($\check{\gamma}_r, \check{\gamma}_b$ for each boundary).

Specifically, the bulk Hamiltonian has the following form, using a graphic notation that agrees with Fig. 3 in the main text:

Step 1: diagonal couplings

$$\left(\begin{array}{c} \bullet \swarrow \\ \nearrow \circ \end{array} \right)_1 = \begin{pmatrix} -i\gamma_r & J \\ J & -i\gamma_r \end{pmatrix} \quad (17)$$

$$\left(\begin{array}{c} \bullet \swarrow \\ \searrow \circ \end{array} \right)_1 = \begin{pmatrix} -i\gamma_b & J \\ J & -i\gamma_b \end{pmatrix} \quad (18)$$

Step 2: horizontal couplings

$$\left(\begin{array}{c} \bullet \leftarrow \\ \rightarrow \bullet \end{array} \right)_2 = \begin{pmatrix} -i\gamma_h & J' \\ J' & -i\gamma_h \end{pmatrix} \quad (19)$$

$$\left(\begin{array}{c} \circ \leftarrow \\ \rightarrow \circ \end{array} \right)_2 = \begin{pmatrix} -i\gamma_h & J' \\ J' & -i\gamma_h \end{pmatrix} \quad (20)$$

Step 3: diagonal couplings

$$\left(\begin{array}{c} \bullet \searrow \\ \swarrow \circ \end{array} \right)_3 = \begin{pmatrix} -i\gamma_r & J \\ J & -i\gamma_r \end{pmatrix} \quad (21)$$

$$\left(\begin{array}{c} \bullet \searrow \\ \swarrow \circ \end{array} \right)_3 = \begin{pmatrix} -i\gamma_b & J \\ J & -i\gamma_b \end{pmatrix} \quad (22)$$

Step 4: diagonal couplings

$$\left(\begin{array}{c} \bullet \nearrow \\ \swarrow \circ \end{array} \right)_4 = \begin{pmatrix} -i\gamma_r & J \\ J & -i\gamma_r \end{pmatrix} \quad (23)$$

$$\left(\begin{array}{c} \bullet \searrow \\ \swarrow \circ \end{array} \right)_4 = \begin{pmatrix} -i\gamma_b & J \\ J & -i\gamma_b \end{pmatrix} \quad (24)$$

Step 5: horizontal couplings

$$\left(\begin{array}{c} \bullet \leftarrow \\ \rightarrow \bullet \end{array} \right)_5 = \begin{pmatrix} -i\gamma_h & -J' \\ -J' & -i\gamma_h \end{pmatrix} \quad (25)$$

$$\left(\begin{array}{c} \circ \leftarrow \\ \rightarrow \circ \end{array} \right)_5 = \begin{pmatrix} -i\gamma_h & -J' \\ -J' & -i\gamma_h \end{pmatrix} \quad (26)$$

Step 6: diagonal couplings

$$\left(\begin{array}{c} \bullet \swarrow \\ \searrow \circ \end{array} \right)_6 = \begin{pmatrix} -i\gamma_r & J \\ J & -i\gamma_r \end{pmatrix} \quad (27)$$

$$\left(\begin{array}{c} \bullet \swarrow \\ \searrow \circ \end{array} \right)_6 = \begin{pmatrix} -i\gamma_b & J \\ J & -i\gamma_b \end{pmatrix} \quad (28)$$

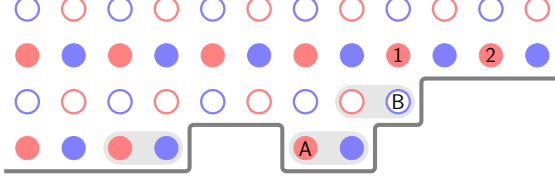


FIG. 1. Sketch of an imperfect “bottom boundary”.

For consistency, we have included losses γ_h also for the horizontal steps 2 and 5. Since these affect all sites equally, they can be absorbed in the shift $H(t) + \sigma(t)$ of the Hamiltonian, and are thus redundant.

Isolated boundary sites, i.e., lattice sites that are not coupled in one step of the driving protocol, incur individual losses specified by the parameters $\check{\gamma}_r$ and $\check{\gamma}_b$ for red and blue sites. Isolated sites occur only at boundaries, and the set of isolated sites changes during the six steps of the protocol. In the situation of Fig. 1, which shows an imperfect “bottom” boundary in generalization of Fig. 4 in the main text, the “filled red” site A is isolated in steps 4 and 6, and the “hollow blue” site B is isolated only in step 4. This statement about lattice sites should not be confused with a statement about states starting at the respective site. A state starting at site A is a boundary state that (at perfect coupling) moves to site 1 and 2 in one and two cycles of the driving protocol. A state starting at site B is a bulk state that (still at perfect coupling) returns to site B in every cycle of the protocol.

Note that with TRS, a boundary has to be compatible with the symmetry operator $S = \hat{\sigma}_y \otimes \hat{\sigma}_y$ introduced in Fig. 3 in the main text. For example, if a “filled red” site is included also the “filled blue” site to the right must be included, as indicated by the grey ovals in Fig. 1. This implies that in steps 2 and 5, all boundary sites are coupled through the horizontal couplings $\pm J'$, such that individual losses do not occur.

In principle, the individual losses can differ for each isolated boundary site, restricted only by the corresponding TRS constraints. In the present study, we only consider the possibility of different losses on different boundaries.

III. PARAMETER CONSTRAINTS FROM TIME-REVERSAL SYMMETRY

The constraints on parameter values resulting from TRS can be obtained along the lines of Ref. [2], extended to the non-Hermitian case. For example, using the graphical notation of the previous section to denote the coupling parameters, we have with the symmetry operator $S = \hat{\sigma}_y \otimes \hat{\sigma}_y$ that

$$S \begin{pmatrix} \bullet & \swarrow \\ \nearrow & \circ \end{pmatrix}_1 S^{-1} = \begin{pmatrix} \bullet & \swarrow \\ \nearrow & \circ \end{pmatrix} \stackrel{\text{TRS}}{=} \begin{pmatrix} \bullet & \swarrow \\ \nearrow & \circ \end{pmatrix}_6 \quad (29)$$

relating the parameters of “red” diagonal couplings in step 1 to the “blue” diagonal couplings in step 6, but

$$S \begin{pmatrix} \bullet & \leftarrow \\ \rightarrow & \bullet \end{pmatrix}_2 S^{-1} = \begin{pmatrix} \bullet & -(\rightarrow) \\ -(\leftarrow) & \bullet \end{pmatrix} \stackrel{\text{TRS}}{=} \begin{pmatrix} \bullet & \leftarrow \\ \rightarrow & \bullet \end{pmatrix}_5, \quad (30)$$

which explains the minus sign between the horizontal couplings $\pm J'$ in step 2 and step 5.

From these transformations it is straightforward to obtain the constraints required for TRS. In the general case, say with

$$\begin{pmatrix} \bullet & \swarrow \\ \nearrow & \circ \end{pmatrix}_1 = \begin{pmatrix} A_{r1} & B_{r1} \\ C_{r1} & D_{r1} \end{pmatrix} \quad (31)$$

for the diagonal coupling of red sites in step 1 and

$$\begin{pmatrix} \bullet & \swarrow \\ \nearrow & \circ \end{pmatrix}_6 = \begin{pmatrix} A_{b6} & B_{b6} \\ C_{b6} & D_{b6} \end{pmatrix} \quad (32)$$

for the diagonal coupling of blue sites in step 6, the TRS constraints on the eight parameters A_{r1}, \dots, D_{b6} are

$$(\text{TRS}^*) : A_{r1} = A_{b6}^* + \sigma_1 - \sigma_6^*, B_{r1} = B_{b6}^*, \quad (33a)$$

$$C_{r1} = C_{b6}^*, D_{r1} = D_{b6}^* + \sigma_1 - \sigma_6^*, \quad (33b)$$

$$(\text{TRS}^t) : A_{r1} = A_{b6} + \sigma_1 - \sigma_6, B_{r1} = C_{b6}, \quad (33c)$$

$$C_{r1} = B_{b6}, D_{r1} = D_{b6} + \sigma_1 - \sigma_6. \quad (33d)$$

On the other hand, with

$$\begin{pmatrix} \bullet & \leftarrow \\ \rightarrow & \bullet \end{pmatrix}_2 = \begin{pmatrix} A_{f2} & B_{f2} \\ C_{f2} & D_{f2} \end{pmatrix} \quad (34)$$

for the horizontal coupling of the filled sites in step 2 and

$$\begin{pmatrix} \bullet & \leftarrow \\ \rightarrow & \bullet \end{pmatrix}_5 = \begin{pmatrix} A_{f5} & B_{f5} \\ C_{f5} & D_{f5} \end{pmatrix} \quad (35)$$

for the horizontal coupling of the filled sites in step 5, the TRS constraints are

$$(\text{TRS}^*) : A_{f2} = A_{f5}^* + \sigma_2 - \sigma_5^*, B_{f2} = -C_{f5}^*, \quad (36a)$$

$$C_{f2} = -B_{f5}^*, D_{f2} = D_{f5}^* + \sigma_2 - \sigma_5^*, \quad (36b)$$

$$(\text{TRS}^t) : A_{f2} = A_{f5} + \sigma_2 - \sigma_5, B_{f2} = -B_{f5}, \quad (36c)$$

$$C_{f2} = -C_{f5}, D_{f2} = D_{f5} + \sigma_2 - \sigma_5. \quad (36d)$$

Analogous constraints are obtained for all other parameters. In total, TRS introduces 24 constraints on the 48 complex parameters of the general protocol. For the Hermitian protocol, this number reduces to exactly the 12 + 6 constraints for the 24 + 12 real and complex parameters that have been listed in Ref. [2].

For the restricted set of parameters in Eqs. (17)–(28) used in the present study, where $A_{r1} = -i\gamma_r$, $B_{r1} = J$ etc., we immediately identify the TRS constraints in Eq. (5) in the main text.

IV. DETUNINGS AND DISORDER

With the minimal set of parameters used for the non-Hermitian driving protocol in the present study, diagonal (i.e., on-site) terms in the Hamiltonian arise from losses and are purely imaginary, e.g., $-i\gamma_r, -i\gamma_b$ as listed in Eqs. (17)–(28). For Figs. 5, 6 we add real diagonal terms to the Hamiltonian that account for local potentials or fields. In a photonic waveguide system, these terms account for detunings that arise from variations in the optical path length of the different waveguides.

In the translational invariant situation, we have four parameters $\Delta_k, \dots, \Delta_k''' \in \mathbb{R}$ in each step $k = 1, \dots, 6$ of the driving protocol, corresponding to the four different types of sites. Graphically, we may write the detuning term as

$$\begin{pmatrix} \circ & \circ \\ \bullet & \bullet \end{pmatrix}_k = \begin{pmatrix} \Delta_k' & \Delta_k''' \\ \Delta_k & \Delta_k'' \end{pmatrix}. \quad (37)$$

As before, constraints are required to preserve TRS. Here, the symmetry operator S gives (cf. Fig. 3)

$$S \begin{pmatrix} \circ & \circ \\ \bullet & \bullet \end{pmatrix}_k S^{-1} = \begin{pmatrix} \circ & \circ \\ \bullet & \bullet \end{pmatrix}_{n-k+1}^{\text{TRS}}, \quad (38)$$

relating the detunings in steps $1 \leftrightarrow 6$, $2 \leftrightarrow 5$, and $3 \leftrightarrow 4$. Since the detunings are real, TRS^* and TRS^t give the same constraints.

For constant detunings $\Delta_k \equiv \Delta$ etc., TRS requires $\Delta = \Delta''$ and $\Delta' = \Delta'''$. In other words, TRS preserving detunings have the form

$$\begin{pmatrix} \circ & \circ \\ \bullet & \bullet \end{pmatrix} = \begin{pmatrix} \Delta' & \Delta' \\ \Delta & \Delta \end{pmatrix}, \quad (39)$$

with two remaining parameters $\Delta, \Delta' \in \mathbb{R}$. In Fig. 5 in the main text, constant detunings

$$\begin{pmatrix} \circ & \circ \\ \bullet & \bullet \end{pmatrix}_k \equiv \begin{pmatrix} -\Delta & \Delta \\ \Delta & -\Delta \end{pmatrix} \quad (40)$$

with $\Delta = 0.5$ are used to break TRS^t or TRS^* .

For the real-space propagation in panels (E), (F) in Fig. 6 in the main text, spatial and temporal disorder is included through randomly fluctuating detunings. For each site \mathbf{r} and step k the respective detuning parameter $\Delta_k^{\mathbf{r}}$ is independently drawn from a uniform probability distribution in the interval $[-\delta, \delta]$, here with $\delta = 0.2$. This gives the TRS-breaking disorder used in the upper half of panels (E), (F).

To preserve TRS, we enforce the constraints of Eq. (38) locally, for each pair of sites $(\circ \circ)$ or $(\bullet \bullet)$ that is mapped onto itself by the symmetry operator S , and for each period of the driving protocol. Apart from these constraints, the detunings still fluctuate randomly in space and time. In particular, they change with each step and period of the driving protocol. This gives the TRS-preserving disorder used in the lower half of panels (E), (F).

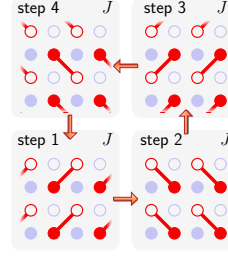


FIG. 2. Sketch of the four central steps of the driving protocol from Ref. [3], depicted in a way that highlights the connection to the TR symmetric driving protocol in the main text [2].

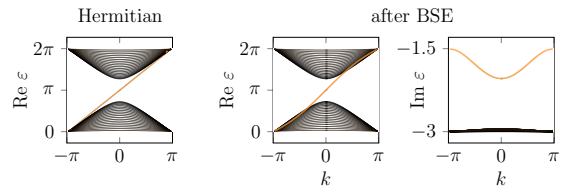


FIG. 3. Left panel: Anomalous Floquet topological phase in the driving protocol from Ref. [3] (with coupling $J = 1$). Central and right panel: Bulk and boundary states after BSE (with bulk losses $\gamma = 0.75$).

V. ADDITIONAL EXAMPLES FOR NON-HERMITIAN BOUNDARY STATE ENGINEERING

To demonstrate the concept of non-Hermitian boundary state engineering (BSE) in the main text, we choose the TR symmetric driving protocol because it combines experimental relevance with a number of novel transport scenarios. Being a general concept, BSE applies to any system that supports an anomalous Floquet topological phase. Here, we demonstrate the general applicability of BSE with three additional examples.

A. Driving protocols without fermionic time-reversal symmetry

The first example is the driving protocol from Ref. [3]. As the sketch in Fig. 2 illustrates, the TR symmetric protocol in the main text essentially comprises two interwoven copies of this protocol, with additional provisions to guarantee TRS and allow for coupling between the “red” and “blue” sublattice (for details of the construction, see Ref. [2]). The present protocol, which by itself does not possess (fermionic) TRS, features an anomalous Floquet topological phase with a single chiral boundary state (left panel in Fig. 3), instead of the counterpropagating states of the TR symmetric protocol (Fig. 3 in the main text).

To apply BSE to this protocol, we simply introduce

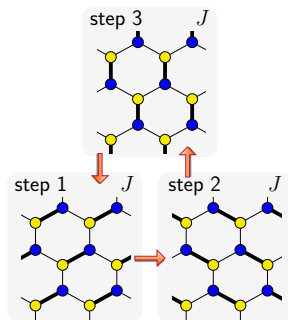


FIG. 4. Sketch of the three central steps of the driving protocol from Ref. [4] acting on a hexagonal lattice.

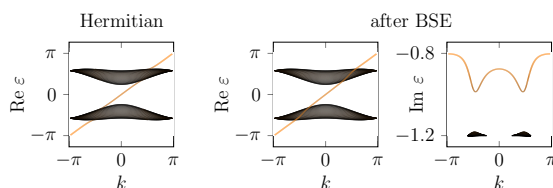


FIG. 5. Left panel: Anomalous Floquet topological phase in the driving protocol from Ref. [4] (with coupling $J = 1.3$). Central and right panel: Bulk and boundary states after BSE (with bulk losses $\gamma = 0.4$).

uniform losses in the bulk (γ), excluding the boundary sites (of course, more complex variants are possible). In accordance with the BSE concept, we can thus manipulate the imaginary quasienergies of the bulk and boundary states relative to each other, and let the boundary states detach from the bulk bands (central and right panel in Fig. 3). Here, however, with only a single chiral state per boundary, the potential of BSE is more limited in comparison to what is demonstrated in the main text: Still, boundary transport can be amplified or suppressed relative to bulk motion (Fig. 3 shows amplification), but manipulation of the direction of boundary transport as in Fig. 6 in the main text is no longer possible. This explains why we choose the more complicated TR symmetric driving protocol as our primary example.

As the second example, we consider the related driving protocol from Ref. [4], which takes place on a hexagonal instead of square lattice (see Fig. 4). BSE proceeds exactly as before, assigning uniform losses to the bulk (γ) but not the boundary sites, and allows for complete detachment of boundary from bulk states, or for any other suitable manipulation (see Fig. 5).

B. Driven Kane-Mele model

The third example is a periodically driven Kane-Mele model, which has been considered, e.g., in the context of

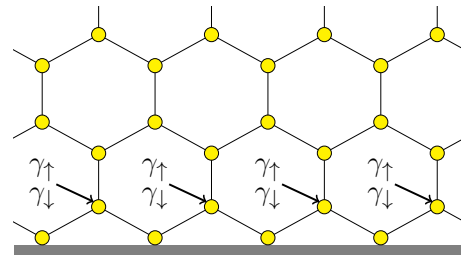


FIG. 6. Assignment of boundary losses for BSE in the driven Kane-Mele model, for a zigzag boundary of the hexagonal lattice. Spin-dependent losses $\gamma_\uparrow, \gamma_\downarrow$ are introduced on every second boundary site, as indicated by the arrows.

cold atomic systems [5]. This example does not belong to the category of driving protocols with discrete steps, but features a continuous time dependence. The Hamiltonian

$$H_{\text{KM}}(t) = (J_1 + J_2 \cos(\omega t)) \sum_{\langle ij \rangle} c_i^\dagger c_j + \lambda_\nu \sum_i \xi_i c_i^\dagger c_i + i(\lambda_{\text{SO},1} + \lambda_{\text{SO},2} \cos(\omega t)) \sum_{\langle\langle ij \rangle\rangle} \nu_{ij} c_i^\dagger \sigma_z c_j \quad (41)$$

extends the celebrated Kane-Mele model [6] with a periodic modulation of the hopping ($\propto J_2$) and spin-orbit coupling ($\propto \lambda_{\text{SO},2}$). The driven Kane-Mele model still possesses fermionic TRS, and supports an anomalous \mathbb{Z}_2 topological Floquet phase (left panel in Fig. 7). The anomalous nature of this phase is not obvious from the quasienergy plot in Fig. 7, but is corroborated by the vanishing \mathbb{Z}_2 invariant of the Floquet bands.

To apply BSE we introduce boundary losses, similar to the examples of the driving protocols. For a zigzag boundary, a minimal assignment is shown in Fig. 6, selecting sites with a large amplitude of the boundary state wave function. The boundary losses $\gamma_\uparrow, \gamma_\downarrow$ depend on the spin degree of freedom in the Kane-Mele model. To preserve TRS, it must $\gamma_\uparrow = \gamma_\downarrow = \gamma_t$ for TRS^t and $\gamma_\uparrow = -\gamma_\downarrow = \gamma_*$ for TRS^* .

The central and right panel in Fig. 7 show how BSE allows us to detach the boundary states from the bulk bands, in exact analogy to the result for the driving protocols. The topological preservation and the consequences of TRS could now be discussed along the lines established in the main text for the TR symmetric protocol. Note that after BSE, the real part of the quasienergy dispersion of the boundary states visibly crosses the bulk bands and connects at the $\pm\pi$ quasienergy (which nicely shows the anomalous nature of this phase). This apparent crossing, which we also observe in Fig. 5 in the main text, becomes possible since BSE separates the imaginary part of the boundary states and bulk bands. In the complex plane (recall Fig. 1 in the main text), the quasienergy dispersions are fully separated and do not cross.

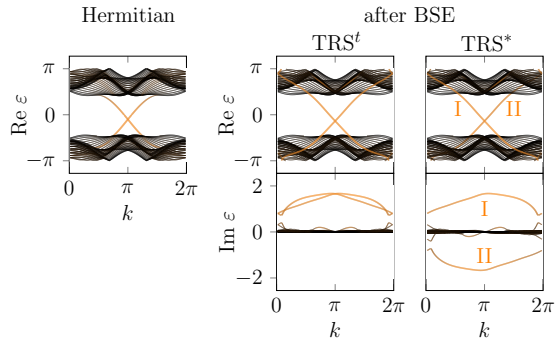


FIG. 7. Left panel: Anomalous Floquet topological \mathbb{Z}_2 -phase in the driven Kane-Mele model, with counterpropagating states on a zigzag boundary. Model parameters are $J_1 = J_2 = 1$, $\lambda_\nu = 0.3$, $\lambda_{\text{SO},1} = 0.25$, $\lambda_{\text{SO},2} = 0.5$, $T = 2\pi/\omega = 1.5$. Central and right panel: Bulk and boundary states after BSE, with TRS^t and TRS^* symmetry (for $\gamma_{t,*} = -1.25$, see text).

-
- [1] K. Kawabata, K. Shiozaki, M. Ueda, and M. Sato, [arXiv:1812.09133](https://arxiv.org/abs/1812.09133) (2018).
[2] B. Höckendorf, A. Alvermann, and H. Fehske, *Phys. Rev. B* **99**, 245102 (2019).
[3] M. S. Rudner, N. H. Lindner, E. Berg, and M. Levin, *Phys. Rev. X* **3**, 031005 (2013).
[4] T. Kitagawa, E. Berg, M. Rudner, and E. Demler, *Phys. Rev. B* **82**, 235114 (2010).
[5] Z. Yan, B. Li, X. Yang, and S. Wan, *Sci. Rep.* **5**, 16197 (2015).
[6] C. L. Kane and E. J. Mele, *Phys. Rev. Lett.* **95**, 146802 (2005).

Non-Hermitian Floquet Chains as Topological Charge Pumps

Bastian Höckendorf, Andreas Alvermann,* and Holger Fehske
Institut für Physik, Universität Greifswald, Felix-Hausdorff-Str. 6, 17489 Greifswald, Germany

We show that non-Hermiticity enables topological phases with unidirectional transport in one-dimensional Floquet chains. The topological signatures of these phases are non-contractible loops in the spectrum of the Floquet propagator that are separated by an imaginary gap. Such loops occur exclusively in non-Hermitian Floquet systems. We define the corresponding topological invariant as the winding number of the Floquet propagator relative to the imaginary gap. To relate topology to transport, we first introduce the concept of regularized dynamics of non-Hermitian chains, and then establish that the charge transferred over one period equals the winding number. We illustrate these theoretical findings with a Floquet chain that features a topological phase transition. In the non-trivial phase, this chain acts as a topological charge pump which, in fundamental difference to the situation for static or Hermitian chains, implements quantized unidirectional transport.

Quantum Hall systems [1, 2] and topological insulators [3, 4] are manifestations of a fundamental connection between topology and transport. Topological transport is characterized by two properties: It is quantized and robust [5, 6]. Ultimately, quantization and robustness are consequences of the bulk-boundary correspondence, which relates transport via chiral (or helical) boundary states to the topological properties of an insulating bulk [2, 3]. Importantly, topological transport requires boundary or surface states. One-dimensional systems can exhibit non-trivial topology [7, 8], but do not support robust transport without additional assumptions [9–11].

Recent research has shown that non-Hermiticity considerably extends this picture [12–16]. While the new non-Hermitian topological phases, with imaginary and point gaps in addition to the real gaps of the Hermitian case [17–19], have been classified for static systems, conclusive results on non-Hermitian topological transport are still rare. Even the status of a non-Hermitian bulk-boundary correspondence remains debatable, since boundary transport can be modified outside of the constraints the correspondence imposes on Hermitian systems [20–23]. Notably, non-Hermiticity is not a theoretical construct but appears naturally in, e.g., acoustics [24], electronics [25], or optics and photonics [26–30].

The subject of this work is topological transport in one-dimensional non-Hermitian chains. We show that, contrary to the Hermitian case, these chains can act as topological charge pumps if—but only if—we consider Floquet chains with a time-periodic Hamiltonian $H(t+T) = H(t)$. To obtain this result we identify a topological phase that occurs exclusively in non-Hermitian Floquet systems, and lies outside of the established classification [17–19] for static non-Hermitian systems.

An overview of the different topological scenarios for non-Hermitian chains is given in Fig. 1, using simple generic models as illustrative examples. We start with the standard non-Hermitian chain (St) with directional hopping [17, 25]. In all examples, the parameter J specifies the strength, the parameter γ the directionality of hopping. As a function of momentum k , the

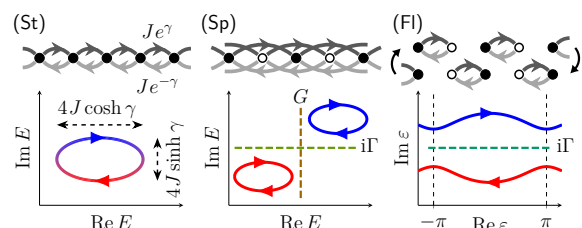


FIG. 1. Conceptual overview of the topological scenarios for non-Hermitian chains. Left column: The dispersion of a static chain (St) with directional nearest-neighbor hopping is an elliptical loop in the complex energy plane. Central column: By splitting the hopping spatially, the chain (Sp) supports two loops separated by a real (G) and imaginary ($i\Gamma$) line gap. Right column: By splitting the hopping temporally, the Floquet chain (Fl) supports loops that traverse the complex quasienergy zone with its $\varepsilon \mapsto \varepsilon + 2\pi$ periodicity.

spectrum $E(k) = J(e^{-ik+\gamma} + e^{ik-\gamma})$ of the Hamiltonian $H = J \sum_{n \in \mathbb{Z}} e^{\gamma} |n+1\rangle \langle n| + e^{-\gamma} |n\rangle \langle n+1|$ is an ellipse with real (imaginary) semi-axis $2J \cosh \gamma$ ($2J \sinh \gamma$). The elliptical loop $k \mapsto E(k)$ is contractible, and thus topologically trivial. Non-trivial topology can be enforced with a point gap inside of the loop [17–19], but a point gap will not provide us with a notion of topological transport. Splitting the hopping spatially, as in the chain (Sp), doubles the unit cell such that the spectrum contains two elliptical loops. These loops can be separated with a staggered potential $\pm \Delta \in \mathbb{C}$, leading to a real (G) or imaginary ($i\Gamma$) line gap, but remain contractible.

The situation changes qualitatively if we split the hopping temporally to obtain the Floquet chain (Fl). One period (length $T \equiv 1$) in this chain comprises two alternating directional hopping steps, with Hamiltonian $H^{(1)} = J \sum_{n \in \mathbb{Z}} e^{\gamma} |2n+1\rangle \langle 2n| + e^{-\gamma} |2n\rangle \langle 2n+1|$ in the first and $H^{(2)} = J \sum_{n \in \mathbb{Z}} e^{\gamma} |2n\rangle \langle 2n-1| + e^{-\gamma} |2n-1\rangle \langle 2n|$ in the second half-period. For a Floquet chain, we must consider quasienergies $\varepsilon(k)$ which, in contrast to the energies $E(k)$ of a static chain, are determined only up to multiples of 2π . The multi-valuedness allows for the two

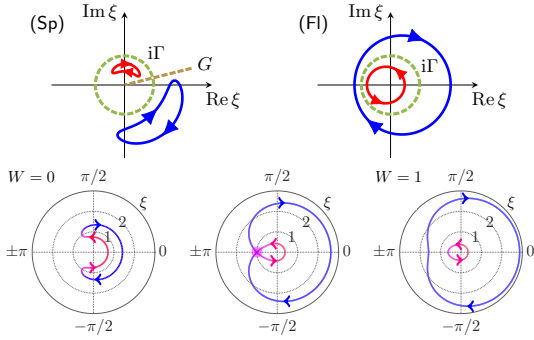


FIG. 2. Top row: Spectrum of the (Floquet) propagator for the chains (Sp), (Fl) from Fig. 1. Only the Floquet chain (Fl) can exhibit non-contractible loops with non-zero winding number. Bottom row: Topological phase transition in the Floquet chain (Fl) with $J = \pi/3$. The transition at $\gamma = \gamma_c \approx 0.55$ (central panel) separates the trivial ($\gamma = 0.2$, left panel) from the non-trivial ($\gamma = 0.6$, right panel) phase.

loops $k \mapsto \varepsilon_{1,2}(k)$ of the Floquet chain (Fl) in Fig. 1, which wrap around the quasienergy zone and thus are non-contractible. Note that the loops appear with opposite chirality $\varepsilon_{1,2}(k + 2\pi) = \varepsilon_{1,2}(k) \pm 2\pi$. We will now identify these non-contractible loops as the signatures of the topological phase of a non-Hermitian Floquet chain, and later also as the origin of topological transport.

To illustrate the specific topology of the one-dimensional non-Hermitian setting we consider the spectrum of the Floquet-Bloch propagator $\hat{U}(k) \equiv U(T, k)$ (see Fig. 2), which is the solution of the Schrödinger equation $i\partial_t U(t, k) = H(t, k)U(t, k)$ after one period $t = T$. The eigenvalues $\xi_m(k) = e^{-i\varepsilon_m(k)}$ of $\hat{U}(k)$ lie in the punctured complex plane $\mathbb{C} \setminus \{0\}$. Exclusion of the origin results from invertibility $U(t)^{-1} = U(-t)$ of the propagator, which also holds in the non-Hermitian setting.

Note that static chains can be embedded into the Floquet picture by choosing an artificial period T . Since the Floquet propagator of a static chain is $U = \exp(-iTH)$, quasienergies and energies are in one-to-one correspondence $\varepsilon_m(k) \equiv TE_m(k) \bmod 2\pi$ for sufficiently small T , as long as $\text{Re } E_m(k) \in (-\pi/T, \pi/T)$.

Fig. 2 provides us with three topological insights. First, non-contractible loops of a Floquet chain wind around the origin. Conceptually, the origin serves as a natural point gap for the Floquet propagator (but *not* for the Hamiltonian). Second, an imaginary gap $i\Gamma$ partitions the spectrum into an inner and outer part, separated by the circle $\phi \mapsto e^{-i\phi + \Gamma}$. A non-trivial imaginary gap requires a non-Hermitian Hamiltonian, where the spectrum of the propagator is not restricted to the unit circle by unitarity. Third, a real gap G , which corresponds to a radial line $r \mapsto re^{-iG}$ ($r \in \mathbb{R}_+$), prohibits non-contractible loops and implies trivial topology.

We here observe a fundamental difference between static and Floquet chains. For static chains (without symmetries), real and imaginary gaps are equivalent via multiplication $H \mapsto iH$ of the Hamiltonian by the imaginary unit i . For Floquet chains, real and imaginary gaps are strictly inequivalent. In consequence, non-Hermitian Floquet chains can support topological phases that do not appear in static chains.

Translating the topological concepts of Fig. 2 into an invariant, we are led to the \mathbb{Z} -valued winding number

$$W(\Gamma) = \frac{i}{2\pi} \sum_{e^\Gamma < |\xi_m|} \int_{-\pi}^{\pi} \xi_m(k)^{-1} \partial_k \xi_m(k) dk \quad (1)$$

$$= \frac{1}{2\pi} \sum_{\Gamma < \text{Im } \varepsilon_m} [\text{Re } \varepsilon_m(k)]_{k=-\pi}^{k=\pi}.$$

$W(\Gamma)$ is defined with respect to an imaginary gap $i\Gamma$. Only eigenvalues $\xi_m(k)$ outside (or quasienergies $\varepsilon_m(k)$ above) the gap contribute. A non-contractible loop in clockwise direction contributes with a positive integer. Note that we normalize the Brillouin zone to $k \in (-\pi, \pi]$, independently of the size of the unit cell.

The trivial imaginary gap $\Gamma = -\infty$, where the entire spectrum of U contributes, gives the total winding number $W(-\infty) = 0$. This result follows because the spectrum of U cannot move through the origin, such that non-contractible loops appear with opposite chirality.

Hermitian chains, where loops cannot be separated by imaginary gaps, as well as static non-Hermitian chains, which have only contractible loops, necessarily have zero winding number $W(\Gamma) = 0$ for all Γ .

In contrast, non-zero winding numbers are possible in non-Hermitian Floquet chains. The chain (Fl) features a topological phase transition at the critical value $\gamma_c = \text{arcosh}(1/\sin |J|)$ (see the supplemental material (SM) for a derivation from the eigenvalues of the Floquet propagator). As shown in Fig. 2, the spectrum below the transition ($|\gamma| < \gamma_c$) consists of a single loop with periodicity $k \mapsto k + 4\pi$. The winding number is zero. At the transition ($|\gamma| = \gamma_c$), the spectrum possesses an exceptional point at $k = 0$. Starting from the exceptional point, the spectrum splits into two loops above the transition ($|\gamma| > \gamma_c$). The loops occur with opposite chirality, and are separated by an imaginary gap $i\Gamma$ at $\Gamma = 0$. The associated winding number is non-zero, with $W(\Gamma) = 1$ for $\gamma > 0$ (as in Fig. 2) and $W(\Gamma) = -1$ for $\gamma < 0$.

Although the appearance of non-contractible loops in the spectrum of the propagator is reminiscent of the anomalous phase of two-dimensional Hermitian Floquet insulators [31–40], the topological phase observed here is specific to one-dimensional non-Hermitian Floquet chains. Formally, it requires a non-trivial imaginary gap. Physically, the non-contractible loops that appear here are not associated with boundary states as in the Floquet insulator, but with the spectrum of the infinite chain.

The second major aspect of non-Hermitian chains is transport, which can be quantified with the charge

$$C(n) = \text{tr}_Z(U^\dagger[P_n, U]) \quad (2)$$

transferred over one period through a fictitious layer between sites $n - 1$ and n from the left to the right of the chain (see the SM for a derivation). Here, P_n is the projection onto sites $i \geq n$, that is $P_n|i\rangle = |i\rangle$ for $i \geq n$ and $P_n|i\rangle = 0$ for $i < n$. Eq. (2) generalizes standard expressions (e.g., [41]) for $C(n)$ to the non-Hermitian setting.

Note that the transferred charge can be measured by real-space propagation of wave packets, which could be the method of choice, e.g., in photonic waveguide systems. In wave packet propagation, the transferred charge gives the average propagation distance, weighted by the norm of the propagated wave packets, which can deviate from unity in the non-Hermitian setting (see the SM).

For a Hermitian chain, evaluation of the trace shows that the total charge transfer is $C(n) = 0$. This is only true in dimension one: The analogous expression in two dimensions gives the charge transferred by chiral boundary states, which, of course, can be non-zero [41, 42].

For a non-Hermitian chain, whether static or Floquet, $C(n) \neq 0$ becomes possible (see Fig. 3). However, allowing for non-Hermiticity involves intrinsic complications for the physical interpretation of (topological) transport. First, current is no longer conserved but a charge $c(n) = \langle n|[U, U^\dagger]|n\rangle$ can accumulate at site n . To get rid of the resulting site dependence of $C(n)$, we average the transferred charge $\bar{C} = (1/L) \sum_{n=0}^{L-1} C(n)$ over a unit cell of L sites of a translationally invariant chain.

We can now derive the momentum space expression $\bar{C} = \frac{i}{2\pi} \int_{-\pi}^{\pi} \text{tr}_L(\hat{U}^\dagger(k) \partial_k \hat{U}(k)) dk$, where the trace tr_L runs over the unit cell (see the SM). The second complication in comparison to the Hermitian setting is that this expression depends explicitly on the eigenvectors of $\hat{U}(k)$, and is not invariant under unitary transformations. This is not an artefact of the derivation, but a fundamental consequence of the fact that non-Hermiticity allows for non-orthogonal eigenvectors of $\hat{U}(k)$.

If, however, the eigenvectors of $\hat{U}(k)$ are orthogonal (a requirement equivalent to the normality condition $[\hat{U}(k), \hat{U}(k)^\dagger] = 0$ known from linear algebra [43]),

$$\bar{C} \stackrel{(\text{orth})}{=} \frac{i}{2\pi} \sum_{m=1}^L \int_{-\pi}^{\pi} \xi_m(k)^* \partial_k \xi_m(k) dk \quad (3)$$

is given entirely in terms of the eigenvalues $\xi_m(k)$ of $\hat{U}(k)$. This equation will allow us to proceed towards a formulation of non-Hermitian topological transport. Note that it has a geometric interpretation as the area (with orientation) enclosed by the eigenvalue loops $k \mapsto \xi_m(k)$.

Fig. 3 shows that, without further provisions, the transferred charge \bar{C} does not reveal much about the possible topological nature of transport in the chains

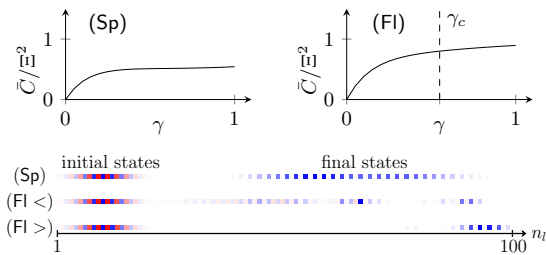


FIG. 3. Top row: Transferred charge \bar{C} in the chains (Sp), (Fl), as a function of γ (with $J = \pi/3, \Delta = 3i$). The curve is normalized with the spectral radius $\Xi = \max_\xi |\xi|$. Hermiticity (at $\gamma = 0$) enforces $\bar{C} = 0$. Bottom row: Probing transport with wave packet propagation in the chains (Sp), (Fl) (with $\gamma = 0.8, 0.09, 1.5$ from top to bottom, and $n_p = 40$ periods).

(Sp), (Fl). However, probing transport by means of wave packet propagation we observe a significant difference: While wave packets usually spread out during propagation, they propagate almost without spreading in the Floquet chain (Fl) above the topological phase transition (row “(Fl >)” in Fig. 3), where $\bar{C} \rightarrow 1$.

To strictly relate transport and topology, we have to introduce the concept of regularized dynamics (RD) of non-Hermitian chains. For RD we demand that (i) the dominant eigenvalues of the Floquet propagator have modulus one, (ii) the modulus of all other eigenvalues is infinitesimally close to zero, and (iii) the eigenvectors are mutually orthogonal. Then, Eq. (3) can be used. Since $\xi^* = \xi^{-1}$ for $|\xi| = 1$, this equation reduces to Eq. (1) for the winding number, if $W(\Gamma)$ is computed for an imaginary gap $-\infty < \Gamma < 0$, that separates the eigenvalues with modulus zero ($\text{Im } \varepsilon \rightarrow -\infty$) from those with modulus one ($\text{Im } \varepsilon = 0$). We thus obtain the fundamental relation

$$\bar{C} \stackrel{(\text{RD})}{=} W(\Gamma) \quad (4)$$

between transport and topology in non-Hermitian chains with RD. In particular, the transferred charge \bar{C} is quantized, and vanishes in a static chain where $W(\Gamma) = 0$.

It remains to assess whether RD of non-Hermitian chains is an artificial construction or a relevant concept. First, it should not be surprising that some assumptions are required for a quantitative relation between transport and topology [11]—the same being true also for Hermitian Floquet insulators where a condition $\hat{U}(k) \equiv 1$ is imposed [32]. The RD of non-Hermitian Floquet chains differs from previous regularization concepts in so far as (i) RD applies to the Floquet propagator, not to a static Hamiltonian [19], (ii) RD requires an imaginary gap $i\Gamma$ instead of a real gap of a unitary Floquet propagator [32].

For a non-Hermitian chain, RD can be achieved either (i) through regularization of the propagator, or (ii) as a physical limit in parameter regimes with strong damping. Regularization of the propagator corresponds to a

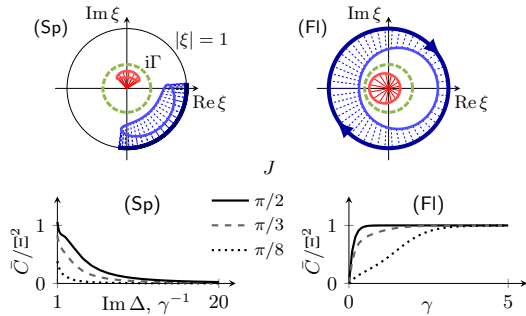


FIG. 4. Top row: In the RD limit the spectrum of the propagator outside (inside) of the imaginary gap $i\Gamma$ moves to the unit circle (origin). Bottom row: Transferred charge \bar{C} , for various hopping $J = \pi/2, \pi/3, \pi/8$, as one approaches the RD limit in the static chain (Sp) (for $\text{Im } \Delta, \gamma^{-1} \rightarrow \infty$) or the Floquet chain (Fl) (for $\gamma \rightarrow \infty$). In this limit, $\bar{C} = W(\Gamma)$.

continuous deformation of $\hat{U}(k)$ such that the eigenvalues $\xi_m(k)$ move in- or outwards to the origin or the unit circle, as illustrated in Fig. 4. As a technical complication of the non-Hermitian setting, also the eigenvectors of the propagator have to be deformed. Regarding topological properties, details of the regularization procedure are not relevant, as long as the imaginary gap $i\Gamma$ stays open during the deformation such that the winding number does not change (two techniques are described in the SM).

As a physical limit, RD is realized in parameter regimes where strong damping suppresses some eigenvalues of the Floquet propagator, while the dominant states incur uniform loss or gain. We can drop a factor $\Xi = \max_{\xi} |\xi|$, in order to normalize $\hat{U}(k)$ with a uniform imaginary shift of H , such that the dominant states have zero loss. For the static chain (Sp), RD is achieved for example in the limit $\gamma \rightarrow 0, \text{Im } \Delta \rightarrow \infty$ (shown in Fig. 4). With the interpretation of Eq. (3) as an area it is evident that $\bar{C} \rightarrow 0$ in the RD limit, in accordance with the fundamental relation (4). Note that absence of transport is compatible with a point gap, which can enforce non-contractible eigenvalue loops but does not prevent minimization of the enclosed area by continuous deformation.

For the Floquet chain (Fl), RD is realized in the limit $\gamma \rightarrow 0$, or $\gamma \rightarrow \pm\infty$ (shown in Fig. 4). For $\gamma \rightarrow 0$, we end up below the topological phase transition, with a trivial gap $\Gamma = -\infty$. This results in a unitary propagator without directed transport ($\bar{C} = 0 = W(\Gamma)$). For $\gamma \rightarrow \pm\infty$, we end up above the topological phase transition. One non-contractible eigenvalue loop $k \mapsto e^{\mp ik}$ survives on the unit circle. This eigenvalue loop encloses the circle area $\pm 2\pi$, such that Eq. (3) gives $\bar{C} = \pm 1 = W(\Gamma)$ in accordance with the fundamental relation (4).

While quantization of transport in the RD limit follows from Eq. (4), robustness occurs in two ways. First, we

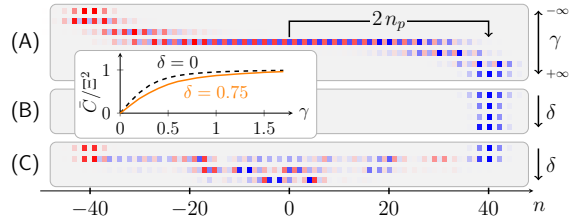


FIG. 5. The Floquet chain (Fl) as a charge pump: Shown is a wave packet, centered initially at site $n = 0$, after propagation over $n_p = 20$ periods. Panel (A): Propagation for $\gamma = -\infty, -1, -0.25, 0, 0.25, 1, \infty$ from top to bottom (with $J = \pi/3$). Panel (B): Propagation in the RD limit $\gamma \rightarrow \infty$, for disorder $\delta = 0, 0.25, 0.5, 0.75$ from top to bottom (with $J = \pi/3$). Inset: Charge \bar{C} transferred per period. Panel (C): Propagation at $J = \pi/2, \gamma = 0$, with δ as in panel (B).

note that \bar{C} does not depend on the remaining free model parameters (in Fig. 4, the hopping J). Importantly, RD does not require fine-tuning of the system to a point in parameter space, but is realized on a parameter manifold where transport and topology are invariant.

Second, Fig. (5) probes the robustness of transport in the chain (Fl) via wave packet propagation. Panel (A) shows propagation in the translationally invariant chain. In the RD limit $\gamma \rightarrow \pm\infty$, half of the wave packet (on either blue or red sites) survives propagation. Over n_p periods, the wave packet moves without spreading by $2\bar{C}n_p$ sites, with $\bar{C} = \pm 1$. Disorder in panel (B), with hoppings chosen randomly per bond from the interval $[J(1-\delta), J(1+\delta)]$, does *not* affect transport in the RD limit, which is thus revealed to be truly robust. Note that the wave packets depends on disorder even for $\gamma \rightarrow \infty$, but the averaged charge \bar{C} does not (see inset). Quite differently, panel (C) shows that fine-tuning to ‘perfect coupling’ ($J = \pi/2, \gamma = 0$), with distinct propagation in the ordered chain, does not survive addition of disorder.

In conclusion, we present a theory of topology and transport in non-Hermitian chains. While transport can occur in any non-Hermitian chain, only Floquet chains allow for non-trivial topology and can act as topological charge pumps with quantized and robust transport. This observation implies that non-Hermitian Floquet systems possess topological phases with interesting transport or dynamical properties that are not realized in static or Hermitian systems. Therefore, future research on non-Hermitian systems should focus increasingly on the relation between topology and transport. Certainly, further investigation of situations with disorder, defects, or interfaces is required especially with a view towards the experiment. Already the present theory opens up new avenues for experiments on non-Hermitian topological systems using, e.g., photonic waveguides or electric circuits to implement Floquet instead of static non-Hermitian chains [25]. Very recent evidence for the relevance of

the theoretical concepts developed here is provided by the observation of quantized non-Hermitian transport in a non-adiabatic Floquet chain realized with plasmonic waveguide arrays [44].

* alvermann@physik.uni-greifswald.de; Corresponding author

- [1] K. v. Klitzing, G. Dorda, and M. Pepper, *Phys. Rev. Lett.* **45**, 494 (1980).
- [2] D. J. Thouless, M. Kohmoto, M. P. Nightingale, and M. den Nijs, *Phys. Rev. Lett.* **49**, 405 (1982).
- [3] C. L. Kane and E. J. Mele, *Phys. Rev. Lett.* **95**, 146802 (2005).
- [4] M. König, S. Wiedmann, C. Brüne, A. Roth, H. Buhmann, L. W. Molenkamp, X.-L. Qi, and S.-C. Zhang, *Science* **318**, 766 (2007).
- [5] M. Z. Hasan and C. L. Kane, *Rev. Mod. Phys.* **82**, 3045 (2010).
- [6] X.-L. Qi and S.-C. Zhang, *Rev. Mod. Phys.* **83**, 1057 (2011).
- [7] W. P. Su, J. R. Schrieffer, and A. J. Heeger, *Phys. Rev. Lett.* **42**, 1698 (1979).
- [8] A. Y. Kitaev, *Phys.-Usp.* **44**, 131 (2001).
- [9] D. J. Thouless, *Phys. Rev. B* **27**, 6083 (1983).
- [10] D. Xiao, M.-C. Chang, and Q. Niu, *Rev. Mod. Phys.* **82**, 1959 (2010).
- [11] L. Privitera, A. Russomanno, R. Citro, and G. E. Santoro, *Phys. Rev. Lett.* **120**, 106601 (2018).
- [12] H. Shen, B. Zhen, and L. Fu, *Phys. Rev. Lett.* **120**, 146402 (2018).
- [13] Z. Lin, H. Ramezani, T. Eichelkraut, T. Kottos, H. Cao, and D. N. Christodoulides, *Phys. Rev. Lett.* **106**, 213901 (2011).
- [14] G. Harari, M. A. Bandres, Y. Lumer, M. C. Rechtsman, Y. D. Chong, M. Khajavikhan, D. N. Christodoulides, and M. Segev, *Science* **359**, eaar4003 (2018).
- [15] J. Y. Lee, J. Ahn, H. Zhou, and A. Vishwanath, *Phys. Rev. Lett.* **123**, 206404 (2019).
- [16] D. S. Borgnia, A. J. Kruchkov, and R.-J. Slager, *Phys. Rev. Lett.* **124**, 056802 (2020).
- [17] Z. Gong, Y. Ashida, K. Kawabata, K. Takasan, S. Higashikawa, and M. Ueda, *Phys. Rev. X* **8**, 031079 (2018).
- [18] H. Zhou and J. Y. Lee, *Phys. Rev. B* **99**, 235112 (2019).
- [19] K. Kawabata, K. Shiozaki, M. Ueda, and M. Sato, *Phys. Rev. X* **9**, 041015 (2019).
- [20] S. Yao and Z. Wang, *Phys. Rev. Lett.* **121**, 086803 (2018).
- [21] S. Yao, F. Song, and Z. Wang, *Phys. Rev. Lett.* **121**, 136802 (2018).
- [22] B. Höckendorf, A. Alvermann, and H. Fehske, *Phys. Rev. Lett.* **123**, 190403 (2019).
- [23] C. H. Lee and R. Thomale, *Phys. Rev. B* **99**, 201103 (2019).
- [24] W. Zhu, X. Fang, D. Li, Y. Sun, Y. Li, Y. Jing, and H. Chen, *Phys. Rev. Lett.* **121**, 124501 (2018).
- [25] T. Helbig, T. Hofmann, S. Imhof, M. Abdelghany, T. Kiessling, L. W. Molenkamp, C. H. Lee, A. Szameit, M. Greiter, and R. Thomale, [arXiv:1907.11562](https://arxiv.org/abs/1907.11562) (2019).
- [26] T. Ozawa, H. M. Price, A. Amo, N. Goldman, M. Hafezi, L. Lu, M. C. Rechtsman, D. Schuster, J. Simon, O. Zeitlinger, and I. Carusotto, *Rev. Mod. Phys.* **91**, 015006 (2019).
- [27] A. Regensburger, C. Bersch, M.-A. Miri, G. Onishchukov, D. N. Christodoulides, and U. Peschel, *Nature* **488**, 167 (2012).
- [28] S. Weimann, M. Kremer, Y. Plotnik, Y. Lumer, S. Nolte, K. G. Makris, M. Segev, M. C. Rechtsman, and A. Szameit, *Nat. Mat.* **16**, 433 (2016).
- [29] J. M. Zeuner, M. C. Rechtsman, Y. Plotnik, Y. Lumer, S. Nolte, M. S. Rudner, M. Segev, and A. Szameit, *Phys. Rev. Lett.* **115**, 040402 (2015).
- [30] M. A. Bandres, S. Wittek, G. Harari, M. Parto, J. Ren, M. Segev, D. N. Christodoulides, and M. Khajavikhan, *Science* **359**, eaar4005 (2018).
- [31] T. Kitagawa, E. Berg, M. Rudner, and E. Demler, *Phys. Rev. B* **82**, 235114 (2010).
- [32] M. S. Rudner, N. H. Lindner, E. Berg, and M. Levin, *Phys. Rev. X* **3**, 031005 (2013).
- [33] F. Nathan and M. S. Rudner, *New J. Phys.* **17**, 125014 (2015).
- [34] B. Höckendorf, A. Alvermann, and H. Fehske, *J. Phys. A* **50**, 295301 (2017).
- [35] B. Höckendorf, A. Alvermann, and H. Fehske, *Phys. Rev. B* **97**, 045140 (2018).
- [36] B. Höckendorf, A. Alvermann, and H. Fehske, *Phys. Rev. B* **99**, 245102 (2019).
- [37] L. J. Maczewsky, J. M. Zeuner, S. Nolte, and A. Szameit, *Nat. Comm.* **8**, 13756 (2017).
- [38] S. Mukherjee, A. Spracklen, M. Valiente, E. Andersson, P. Öhberg, N. Goldman, and R. R. Thomson, *Nat. Comm.* **8**, 13918 (2017).
- [39] Y.-G. Peng, C.-Z. Qin, D.-G. Zhao, Y.-X. Shen, X.-Y. Xu, M. Bao, H. Jia, and X.-F. Zhu, *Nat. Comm.* **7**, 13368 (2016).
- [40] L. J. Maczewsky, B. Höckendorf, M. Kremer, T. Biesenhal, M. Heinrich, A. Alvermann, H. Fehske, and A. Szameit, [arXiv:1812.07930](https://arxiv.org/abs/1812.07930) (2018).
- [41] G. M. Graf and C. Tauber, *Ann. Henri Poincaré* **19**, 709 (2018).
- [42] C. Tauber, *Phys. Rev. B* **97**, 195312 (2018).
- [43] G. H. Golub and C. F. Van Loan, *Matrix Computations*, 4th ed. (The Johns Hopkins University Press, 2013).
- [44] Z. Fedorova, H. Qiu, S. Linden, and J. Kroha, [arXiv:1911.03770](https://arxiv.org/abs/1911.03770) (2019).

**Supplemental material for:
Non-Hermitian Floquet Chains as Topological Charge Pumps**

Bastian Höckendorf, Andreas Alvermann, and Holger Fehske
Institut für Physik, Universität Greifswald, Felix-Hausdorff-Str. 6, 17489 Greifswald, Germany

The supplemental material (i) derives different expressions for the transferred charge $C(n)$ and \bar{C} and explains the computation by means of wave packet propagation, (ii) computes the transferred charge in the three chains (St), (Sp), (Fl) and the topological phase transition in the Floquet chain (Fl), and (iii) introduces regularization procedures for the propagator.

THE TRANSFERRED CHARGE

The transferred charge $C(n)$ measures the net amount of charge moving from the left part (sites $i < n$) to the right part (sites $i \geq n$) of a chain.

A wave function initially localized at site $|i\rangle$ evolves into $|\Psi_i\rangle = U|i\rangle$, where the propagator U is given in real space, e.g., as the Floquet propagator $U(T)$. For a wave function starting in the left part of the chain, the amount of charge transferred to the right is $\sum_{j \geq n} |\langle j|\Psi_i\rangle|^2$. For a wave function starting in the right part of the chain, the amount of charge transferred to the left is $\sum_{j < n} |\langle j|\Psi_i\rangle|^2$, and has to be counted with a minus sign. Therefore, the contribution of $|\Psi_i\rangle$ to $C(n)$ is

$$C(n)|_i = \begin{cases} \sum_{j \geq n} |\langle j|\Psi_i\rangle|^2 & \text{for } i < n, \\ -\sum_{j < n} |\langle j|\Psi_i\rangle|^2 & \text{for } i \geq n. \end{cases} \quad (1)$$

Summing over all initial sites gives the transferred charge

$$\begin{aligned} C(n) &= \sum_{i \in \mathbb{Z}} C(n)|_i = \sum_{\substack{i < n \\ j \geq n}} |\langle j|\Psi_i\rangle|^2 - \sum_{\substack{i \geq n \\ j < n}} |\langle j|\Psi_i\rangle|^2 \\ &= \sum_{i \in \mathbb{Z}} \langle i|U^\dagger P_n U (1 - P_n) - U^\dagger (1 - P_n) U P_n|i\rangle \\ &= \sum_{i \in \mathbb{Z}} \langle i|U^\dagger P_n U - U^\dagger U P_n|i\rangle \\ &= \text{tr}_{\mathbb{Z}} (U^\dagger [P_n, U]), \end{aligned} \quad (2)$$

where the projection P_n gives $P_n|i\rangle = \Theta(i - n)|i\rangle$ with $\Theta(x) = 1$ for $x \geq 0$, $\Theta(x) = 0$ for $x < 0$. The trace is $\text{tr}_{\mathbb{Z}} A = \sum_{i \in \mathbb{Z}} \langle i|A|i\rangle$. This gives Eq. (2) in the main text.

Eq. (2) generalizes the expressions for the Hermitian case (see, e.g., Eq. (3.3) in Ref. [1]) to the non-Hermitian setting. Note that the operator $U^\dagger [P_n, U]$ in the trace is not Hermitian, but $C(n) \in \mathbb{R}$ follows from the first line.

Similarly, we find the charge accumulated at site n as

$$\begin{aligned} c(n) &= \sum_{\substack{i \in \mathbb{Z} \\ i \neq n}} |\langle n|\Psi_i\rangle|^2 - \sum_{\substack{i \in \mathbb{Z} \\ i \neq n}} |\langle i|\Psi_n\rangle|^2 \\ &= \langle n|[U, U^\dagger]|n\rangle, \end{aligned} \quad (3)$$

the difference of charge moving to site n and charge moving away from site n .

The accumulated charge gives the difference between $C(n)$ at different sites. We have, for $n \geq m$,

$$\begin{aligned} C(m) - C(n) &= \sum_{i \in \mathbb{Z}} C(m)|_i - C(n)|_i \\ &= \sum_{\substack{i < m \\ j \geq m}} |\langle j|\Psi_i\rangle|^2 - \sum_{\substack{i \geq m \\ j < m}} |\langle j|\Psi_i\rangle|^2 \\ &\quad - \sum_{\substack{i < n \\ j \geq n}} |\langle j|\Psi_i\rangle|^2 + \sum_{\substack{i \geq n \\ j < n}} |\langle j|\Psi_i\rangle|^2 \\ &= \sum_{l=m}^{n-1} c(l), \end{aligned} \quad (4)$$

which expresses the conservation of charge, even in the non-Hermitian setting. Hermiticity or regularized dynamics (RD), where $[U, U^\dagger] = 0$, implies $c(n) = 0$ and thus $C(m) = C(n)$.

The translationally invariant case

Assume that H , and thus also U , is invariant under translations by L sites, that is $U_{m+L, n+L} = U_{mn}$ for the matrix elements $U_{mn} = \langle m|U|n\rangle$ of the propagator. Translational invariance implies $C(n)|_i = C(n+L)|_{i+L}$, in the notation of Eq. (1).

The charge \bar{C} , averaged over a unit cell, is

$$\begin{aligned} \bar{C} &= \frac{1}{L} \sum_{n=0}^{L-1} C(n) = \frac{1}{L} \sum_{n=0}^{L-1} \sum_{i \in \mathbb{Z}} C(n)|_i \\ &= \frac{1}{L} \sum_{n=0}^{L-1} \sum_{i=0}^{L-1} \sum_{m \in \mathbb{Z}} C(n)|_{i+mL} \\ &= \frac{1}{L} \sum_{n=0}^{L-1} \sum_{i=0}^{L-1} \sum_{m \in \mathbb{Z}} C(n - mL)|_i \\ &= \frac{1}{L} \sum_{i=0}^{L-1} \sum_{n \in \mathbb{Z}} C(n)|_i = \frac{1}{L} \sum_{i=0}^{L-1} \bar{C}|_i, \end{aligned} \quad (5)$$

where we replace $i \rightarrow i + mL$ in line two, $n - mL \rightarrow n$ in line four, and use translational invariance in line three. In the last line, we introduce the abbreviation

$$\bar{C}|_i = \sum_{n \in \mathbb{Z}} C(n)|_i. \quad (6)$$

Note that translational invariance has allowed us to exchange the summation $0 \leq n < L, i \in \mathbb{Z}$ with the summation $n \in \mathbb{Z}, 0 \leq i < L$.

Inserting Eq. (1) into Eq. (6) and rearranging summations we get

$$\begin{aligned} \bar{C}|_i &= \sum_{n>i} \sum_{j \geq n} \langle j|\Psi_i\rangle|^2 - \sum_{n \leq i} \sum_{j < n} \langle j|\Psi_i\rangle|^2 \\ &= \sum_{j>i} (j-i) \langle j|\Psi_i\rangle|^2 - \sum_{j<i} (i-j) \langle j|\Psi_i\rangle|^2 \\ &= \sum_{j \in \mathbb{Z}} (j-i) |\langle j|\Psi_i\rangle|^2 = \langle \Psi_i|\hat{x} - i|\Psi_i\rangle, \end{aligned} \quad (7)$$

where $\hat{x} = \sum_{j \in \mathbb{Z}} j|j\rangle\langle j|$ is the position operator. In other words, $\bar{C}|_i$ is the propagation distance of a wave packet initially localized at site i . Therefore, \bar{C} is the average propagation distance.

Note that in the non-Hermitian setting the norm of a wave function is not conserved, such that the propagation distance in Eq. (7) is weighted by different $\langle \Psi_i|\Psi_i\rangle$.

Momentum space expressions

We define the Fourier transform as

$$\hat{U}_{mn}(k) = \sum_{l \in \mathbb{Z}} e^{-i(k/L)(m+lL-n)} U_{m+lL,n}, \quad (8)$$

which is an $L \times L$ matrix with indices $m, n \in \mathbb{L} := \{0, \dots, L-1\}$, parametrized by momentum k . The inverse Fourier transform is

$$U_{mn} = \frac{1}{2\pi} \int_{-\pi}^{\pi} e^{i(k/L)(m-n)} \hat{U}_{[m]_L, [n]_L}(k) dk, \quad (9)$$

where $[m]_L, [n]_L \in \mathbb{L}$ denotes the remainder after division by L .

A standard Fourier computation with Eq. (9) gives

$$\begin{aligned} \langle n|U^\dagger(\hat{x} - n)U|n\rangle &= \\ \frac{iL}{2\pi} \sum_{m=0}^{L-1} \int_{-\pi}^{\pi} \hat{U}_{[n]_L, m}^\dagger(k) \partial_k \hat{U}_{m, [n]_L}(k) dk \end{aligned} \quad (10)$$

for the interplay between the Fourier transform and the position operator \hat{x} .

Using this expression together with Eqs. (5), (7) immediately gives

$$\bar{C} = \frac{i}{2\pi} \int_{-\pi}^{\pi} \text{tr}_{\mathbb{L}} \left(\hat{U}^\dagger(k) \partial_k \hat{U}(k) \right) dk. \quad (11)$$

Here, $\text{tr}_{\mathbb{L}} A = \sum_{n=0}^{L-1} A_{nn}$ sums over the indices of the Fourier transform, which correspond to the L sites of a unit cell. This is the expression given on page 3 in the main text.

Note that the Fourier transform in Eq. (8) is 2π -periodic only up to phase factors. We have $\hat{U}(k+2\pi) = G(2\pi)\hat{U}(k)G^\dagger(2\pi)$, where $G(k)$ is a diagonal unitary matrix with entries $G_{nn} = \exp(-ikn/L)$. By this relation, the spectrum of $\hat{U}(k)$ is 2π -periodic. Only 2π -periodicity of the spectrum, not of the Fourier transform, is required in the main text.

The alternative definition

$$\hat{U}_{mn}^{(\text{alt})}(k) = \sum_{l \in \mathbb{Z}} e^{-ikl} U_{m+lL,n}, \quad (12)$$

where the factor e^{-ikl} is constant within a unit cell, is 2π -periodic. The two Fourier transforms (8), (12) are connected by the unitary transformation $\tilde{U}(k) = G(k)\hat{U}^{(\text{alt})}(k)G(k)^\dagger$, such that the spectrum of the Floquet-Bloch propagator is independent of the choice of the Fourier transform. Use of $\hat{U}_{mn}^{(\text{alt})}(k)$ would require replacing Eq. (11) by a more complicated expression that includes the matrix $G(k)$. This is why we prefer to work with $\hat{U}_{mn}(k)$.

We stress that, in contrast to the Hermitian case, Eq. (11) is *not* invariant under k -dependent unitary transformations. If we replace $\hat{U}(k)$ by $Q(k)\hat{U}(k)Q(k)^\dagger$, Eq. (11) changes into

$$\begin{aligned} \bar{C} &= \frac{i}{2\pi} \int_{-\pi}^{\pi} \text{tr}_{\mathbb{L}} \left(\hat{U}^\dagger(k) \partial_k \hat{U}(k) \right. \\ &\quad \left. + [\hat{U}(k), \hat{U}(k)^\dagger] Q(k)^\dagger \partial_k Q(k) \right) \end{aligned} \quad (13)$$

(we have used $(\partial_k Q(k)^\dagger)Q(k) = -Q(k)^\dagger \partial_k Q(k)$ for unitary $Q(k)$). Through the additional term in the second line, \bar{C} depends explicitly on the eigenvectors of $\hat{U}(k)$. Therefore, we cannot diagonalize $\hat{U}(k)$ and express Eq. (11) entirely in terms of its eigenvalues. This complication is intrinsic to the non-Hermitian setting.

If, however, $[\hat{U}(k), \hat{U}(k)^\dagger] = 0$, the additional term drops out of Eq. (13). This condition is known from linear algebra [2], where it defines a normal matrix. Under this condition we can diagonalize the propagator with a unitary transformation as in the Hermitian case, write $\hat{U}(k) = Q(k)D(k)Q(k)^\dagger$ with a diagonal matrix $D(k)$ that contains the eigenvalues $\xi_1(k), \dots, \xi_L(k)$ of $\hat{U}(k)$, and arrive at

$$\bar{C} = \frac{i}{2\pi} \sum_{m=1}^L \int_{-\pi}^{\pi} \xi_m(k)^* \partial_k \xi_m(k) dk. \quad (14)$$

This is Eq. (3) in the main text. It does not depend on the choice of the Fourier transform.

Since $\bar{C} \in \mathbb{R}$, we can rewrite this equation as

$$\bar{C} = -\frac{1}{2\pi} \sum_{m=1}^L \int_{-\pi}^{\pi} \text{Im} (\xi_m(k)^* \partial_k \xi_m(k)) dk, \quad (15)$$

which suggests the geometric interpretation that the transferred charge \bar{C} is the area in the ξ -plane enclosed by the eigenvalue loops $k \mapsto \xi_m(k)$. The sign of \bar{C} is such that a clockwise loop gives a positive contribution.

Regularized dynamics

The transferred charge \bar{C} is not invariant under (imaginary) shifts of the Hamiltonian $H \mapsto H + s$, where $U(T) \mapsto e^{Ts}U(T)$, hence $\bar{C} \mapsto \bar{C} + e^{2T \text{Im } s}$. Therefore, it is useful to consider the normalized transferred charge \bar{C}/Ξ^2 , with an appropriate normalization factor Ξ . We set $\Xi = \max_{\xi} |\xi|$ to the maximal modulus of the eigenvalues ξ of U , i.e., the spectral radius (normalization for disordered chains is addressed in the next subsection). In this way, the dominant eigenvalue of the normalized propagator U/Ξ has modulus one. This is the normalization chosen in the main text to define the RD limit, where the ‘surviving’ loops should have zero gain or loss.

RD as defined in the main text requires that the eigenvectors of U (or $\hat{U}(k)$) are orthogonal and the eigenvalues fulfill $|\xi|^2 = |\xi|$, i.e., have modulus zero or one. These conditions are equivalent to the statement that U is a normal operator (orthogonal eigenvectors) and a partial isometry ($|\xi| \in \{0, 1\}$), that is, $P = U^\dagger U = U U^\dagger$ and P is a projection ($P^2 = P$). This generalizes the Hermitian case, where U is unitary and $P = \mathbb{1}$. Note that the statement $(U U^\dagger)^2 = U U^\dagger$ is equivalent to $U^\dagger U U^\dagger = U^\dagger$.

How the RD conditions allow one to relate transport and topology is explored in the main text. The RD conditions can also be motivated if we consider the transferred charge as a function $\bar{C}(t)$ of time, or as a function $\bar{C}(n_p)$ of periods n_p in a Floquet chain, and ask for the persistent current given by the limit $\lim_{t \rightarrow \infty} \bar{C}(t)/t$ or $\lim_{n_p \rightarrow \infty} \bar{C}(n_p)/n_p$. For a (topological) charge pump the persistent current should be non-zero.

This leads us to ask for the conditions under which

$$\bar{C}(n_p) = n_p \bar{C} \quad (16)$$

holds. This equation is generally not true. For example, we have

$$\begin{aligned} \bar{C}(2) &= \frac{i}{2\pi} \int_{-\pi}^{\pi} \text{tr}_{\mathbb{L}} \left(\hat{U}^{\dagger 2} \partial_k (\hat{U}^2) \right) dk \\ &= \frac{i}{2\pi} \int_{-\pi}^{\pi} \text{tr}_{\mathbb{L}} \left((\hat{U} \hat{U}^{\dagger 2} + \hat{U}^{\dagger 2} \hat{U}) \partial_k \hat{U} \right) dk \end{aligned} \quad (17)$$

from Eq. (11), if we replace $\hat{U} \equiv U(T, k)$ by $U(2T, k) = \hat{U}^2$. To make progress towards Eq. (16) we have to relate the operator expression $\hat{U} \hat{U}^{\dagger 2} + \hat{U}^{\dagger 2} \hat{U}$ to $2\hat{U}^\dagger$. Without aiming for a mathematically strict statement we note that if $\hat{U}^\dagger \hat{U} = \hat{U} \hat{U}^\dagger$ we have $\hat{U} \hat{U}^{\dagger 2} + \hat{U}^{\dagger 2} \hat{U} = 2\hat{U}^\dagger \hat{U} \hat{U}^\dagger$, and we obtain the desired relation if additionally $\hat{U}^\dagger \hat{U} \hat{U}^\dagger = \hat{U}^\dagger$. These are precisely the RD conditions formulated above.

That, conversely, RD implies Eq. (16) is obvious with Eq. (14) (which can be used here), if $\xi_m(k)$ is replaced by $\xi_m(k)^{n_p}$ and one uses $|\xi_m(k)| = 1$ for the eigenvalue loops that contribute in this equation.

Therefore, in the RD limit, a non-zero charge transfer $\bar{C} \neq 0$ corresponds to a non-zero persistent current $\lim_{n_p \rightarrow \infty} \bar{C}(n_p)/n_p = \bar{C}$, which is given by the relation $\bar{C} = W(\Gamma)$ between transport and topology.

Measuring the transferred charge by wave packet propagation

The transferred charge $C(n)$ or \bar{C} can be computed or measured also with real-space wave packet propagation. The principal procedure is to prepare a wave packet $|\psi(0)\rangle = |i\rangle$ at a single site i of the chain, let it evolve in time to $|\Psi_i\rangle = |\psi(T)\rangle = U|\psi(0)\rangle$, and then determine the quantity $C(n)|_i$ in Eq. (1) or the quantity \bar{C}_i in Eq. (7). For $C(n)$ the contribution from wave packets for all sites of the chain has to be summed, but $C(n)|_i$ will be negligible for $|i - n| \gg 1$. Owing to translational invariance, the averaged charge \bar{C} can be obtained exactly from the propagation of only L individual wave packets, prepared at the sites $i \in \{0, \dots, L - 1\}$ of the unit cell. Experimentally, this procedure requires preparation of a wave packet at a single site, and measurement of the weight of the propagated wave packet at multiple sites. This is possible, e.g., in experiments using photonic waveguide lattices [3, 4].

In other situations one may wish for a more relaxed approach that does not require preparation of a wave packet at a single site. A practical way is to measure the persistent current of a Floquet chain close to the RD limit: let a wave packet $|\psi\rangle$ propagate over $n_p \geq 1$ periods to $|\Psi\rangle = U^{n_p}|\psi\rangle$, measure the propagation distance $\Delta x = (\langle \Psi | \hat{x} | \Psi \rangle - \langle \psi | \hat{x} | \psi \rangle) / \langle \Psi | \Psi \rangle$, appropriately normalized by $\langle \Psi | \Psi \rangle$, and approximate the transferred charge by $\bar{C} \approx \Delta x / n_p$. If the width of the initial wave packet is small compared to the propagation distance, but still large enough to average over multiple sites of the chain, this will give a good approximation of \bar{C} for a (topological) charge pump. Sampling over multiple wave packets is possible.

Wave packet propagation remains applicable in a disordered chain, where the momentum space expressions (11), (14) cannot be used. We can still define the transferred charge \bar{C} as an average

$$\bar{C}^{(\text{wp})} = \lim_{n \rightarrow \infty} \frac{1}{2n + 1} \sum_{i=-n}^n \bar{C}_i, \quad (18)$$

now over the entire chain instead of only one unit cell.

In this context, one has to reconsider the meaning of normalization, since the normalization factor Ξ can no longer be easily set to the spectral radius of the (Floquet-Bloch) propagator. Instead, we can also consider an average

$$(\bar{\Xi}^{(\text{wp})})^2 = \eta \lim_{n \rightarrow \infty} \frac{1}{2n + 1} \sum_{i=-n}^n \langle \Psi_i | \Psi_i \rangle, \quad (19)$$

over the norm of wave packets $|\Psi_i\rangle = U|i\rangle$ starting from all sites of the chain. This expression for $\Xi^{(\text{wp})}$ contains a prefactor η that has to be determined from comparison with the previous normalization for a chain without disorder. Reverting to momentum space, we find

$$\lim_{n \rightarrow \infty} \frac{1}{2n+1} \sum_{i=-n}^n \langle \Psi_i | \Psi_i \rangle = \frac{1}{2\pi L} \sum_{m=1}^L \int_{-\pi}^{\pi} |\xi_m(k)|^2 dk \quad (20)$$

for a unit cell of L sites. In the RD limit, we thus have $(\Xi^{(\text{wp})})^2 = \eta(N_\Gamma/L)\Xi^2$ in comparison to the previous factor $\Xi = \max_\xi |\xi|$, where N_Γ is the number of ‘surviving’ eigenvalue loops above the imaginary gap. Therefore, we set $\eta = L/N_\Gamma$. For the chains (Sp), (Fl), with $L = 2, N_\Gamma = 1$, this means $\eta = 2$. In this way, the expressions for a disordered chain agree with the previous expressions for a chain without disorder at least in the RD limit. A difference persists away from this limit, and other ways of normalization are certainly possible.

Eqs. (18), (19) are used to compute the transferred charge for the inset of Fig. 5 in the main text. Explicit expressions are given in Eqs. (46), (47).

THE THREE CHAINS (St), (Sp), (Fl)

To specify the Hamiltonians of the three chains (St), (Sp), (Fl) we use the usual bra-ket notation, where $|n\rangle$ denotes the state at site $n \in \mathbb{Z}$. For the chains (Sp), (Fl), we identify ‘filled’ sites \bullet in Fig. 1 in the main text with even n , and ‘open’ sites \circ with odd n .

The static chain (St)

The Hamiltonian of the chain (St),

$$H_{\text{St}} = J \sum_{n \in \mathbb{Z}} (e^\gamma |n+1\rangle \langle n| + e^{-\gamma} |n\rangle \langle n+1|), \quad (21)$$

includes directional hopping between nearest neighbors. For $\gamma > 0$ ($\gamma < 0$) hopping to the right (left) is enhanced. The Hamiltonian is Hermitian only for $\gamma = 0$, when it reduces to that of a tight-binding chain with non-directional hopping.

The Hamiltonian H_{St} is invariant under translations by $L = 1$ sites, and has a scalar Bloch Hamiltonian

$$\hat{H}_{\text{St}}(k) = J(e^{-ik+\gamma} + e^{ik-\gamma}). \quad (22)$$

This gives the elliptical energy loop $E_{\text{St}}(k) \equiv \hat{H}_{\text{St}}(k)$ shown in Fig. 1 in the main text. Note that we can also write $E_{\text{St}}(k) = 2J(\cosh \gamma \cos k - i \sinh \gamma \sin k)$.

(St): Transferred charge

The Hamiltonian H_{St} , and thus also the propagator $U_{\text{St}}(t) = \exp(-itH_{\text{St}})$, satisfies the prerequisite $[U^\dagger, U] = 0$ of Eq. (14). We thus compute, with $\xi(k) = e^{-itE_{\text{St}}(k)}$,

$$\begin{aligned} \bar{C} &= \frac{i}{2\pi} \int_{-\pi}^{\pi} \xi(k)^* \partial_k \xi(k) dk \\ &= \frac{t}{2\pi} \int_{-\pi}^{\pi} \partial_k E_{\text{St}}(k) e^{2t \text{Im} E_{\text{St}}(k)} dk \\ &= -\frac{2Jt \cosh \gamma}{2\pi} \int_{-\pi}^{\pi} \sin k e^{4Jt \sinh \gamma \sin k} dk \end{aligned} \quad (23)$$

Using the integral representation of the Bessel functions [5] we get

$$\bar{C} = 2Jt \cosh \gamma I_1(4Jt \sinh \gamma), \quad (24)$$

with the modified Bessel function $I_1(\cdot)$. We have $\bar{C} = 0$ in the Hermitian case $\gamma = 0$ (as it must), but the non-Hermitian case $\gamma \neq 0$ allows for $\bar{C} \neq 0$.

(St): Regularized dynamics

The spectrum $E_{\text{St}}(k)$ of the Hamiltonian $\hat{H}_{\text{St}}(k)$ consists of a single loop. In the RD limit, the loop should have constant imaginary part, corresponding to constant magnitude $|\xi| = e^{t \text{Im} E}$ of the eigenvalues of the corresponding propagator $U(t)$. The only way to achieve this is to set $\gamma = 0$, recovering a Hermitian chain (possibly with a uniform complex shift of the Hamiltonian). Therefore, $\bar{C} = 0$ in the RD limit.

The static chain (Sp)

The chain (Sp) essentially consists of two identical copies of the chain (St), placed either on the ‘filled’ or ‘open’ sites. To separate the two copies, we include a staggered potential $\Delta \in \mathbb{C}$. To couple the two copies, we can allow for hopping $\lambda \in \mathbb{R}$ between the ‘filled’ and ‘open’ sites (although not particularly relevant for the present investigation). This results in the Hamiltonian

$$\begin{aligned} H_{\text{Sp}} &= J \sum_{n \in \mathbb{Z}} (e^\gamma |n+2\rangle \langle n| + e^{-\gamma} |n\rangle \langle n+2|) \\ &\quad + \Delta \sum_{n \in \mathbb{Z}} (|2n\rangle \langle 2n| - |2n+1\rangle \langle 2n+1|) \\ &\quad + \lambda \sum_{n \in \mathbb{Z}} (|n\rangle \langle n+1| + |n+1\rangle \langle n|), \end{aligned} \quad (25)$$

with translational invariance by $L = 2$ sites.

The corresponding 2×2 Bloch Hamiltonian is

$$\hat{H}_{\text{Sp}}(k) = \begin{pmatrix} E_{\text{St}}(k) + \Delta & 2\lambda \cos(k/2) \\ 2\lambda \cos(k/2) & E_{\text{St}}(k) - \Delta \end{pmatrix}, \quad (26)$$

with eigenvalues

$$E_{\text{Sp}}(k) = E_{\text{St}}(k) \pm \sqrt{4\lambda^2 \cos^2(k/2) + \Delta^2}. \quad (27)$$

For sufficiently large Δ this gives two separated energy loops (for $\text{Re} \Delta = \lambda = 0$, the condition is $|\text{Im} \Delta| > 2|J \sinh \gamma|$), as sketched in Fig. 1 in the main text. We use $\Delta = 3i$ and $\lambda = 0.5$ in Fig. 3 in the main text.

Note that we normalize the Brillouin zone to the interval $k \in (-\pi, \pi]$, independently of the size of the unit cell (hence the factor $k/2$ in Eqs. (26), (27)). The eigenvalues $E_{\text{Sp}}(k)$ are 2π -periodic, while $\tilde{H}_{\text{Sp}}(k)$ acquires an irrelevant phase (cf. the Fourier transform in Eq. (8)).

(Sp): *Transferred charge*

For $\lambda = 0$ the chain (Sp) consists of two copies of the chain (St), such that the transferred charge

$$\tilde{C} = 4Jt \cosh \gamma \cosh(2t \text{Im} \Delta) I_1(4Jt \sinh \gamma) \quad (28)$$

is the weighted sum of twice Eq. (23), with weighting factors $e^{\pm 2t \text{Im} \Delta}$ derived from the imaginary part of the staggered potential Δ . For $\lambda \neq 0$ the analytic computation of \tilde{C} becomes tedious, and will not be pursued here. Numerical data are given in Figs. 3, 4 in the main text.

(Sp): *Regularized dynamics*

Just as for the chain (St), the RD limit in the chain (Sp) requires $\gamma = 0$, such that $\tilde{C} = 0$. Now, however, we can separate loops with the staggered potential Δ . A trivial RD limit is obtained for $\Delta = 0$, reducing the chain to a Hermitian chain. In the non-trivial RD limit $|\text{Im} \Delta| \rightarrow \infty$, there exists one loop below and one loop above the imaginary gap at $\Gamma = 0$. This is the situation sketched in Fig. 4 in the main text. Still, we have $\tilde{C} = 0$.

The Floquet chain (Fl)

The Hamiltonian of the Floquet chain (Fl)

$$H_{\text{Fl}}(t) = \begin{cases} \frac{2}{T} H_{\text{Fl}}^{(1)} & \text{if } n_p \leq t/T < n_p + \frac{1}{2}, \\ \frac{2}{T} H_{\text{Fl}}^{(2)} & \text{if } n_p + \frac{1}{2} \leq t/T < n_p + 1 \end{cases} \quad (29)$$

consists of the two alternating steps

$$H_{\text{Fl}}^{(1)} = J \sum_{n \in \mathbb{Z}} (e^\gamma |2n+1\rangle \langle 2n| + e^{-\gamma} |2n\rangle \langle 2n+1|), \quad (30a)$$

$$H_{\text{Fl}}^{(2)} = J \sum_{n \in \mathbb{Z}} (e^\gamma |2n\rangle \langle 2n-1| + e^{-\gamma} |2n-1\rangle \langle 2n|) \quad (30b)$$

in each period ($n_p \in \mathbb{Z}$) of length T . As for the chain (Sp), $H_{\text{Fl}}(t)$ is invariant under translations by $L = 2$ sites.

Note that we use $T = 1$ throughout the present manuscript, both to obtain quasienergies ε_m from eigenvalues ξ_m via the relation $\xi_m = e^{-i\varepsilon_m T} \equiv e^{-i\varepsilon_m}$, as well as to interpret static chains as Floquet chains with an artificial period T . We do however keep the symbol T wherever suitable to remind us of the meaning of the respective variable, e.g., we write $U(T)$ instead of $U(1)$.

The Floquet propagator $U_{\text{Fl}} \equiv U_{\text{Fl}}(T)$ in real space is

$$\begin{aligned} U_{\text{Fl}} &= e^{-iH_{\text{Fl}}^{(2)} T/2} e^{-iH_{\text{Fl}}^{(1)} T/2} \\ &= c^2 \sum_{n \in \mathbb{Z}} |n\rangle \langle n| \\ &\quad - s^2 \sum_{n \in \mathbb{Z}} (e^{2\gamma} |2n+2\rangle \langle 2n| + e^{-2\gamma} |2n-1\rangle \langle 2n+1|) \\ &\quad - isc \sum_{n \in \mathbb{Z}} (e^\gamma |2n+1\rangle \langle 2n| + e^{-\gamma} |2n\rangle \langle 2n+1|) \\ &\quad - isc \sum_{n \in \mathbb{Z}} (e^\gamma |2n\rangle \langle 2n-1| + e^{-\gamma} |2n-1\rangle \langle 2n|), \end{aligned} \quad (31)$$

with the abbreviations $c \equiv \cos J$, $s \equiv \sin J$. The Floquet-Bloch propagator in momentum space is

$$\tilde{U}_{\text{Fl}}(k) = \begin{pmatrix} c^2 - s^2 e^{-ik+2\gamma} & -2isc \cos(k/2 + i\gamma) \\ -2isc \cos(k/2 + i\gamma) & c^2 - s^2 e^{ik-2\gamma} \end{pmatrix}, \quad (32)$$

with eigenvalues

$$\begin{aligned} \xi_{1,2}(k) &= 1 - 2s^2 \cos^2(k/2 + i\gamma) \\ &\quad \pm 2s \cos(k/2 + i\gamma) \sqrt{s^2 \cos^2(k/2 + i\gamma) - 1}. \end{aligned} \quad (33)$$

From the eigenvalues we obtain the quasienergies $\varepsilon_{1,2}(k)$ via the relation $\xi_{1,2}(k) = e^{-i\varepsilon_{1,2}(k)}$. Eigenvalues and quasienergies are shown in Fig. 1.

(Fl): *Topological phase transition*

The topological phase transition in the chain (Fl) occurs when the square root in Eq. (33) vanishes, which happens for $\gamma = \pm\gamma_c$ with the critical value

$$\gamma_c = \text{arcosh}(1/\sin |J|). \quad (34)$$

The spectrum of $\tilde{U}_{\text{Fl}}(k)$ consists of a single loop for $|\gamma| < \gamma_c$, and of two loops for $|\gamma| > \gamma_c$ (see Fig. 1). The loops are separated by an imaginary gap at $\Gamma = 0$, and have (necessarily) opposite winding number. Note that at the transition, the spectrum possesses an exceptional point at momentum $k = 0$ (and $\xi_1 = \xi_2 = -1$).

(Fl): *Transferred charge*

The Floquet-Bloch propagator from Eq. (32) does not satisfy the prerequisite $[\tilde{U}_{\text{Fl}}^\dagger, \tilde{U}_{\text{Fl}}]$ of Eq. (14), and we have

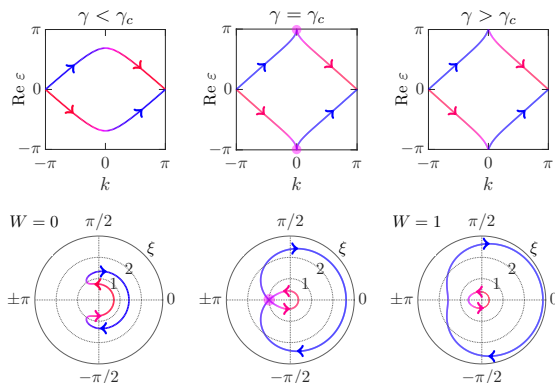


FIG. 1. Topological phase transition in the Floquet chain (FI) with $J = \pi/3$, as already shown in Fig. 2 in the main text. The top row shows the real part $\text{Re } \varepsilon_{1,2}(k)$ of the quasienergies, which have been omitted in the main text. The bottom row shows the spectrum of eigenvalues $\xi_{1,2}(k)$. The pink dots in the central panels indicate the exceptional point at the transition.

to use Eq. (11) to obtain the transferred charge

$$\bar{C} = 2s^4 \sinh 4\gamma + 2s^2 c^2 \sinh 2\gamma, \quad (35)$$

reusing the previous abbreviations $c \equiv \cos J$, $s \equiv \sin J$. In the Hermitian case $\gamma = 0$, we have $\bar{C} = 0$.

The normalization factor

$$\Xi = 1 + 2s^2 \sinh^2 \gamma + 2|s \sinh \gamma| \sqrt{1 + s^2 \sinh^2 \gamma} \quad (36)$$

is obtained from the dominant eigenvalue at $k = \pi$ (see Eq. (33)). Combining the expression for \bar{C} and Ξ we obtain an explicit expression for the normalized charge transfer plotted in Figs. (3), (4) in the main text.

(FI): *Regularized dynamics*

Just as the static chains (St), (Sp), the Floquet chain (FI) has the trivial RD limit $\gamma = 0$ of a Hermitian chain, where $\bar{C} = 0$. In addition, there is the non-trivial RD limit $|\gamma| \rightarrow \infty$.

For large $|\gamma| \gg \gamma_c$, the spectrum consists of two loops $\xi_{1,2}(k) \sim -s^2 e^{\pm(i k - 2\gamma)}$, separated by an imaginary gap $i\Gamma$ at $\Gamma = 0$. We have $\Xi \sim s^2 e^{2|\gamma|}$. Being above the topological phase transition, the winding number is $W = \text{sgn } \gamma \neq 0$. The (normalized) transferred charge is

$$\bar{C}/\Xi^2 = \frac{2 \sinh 4\gamma}{e^{4|\gamma|}} + O(e^{-|\gamma|}), \quad (37)$$

which converges to W in the limit $|\gamma| \rightarrow \infty$. As expected from the general arguments, the transferred charge in the RD limit is quantized, equal to the winding number,

and does not depend on the remaining model parameters (here, the hopping J). This behavior is depicted in Fig. 4 in the main text.

The propagator in the RD limit can be expressed in terms of the right (S_+) and left (S_-) shift operator

$$S_+ = \sum_{n \in \mathbb{Z}} |2n+2\rangle \langle 2n|, \quad S_- = \sum_{n \in \mathbb{Z}} |2n-1\rangle \langle 2n+1|. \quad (38)$$

These operators shift wave packets exactly by two sites. S_+ acts only on even sites ('filled' sites \bullet in Fig. 1, blue sites in Figs. 3, 5 in the main text), S_- on odd sites ('open' or red sites \circ).

Shift operators are prototypical examples of charge pumps. Having non-zero winding number, they cannot be realized individually by continuous time propagation (which leaves the total winding number, summed over all states, invariant and equal to the initial value zero, cf. main text), but have to appear in pairs. Especially a simple shift operator $\sum_{n \in \mathbb{Z}} |n+1\rangle \langle n|$ cannot be realized by continuous time evolution.

In the RD limit of the Floquet chain, the normalized propagator $-U_{\text{FI}}/\Xi$ (with an additional minus sign) converges to S_+ for $\gamma \rightarrow \infty$, and to S_- for $\gamma \rightarrow -\infty$. Here, the 'missing' shift operator S_- or S_+ is asymptotically suppressed by the strong damping $\sim e^{-4|\gamma|}$ relative to the other operator S_+ or S_- that survives in the RD limit.

(FI): *Perfect coupling*

All expressions for the chain (FI) simplify in the case of perfect coupling $J = \pi/2$. The name 'perfect coupling' expresses the fact that amplitude is transferred perfectly between adjacent sites in each step, which is equivalent to the condition $c \equiv \cos J = 0$ in Eq. (31).

At perfect coupling, the spectrum of $\hat{U}_{\text{FI}}(k)$ consists of two perfectly circular loops $\xi_{1,2}(k) = -e^{\pm(i k - 2\gamma)}$. Note that $\gamma_c = 0$: Away from the Hermitian case, the Floquet chain (FI) at perfect coupling is always in a non-trivial topological phase.

The Floquet propagator in real space (see Eq. (31)) is a weighted sum $U_{\text{FI}} = -e^{2\gamma} S_+ - e^{-2\gamma} S_-$ of the right and left shift operator S_+ , S_- , even away from the RD limit. In the RD limit, only one of the two shift operators survives, repeating the result given earlier for general J .

The transferred charge is

$$\bar{C}/\Xi^2 = \frac{2 \sinh 4\gamma}{e^{4|\gamma|}} \quad (39)$$

for all γ (cf. Eq. (37)).

(FI): *Disordered chain*

For Fig. 5 in the main text we add disorder to the hopping. One can also include random detunings, and

replace the two steps in Eq. (30) with

$$H_{\text{Fl}}^{(1)} = \sum_{n \in \mathbb{Z}} J_n^{(a)} e^{\gamma} |2n+1\rangle \langle 2n| + J_n^{(b)} e^{-\gamma} |2n\rangle \langle 2n+1| + \Delta_n^{(1)} |n\rangle \langle n|, \quad (40a)$$

$$H_{\text{Fl}}^{(2)} = \sum_{n \in \mathbb{Z}} J_n^{(c)} e^{\gamma} |2n\rangle \langle 2n-1| + J_n^{(d)} e^{-\gamma} |2n-1\rangle \langle 2n| + \Delta_n^{(2)} |n\rangle \langle n|, \quad (40b)$$

where the $J_n^{(a)}, \dots, J_n^{(d)}$ are drawn independently and uniformly from the interval $[J(1-\delta), J(1+\delta)]$, with relative disorder strength δ just as in the main text, and the $\Delta_n^{(1)}, \Delta_n^{(2)}$ from $[-\Delta, \Delta]$.

The RD limit $|\gamma| \rightarrow \infty$ of this disordered Floquet chain can be analyzed completely through a purely algebraic but rather lengthy computation of the Floquet propagator that we cannot repeat here. The central result is that also in the disordered chain directional hopping suppresses one direction of propagation in favor of the other.

The limit $\gamma \rightarrow \infty$ of the normalized propagator $-U_{\text{Fl}}/\Xi$ (still $\Xi = s^2 e^{2\gamma}$) results in a disordered shift operator

$$S_+ = \sum_{n \in \mathbb{Z}} \zeta_n |2n+2\rangle \langle 2n|, \quad (41)$$

where the ζ_n are random variables of the same magnitude ($\zeta_n \approx 1$ for small δ). For $\delta = 0$, we recover the result $\zeta_n = 1$ of the ordered Floquet chain (see Eq. (38)). Analogously, a left shift is obtained for $\gamma \rightarrow -\infty$.

The action of the disordered shift operator on wave packets is seen in Fig. 5, panel (B) in the main text, which essentially shows $(S_+)^{np} |\psi\rangle$ for an initial Gaussian wave packet on ≈ 5 sites. The amplitude at individual sites depends on the ζ_n , and thus is random, but the entire wave packet propagates without spreading.

For a slightly simplified disordered Floquet chain even the transferred charge can be calculated explicitly, using Eqs. (18), (19) derived from wave packet propagation. To simplify, we drop the detunings ($\Delta_n^{(1,2)} \equiv 0$), and use equal disordered hopping ($J_n^{(a)} = J_n^{(b)} \equiv J_n^{(1)}$, $J_n^{(c)} = J_n^{(d)} \equiv J_n^{(2)}$) in each step. Then, the wave functions $|\Psi_i\rangle = U_{\text{Fl}}|i\rangle$ are given by

$$\begin{aligned} |\Psi_{2i}\rangle &= -i \cos J_i^{(1)} \sin J_i^{(2)} e^{-\gamma} |2i-1\rangle \\ &\quad + \cos J_i^{(1)} \cos J_i^{(2)} |2i\rangle \\ &\quad -i \sin J_i^{(1)} \cos J_{i+1}^{(2)} e^{\gamma} |2i+1\rangle \\ &\quad - \sin J_i^{(1)} \sin J_{i+1}^{(2)} e^{2\gamma} |2i+2\rangle, \\ |\Psi_{2i+1}\rangle &= -\sin J_i^{(1)} \sin J_i^{(2)} e^{-2\gamma} |2i-1\rangle \\ &\quad -i \sin J_i^{(1)} \cos J_i^{(2)} e^{-\gamma} |2i\rangle \\ &\quad + \cos J_i^{(1)} \cos J_{i+1}^{(2)} |2i+1\rangle \\ &\quad -i \cos J_i^{(1)} \sin J_{i+1}^{(2)} e^{\gamma} |2i+2\rangle. \end{aligned} \quad (42)$$

We thus have

$$\begin{aligned} \langle \Psi_{2i} | \Psi_{2i} \rangle &= \cos^2 J_i^{(1)} \sin^2 J_i^{(2)} e^{-2\gamma} \\ &\quad + \cos^2 J_i^{(1)} \cos^2 J_i^{(2)} \\ &\quad + \sin^2 J_i^{(1)} \cos^2 J_{i+1}^{(2)} e^{2\gamma} \\ &\quad + \sin^2 J_i^{(1)} \sin^2 J_{i+1}^{(2)} e^{4\gamma}, \end{aligned} \quad (43)$$

$$\begin{aligned} \langle \Psi_{2i+1} | \Psi_{2i+1} \rangle &= \sin^2 J_i^{(1)} \sin^2 J_i^{(2)} e^{-4\gamma} \\ &\quad + \sin^2 J_i^{(1)} \cos^2 J_i^{(2)} e^{-2\gamma} \\ &\quad + \cos^2 J_i^{(1)} \cos^2 J_{i+1}^{(2)} \\ &\quad + \cos^2 J_i^{(1)} \sin^2 J_{i+1}^{(2)} e^{2\gamma}, \end{aligned}$$

and

$$\begin{aligned} \langle \Psi_{2i} | \hat{x} - 2i | \Psi_{2i} \rangle &= -\cos^2 J_i^{(1)} \sin^2 J_i^{(2)} e^{-2\gamma} \\ &\quad + \sin^2 J_i^{(1)} \cos^2 J_{i+1}^{(2)} e^{2\gamma} + 2 \sin^2 J_i^{(1)} \sin^2 J_{i+1}^{(2)} e^{4\gamma}, \\ \langle \Psi_{2i+1} | \hat{x} - (2i+1) | \Psi_{2i+1} \rangle &= -2 \sin^2 J_i^{(1)} \sin^2 J_i^{(2)} e^{-4\gamma} \\ &\quad - \sin^2 J_i^{(1)} \cos^2 J_i^{(2)} e^{-2\gamma} + \cos^2 J_i^{(1)} \sin^2 J_{i+1}^{(2)} e^{2\gamma}. \end{aligned} \quad (44)$$

To proceed, we require the averages of the \cos^2, \sin^2 terms over the uniform probability distribution of the $J_n^{(1)}, J_n^{(2)}$,

$$\begin{aligned} \overline{c^2} &\equiv \overline{\cos^2 J_i} = \frac{1}{2}(1 - \zeta) + \zeta \cos^2 J, \\ \overline{s^2} &\equiv \overline{\sin^2 J_i} = \frac{1}{2}(1 + \zeta) + \zeta \sin^2 J, \end{aligned} \quad (45)$$

where $\zeta = \text{sinc}(2J\delta)$ with the sinc-function (with $\text{sinc } x = (\sin x)/x$ for $x \neq 0$).

Therefore, the quantities in Eqs. (18), (19) are

$$\begin{aligned} \bar{C}^{(\text{wp})} &= \frac{1}{2} (\overline{\langle \Psi_{2i} | \hat{x} - 2i | \Psi_{2i} \rangle} + \overline{\langle \Psi_{2i+1} | \hat{x} - (2i+1) | \Psi_{2i+1} \rangle}) \\ &= 2(\overline{s^2})^2 \sinh 4\gamma + 2(\overline{s^2})(\overline{c^2}) \sinh 2\gamma \end{aligned} \quad (46)$$

and, using the prefactor $\eta = 2 = L/N_{\Gamma}$ for the chain (Fl) (see the discussion after Eq. (19)),

$$\begin{aligned} (\bar{\Xi}^{(\text{wp})})^2 &= \eta^2 \frac{1}{2} (\overline{\langle \Psi_{2i} | \Psi_{2i} \rangle} + \overline{\langle \Psi_{2i+1} | \Psi_{2i+1} \rangle}) \\ &= 2(\overline{s^2})^2 \cosh 4\gamma + 4(\overline{s^2})(\overline{c^2}) \cosh 2\gamma + 2(\overline{c^2})^2. \end{aligned} \quad (47)$$

The averages from Eq. (45) could now be inserted, to obtain the normalized transferred charge $\bar{C}^{(\text{wp})}/(\bar{\Xi}^{(\text{wp})})^2$ of a disordered Floquet chain. In the RD limit $|\gamma| \rightarrow \infty$, only the first term in the numerator and denominator survives, and we recover the result $\bar{C}^{(\text{wp})}/(\bar{\Xi}^{(\text{wp})})^2 = \text{sgn } \gamma$ of topological transport also with disorder. For $\gamma \rightarrow \infty$, the parameters of the disordered shift operator from Eq. (41) are given by $\zeta_n = \sin J_n^{(1)} \sin J_n^{(2)} / \sin^2 J$. For $\delta = 0$ we recover the result $\zeta_n \equiv 1$ of the ordered chain (Fl).

REGULARIZATION OF THE PROPAGATOR

In this section all matrices depend on momentum k , and we take it for granted that matrix functions $k \mapsto \hat{U}(k)$ etc. are at least continuous. We also demand 2π -periodicity of such functions, but only up to phase factors, similar to the behavior of the Fourier transform in Eq. (8). In the following equations, we occasionally drop the k -dependence to allow for simpler notation.

Regularization starts with a Floquet-Bloch propagator $\hat{U}(k)$ with imaginary gap $i\Gamma$. For a unit cell of L sites, $\hat{U}(k)$ is an $L \times L$ matrix. If the eigenspace to eigenvalues $|\xi_m(k)| > e^\Gamma$ outside of the imaginary gap has dimension l , with $1 \leq l \leq L$, the eigenspace to eigenvalues $|\xi_m(k)| < e^\Gamma$ inside of the imaginary gap has dimension $L-l$. Note that l does not depend on k .

We first consider the case that the eigenvectors of the propagator are already orthogonal before regularization, that is $[\hat{U}, \hat{U}^\dagger] = 0$ (this is the case, e.g., for the static chains (St), (Sp), but not for the Floquet chain (Fl)). Then, regularization deforms only the eigenvalues of \hat{U} .

To implement the deformation, diagonalize $\hat{U}(k)$ with a unitary transformation $Q(k)$, such that $\hat{U}(k) = Q(k)D(k)Q(k)^\dagger$ with a diagonal matrix $D(k)$ that contains the eigenvalues $\xi_1(k), \dots, \xi_L(k)$ of $\hat{U}(k)$. The deformation of the propagator is given by

$$\check{U}(s) = Q f_\Gamma(D, s) Q^\dagger, \quad (48)$$

with the function

$$f_\Gamma(z, s) = \begin{cases} (1-s)z & \text{if } |z| < e^\Gamma, \\ \left(1-s + \frac{s}{|z|}\right)z & \text{if } |z| > e^\Gamma. \end{cases} \quad (49)$$

We have $f_\Gamma(z, 0) = z$, and $f_\Gamma(z, 1) = 0$ for $|z| < e^\Gamma$ but $f_\Gamma(z, 1) = z/|z|$ for $|z| > e^\Gamma$. $\check{U}(s)$ does not depend on the choice of the transformation Q , and we are justified to write directly $\check{U}(s) = f_\Gamma(\hat{U}, s)$.

With this definition, $\check{U}(0) = \hat{U}$, while the eigenvalues of $f_\Gamma(D, 1)$, hence of $\check{U}(1)$, have modulus zero or one. Furthermore, eigenvalues move radially towards the unit circle or the origin such that an imaginary gap stays open during the deformation from $\check{U}(0)$ to $\check{U}(1)$. This completes regularization in this situation.

In the general case $[\hat{U}, \hat{U}^\dagger] \neq 0$, also the eigenvectors of \hat{U} must be deformed during regularization. One approach is to use the Schur decomposition [2], where we write the propagator as $\hat{U}(k) = Q(k)A(k)Q(k)^\dagger$ with unitary $Q(k)$ and triangular $A(k)$. One reason to use the Schur decomposition is that, e.g., the spectral decomposition fails to exist at exceptional points.

Write $A(k) = D(k) + N(k)$, where the diagonal part $D(k)$ contains the eigenvalues of $\hat{U}(k)$, and $N(k)$ is strictly upper triangular. Note that $N(k)$ is zero if and only if $[\hat{U}, \hat{U}^\dagger] = 0$.

Now we define the continuous deformation

$$A(s) = f_\Gamma(D, s) + (1-s)N \quad (50)$$

for $0 \leq s \leq 1$. This deformation still moves the eigenvalues on the diagonal of A radially towards the unit circle or the origin, and sends the triangular part N above the diagonal to zero such that $[A(1), A(1)^\dagger] = 0$. Reinserting into the Schur decomposition gives a continuous deformation of $\hat{U}(k)$ to a regularized propagator.

The problem with using the Schur decomposition is that the deformation of $A(k)$ depends explicitly on N , and is not invariant under unitary transformations. Conceptually, for $N \neq 0$ the deformation in Eq. (50) involves a specific choice how the eigenvectors of $A(k)$ (equivalently, of $\hat{U}(k)$) are made orthogonal during regularization. Since the Schur decomposition is not unique, it can happen that $N(0) \neq N(2\pi)$. Then, the Schur-based regularization can fail to preserve the 2π -periodicity of $\hat{U}(k)$, even if required only up to phase factors.

Incidentally, for the present examples with $l = L - l = 1$, this problem does not arise. Here, the Schur decomposition is unique (up to phase factors) since the imaginary gap separates the one-dimensional eigenspaces for all k .

We shall briefly introduce an alternative approach to regularization that avoids the complications of the Schur decomposition. Let $P_{>}(k)$ denote the projection onto the eigenspace to eigenvalues $|\xi(k)| > e^\Gamma$ outside of the imaginary gap, and $P_{<}(k)$ the projection onto the eigenspace to eigenvalues $|\xi(k)| < e^\Gamma$ inside of the imaginary gap. Note that we cannot assume that the projections are orthogonal, unless \hat{U} is normal.

Using the projections, split $\hat{U}(k)$ as

$$\begin{aligned} \hat{U}(k) &= P_{>}\hat{U}P_{>} + P_{<}\hat{U}P_{<} \\ &= \hat{U}_{>} + \hat{U}_{<}. \end{aligned} \quad (51)$$

We now deform $\hat{U}_{>}$ to a partial isometry, and let $\hat{U}_{<} \rightarrow 0$.

By assumption, $\hat{U}_{>}$ is a matrix with rank l . Therefore, it can be written in the form

$$\hat{U}_{>} = QBQ^\dagger, \quad (52)$$

where Q is a $L \times l$ matrix with orthogonal columns (such that $Q^\dagger Q = \mathbf{1}_l$), and B an $l \times l$ matrix. The spectrum of B is equal to the non-zero spectrum of $\hat{U}_{>}$, in particular, B has full rank l .

Note that here no problem arises since we do not assume a specific form of B as we did in the Schur decomposition for the matrix A . The functions $k \mapsto Q(k), B(k)$ can always be chosen with periodicity 2π .

Now we use a polar decomposition [2]

$$B = RS, \quad (53)$$

with a unitary $l \times l$ matrix R and a Hermitian and positive definite $l \times l$ matrix S (the latter is guaranteed since B

has full rank l). Using the polar decomposition, which is unique for full rank B , avoids the complications arising from the non-uniqueness of the Schur decomposition.

Since S is positive definite, we can write $S = e^X$ with Hermitian X , and define a continuous deformation

$$\check{U}(s) = QRe^{(1-s)X}Q^\dagger + g(s)\hat{U}_< \quad (54)$$

of \hat{U} with parameter $s \in [0, 1]$. Here, $g(s)$ is a (largely arbitrary) function with $g(s) > 0$, $g(0) = 1$, and $g(1) = 0$.

The map $s \mapsto \check{U}(s)$ is a continuous deformation of the propagator, such that $\check{U}(1) = QRQ^\dagger$ is a regularized propagator. Since the smallest eigenvalue of the matrix $QRe^{(1-s)X}Q^\dagger$ is bounded away from zero for $0 \leq s \leq 1$, we can always achieve that an imaginary gap stays open during the deformation by letting $g(s)$ approach zero sufficiently fast.

Note that the deformation (54) does not move eigen-

values along radial lines as the previous deformation (50) did, unless \hat{U} is normal and we can choose a diagonal B in Eq. (52). We recall that, regarding topological properties, details of the regularization procedure are irrelevant.

-
- [1] G. M. Graf and C. Tauber, *Ann. Henri Poincaré* **19**, 709 (2018).
 - [2] G. H. Golub and C. F. Van Loan, *Matrix Computations*, 4th ed. (The Johns Hopkins University Press, 2013).
 - [3] A. Szameit and S. Nolte, *J. Phys. B* **43**, 163001 (2010).
 - [4] T. Ozawa, H. M. Price, A. Amo, N. Goldman, M. Hafezi, L. Lu, M. C. Rechtsman, D. Schuster, J. Simon, O. Zeitler, and I. Carusotto, *Rev. Mod. Phys.* **91**, 015006 (2019).
 - [5] M. Abramowitz and I. A. Stegun, eds., *Handbook of Mathematical Functions with Formulas, Graphs, and Mathematical Tables* (Dover Publications, 1970).

Cutting off the non-Hermitian boundary from an anomalous Floquet topological insulator

BASTIAN HÖCKENDORF^(a), ANDREAS ALVERMANN and HOLGER FEHSKE

Institut für Physik, Universität Greifswald, Felix-Hausdorff-Str. 6, 17489 Greifswald, Germany

PACS 03.65.Vf – Phases: geometric; dynamic or topological
 PACS 73.20.-r – Electron states at surfaces and interfaces
 PACS 05.60.Gg – Quantum transport

Abstract – In two-dimensional anomalous Floquet insulators, chiral boundary states can spectrally detach from the bulk bands through non-Hermitian boundary state engineering. We show that this spectral detachment enables spatial detachment: The non-Hermitian boundary can be physically cut off from the bulk while retaining its topological transport properties. The resulting one-dimensional chain is identified as a non-Hermitian Floquet chain with non-zero winding number. Through the spatial detachment, the conventional bulk-boundary correspondence is recovered in the anomalous Floquet insulator. We demonstrate our theoretical findings for the standard model of an anomalous Floquet insulator and discuss their experimental relevance.

The cornerstone of topological band theory is the bulk-boundary correspondence which provides a fundamental connection between the insulating bulk and chiral boundaries of a topological insulator [1–6]. Quantized transport emerges at a boundary via chiral boundary states if and only if the boundary is attached to a topologically non-trivial bulk. Since the transport is exclusively determined by the bulk topology, it is impervious to boundary deformations. This provides robustness but also serves as a fundamental restriction. Suppose we tried to extract a chiral boundary state from a topological insulator by cutting off one of its boundaries. Any such attempt would necessarily fail. In agreement with the bulk-boundary correspondence, the chiral boundary state would move towards the newly created boundary of the topological insulator. On the cut off boundary, chiral transport would no longer occur.

In this work, we demonstrate that the boundary of a two-dimensional anomalous Floquet insulator can retain its topological transport properties when it is cut off, provided that its boundary states are spectrally detached from the bulk bands. Before we explain our idea in greater detail, let us briefly review its three essential ingredients: anomalous Floquet insulators, non-Hermitian Floquet chains, and non-Hermitian boundary state engineering (BSE).

In anomalous Floquet insulators [7–18], each of the individual Floquet bands is topologically trivial. Nevertheless, non-trivial topology emerges through the dynamical evolution of the system, resulting in a non-zero W_3 invariant [8, 9]. The signature of this topological phase is found in the spectrum of the Floquet-Bloch propagator $\hat{U}(k) \equiv U(T, k)$, which is the solution of the Schrödinger equation $i\partial_t U(t, k) = H(t, k)U(t, k)$ after one period of a time-periodic Bloch Hamiltonian $H(t, k) = H(t + T, k)$. Here, we impose a strip geometry, as in the top row of Fig. 1, such that k denotes the momentum parallel to the boundaries of the strip. The spectrum $\{e^{-i\varepsilon(k)}\}$ of $\hat{U}(k)$ with the real-valued Floquet quasienergies $\varepsilon(k)$ lies on the unit circle. The boundary states of an anomalous Floquet insulator form non-contractible chiral loops $k \mapsto e^{-i\varepsilon(k)}$ that wind around the unit circle (see the first panel in the bottom row of Fig. 1). Loops with opposite chirality, belonging to boundary states on opposite boundaries, do not cancel each other because the boundary states are spatially separated by the bulk.

One-dimensional non-Hermitian Floquet chains are distinguished from static or Hermitian chains by their capability to realize topological transport through quantized charge pumping [19, 20]. The bulk states of these chains appear as non-contractible loops with opposite chirality in the now complex-valued quasienergy spectrum, in analogy to the boundary states of anomalous Floquet insulators. Here, cancellation of the loops is avoided through spectral

^(a)bastian.hoeckendorf@uni-greifswald.de

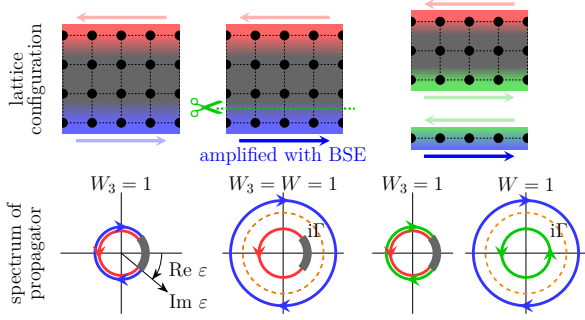


Fig. 1: Blueprint for the construction of a one-dimensional non-Hermitian Floquet chain with non-zero winding number W from the boundary of an anomalous Floquet insulator with non-zero W_3 invariant. In the bottom row, the bulk bands of the insulator are indicated by thick gray arcs and the arrows indicate the chirality of the loops, which is extracted from the functional dependence $k \mapsto e^{-i\varepsilon(k)}$ of the spectrum.

separation in the form of an imaginary gap $i\Gamma$ (see the last panel in the bottom row of Fig. 1). The direction of chiral transport is determined by the non-contractible loops above the imaginary gap. This situation is classified by the \mathbb{Z} -valued winding number [19]

$$W(\Gamma) = \frac{i}{2\pi} \sum_{e^\Gamma < |e^{-i\varepsilon_j}|} \int_{-\pi}^{\pi} e^{i\varepsilon_j(k)} \partial_k e^{-i\varepsilon_j(k)} dk, \quad (1)$$

which simply counts the chirality of the non-contractible loops above the imaginary gap. By definition, the winding number can only change when the imaginary gap closes. For the trivial imaginary gap $\Gamma = -\infty$, we obtain the total chirality $W(-\infty) = 0$ of the spectrum, which is necessarily zero due to the invertibility of the propagator [19].

BSE [21] establishes a connection between anomalous Floquet insulators and non-Hermitian Floquet chains. This connection provides the basis for our analysis. BSE denotes a process in which non-Hermiticity is used to spectrally detach the boundary states of an anomalous Floquet insulator from the bulk bands. Consider now, e.g., the configuration in the central panel of the top row of Fig. 1 where BSE is applied to the bottom boundary of an anomalous Floquet insulator. Since an imaginary gap separates the boundary state on the bottom boundary from the rest of the quasienergy spectrum, the two-dimensional system is no longer just described by a non-zero W_3 invariant, but also by a non-zero winding number W .

The non-Hermitian boundary can now be cut off by setting all couplings between it and the bulk to zero, as in the right panel of the top row of Fig. 1. On the newly created Hermitian bottom boundary of the anomalous Floquet insulator, a chiral boundary state emerges in accordance with the bulk-boundary correspondence. At the same time, an additional chiral mode with opposite chirality is created on the cut off boundary since the total

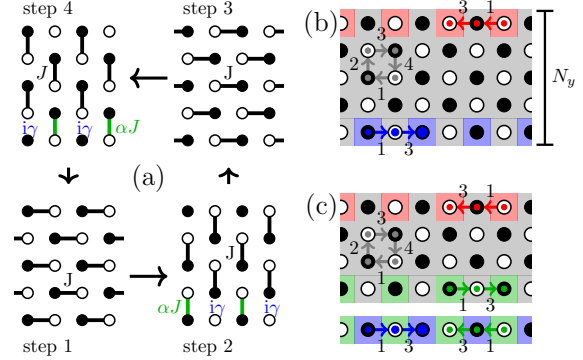


Fig. 2: (a) Driving protocol of an anomalous Floquet insulator on a semi-infinite strip along the x -axis, with pairwise coupling between adjacent lattice sites (filled and open circles). Panel (b) [panel (c)] shows the patterns of motion during one cycle of the driving protocol for perfect coupling, $\gamma > 0$ and $\alpha = 1$ ($\alpha = 0$).

chirality $W(-\infty)$ must remain zero. Due to the BSE, this additional mode is separated from the original boundary state by an imaginary gap. The winding number of the cut off boundary is non-zero. The cut off boundary has become a non-Hermitian Floquet chain.

We demonstrate our findings for the standard model [8] of an anomalous Floquet insulator which is sketched in Fig. 2(a). The $2 + 1$ -dimensional driving protocol is implemented on a square lattice with lattice sites \bullet (filled circles) and \circ (open circles). We enforce translational invariance along the x -axis and open boundary conditions along the y -axis such that the lattice possesses a top and bottom boundary. The number of sites between the two boundaries is indexed by the parameter N_y [see Fig. 2(b)]. The time-periodic Bloch Hamiltonian $H(t, k)$ of the driving protocol, with momentum k along the x -axis, cycles through four consecutive steps $H^{(1)}(k), \dots, H^{(4)}(k)$ of duration $\delta t = T/4$, each of which couples two different adjacent sites of the lattice. The propagators of each step are $U^{(i)}(k) = \exp(-i\delta t H^{(i)}(k))$ and the Floquet-Bloch propagator of the full driving protocol is given by $\hat{U}(k) = U^{(4)}(k) \dots U^{(1)}(k)$.

To specify the Hamiltonians of the individual steps, we use standard bra-ket notation, where $|\bullet, n_y\rangle$ ($|\circ, n_y\rangle$) denotes the Bloch state of a particle on the \bullet (\circ) sites in the n_y -th layer between the bottom and top boundary with $n_y = 1, \dots, N_y$. To avoid notational clutter, we omit the explicit momentum dependence $|\bullet, n_y\rangle \equiv |\bullet, n_y, k\rangle$, $|\circ, n_y\rangle \equiv |\circ, n_y, k\rangle$ of the Bloch states. With these con-

ventions, the four steps are expressed as

$$H^{(1)}(k) = \frac{J}{\delta t} \sum_{n_y=1}^{N_y} \left(e^{-ik/2} |\circ, n_y\rangle \langle \bullet, n_y| + e^{ik/2} |\bullet, n_y\rangle \langle \circ, n_y| \right), \quad (2a)$$

$$H^{(2)}(k) = \frac{J}{\delta t} \sum_{n_y=3}^{N_y} \left(|\circ, n_y\rangle \langle \bullet, n_y - 1| + |\bullet, n_y - 1\rangle \langle \circ, n_y| \right) + \frac{\alpha J}{\delta t} \left(|\circ, 2\rangle \langle \bullet, 1| + |\bullet, 1\rangle \langle \circ, 2| \right) + i \frac{\gamma}{\delta t} |\circ, 1\rangle \langle \circ, 1|, \quad (2b)$$

$$H^{(3)}(k) = S(k) H^{(1)}(k) S^{-1}(k), \quad (2c)$$

$$H^{(4)}(k) = S(k) H^{(2)}(k) S^{-1}(k). \quad (2d)$$

The symmetry operator $S(k) = \sum_{n_y=1}^{N_y} (|\circ, n_y\rangle \langle \bullet, n_y| + |\bullet, n_y\rangle \langle \circ, n_y|)$ exchanges the two types of sites. Note that we normalize the Brillouin zone to the interval $k \in [-\pi, \pi)$. The three parameters J , γ , and α control the coupling strength, the spectral attachment/detachment of the boundary state on the bottom boundary, and the spatial attachment/detachment of the bottom boundary, respectively.

We first focus on the case $\alpha = 1$, where the bottom boundary is fully attached to the rest of the lattice. The pairwise coupling between two sites in each of the four steps is effectively described by the 2×2 Hermitian Hamiltonian

$$H_J = \frac{J}{\delta t} \begin{pmatrix} 0 & 1 \\ 1 & 0 \end{pmatrix} = \frac{J}{\delta t} \sigma_x. \quad (3)$$

The associated propagator $U_J = \exp(-i\delta t H_J) = \cos(J) - i \sin(J) \sigma_x$, of a time step, is a periodic function of J . Since $U_J = (-1)^m U_{J+m\pi}$ for every $m \in \mathbb{Z}$, we may restrict ourselves to the parameter range $J \in [0, \pi)$. For $0 \leq J < \pi/4$ and $3\pi/4 < J < \pi$, the W_3 invariant vanishes, which indicates that the system is topologically trivial. On the other hand, the W_3 invariant is non-zero for $\pi/4 < J < 3\pi/4$. This indicates that the system is in the anomalous Floquet topological phase, which makes it a candidate for BSE.

The simplest way to facilitate the BSE is to implement gain or loss on the isolated boundary sites that, in the respective step of the protocol, do not couple to other sites [21]. Here, we place a non-Hermitian imaginary potential $i\gamma/\delta t$ onto the isolated sites in steps 2 [see Eq. (2b)] and 4 [see Eq. (2d)] at the bottom boundary. For $\gamma > 0$, the imaginary potential corresponds to gain and for $\gamma < 0$ to loss. Note that the remaining lattice, including the top boundary, is Hermitian.

For the special value $J = \pi/2$, which we call perfect coupling, we have $U_J = -i\sigma_x$. A full amplitude transfer occurs between coupled sites and the driving protocol enforces the trajectories shown in Fig. 2(b). An excitation in the bulk moves in a closed loop, while an excitation

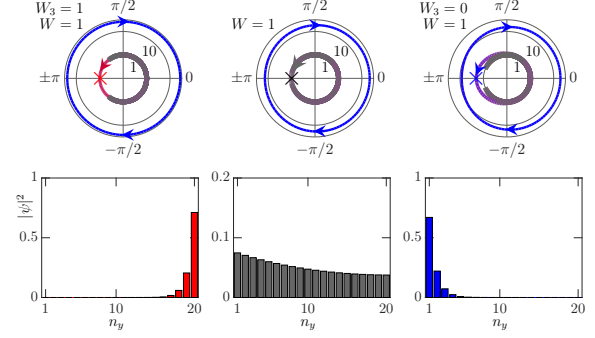


Fig. 3: Top row: Spectrum of the Floquet-Bloch propagator for the driving protocol in Fig. 2 with $N_y = 20$ sites between the bottom and top boundary and $\alpha = 1$, $\gamma = 1.8$. The bulk phase transition at $J = \pi/4$ (central panel) separates the phase with a non-trivial (left panel) and trivial bulk (right panel). Note that we use a logarithmic radial axis in all panels. The color of the curves indicates the amplitude distribution of the eigenfunctions on the red, blue, and gray colored area of the lattice in Fig. 2(b). Bottom row: Amplitude distribution of the eigenfunctions $\psi(k)$ of $\tilde{U}(k)$ at $k = 0$ as a function of n_y for the eigenvalues marked with an \times in the top row.

starting on a \bullet site (\circ site) at the bottom (top) boundary is transported two sites to the right (left). This pattern of motion gives rise to boundary states on the bottom and top boundary with opposite chirality. The chiral boundary state on the bottom boundary gets amplified (attenuated) by a factor $e^{2\gamma}$ for $\gamma > 0$ ($\gamma < 0$). All other excitations have constant amplitude. This corresponds to the quasienergy dispersions $\varepsilon(k) = 0$ for the bulk band and $\varepsilon(k) = \pi + k + 2i\gamma$ [$\varepsilon(k) = \pi - k$] for the chiral boundary state on the bottom [top] boundary. We have $W(\Gamma) = 1$ for $\gamma > 0$ and $W(\Gamma) = -1$ for $\gamma < 0$ with the imaginary gap $i\Gamma$ at $\Gamma = \gamma$.

For sufficiently large values of $|\gamma|$, the boundary state on the bottom boundary remains detached from the rest of the spectrum for any non-perfect but non-zero coupling even if the W_3 invariant vanishes. We here observe the breakdown of the bulk-boundary correspondence. Notably, the breakdown is restricted to the non-Hermitian bottom boundary. Fig. 3 demonstrates this phenomenon. At $J = 1$ (left panels), the W_3 invariant and winding number W are both non-zero. At $J = \pi/4$ (middle panels), the topological phase transition occurs and the W_3 invariant changes to zero. The imaginary gap, however, stays open, which means that the winding number W does not change. Consequently, the detached boundary state can not disappear and persists even beyond the phase transition at $J = 0.7$ (right panels).

The top boundary still fulfills the bulk-boundary correspondence, since it is Hermitian, so the boundary state that is localized on it disappears during the phase transition. It is replaced by a boundary state with the same

chirality which is now localized on the bottom boundary (see the bottom row of Fig. 3). This new boundary state forms a non-contractible loop with the bulk bands in accordance with the non-zero value of the winding number W . Here, we directly observe that the bottom boundary is essentially a non-Hermitian Floquet chain that is glued to a trivial insulator with $W_3 = 0$.

The breakdown of the bulk-boundary correspondence has previously been observed in many different non-Hermitian static systems [22–29]. In these system, the breakdown is a consequence of the non-Hermitian skin effect, in which bulk states are exponentially localized upon the introduction of an open boundary condition, leading to a significant change in the energy spectrum. In our case of an anomalous Floquet insulator, the bulk quasienergies do not depend on the boundary condition. The breakdown of the bulk-boundary correspondence is a consequence of the spectral detachment between bulk and boundary states induced through BSE. The conventional bulk-boundary correspondence is immediately recovered when the non-Hermitian boundary is cut off.

By setting $\alpha = 0$, the bottom boundary is cut off from the remaining lattice and can be regarded as a separate one-dimensional chain. The trajectories for perfect coupling are shown in Fig. 2(c). The two counterpropagating bulk states of the chain coincide with the boundary states of Fig. 2(b) in terms of both trajectories and quasienergies. We again have $W(\Gamma) = 1$ for $\gamma > 0$ and $W(\Gamma) = -1$ for $\gamma < 0$ with the imaginary gap $i\Gamma$ at $\Gamma = \gamma$. Note that there is no spatial overlap between the wave functions of the two bulk states for perfect coupling.

For non-perfect coupling, this is no longer the case. Therefore, the imaginary gap only persists for sufficiently large values of γ . The critical value γ_c , at which the imaginary gap closes, follows from the eigenvalues of $\hat{U}(k)$ for the chain, analogous to Ref. [19]. The two eigenvalues are

$$e^{-i\epsilon_{1,2}(k)} = e^{\gamma} \left(1 - 2 \sin^2 J \cos^2 \kappa \pm 2 \sin J \cos \kappa \sqrt{\sin^2 J \cos^2 \kappa - 1} \right), \quad (4)$$

with $\kappa = k/2 + i\gamma/2$. The topological phase transition between a trivial chain with $W = 0$ and a non-trivial chain with $W = 1$ occurs when the square root in Eq. (4) vanishes, which happens at $\gamma = \pm\gamma_c$ for $\gamma_c(J) = 2 \operatorname{arcosh}(1/\sin |J|)$.

The critical value γ_c is generally larger than the value of γ at which the boundary state detachment occurs for $\alpha = 1$. This is due to the spatial overlap between the counterpropagating bulk states in the chain for $\alpha = 0$ which reduces the imaginary gap induced by BSE. The various scenarios that emerge in the present driving protocol after the bottom boundary has been cut off are shown in Fig. 4. In all cases, we recover the conventional bulk-boundary correspondence in the anomalous Floquet insulator. Non-Hermitian Floquet chains with non-zero winding numbers are generated if γ is above the critical value γ_c as in the

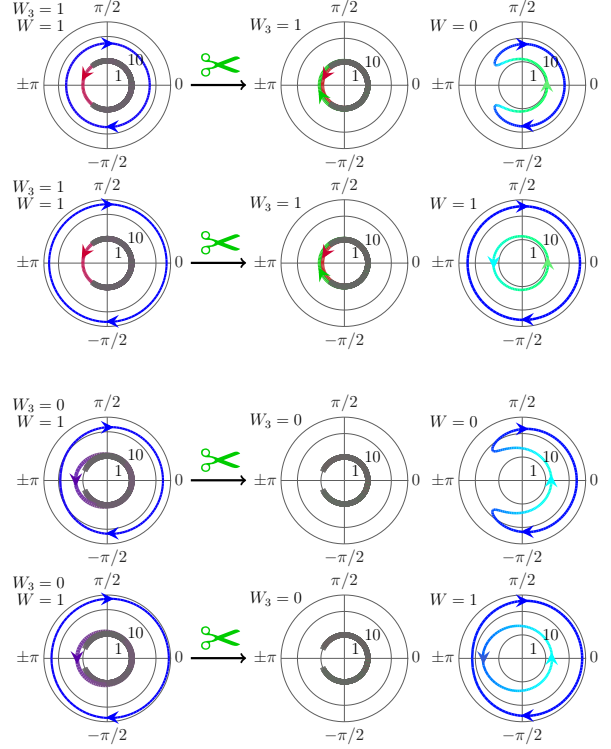


Fig. 4: Same as Fig. 3, now showing the spectra before ($\alpha = 1$, left panels) and after ($\alpha = 0$, central and right panels) the bottom boundary has been cut off. In the top row we use the parameters $J = \gamma = 1$, in the second row we use $J = 1$, $\gamma = 1.8$, in the third row we use $J = 0.7$, $\gamma = 1.8$, and in the bottom row we use $J = 0.7$, $\gamma = 2.1$. In all panels, we have $N_y = 20$. The color of the curves now indicates the amplitude distribution of the eigenfunctions on the red, blue, gray, and green colored area of the lattice in Fig. 2(c).

second and fourth row of Fig. 4.

In conclusion, non-Hermitian Floquet chains can be constructed from the non-Hermitian boundaries of two-dimensional anomalous Floquet insulators. The crucial aspect in this construction is the imaginary gap created with the help of BSE. The imaginary gap provides topological protection for the spectrally detached boundary states irrespective of the bulk topology. Our construction enables a straightforward experimental realization of non-Hermitian Floquet chains by exploiting existing experimental designs [15–18] for anomalous Floquet insulators. The present model can be implemented in photonic waveguide lattices [15,16]. In that context, the BSE could be realized through waveguide bending [30].

An interesting route for future research is the application of our procedure to symmetry-protected anomalous Floquet topological phases or systems with different spatial dimensionality [12]. We expect that by cutting off the

boundaries from other anomalous Floquet insulators, e.g. those with fermionic time-reversal symmetry [18,21], novel non-Hermitian Floquet topological phases will emerge, which may also possess interesting (quantized) transport properties.

REFERENCES

- [1] HASAN M. Z. and KANE C. L., *Rev. Mod. Phys.*, **82** (2010) 3045.
<https://link.aps.org/doi/10.1103/RevModPhys.82.3045>
- [2] QI X.-L. and ZHANG S.-C., *Rev. Mod. Phys.*, **83** (2011) 1057.
<https://link.aps.org/doi/10.1103/RevModPhys.83.1057>
- [3] CHIU C.-K., TEO J. C. Y., SCHNYDER A. P. and RYU S., *Rev. Mod. Phys.*, **88** (2016) 035005.
<https://link.aps.org/doi/10.1103/RevModPhys.88.035005>
- [4] OZAWA T., PRICE H. M., AMO A., GOLDMAN N., HAFEZI M., LU L., RECHTSMAN M. C., SCHUSTER D., SIMON J., ZILBERBERG O. and CARUSOTTO I., *Rev. Mod. Phys.*, **91** (2019) 015006.
<https://link.aps.org/doi/10.1103/RevModPhys.91.015006>
- [5] KANE C. L. and MELE E. J., *Phys. Rev. Lett.*, **95** (2005) 146802.
<https://link.aps.org/doi/10.1103/PhysRevLett.95.146802>
- [6] KÖNIG M., WIEDMANN S., BRÜNE C., ROTH A., BUHMANN H., MOLENKAMP L. W., QI X.-L. and ZHANG S.-C., *Science*, **318** (2007) 766.
<http://science.sciencemag.org/content/318/5851/766>
- [7] KITAGAWA T., BERG E., RUDNER M. and DEMLER E., *Phys. Rev. B*, **82** (2010) 235114.
<http://link.aps.org/doi/10.1103/PhysRevB.82.235114>
- [8] RUDNER M. S., LINDNER N. H., BERG E. and LEVIN M., *Phys. Rev. X*, **3** (2013) 031005.
<http://link.aps.org/doi/10.1103/PhysRevX.3.031005>
- [9] HÖCKENDORF B., ALVERMANN A. and FEHSKE H., *J. Phys. A*, **50** (2017) 295301.
<http://stacks.iop.org/1751-8121/50/i=29/a=295301>
- [10] NATHAN F. and RUDNER M. S., *New J. Phys.*, **17** (2015) 125014.
<http://stacks.iop.org/1367-2630/17/i=12/a=125014>
- [11] HÖCKENDORF B., ALVERMANN A. and FEHSKE H., *Phys. Rev. B*, **97** (2018) 045140.
<https://link.aps.org/doi/10.1103/PhysRevB.97.045140>
- [12] ROY R. and HARPER F., *Phys. Rev. B*, **96** (2017) 155118.
<https://link.aps.org/doi/10.1103/PhysRevB.96.155118>
- [13] TITUM P., BERG E., RUDNER M. S., REFAEL G. and LINDNER N. H., *Phys. Rev. X*, **6** (2016) 021013.
<https://link.aps.org/doi/10.1103/PhysRevX.6.021013>
- [14] HÖCKENDORF B., ALVERMANN A. and FEHSKE H., *Phys. Rev. B*, **99** (2019) 245102.
<https://link.aps.org/doi/10.1103/PhysRevB.99.245102>
- [15] MACZEWSKY L. J., ZEUNER J. M., NOLTE S. and SZAMEIT A., *Nat. Comm.*, **8** (2017) 13756.
<http://dx.doi.org/10.1038/ncomms13756>
- [16] MUKHERJEE S., SPRACKLEN A., VALIENTE M., ANDERSSON E., ÖHBERG P., GOLDMAN N. and THOMSON R. R., *Nat. Comm.*, **8** (2017) 13918.
<http://dx.doi.org/10.1038/ncomms13918>
- [17] PENG Y.-G., QIN C.-Z., ZHAO D.-G., SHEN Y.-X., XU X.-Y., BAO M., JIA H. and ZHU X.-F., *Nat. Comm.*, **7** (2016) 13368.
<https://doi.org/10.1038/ncomms13368>
- [18] MACZEWSKY L. J., HÖCKENDORF B., KREMER M., BIESENTHAL T., HEINRICH M., ALVERMANN A., FEHSKE H. and SZAMEIT A., *Nat. Mater.*, (2020) .
<https://doi.org/10.1038/s41563-020-0641-8>
- [19] HÖCKENDORF B., ALVERMANN A. and FEHSKE H., *arXiv:1911.11413*, (2019) .
<https://arxiv.org/abs/1911.11413>
- [20] FEDOROVA Z., QIU H., LINDEN S. and KROHA J., *arXiv:1911.03770*, (2019) .
<https://arxiv.org/abs/1911.03770>
- [21] HÖCKENDORF B., ALVERMANN A. and FEHSKE H., *Phys. Rev. Lett.*, **123** (2019) 190403.
<https://link.aps.org/doi/10.1103/PhysRevLett.123.190403>
- [22] GONG Z., ASHIDA Y., KAWABATA K., TAKASAN K., HIGASHIKAWA S. and UEDA M., *Phys. Rev. X*, **8** (2018) 031079.
<https://link.aps.org/doi/10.1103/PhysRevX.8.031079>
- [23] ZHOU H. and LEE J. Y., *Phys. Rev. B*, **99** (2019) 235112.
<https://link.aps.org/doi/10.1103/PhysRevB.99.235112>
- [24] KAWABATA K., SHIOZAKI K., UEDA M. and SATO M., *Phys. Rev. X*, **9** (2019) 041015.
<https://link.aps.org/doi/10.1103/PhysRevX.9.041015>
- [25] YAO S. and WANG Z., *Phys. Rev. Lett.*, **121** (2018) 086803.
<https://link.aps.org/doi/10.1103/PhysRevLett.121.086803>
- [26] YAO S., SONG F. and WANG Z., *Phys. Rev. Lett.*, **121** (2018) 136802.
<https://link.aps.org/doi/10.1103/PhysRevLett.121.136802>
- [27] LEE C. H. and THOMALE R., *Phys. Rev. B*, **99** (2019) 201103.
<https://link.aps.org/doi/10.1103/PhysRevB.99.201103>
- [28] KUNST F. K., EDVARDSSON E., BUDICH J. C. and BERGHOLTZ E. J., *Phys. Rev. Lett.*, **121** (2018) 026808.
<https://link.aps.org/doi/10.1103/PhysRevLett.121.026808>
- [29] HELBIG T., HOFMANN T., IMHOF S., ABDELGHANY M., KIESSLING T., MOLENKAMP L. W., LEE C. H., SZAMEIT A., GREITER M. and THOMALE R., *arXiv:1906.08782*, (2019) .

Bastian Höckendorf *et al.*

- <https://arxiv.org/abs/1907.11562>
[30] WEIMANN S., KREMER M., PLOTNIK Y., LUMER Y.,
NOLTE S., MAKRIS K. G., SEGEV M., RECHTSMAN
M. C. and SZAMEIT A., *Nat. Mater.*, **16** (2016) 433.
<https://doi.org/10.1038/nmat4811>

Bibliography

- [1] T. Kitagawa, E. Berg, M. Rudner, and E. Demler, Phys. Rev. B **82**, 235114 (2010).
- [2] M. S. Rudner, N. H. Lindner, E. Berg, and M. Levin, Phys. Rev. X **3**, 031005 (2013).
- [3] M. Z. Hasan and C. L. Kane, Rev. Mod. Phys. **82**, 3045 (2010).
- [4] X.-L. Qi and S.-C. Zhang, Rev. Mod. Phys. **83**, 1057 (2011).
- [5] B. A. Bernevig and T. L. Hughes, *Topological Insulators and Topological Superconductors* (Princeton University Press, 2013).
- [6] K. v. Klitzing, G. Dorda, and M. Pepper, Phys. Rev. Lett. **45**, 494 (1980).
- [7] B. A. Bernevig and S.-C. Zhang, Phys. Rev. Lett. **96**, 106802 (2006).
- [8] B. A. Bernevig, T. L. Hughes, and S.-C. Zhang, Science **314**, 1757 (2006).
- [9] M. König, S. Wiedmann, C. Brüne, A. Roth, H. Buhmann, L. W. Molenkamp, X.-L. Qi, and S.-C. Zhang, Science **318**, 766 (2007).
- [10] D. Hsieh, D. Qian, L. Wray, Y. Xia, Y. S. Hor, R. J. Cava, and M. Z. Hasan, Nature **452**, 970 (2008).
- [11] M. C. Rechtsman, J. M. Zeuner, Y. Plotnik, Y. Lumer, D. Podolsky, F. Dreisow, S. Nolte, M. Segev, and A. Szameit, Nature **496**, 196 (2013).
- [12] T. Kitagawa, T. Oka, A. Brataas, L. Fu, and E. Demler, Phys. Rev. B **84**, 235108 (2011).
- [13] N. H. Lindner, G. Refael, and V. Galitski, Nat. Phys. **7**, 490 (2011).
- [14] Z. Gu, H. A. Fertig, D. P. Arovas, and A. Auerbach, Phys. Rev. Lett. **107**, 216601 (2011).
- [15] C.-K. Chiu, J. C. Y. Teo, A. P. Schnyder, and S. Ryu, Rev. Mod. Phys. **88**, 035005 (2016).
- [16] D. J. Thouless, M. Kohmoto, M. P. Nightingale, and M. den Nijs, Phys. Rev. Lett. **49**, 405 (1982).
- [17] C. L. Kane and E. J. Mele, Phys. Rev. Lett. **95**, 146802 (2005).
- [18] G. M. Graf and C. Tauber, Ann. Henri Poincaré **19**, 709 (2018).
- [19] F. Nathan and M. S. Rudner, New J. Phys. **17**, 125014 (2015).

- [20] B. Höckendorf, A. Alvermann, and H. Fehske, *J. Phys. A* **50**, 295301 (2017).
- [21] Z. Yan, B. Li, X. Yang, and S. Wan, *Sci. Rep.* **5**, 16197 (2015).
- [22] B. Höckendorf, A. Alvermann, and H. Fehske, *Phys. Rev. B* **97**, 045140 (2018).
- [23] T. Kitagawa, M. S. Rudner, E. Berg, and E. Demler, *Phys. Rev. A* **82**, 033429 (2010).
- [24] D. Leykam, M. C. Rechtsman, and Y. D. Chong, *Phys. Rev. Lett.* **117**, 013902 (2016).
- [25] D. Carpentier, P. Delplace, M. Fruchart, and K. Gawędzki, *Phys. Rev. Lett.* **114**, 106806 (2015).
- [26] B. Höckendorf, A. Alvermann, and H. Fehske, *Phys. Rev. B* **99**, 245102 (2019).
- [27] K. Wintersperger, C. Braun, F. N. Ünal, A. Eckardt, M. Di Liberto, N. Goldman, I. Bloch, and M. Aidelsburger, *arXiv:2002.09840* (2020).
- [28] T. Ozawa, H. M. Price, A. Amo, N. Goldman, M. Hafezi, L. Lu, M. C. Rechtsman, D. Schuster, J. Simon, O. Zilberberg, and I. Carusotto, *Rev. Mod. Phys.* **91**, 015006 (2019).
- [29] A. Szameit and S. Nolte, *J. Phys. B* **43**, 163001 (2010).
- [30] L. J. Maczewsky, J. M. Zeuner, S. Nolte, and A. Szameit, *Nat. Comm.* **8**, 13756 (2017).
- [31] S. Mukherjee, A. Spracklen, M. Valiente, E. Andersson, P. Öhberg, N. Goldman, and R. R. Thomson, *Nat. Comm.* **8**, 13918 (2017).
- [32] L. J. Maczewsky, B. Höckendorf, M. Kremer, T. Biesenthal, M. Heinrich, A. Alvermann, H. Fehske, and A. Szameit, *Nat. Mater.* (2020).
- [33] Z. Gong, Y. Ashida, K. Kawabata, K. Takasan, S. Higashikawa, and M. Ueda, *Phys. Rev. X* **8**, 031079 (2018).
- [34] K. Kawabata, K. Shiozaki, M. Ueda, and M. Sato, *Phys. Rev. X* **9**, 041015 (2019).
- [35] H. Zhou and J. Y. Lee, *Phys. Rev. B* **99**, 235112 (2019).
- [36] H. Shen, B. Zhen, and L. Fu, *Phys. Rev. Lett.* **120**, 146402 (2018).
- [37] S. Yao and Z. Wang, *Phys. Rev. Lett.* **121**, 086803 (2018).
- [38] S. Yao, F. Song, and Z. Wang, *Phys. Rev. Lett.* **121**, 136802 (2018).
- [39] Z. Lin, H. Ramezani, T. Eichelkraut, T. Kottos, H. Cao, and D. N. Christodoulides, *Phys. Rev. Lett.* **106**, 213901 (2011).
- [40] G. Harari, M. A. Bandres, Y. Lumer, M. C. Rechtsman, Y. D. Chong, M. Khajavikhan, D. N. Christodoulides, and M. Segev, *Science* **359**, eaar4003 (2018).

-
- [41] M. A. Bandres, S. Wittek, G. Harari, M. Parto, J. Ren, M. Segev, D. N. Christodoulides, and M. Khajavikhan, *Science* **359**, eaar4005 (2018).
- [42] A. Regensburger, C. Bersch, M.-A. Miri, G. Onishchukov, D. N. Christodoulides, and U. Peschel, *Nature* **488**, 167 (2012).
- [43] S. Weimann, M. Kremer, Y. Plotnik, Y. Lumer, S. Nolte, K. G. Makris, M. Segev, M. C. Rechtsman, and A. Szameit, *Nat. Mater.* **16**, 433 (2016).
- [44] J. M. Zeuner, M. C. Rechtsman, Y. Plotnik, Y. Lumer, S. Nolte, M. S. Rudner, M. Segev, and A. Szameit, *Phys. Rev. Lett.* **115**, 040402 (2015).
- [45] C. H. Lee and R. Thomale, *Phys. Rev. B* **99**, 201103 (2019).
- [46] J. Y. Lee, J. Ahn, H. Zhou, and A. Vishwanath, *Phys. Rev. Lett.* **123**, 206404 (2019).
- [47] T. Helbig, T. Hofmann, S. Imhof, M. Abdelghany, T. Kiessling, L. W. Molenkamp, C. H. Lee, A. Szameit, M. Greiter, and R. Thomale, arXiv:1906.08782 (2019).
- [48] P. Titum, E. Berg, M. S. Rudner, G. Refael, and N. H. Lindner, *Phys. Rev. X* **6**, 021013 (2016).
- [49] F. Nathan, M. S. Rudner, N. H. Lindner, E. Berg, and G. Refael, *Phys. Rev. Lett.* **119**, 186801 (2017).
- [50] A. Kundu, M. Rudner, E. Berg, and N. H. Lindner, *Phys. Rev. B* **101**, 041403 (2020).
- [51] F. Nathan, D. Abanin, E. Berg, N. H. Lindner, and M. S. Rudner, *Phys. Rev. B* **99**, 195133 (2019).
- [52] F. Nathan, D. A. Abanin, N. H. Lindner, E. Berg, and M. S. Rudner, arXiv:1907.12228 (2019).
- [53] S. Mukherjee and M. C. Rechtsman, arXiv:1911.05260 (2019).
- [54] T. Dittrich, P. Hanggi, G.-L. Ingold, B. Kramer, G. Schön, and W. Zwerger, *Quantum Transport and Dissipation* (Wiley-VCH, 1997).
- [55] T. Fukui, Y. Hatsugai, and H. Suzuki, *J. Phys. Soc. Jpn.* **74**, 1674 (2005).
- [56] L. Fu and C. L. Kane, *Phys. Rev. B* **74**, 195312 (2006).
- [57] T. Fukui and Y. Hatsugai, *J. Phys. Soc. Jpn.* **76**, 053702 (2007).
- [58] D. J. Thouless, *Phys. Rev. B* **27**, 6083 (1983).
- [59] R. Roy and F. Harper, *Phys. Rev. B* **96**, 155118 (2017).
- [60] S. Yao, Z. Yan, and Z. Wang, *Phys. Rev. B* **96**, 195303 (2017).
- [61] M. Fruchart, *Phys. Rev. B* **93**, 115429 (2016).

- [62] M. Lababidi, I. I. Satija, and E. Zhao, *Phys. Rev. Lett.* **112**, 026805 (2014).
- [63] I. C. Fulga and M. Maksymenko, *Phys. Rev. B* **93**, 075405 (2016).
- [64] L. Zhou, H. Wang, Y. D. Ho, and J. Gong, *Eur. Phys. J. B* **87**, 1 (2014).
- [65] M. Hafezi, S. Mittal, J. Fan, A. Migdall, and J. M. Taylor, *Nat. Phot.* **7**, 1001 (2013).
- [66] J. Ningyuan, C. Owens, A. Sommer, D. Schuster, and J. Simon, *Phys. Rev. X* **5**, 021031 (2015).
- [67] R. Süsstrunk and S. D. Huber, *Science* **349**, 47 (2015).
- [68] X. Cheng, C. Jouvaud, X. Ni, S. H. Mousavi, A. Z. Genack, and A. B. Khanikaev, *Nat. Mater.* **15**, 542 (2016).
- [69] A. P. Slobozhanyuk, A. B. Khanikaev, D. S. Filonov, D. A. Smirnova, A. E. Miroshnichenko, and Y. S. Kivshar, *Sci. Rep.* **6**, 22270 (2016).
- [70] C. He, X.-C. Sun, X.-P. Liu, M.-H. Lu, Y. Chen, L. Feng, and Y.-F. Chen, *Proc. Natl. Acad. Sci. USA* **113**, 4924 (2016).
- [71] R. Keil, C. Poli, M. Heinrich, J. Arkininstall, G. Weihs, H. Schomerus, and A. Szaemitt, *Phys. Rev. Lett.* **116**, 213901 (2016).
- [72] Z. Fedorova, H. Qiu, S. Linden, and J. Kroha, *arXiv:1911.03770* (2019).
- [73] W. D. Heiss, *J. Phys. A* **45**, 444016 (2012).
- [74] K. Kawabata, T. Bessho, and M. Sato, *Phys. Rev. Lett.* **123**, 066405 (2019).
- [75] J. Li, A. K. Harter, J. Liu, L. de Melo, Y. N. Joglekar, and L. Luo, *Nat. Comm.* **10**, 855 (2019).

Scientific contributions

- (a) “*Efficient computation of the W_3 topological invariant and application to Floquet-Bloch systems*”
B. Höckendorf, A. Alvermann and H. Fehske, *J. Phys. A* **50**, 295301 (2017).
Copyright (2017) by IOP Publishing Ltd.
- (b) “*Topological invariants for Floquet-Bloch systems with chiral, time-reversal, or particle-hole symmetry*”
B. Höckendorf, A. Alvermann and H. Fehske, *Phys. Rev. B* **97**, 045140 (2018).
Copyright (2018) by the American Physical Society.
- (c) “*Universal driving protocol for symmetry-protected Floquet topological phases*”
B. Höckendorf, A. Alvermann and H. Fehske, *Phys. Rev. B* **99**, 245102 (2019).
Copyright (2019) by the American Physical Society.
- (d) “*Non-Hermitian Boundary State Engineering in Anomalous Floquet Topological Insulators*”
B. Höckendorf, A. Alvermann and H. Fehske, *Phys. Rev. Lett.* **123**, 190403 (2019). Copyright (2019) by the American Physical Society.
- (e) “*Fermionic time-reversal symmetry in a photonic topological insulator*”
L. J. Maczewsky, B. Höckendorf, M. Kremer, T. Biesenthal, M. Heinrich, A. Alvermann, H. Fehske and A. Szameit, *Nat. Mat.*, (2020). Copyright (2020) by Springer Nature.
- (f) “*Non-Hermitian Floquet Chains as Topological Charge Pumps*”
B. Höckendorf, A. Alvermann and H. Fehske, submitted to *Phys. Rev. Lett.*
- (g) “*Cutting off the non-Hermitian boundary from an anomalous Floquet topological insulator*”
B. Höckendorf, A. Alvermann and H. Fehske, submitted to *Europhys. Lett.*

Acknowledgement

I want to thank everyone who supported and encouraged me over the past years. My deepest gratitude goes to Prof. Dr. Holger Fehske and Dr. Andreas Alvermann who guided me through my Bachelor, Master, and now PhD studies with unwavering support. The scope and quality of this thesis would not have been possible without the expertise and help of Andreas. I also want to thank the group of Prof. Dr. Alexander Szameit, in particular Lukas Maczewsky, for the successful collaboration on the photonic \mathbb{Z}_2 insulator.

Finally, I wish to thank my family and friends for their love and affection.